

Quantitative appearance comparison of BIPV products to existing building materials

Sustainable Energy

Master Thesis



Appearance comparison of BIPV products to existing building materials
Sustainable Energy

Master Thesis
June 30, 2023

By
Pedro José Morenilla Murillo (s212747)

Copyright: Reproduction of this publication in whole or in part must include the customary bibliographic citation, including author attribution, report title, etc.

Cover photo: Vibeke Hempler, 2012

Published by: DTU, Department of Electrical and Photonics Engineering, Ørsteds Plads, Building 343, 2800 Kgs. Lyngby, Denmark
<https://electro.dtu.dk/>

Approval

This thesis has been prepared over five months at the Section for BIPV, Department of electrical and Photonics Engineering, at the Technical University of Denmark, DTU, in partial fulfilment for the degree Master of Sustainable Energy, MSc Eng.

It is assumed that the reader has basic knowledge in solar energy, engineering and basic programming.

Pedro José Morenilla Murillo - s212747

.....
Signature

.....
Date

Contents

Preface	ii
Contents	iii
Abstract	v
Acknowledgements	vi
List of Figures	vii
List of Tables	xiv
Acronyms	xv
1 Introduction	1
1.1 Motivation	1
1.2 Thesis structure	2
2 Theoretical background	3
2.1 Previous research	4
2.2 Radiometry and photometry	5
2.3 Bidirectional Reflectance Distribution Function (BRDF) measurement	6
2.4 Colorimetry	7
2.5 State of the art in Building Integrated Photovoltaics (BIPV) and construction materials	11
3 BRDF methodology	16
3.1 Setup description	17
3.2 Calculations	19
3.3 White Reference	24
3.4 Colorimetry transformations	28
4 Construction materials and BIPV samples	30
4.1 Construction materials	31
4.2 BIPV samples	33
5 Results presentation	36
5.1 RT 811 Yellow Roof Tile	37
5.2 RT 845 Laumans Glazed Black	39
5.3 RT 840 Højslev Lille Black	40
5.4 RT 844 Laumans Red	41
5.5 RT 841 Laumans Dark Red	43
5.6 Faro Vidar Clay Shingles	45

5.7	Natural Black Slate	46
6	Other results	48
6.1	Theoretical RGB vs Practical RGB	49
6.2	Quantitative color difference	50
6.3	Measurement uncertainty	54
7	Results analysis and further research	61
7.1	Results analysis	61
7.2	Further Research	63
8	Conclusions	64
	Bibliography	65
A	Appendix A	69
A.1	RT 811 Yellow Roof Tile	69
A.2	RT 845 Laumans Glazed Black	72
A.3	RT 840 Højslev Lille Black	79
A.4	RT 844 Laumans Red	83
A.5	RT 841 Laumans Dark Red	86
A.6	Faro Vidar Clay Shingles	89
A.7	Natural Black Slate	93
B	Appendix B	98
B.1	Reproducibility of Black BIPV	99
B.2	Reproducibility of Komproment	100
B.3	Reproducibility of Komproment Rotated	101
B.4	Reproducibility of Black Slate	102
B.5	Reproducibility of Black Slate Rotated	103
B.6	Reproducibility of Black Tile	104
B.7	Reproducibility of Black Tile Rotated	105
B.8	Reproducibility of Clear Red BIPV	106
B.9	Reproducibility of Clear Red Tile	107
B.10	Reproducibility of Clear Red Tile Rotated	108
B.11	Reproducibility of Dark Red BIPV	109
B.12	Reproducibility of Dark Red Tile	110
B.13	Reproducibility of Dark Red Tile Rotated	111
B.14	Reproducibility of Glazed Black Tile	112
B.15	Reproducibility of Glazed Black Tile Rotated	113
B.16	Reproducibility of Gold BIPV	114
B.17	Reproducibility of Normal Black BIPV	115
B.18	Reproducibility of Red BIPV	116
B.19	Reproducibility of Special Black BIPV	117
B.20	Reproducibility of Special Black BIPV Rotated	118
B.21	Reproducibility of Yellow BIPV	119
B.22	Reproducibility of Yellow Tile	120
B.23	Reproducibility of Yellow Tile Rotated	121

Abstract

The rapid growth of BIPV technology has led to an increasing demand for visually harmonious solar products that seamlessly integrate with conventional construction materials. This master thesis aims to investigate the appearance comparison between BIPV products and traditional construction materials, providing valuable insights into their visual integration.

The comparison is carried out using a setup capable of measuring the BRDF of the samples. These measurements are then converted into color coordinates for the purpose of comparison. Two distinct sets of samples are utilized for the comparative analysis: construction materials from different manufacturers and BIPV samples. The comparison is conducted quantitatively and qualitatively, with an additional focus on assessing the replicability of the results.

The findings reveal variations among the samples, highlighting a significant disparity between the two fields. Samples with high reflectance exhibit angle-dependent results, leading to increased variability in their measurements. Conversely, satin-finished and smooth samples demonstrate consistent results across different viewing angles. Moreover, the study indicates a high level of replicability even among the construction materials.

These outcomes suggest that there is still a substantial gap between the visual characteristics of BIPV products and conventional construction materials. The results emphasize the importance of considering angle-dependent effects and surface finishes when evaluating their visual integration.

Acknowledgements

I would like to express my sincere gratitude to my family and friends for their unwavering support, encouragement, and understanding throughout my journey in completing this master thesis. Their constant love, belief in my abilities, and motivational words have been instrumental in keeping me focused and motivated during challenging times.

I am deeply grateful to my supervisors, Sune Thorsteinsson and Markus Babin, for their invaluable guidance, expertise, and mentorship throughout this research. Their extensive knowledge, insightful feedback, and unwavering dedication have been instrumental in shaping the direction of this thesis and enhancing its quality. I would also like to extend my gratitude to the PhD student Nanna Lysgaard for her collaboration, support, and valuable insights.

Lastly, I would like to express my sincere appreciation to DTU for providing an enriching learning environment and the necessary resources to undertake this research.

List of Figures

2.1	Munsell scale [22]	8
2.2	BIPV roof example [36].	12
2.3	Transparent BIPV construction example [37].	12
3.1	2D representation of the setup [6]	18
3.2	Real representation of the setup	18
3.3	Sensor position at the plane of illumination	19
3.4	Reflective collimator internal composition [6]	20
3.5	Area correction factor at $\alpha_z = 70$ [6]	21
3.6	k_A correction factor	21
3.7	Sensor geometry [6]	22
3.8	Sample spectral irradiance	23
3.9	White reference sample Radiant flux	24
3.10	White reference sample Radiant flux	25
3.11	Correction factor k_α	26
3.12	Correction factor k_θ	26
3.13	Total BRDF of white reference sample	26
3.14	Spectral BRDF of white reference sample at $\alpha_x=0^\circ$	27
3.15	Spectral BRDF of white reference sample at $\theta=0^\circ$	27
3.16	Spectral BRDF of white reference sample at $\theta=60^\circ$	28
3.17	Spectral BRDF of white reference sample at $\theta=-60^\circ$	28
3.18	XYZ coordinates for a black sample	29
4.1	RT 811 yellow roof tile [49]	31
4.2	RT 845 Laumans Glazed Black [50]	32
4.3	RT 840 Højslev Lille Black [51]	32
4.4	RT 844 Laumans Red [53]	32
4.5	RT 841 Laumans Dark Red [52]	32
4.6	Faro Vidar Clay Shingles [55]	33
4.7	Natural Black Slate [56]	33
4.8	Yellow BIPV sample	33
4.9	Yellow BIPV sample composition	33
4.10	Dark Red BIPV sample	33
4.11	Dark Red BIPV sample composition	33
4.12	Clear Red BIPV sample	34
4.13	Clear Red BIPV sample composition	34
4.14	Red BIPV sample	34
4.15	Red BIPV sample composition	34
4.16	Black BIPV sample	34
4.17	Black BIPV sample composition	34
4.18	Normal Black BIPV sample	35

4.19	Normal Black BIPV sample composition	35
4.20	Gold BIPV sample	35
4.21	Gold BIPV sample composition	35
4.22	Special Black BIPV sample	35
4.23	Special Black BIPV sample composition	35
5.1	Yellow sample	37
5.2	Yellow sample rotated	37
5.3	Yellow Tile L^* comparison at 0°	37
5.4	Yellow Tile L^* comparison at 45°	37
5.5	Yellow Tile a^* comparison at 0°	38
5.6	Yellow Tile a^* comparison at 45°	38
5.7	Yellow Tile b^* comparison at 0°	38
5.8	Yellow Tile b^* comparison at 45°	38
5.9	Black glazed sample	39
5.10	Black glazed sample rotated	39
5.11	Glazed Black Tile L^* comparison at 0°	39
5.12	Total BRDF	40
5.13	Total BRDF in logarithmic scale	40
5.14	Black tile sample	40
5.15	Black tile sample rotated	40
5.16	Black Tile L^* comparison at 0°	41
5.17	Black Tile L^* comparison at 45°	41
5.18	Clear red sample	41
5.19	Clear red sample rotated	41
5.20	Clear Red Tile L^* comparison at 0°	42
5.21	Clear Red Tile L^* comparison at 45°	42
5.22	Clear Red Tile a^* comparison at 0°	42
5.23	Clear Red Tile a^* comparison at 45°	42
5.24	Clear Red Tile b^* comparison at 0°	43
5.25	Clear Red Tile b^* comparison at 45°	43
5.26	Dark red sample	43
5.27	Dark red sample rotated	43
5.28	Dark Red Tile L^* comparison at 0°	44
5.29	Dark Red Tile L^* comparison at 45°	44
5.30	Dark Red Tile a^* comparison at 0°	44
5.31	Dark Red Tile a^* comparison at 45°	44
5.32	Dark Red Tile b^* comparison at 0°	45
5.33	Dark Red Tile b^* comparison at 45°	45
5.34	Black Komproment sample	45
5.35	Black Komproment sample rotated	45
5.36	Black Komproment L^* comparison at 0°	46
5.37	Black Komproment L^* comparison at 45°	46
5.38	Black slate sample	46
5.39	Black slate sample rotated	46
5.40	Black Slate L^* comparison at 0°	47
5.41	Black Slate L^* comparison at 45°	47
6.1	Total BRDF at 0° sample angle for all samples	52
6.2	Total BRDF at 0° sample angle for all samples in logarithmic scale	52
6.3	Reproducibility of Special Black BIPV at 0° sample angle	55

6.4	Reproducibility of Special Black BIPV Rotated at 0° sample angle	55
6.5	Reproducibility of Yellow BIPV at 0° sample angle	55
6.6	Reproducibility of Yellow Tile at 0° sample angle	55
6.7	Reproducibility of Yellow Tile Rotated at 0° sample angle	56
6.8	Reproducibility of Black Tile Rotated at 0° sample angle	56
6.9	Reproducibility of Clear Red BIPV at 0° sample angle	56
6.10	Reproducibility of Clear Red Tile at 0° sample angle	57
6.11	Reproducibility of Clear Red Tile Rotated at 0° sample angle	57
6.12	Reproducibility of Dark Red Tile Rotated at 0° sample angle	57
6.13	Reproducibility of Glazed Tile at 0° sample angle	57
6.14	Reproducibility of Glazed Tile Rotated at 0° sample angle	58
6.15	Reproducibility of Gold BIPV at 0° sample angle	58
6.16	Reproducibility of Dark Red BIPV at 0° sample angle	58
6.17	Reproducibility of Dark Red Tile at 0° sample angle	58
6.18	Reproducibility of Komproment Rotated at 0° sample angle	59
6.19	Reproducibility of Black Slate at 0° sample angle	59
6.20	Reproducibility of Black Slate Rotated at 0° sample angle	59
6.21	Reproducibility of Black Tile at 0° sample angle	59
6.22	Reproducibility of Black BIPV at 0° sample angle	60
6.23	Reproducibility of Komproment at 0° sample angle	60
6.24	Reproducibility of Normal Black BIPV at 0° sample angle	60
6.25	Reproducibility of Red BIPV at 0° sample angle	60
A.1	Yellow Tile L^* comparison at 15°	69
A.2	Yellow Tile L^* comparison at 30°	69
A.3	Yellow Tile L^* comparison at 60°	69
A.4	Yellow Tile L^* comparison at 75°	69
A.5	Yellow Tile a^* comparison at 15°	70
A.6	Yellow Tile a^* comparison at 30°	70
A.7	Yellow Tile a^* comparison at 60°	70
A.8	Yellow Tile a^* comparison at 75°	70
A.9	Yellow Tile b^* comparison at 15°	71
A.10	Yellow Tile b^* comparison at 30°	71
A.11	Yellow Tile b^* comparison at 60°	71
A.12	Yellow Tile b^* comparison at 75°	71
A.13	Glazed Black Tile L^* comparison at 15°	72
A.14	Glazed Black Tile L^* comparison at 30°	72
A.15	Glazed Black Tile L^* comparison at 45°	72
A.16	Glazed Black Tile L^* comparison at 60°	72
A.17	Glazed Black Tile L^* comparison at 75°	73
A.18	Glazed Black Tile a^* comparison at 0°	73
A.19	Glazed Black Tile a^* comparison at 15°	73
A.20	Glazed Black Tile a^* comparison at 30°	74
A.21	Glazed Black Tile a^* comparison at 45°	74
A.22	Glazed Black Tile a^* comparison at 60°	74
A.23	Glazed Black Tile a^* comparison at 75°	74
A.24	Glazed Black Tile b^* comparison at 0°	75
A.25	Glazed Black Tile b^* comparison at 15°	75
A.26	Glazed Black Tile b^* comparison at 30°	75
A.27	Glazed Black Tile b^* comparison at 45°	75

A.28	Glazed Black Tile b^* comparison at 60°	76
A.29	Glazed Black Tile b^* comparison at 75°	76
A.30	Glazed Black Tile BRDF comparison at 15°	76
A.31	Glazed Black Tile BRDF comparison at 30°	76
A.32	Glazed Black Tile BRDF comparison at 45°	77
A.33	Glazed Black Tile BRDF comparison at 60°	77
A.34	Glazed Black Tile BRDF comparison at 75°	77
A.35	Glazed Black Tile logarithmic BRDF comparison at 15°	78
A.36	Glazed Black Tile logarithmic BRDF comparison at 30°	78
A.37	Glazed Black Tile logarithmic BRDF comparison at 45°	78
A.38	Glazed Black Tile logarithmic BRDF comparison at 60°	78
A.39	Glazed Black Tile logarithmic BRDF comparison at 75°	79
A.40	Black Tile L^* comparison at 15°	79
A.41	Black Tile L^* comparison at 30°	79
A.42	Black Tile L^* comparison at 60°	80
A.43	Black Tile L^* comparison at 75°	80
A.44	Black Tile a^* comparison at 0°	80
A.45	Black Tile a^* comparison at 15°	80
A.46	Black Tile a^* comparison at 30°	81
A.47	Black Tile a^* comparison at 45°	81
A.48	Black Tile a^* comparison at 60°	81
A.49	Black Tile a^* comparison at 75°	81
A.50	Black Tile b^* comparison at 0°	82
A.51	Black Tile b^* comparison at 15°	82
A.52	Black Tile b^* comparison at 30°	82
A.53	Black Tile b^* comparison at 45°	82
A.54	Black Tile b^* comparison at 60°	83
A.55	Black Tile b^* comparison at 75°	83
A.56	Clear Red Tile L^* comparison at 15°	83
A.57	Clear Red Tile L^* comparison at 30°	83
A.58	Clear Red Tile L^* comparison at 60°	84
A.59	Clear Red Tile L^* comparison at 75°	84
A.60	Clear Red Tile a^* comparison at 15°	84
A.61	Clear Red Tile a^* comparison at 30°	84
A.62	Clear Red Tile a^* comparison at 60°	85
A.63	Clear Red Tile a^* comparison at 75°	85
A.64	Clear Red Tile b^* comparison at 15°	85
A.65	Clear Red Tile b^* comparison at 30°	85
A.66	Clear Red Tile b^* comparison at 60°	86
A.67	Clear Red Tile b^* comparison at 75°	86
A.68	Dark Red Tile L^* comparison at 15°	86
A.69	Dark Red Tile L^* comparison at 30°	86
A.70	Dark Red Tile L^* comparison at 60°	87
A.71	Dark Red Tile L^* comparison at 75°	87
A.72	Dark Red Tile a^* comparison at 15°	87
A.73	Dark Red Tile a^* comparison at 30°	87
A.74	Dark Red Tile a^* comparison at 60°	88
A.75	Dark Red Tile a^* comparison at 75°	88
A.76	Dark Red Tile b^* comparison at 15°	88
A.77	Dark Red Tile b^* comparison at 30°	88

A.78	Dark Red Tile b^* comparison at 60°	89
A.79	Dark Red Tile b^* comparison at 75°	89
A.80	Black Komproment L^* comparison at 15°	89
A.81	Black Komproment L^* comparison at 30°	89
A.82	Black Komproment L^* comparison at 60°	90
A.83	Black Komproment L^* comparison at 75°	90
A.84	Black Komproment a^* comparison at 0°	90
A.85	Black Komproment a^* comparison at 15°	90
A.86	Black Komproment a^* comparison at 30°	91
A.87	Black Komproment a^* comparison at 45°	91
A.88	Black Komproment a^* comparison at 60°	91
A.89	Black Komproment a^* comparison at 75°	91
A.90	Black Komproment b^* comparison at 0°	92
A.91	Black Komproment b^* comparison at 15°	92
A.92	Black Komproment b^* comparison at 30°	92
A.93	Black Komproment b^* comparison at 45°	92
A.94	Black Komproment b^* comparison at 60°	93
A.95	Black Komproment b^* comparison at 75°	93
A.96	Black Slate L^* comparison at 15°	93
A.97	Black Slate L^* comparison at 30°	93
A.98	Black Slate L^* comparison at 60°	94
A.99	Black Slate L^* comparison at 75°	94
A.100	Black Slate a^* comparison at 0°	94
A.101	Black Slate a^* comparison at 15°	94
A.102	Black Slate a^* comparison at 30°	95
A.103	Black Slate a^* comparison at 45°	95
A.104	Black Slate a^* comparison at 60°	95
A.105	Black Slate a^* comparison at 75°	95
A.106	Black Slate b^* comparison at 0°	96
A.107	Black Slate b^* comparison at 15°	96
A.108	Black Slate b^* comparison at 30°	96
A.109	Black Slate b^* comparison at 45°	96
A.110	Black Slate b^* comparison at 60°	97
A.111	Black Slate b^* comparison at 75°	97
B.1	Black BIPV L^* reproducibility at 15°	99
B.2	Black BIPV L^* reproducibility at 30°	99
B.3	Black BIPV L^* reproducibility at 45°	99
B.4	Black BIPV L^* reproducibility at 60°	99
B.5	Black BIPV L^* reproducibility at 75°	99
B.6	Black Komproment L^* reproducibility at 15°	100
B.7	Black Komproment L^* reproducibility at 30°	100
B.8	Black Komproment L^* reproducibility at 45°	100
B.9	Black Komproment L^* reproducibility at 60°	100
B.10	Black Komproment L^* reproducibility at 75°	100
B.11	Black Komproment Rotated L^* reproducibility at 15°	101
B.12	Black Komproment Rotated L^* reproducibility at 30°	101
B.13	Black Komproment Rotated L^* reproducibility at 45°	101
B.14	Black Komproment Rotated L^* reproducibility at 60°	101
B.15	Black Komproment Rotated L^* reproducibility at 75°	101

B.16	Black Slate L^* reproducibility at 15°	102
B.17	Black Slate L^* reproducibility at 30°	102
B.18	Black Slate L^* reproducibility at 45°	102
B.19	Black Slate L^* reproducibility at 60°	102
B.20	Black Slate L^* reproducibility at 75°	102
B.21	Black Slate Rotated L^* reproducibility at 15°	103
B.22	Black Slate Rotated L^* reproducibility at 30°	103
B.23	Black Slate Rotated L^* reproducibility at 45°	103
B.24	Black Slate Rotated L^* reproducibility at 60°	103
B.25	Black Slate Rotated L^* reproducibility at 75°	103
B.26	Black Tile L^* reproducibility at 15°	104
B.27	Black Tile L^* reproducibility at 30°	104
B.28	Black Tile L^* reproducibility at 45°	104
B.29	Black Tile L^* reproducibility at 60°	104
B.30	Black Tile L^* reproducibility at 75°	104
B.31	Black Tile Rotated L^* reproducibility at 15°	105
B.32	Black Tile Rotated L^* reproducibility at 30°	105
B.33	Black Tile Rotated L^* reproducibility at 45°	105
B.34	Black Tile Rotated L^* reproducibility at 60°	105
B.35	Black Tile Rotated L^* reproducibility at 17°	105
B.36	Clear Red BIPV L^* reproducibility at 15°	106
B.37	Clear Red BIPV L^* reproducibility at 30°	106
B.38	Clear Red BIPV L^* reproducibility at 45°	106
B.39	Clear Red BIPV L^* reproducibility at 60°	106
B.40	Clear Red BIPV L^* reproducibility at 75°	106
B.41	Clear Red Tile L^* reproducibility at 15°	107
B.42	Clear Red Tile L^* reproducibility at 30°	107
B.43	Clear Red Tile L^* reproducibility at 45°	107
B.44	Clear Red Tile L^* reproducibility at 60°	107
B.45	Clear Red Tile L^* reproducibility at 75°	107
B.46	Clear Red Tile Rotated L^* reproducibility at 15°	108
B.47	Clear Red Tile Rotated L^* reproducibility at 30°	108
B.48	Clear Red Tile Rotated L^* reproducibility at 45°	108
B.49	Clear Red Tile Rotated L^* reproducibility at 60°	108
B.50	Clear Red Tile Rotated L^* reproducibility at 75°	108
B.51	Dark Red BIPV L^* reproducibility at 15°	109
B.52	Dark Red BIPV L^* reproducibility at 30°	109
B.53	Dark Red BIPV L^* reproducibility at 45°	109
B.54	Dark Red BIPV L^* reproducibility at 60°	109
B.55	Dark Red BIPV L^* reproducibility at 75°	109
B.56	Dark Red Tile L^* reproducibility at 15°	110
B.57	Dark Red Tile L^* reproducibility at 30°	110
B.58	Dark Red Tile L^* reproducibility at 45°	110
B.59	Dark Red Tile L^* reproducibility at 60°	110
B.60	Dark Red Tile L^* reproducibility at 75°	110
B.61	Dark Red Tile Rotated L^* reproducibility at 15°	111
B.62	Dark Red Tile Rotated L^* reproducibility at 30°	111
B.63	Dark Red Tile Rotated L^* reproducibility at 45°	111
B.64	Dark Red Tile Rotated L^* reproducibility at 60°	111
B.65	Dark Red Tile Rotated L^* reproducibility at 75°	111

B.66	Glazed Black Tile L^* reproducibility at 15°	112
B.67	Glazed Black Tile L^* reproducibility at 30°	112
B.68	Glazed Black Tile L^* reproducibility at 45°	112
B.69	Glazed Black Tile L^* reproducibility at 60°	112
B.70	Glazed Black Tile L^* reproducibility at 75°	112
B.71	Glazed Black Tile Rotated L^* reproducibility at 15°	113
B.72	Glazed Black Tile Rotated L^* reproducibility at 30°	113
B.73	Glazed Black Tile Rotated L^* reproducibility at 45°	113
B.74	Glazed Black Tile Rotated L^* reproducibility at 60°	113
B.75	Glazed Black Tile Rotated L^* reproducibility at 75°	113
B.76	Gold BIPV L^* reproducibility at 15°	114
B.77	Gold BIPV L^* reproducibility at 30°	114
B.78	Gold BIPV L^* reproducibility at 45°	114
B.79	Gold BIPV L^* reproducibility at 60°	114
B.80	Gold BIPV L^* reproducibility at 75°	114
B.81	Normal Black BIPV L^* reproducibility at 15°	115
B.82	Normal Black BIPV L^* reproducibility at 30°	115
B.83	Normal Black BIPV L^* reproducibility at 45°	115
B.84	Normal Black BIPV L^* reproducibility at 60°	115
B.85	Normal Black BIPV L^* reproducibility at 75°	115
B.86	Red BIPV L^* reproducibility at 15°	116
B.87	Red BIPV L^* reproducibility at 30°	116
B.88	Red BIPV L^* reproducibility at 45°	116
B.89	Red BIPV L^* reproducibility at 60°	116
B.90	Red BIPV L^* reproducibility at 75°	116
B.91	Special Black BIPV L^* reproducibility at 15°	117
B.92	Special Black BIPV L^* reproducibility at 30°	117
B.93	Special Black BIPV L^* reproducibility at 45°	117
B.94	Special Black BIPV L^* reproducibility at 60°	117
B.95	Special Black BIPV L^* reproducibility at 75°	117
B.96	Special Black BIPV Rotated L^* reproducibility at 15°	118
B.97	Special Black BIPV Rotated L^* reproducibility at 30°	118
B.98	Special Black BIPV Rotated L^* reproducibility at 45°	118
B.99	Special Black BIPV Rotated L^* reproducibility at 60°	118
B.100	Special Black BIPV Rotated L^* reproducibility at 75°	118
B.101	Yellow BIPV L^* reproducibility at 15°	119
B.102	Yellow BIPV L^* reproducibility at 30°	119
B.103	Yellow BIPV L^* reproducibility at 45°	119
B.104	Yellow BIPV L^* reproducibility at 60°	119
B.105	Yellow BIPV L^* reproducibility at 75°	119
B.106	Yellow Tile L^* reproducibility at 15°	120
B.107	Yellow Tile L^* reproducibility at 30°	120
B.108	Yellow Tile L^* reproducibility at 45°	120
B.109	Yellow Tile L^* reproducibility at 60°	120
B.110	Yellow Tile L^* reproducibility at 75°	120
B.111	Yellow Tile Rotated L^* reproducibility at 15°	121
B.112	Yellow Tile Rotated L^* reproducibility at 30°	121
B.113	Yellow Tile Rotated L^* reproducibility at 45°	121
B.114	Yellow Tile Rotated L^* reproducibility at 60°	121
B.115	Yellow Tile Rotated L^* reproducibility at 75°	121

List of Tables

- 2.1 Radiometric variables 5
- 3.1 Laboratory equipment 17
- 3.2 Parameters of the reflective collimator used as sensor 17
- 6.1 Construction materials RGB coordinates 49
- 6.2 Construction materials RGB coordinates 50
- 6.3 Yellow Tile comparison matrix 50
- 6.4 Clear Red Tile comparison matrix 51
- 6.5 Dark Red Tile comparison matrix 51
- 6.6 Glazed Black Tile comparison matrix 51
- 6.7 Black Tile comparison matrix 51
- 6.8 Black Komproment comparison matrix 51
- 6.9 Black Slate comparison matrix 51
- 6.10 Yellow Tile comparison matrix modified 52
- 6.11 Clear Red Tile comparison matrix modified 53
- 6.12 Dark Red Tile comparison matrix modified 53
- 6.13 Glazed Black Tile comparison matrix modified 53
- 6.14 Black Tile comparison matrix modified 53
- 6.15 Black Komproment comparison matrix modified 53
- 6.16 Black Slate comparison matrix modified 53

Acronyms

AOI	Angle of Incidence
BAPV	Building Applied Photovoltaics
BIPV	Building Integrated Photovoltaics
BRDF	Bidirectional Reflectance Distribution Function
BSDF	Bidirectional Scattering Distribution Function
CIE	International Commission on Illumination
CMFs	Color Matching Functions
IAM	Incidence Angle Modifier
IEA	International Energy Agency
LDLS	Laser-Driven Light Source
Mono-Si	Monocrystalline Silicon
OAP	Off-Axis Parabolic
POE	Polyolefin Elastomer
PV	Photovoltaic
SPD	Spectral Power Distribution
UV	Ultra-Violet
2BB	Two Busbars

1 Introduction

1.1 Motivation

The world today faces a great challenge in the form of climate change, which has prompted global efforts to reduce greenhouse gas emissions and move towards cleaner energy alternatives, mainly in the occidental countries [1]. One of the key areas for reducing emissions is the building sector, which accounts for a significant portion of global energy consumption [2]. In this context, BIPV has emerged as a promising technology that can help reduce emissions by generating renewable energy from building envelopes.

BIPV products can be integrated into the building envelope in a number of ways, such as solar shingles, solar facades, and solar windows. These products not only generate electricity but also offer additional benefits such as improved thermal insulation and noise reduction. However, the adoption of BIPV products has been slow due to a lack of awareness and limited research on their performance and cost-effectiveness.

This thesis aims to contribute to the growing body of research on BIPV products by comparing their appearance to existing building materials, being this the main objective. The comparison will be based on characteristics such as spectral reflectance, color, and color difference. A matrix will be used to quantify the visual difference of BIPV products and traditional building materials, such as asphalt shingles, metal roofing, tile roofing, etc. This matrix will include variables such as differences in chroma or lightness between BIPV and construction materials. Additionally, the secondary objective of the thesis is to provide a methodology for the comparison, setting the ground for future research.

One of the key advantages of BIPV products is their ability to generate electricity from sunlight, which is a renewable and abundant energy source. According to the International Energy Agency (IEA), solar energy will have to grow at a rate of 25% per year in the period 2022-2030 in order to meet the Net Zero Emissions target of 2050 [3]. The use of BIPV products can help reduce the dependence on fossil fuels and contribute to a more sustainable energy future.

Moreover, BIPV products can help reduce the energy consumption of buildings by generating electricity on-site, thereby reducing the need for grid-supplied electricity. This can result in significant cost savings for building owners and occupants, as well as reduce the strain on the electric grid during peak hours.

In addition to their energy benefits, BIPV products can also enhance the aesthetic appeal of buildings. With advancements in technology, BIPV products are now available in a variety of colors and textures, which can be customized to match the architectural style and design of a building [4]. This is particularly important in older neighbourhoods where the visual character of the buildings is an important aspect of their cultural heritage.

In summary, this thesis aims to contribute to the growing body of research on BIPV products by comparing their appearance to traditional building materials. BIPV products offer a number of advantages over traditional building materials, including the generation of renewable energy and cost savings. Additionally, it presents some advantages over Building Applied Photovoltaics (BAPV), such as improved aesthetic appeal. The matrix comparison of the visual appearance of BIPV products and traditional building materials will provide important information for architects, builders, and designers considering the use of BIPV products in building

design. This study will contribute to a better understanding of the potential and performance of BIPV products, and help promote their adoption in building design for a more sustainable future.

1.2 Thesis structure

This scientific master thesis is structured into several sections to ensure a logical flow of information and facilitate understanding. Section 2 provides the theoretical background, exploring relevant frameworks, concepts, and literature that form the foundation of the study. Section 3 outlines the research methodology, including the design, approach, and data collection methods employed in the study.

Section 4 describes the sample utilized in the research, including the criteria and process of sample selection.

Moving forward, Section 5 presents the results obtained from data analysis, utilizing visual aids for clear interpretation and highlighting significant patterns or relationships. Section 6 discusses additional calculations or statistical analyses performed, providing further insights into the research findings. Section 7 interprets the results in relation to the theoretical framework and existing literature, addressing any unexpected or contrasting findings and discussing their implications. Additionally, it suggests avenues for further research.

Finally, Section 8 offers conclusions drawn from the study.

2 Theoretical background

This section provides a theoretical background for the analysis conducted in this research, focusing on colorimetry, the state-of-the-art in BIPV and construction materials, the BRDF, and radiometry and photometry.

In Section 2.1, an examination of past studies on color comparisons between construction materials and BIPV products underscores the necessity for additional investigation in this field. The subsequent sections focus on different aspects of color assessment. Section 2.2 delves into radiometry and photometry, elucidating their importance in objective color assessment. Section 2.3 explores the BRDF and its role in modeling and analyzing surface appearance. Colorimetry, which is crucial for evaluating color differences between materials, is introduced in Section 2.4. Lastly, Section 2.5 presents an overview of the state-of-the-art in BIPV and construction materials, underscoring their influence on color assessment practices.

These sections establish a theoretical foundation for evaluating color differences between construction materials and BIPV products, contributing to the advancement of knowledge in this field.

2.1 Previous research

A brief review of the prior research will be presented to provide an overview of the current state of the field.

The first presents a comprehensive investigation of the solar properties of different types of construction materials [5]. The study aimed to assess the directional and angular response of the materials by measuring their BRDF. The authors used an experimental setup consisting of a gonireflectometer to measure the BRDF of different materials, including roof tiles, thermal insulation, and plaster. The results showed that the materials have different BRDF curves depending on the angle of incidence and the viewing angle. The authors also found that some materials, such as roof tiles, have a strong specular reflection, while others, such as insulation, have a diffuse reflection. Overall, the study concludes that the BRDF curves are an essential tool for characterizing the solar properties of construction materials. The authors suggest that the BRDF data can be used to improve the accuracy of energy simulations and optimize the design of BIPV systems. The research provides valuable insights into the solar properties of construction materials and lays the foundation for further investigations in this field.

Markus Babin's master thesis, titled "Experimental characterization of angular dependent color perception of colored Photovoltaic (PV) samples in combination with Incidence Angle Modifier (IAM) measurements targeting building integrated photovoltaic products," offers valuable insights into the evaluation of BIPV samples. The thesis presents a thorough analysis of coloration technologies used in BIPV and provides references to expected values and distributions of color and BRDF results. This research is particularly relevant as it validates the results obtained from the BRDF setup employed in the current study [6]. Furthermore, it includes an in-depth examination of colors for various BIPV materials, some of which will be utilized in the ongoing research project. By leveraging Babin's work, the current study aims to build upon his findings and contribute to the advancement of knowledge in BIPV color assessment.

In relation to the absolute color difference thresholds, previous research [7] has established a color difference scale ranging from 0 to 100. However, for the purposes of the current study, which focuses on comparing the appearance of materials, the color difference needs to be minimal and barely perceptible. As a result, the threshold for this study is narrowed down to a range of 0 to 10, with the objective of keeping the difference below 2. This level of difference is only noticeable under close scrutiny.

Furthermore, studies conducted on human teeth provide valuable insights for establishing color difference thresholds. It should be noted that human teeth require a more stringent difference in order to be considered acceptable by individuals. Therefore, the threshold determined in these studies is narrower than what might be expected for building materials. For instance, research indicates that the acceptability threshold for differences in lightness (ΔL^*) is 2.5 points, with perceptibility occurring at levels above 0.74 [8]. In contrast, when considering absolute differences, the perceptible difference is 1.9, with the limit for acceptability being 4.2 [9]. Based on these findings, it can be concluded that the perceptible limit for color difference lies within the range of 2-2.5, while the acceptable limit extends to approximately 4-4.5 for absolute values. It is worth noting that these thresholds are particularly stringent for lightness values.

In conclusion, The absence of research on color comparison between construction materials and BIPV products is noteworthy. Therefore, this study is the first attempt to evaluate the color difference between these two materials. Prior investigations have examined the BRDF curves of construction materials, evaluated the color of BIPV materials, and analyzed color differences in other areas. However, this research provides a novel perspective on color comparison between construction materials and BIPV products, initiating a new chapter in the field.

2.2 Radiometry and photometry

This section draws inspiration and reference from Markus Babin's thesis [6] and the book on Radiometry and Photometry [10]. It provides a concise summary of the key characteristics relevant to this project. For a more comprehensive understanding, it is recommended to refer to the original sources.

2.2.1 Radiometric variables

To provide a comprehensive explanation of the calculation process, it is essential to introduce the primary radiometric variables. Notably, it is important to emphasize the distinction in notation. The subscript "s" will be employed when referring to the spectrometer, while the subscript "n" will be used for the sample under test. Furthermore, the subscripts "l" and "OAP" will be used when referring to the light source or the Off-Axis Parabolic (OAP) mirrors. Table 2.1 shows the variables in integral and spectral form.

Table 2.1: Radiometric variables

Variable	Integral		Spectral	
	Symbol	Unit	Symbol	Unit
Radiant Flux / Spectral Flux	Φ	W	Φ_λ	W/nm
Radiant Intensity / Spectral Intensity	I_Ω	W/sr	$I_{\lambda,\Omega}$	W/nm/sr
(Spectral) Radiance	L_Ω	W/m ² /sr	$L_{\lambda,\Omega}$	W/nm/m ² /sr
(Spectral) Irradiance	E	W/m ²	E_λ	W/nm/m ²
Radiant Exitance / Spectral Exitance	M	W/m ²	M_λ	W/nm/m ²

The table presented highlights two distinct types of variables. Firstly, there are non-directional variables, including radiant flux, which represents the total power received or reflected by a surface. Additionally, there are irradiance and exitance, which denote the respective quantities per unit of area.

The second type of variables pertains to directionality, specifically the solid angle from which power is received or reflected. These variables encompass intensity and radiance, with the latter requiring consideration of the projected area. Equation 2.1 illustrates the influence of the projected area, where ϕ represents the angle between the surface normal and the respective direction.

$$L_\Omega(\phi) = \frac{\partial^2 \Phi}{\partial \Omega \cdot \partial A \cos \phi} \quad (2.1)$$

2.2.2 Specular and diffuse properties

Reflections from the surface of a material can be classified into two main categories: specular reflection and diffuse reflection [10].

Specular reflection refers to the mirror-like reflection of light from a smooth surface. When light rays hit a smooth surface, they bounce off at the same angle of incidence, resulting in a well-defined reflection. Specular reflections produce a clear and focused image or reflection.

Diffuse reflection occurs when light rays hit a rough or textured surface. The light is scattered in various directions upon reflection, resulting in a diffused or scattered reflection. Unlike specular reflection, diffuse reflection does not produce a well-defined or focused image. Instead, it

creates a more dispersed reflection with reduced intensity [11].

It's important to note that in real-world scenarios, surfaces often exhibit a combination of specular and diffuse reflection, with the proportion of each depending on the surface properties and incident light conditions.

2.2.3 Lambertian reflectors

Lambertian reflectors, also known as Lambertian surfaces or Lambertian materials, are idealized surfaces that exhibit a specific type of diffuse reflection. They are named after Johann Heinrich Lambert, a mathematician and physicist who studied the behavior of light and surfaces [12].

Lambertian reflectors are commonly used as reference surfaces in photometry and radiometry due to their predictable and uniform light reflection characteristics. They serve as a standard for calibration and measurement purposes, allowing for accurate comparisons and calculations of light intensity and illuminance. For the present thesis, a white reference sample will be used, presented in chapter 3.

Mathematically, Lambertian reflection follows Lambert's cosine law, which states that the intensity of reflected light is proportional to the cosine of the angle between the surface normal and the direction of the incident light [10]. This relationship holds true for perfectly diffuse and idealized Lambertian surfaces.

To determine the total reflectance of a perfectly Lambertian sample, a single measurement of $L_{\Omega,n}$ is sufficient, as indicated in equation 2.2. The detailed calculation procedure is illustrated in [6]. This methodology enables the accurate assessment of the sample's overall reflectance properties, streamlining the measurement process and facilitating reliable results.

$$M_n = \pi L_{\Omega,n} \quad (2.2)$$

2.3 BRDF measurement

BRDF is a mathematical function that describes the way that a surface reflects light in a 3D environment. It provides a quantitative measure of how light is reflected from a surface in different directions, and it can be used to model the way that surfaces look under different lighting conditions [13].

BRDF is important in computer graphics, computer vision, and remote sensing, as it can be used to create realistic images and animations, analyze images and extract information from them, and model the way that surfaces reflect light in different environments.

The BRDF is usually represented as a 4D function which takes as input the incoming and outgoing directions of the light and the surface reflectance properties (such as diffuse, specular, etc.). Some models of BRDF are physically based and others are empirical, based on measurements of real surfaces. As the main objective of this thesis is the color difference between objects, the spectral BRDF will be the one of the most interest (B_λ). The valid equation for calculating the BRDF is Equation (2.3), which requires some adjustments depending on the studied output.

$$B(\phi_i, \theta_i, \phi_r, \theta_r) = \frac{dL_{\Omega,r}(\phi_r, \theta_r)}{dE_{\Omega,i}(\phi_i, \theta_i)} = \frac{dL_{\Omega,r}(\phi_r, \theta_r)}{L_{\Omega,i}(\phi_i, \theta_i)d\Omega_i} \quad (2.3)$$

It is crucial to acknowledge that the BRDF is a complex function that can present challenges in its comprehensive analysis and understanding. Nevertheless, for practical purposes, many

surfaces can be effectively approximated using simpler and more manageable models [14]. Moreover, it is worth noting that the BRDF remains invariant when reversing the angles of incidence and reflectance, which provides flexibility in its application [15].

A spectrometer is a device that is used to measure the BRDF of a surface. These devices are used to measure the way that a surface reflects light in different directions, and they are typically used in research and development for computer graphics, computer vision, and remote sensing [16].

It typically consists of a light source, a camera, and a sample holder. The sample holder holds the surface that is being measured, and the light source illuminates the surface from different directions. The camera captures images of the surface as it is illuminated, and the images are then used to calculate the BRDF of the surface. Some of these devices can also measure absolute reflectance and can be used to measure surface reflectance properties at different angles and different wavelength ranges. It is important to note that these characteristics can vary depending on the type of construction material and its surface finish. Gonioreflectometry is a powerful tool that can accurately measure these characteristics, providing architects and builders with valuable information when selecting and evaluating construction materials [17]. The measurements obtained with a gonioreflectometer can be used to compare different construction materials and help to choose the most appropriate one for a specific project in terms of visual appearance, energy efficiency, and durability. Additionally, the BRDF measurement device can be used to evaluate the performance of construction material over time, such as how it ages and how it is affected by environmental factors, providing valuable information for the maintenance and durability of the building.

2.4 Colorimetry

Colorimetry is the scientific study of color and the perception of color [18]. It involves measuring and quantifying the characteristics of color, such as hue, chroma, lightness, brightness, and saturation. These characteristics can be used to create a color space, which is a mathematical representation of all the possible colors that can be perceived by the human eye.

The perception of color can be affected by various factors, including the lighting conditions, the background against which the color is viewed, and the individual's own visual system [19]. For example, the same color can appear differently under different lighting conditions, such as natural daylight versus artificial fluorescent lighting. Similarly, the same color can appear different against different backgrounds, such as light-colored walls versus dark-colored walls.

To assess the difference between colors, it is first necessary to introduce the key parameters that allow this comparison.

Hue is one of the main characteristics of a color and refers to the attribute that allows us to distinguish between red, blue, green, yellow, and so on [20]. Hue is determined by the dominant wavelength of light that is reflected or emitted from an object. In other words, it is the pure color of the light, without any variation or shading. Hue is often described as a color's name, such as red, blue, or green. Although it is difficult to assess a number, hue can be quantified using some of the existing color scales/spaces, such as the Munsell color system, which is a color space that organizes colors based on three dimensions: hue, value, and chroma. In this system, hue is represented by a circular arrangement of colors, with each color assigned a specific hue angle. The hue angle is measured in degrees and represents the position of a color on the color wheel, with red at 0°, yellow at 60°, green at 120°, and blue at 240°. Other hues fall in between these primary and secondary hues, creating a continuous spectrum of colors. By assigning each color

a hue angle, it becomes possible to numerically quantify the hue of a color [21].

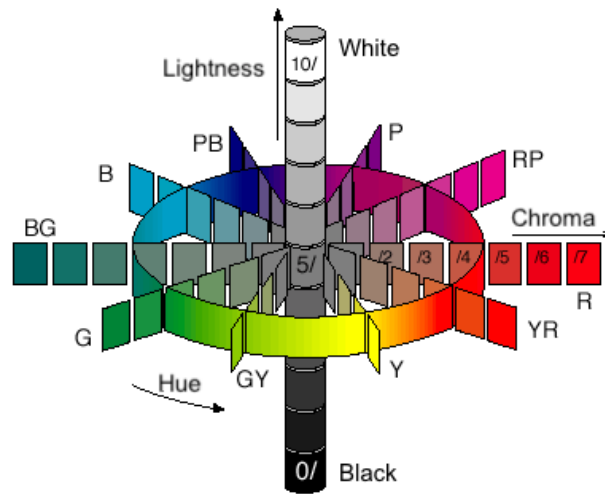


Figure 2.1: Munsell scale [22]

Saturation describes the intensity of a color in relation to pure grey [20]. It is a measure of how vivid or intense a color appears. Chroma, on the other hand, is an absolute term that can be measured on a scale and describes the purity or strength of a color. While both saturation and chroma are measures of color intensity, they differ in their reference points. Saturation is judged in proportion to brightness, while chroma is judged as a proportion of the brightness of a similarly illuminated area that appears white or highly transmitting [23].

Perceived saturation can vary depending on factors such as wavelength and light level. For example, colors of equal luminance may appear less saturated at medium wavelengths (green) than at short or long wavelengths (blue and red). Additionally, saturation can appear most intense at intermediate light levels.

Lightness and brightness can be assessed for any color [24]. Lightness refers to the relative amount of light reflected by an object or its relative brightness normalized for changes in illumination and viewing conditions. It is a measure of how light or dark something appears. Brightness refers to how much light appears to shine from something. Understanding these concepts can be useful for color appearance because they help us understand how colors are perceived under different lighting conditions. For example, a bright red apple would have a high level of both lightness and brightness because it reflects a lot of light and appears to shine brightly. A dark blue object, on the other hand, would have a low level of lightness because it reflects less light but could still have a high level of brightness if it appears to shine brightly. Different wavelengths of light correspond to different colors. The human eye is most sensitive to green light with a wavelength of around 555 nanometers (nm). This means that a given number of green photons per second will appear brighter than the same number of red photons [25].

2.4.1 Color perception

Color perception is the process through which the human brain interprets and responds to different frequencies of light waves detected by the eyes. This complex process involves two fundamental principles: metamerism and trichromacy.

Metamerism refers to the intriguing phenomenon where two colors can appear identical despite being composed of different light wavelengths. It occurs because the human eye possesses

three types of color receptors, or cones, which are sensitive to distinct parts of the visible light spectrum. When different wavelengths of light stimulate these cones in the same way, they create a consistent perception of color, even though the physical stimuli may vary [26].

Trichromacy, on the other hand, explains how the human eye can perceive millions of distinct colors by combining the responses of three different types of cones: red-sensitive, green-sensitive, and blue-sensitive cones. The brain can distinguish between various levels of hue, saturation, and brightness by adjusting the stimulation of each cone type [27].

The perception of color in an object can be influenced by the spectral distribution and intensity of the light source. This can result in metamerism, where different light sources illuminate the same object, leading to variations in color appearance. Therefore, when comparing and measuring the color of materials and products, it is crucial to consider the lighting conditions.

Color vision deficiencies, also known as color blindness, affect a significant portion of the population and can cause reduced sensitivity to specific colors or an inability to distinguish certain hues. This has implications for the selection and design of materials and products that rely on color coding or identification.

To address the challenges associated with metamerism, trichromacy, and color perception, the International Commission on Illumination (CIE) has played a crucial role [28]. The CIE developed the RGB and XYZ color spaces in 1931, enabling the replication of any perceivable color by the human eye using three primary colors. Additionally, the CIE established the 1931 CIE 2° standard observer, which accounts for perceptive differences between cones and rods in the human eye by assuming a view angle of 2°. This standard observer facilitated the conversion of measured spectra into XYZ tristimulus values, forming the basis for modern color spaces and measurement techniques.

In addition, it is essential to consider various color measurement techniques, such as colorimetry and spectrophotometry, and their strengths and limitations in different applications. This consideration helps in selecting the most suitable technique for measuring the color of construction materials and BIPV products.

One widely used color system is XYZ, chosen primarily for its ease of conversion to other color spaces and its widespread adoption in engineering and color science. By understanding the principles of color perception and employing appropriate measurement techniques, researchers and practitioners can accurately analyze and compare the colors of different materials and products [10].

2.4.2 Color matching

The CIE 1931 XYZ color space serves as a standard reference for describing colors in colorimetry [29]. It is based on three imaginary primaries, X, Y, and Z, which mimic the human eye's response to color stimuli. These primaries are designed to be independent, allowing any color to be represented as a combination of these three [30].

To calculate the XYZ coordinates of a color, the color's Spectral Power Distribution (SPD) and Color Matching Functions (CMFs) are needed. The SPD describes the light energy emitted or reflected at each visible wavelength, while the CMFs represent the sensitivity of the three cone cells in the human retina responsible for color vision.

To ensure normalization of the XYZ values, the CIE introduced the CIE Standard Observer, represented by modified color matching functions ($\bar{x}(\lambda)$, $\bar{y}(\lambda)$, and $\bar{z}(\lambda)$). These modifications normalize the XYZ values, with the Y value representing the luminance factor of the color.

The CIE Standard Observer was established through experiments involving observers with nor-

mal color vision. By matching spectral colors to mixtures of red, green, and blue primary lights, the resulting color matching functions were standardized in 1931, forming the basis for colorimetric calculations.

To calculate the XYZ coordinates, the spectral reflectance or transmittance of the color is measured. This data is multiplied by the CIE Standard Observer CMFs and integrated over the visible spectrum, yielding the XYZ tristimulus values. The Y value is normalized using a constant k to ensure equal luminance. The CIE has defined standard illuminants, with the most commonly used being the CIE Standard Illuminant D65, representing average daylight.

The normalization factor k is determined by transforming the XYZ tristimulus values to the CIE 1931 XYZ color space. The formula for k involves the spectral distribution of the standard illuminant ($S(\lambda)$) and the spectral reflectance of the color ($R(\lambda)$) [10].

$$\begin{aligned}
 X &= k \int R(\lambda)S(\lambda)\bar{x}(\lambda)d\lambda \\
 Y &= k \int R(\lambda)S(\lambda)\bar{y}(\lambda)d\lambda \\
 Z &= k \int R(\lambda)S(\lambda)\bar{z}(\lambda)d\lambda \\
 k &= 100 / \int S(\lambda)\bar{y}(\lambda)d\lambda
 \end{aligned} \tag{2.4}$$

The resulting X, Y, and Z values represent the tristimulus values of the color in the XYZ color space. These values can be further utilized to calculate chromaticity coordinates (x, y) and luminance (Y) for various color applications such as color matching and reproduction.

It's important to note that the calculation of XYZ coordinates is a mathematical model approximating human perception of color. While the XYZ color space serves as a useful standard for color measurement and specification, it does not fully capture the complexity and variability of human color vision.

2.4.3 Color spaces

The XYZ color space is a tristimulus color space that represents color as a combination of three values: X, Y, and Z. While the XYZ coordinates are useful for color matching, they are not intuitive or perceptually uniform. Therefore, they are not the ideal representation for color.

CIELAB and CIELUV are two color spaces that were developed by the CIE to address the limitations of the XYZ color space [31]. They are designed to be more perceptually uniform, which means that differences in color can be more accurately measured and represented. In these color spaces, a color difference of a certain value corresponds to a perceptually uniform difference in color.

CIELAB is a three-dimensional color space that describes color using three values: L^* , a^* , and b^* . The L^* value represents the lightness of the color, with $L^*=0$ representing black and $L^*=100$ representing white. The a^* and b^* values represent the color's position on the red-green and blue-yellow axes, respectively. Positive a^* values indicate redness, while negative a^* values indicate greenness. Positive b^* values indicate yellowness, while negative b^* values indicate blueness. In order to calculate the CIELAB coordinates, a white reference is needed (X_n , Y_n and Z_n). Finally the hue h_{ab} and chroma C^*_{ab} are calculated too [32].

$$L^* = 116f\left(\frac{Y}{Y_n} - 16\right) \tag{2.5}$$

$$a^* = 500(f(\frac{X}{X_n}) - f(\frac{Y}{Y_n})) \quad (2.6)$$

$$b^* = 200(f(\frac{Y}{Y_n}) - f(\frac{Z}{Z_n})) \quad (2.7)$$

$$f(t) = \begin{cases} \sqrt[3]{t} & \text{for } t > (\frac{6}{29})^3 \\ t \cdot \frac{1}{3}(\frac{29}{6})^2 + \frac{4}{29} & \text{otherwise} \end{cases} \quad (2.8)$$

$$C_{ab}^* = \sqrt{a^{*2} + b^{*2}} \quad (2.9)$$

$$h_{ab} = \arctan_2(\frac{b^*}{a^*}) \quad (2.10)$$

CIELUV, on the other hand, is also a three-dimensional color space, but it uses different axes than CIELAB. The L^* value in CIELUV represents lightness in the same way as in CIELAB. The u^* and v^* values in CIELUV represent the chromaticity of the color, with negative u^* values indicating a shift towards the red end of the spectrum, and negative v^* values indicating a shift towards the yellow end of the spectrum. Additionally, an equation for saturation s_{uv}^* is added.

$$u^* = 13L^*(u' - u'_n) \quad (2.11)$$

$$v^* = 13L^*(v' - v'_n) \quad (2.12)$$

$$u' = \frac{4X}{X + 15Y + 3Z} \quad (2.13)$$

$$v' = \frac{9Y}{X + 15Y + 3Z} \quad (2.14)$$

$$C_{uv}^* = \sqrt{u^{*2} + v^{*2}} \quad (2.15)$$

$$h_{uv} = \arctan_2(\frac{v^*}{u^*}) \quad (2.16)$$

$$s_{uv} = \frac{C_{uv}^*}{L^*} \quad (2.17)$$

2.4.4 RGB coordinates

The conversion of CIELAB values to RGB coordinates is not a standardized process and lacks a universal method. However, there are various software programs and online tools available that facilitate this conversion. In this thesis, Matlab will be employed to obtain the normalized sRGB values. Subsequently, to obtain the final RGB values, the sRGB values will be multiplied by 255 to eliminate the 1-scale and ensure compatibility with the RGB color space.

2.5 State of the art in BIPV and construction materials

BIPV is a type of PV technology that is designed to be integrated into the structure of a building, such as a roof or walls. BIPV systems generate electricity while also providing protection and insulation to the building, which allows them to replace traditional building materials such as roofing or siding [33].

BIPV systems have several advantages. Despite that the electricity generation is lower compared to a normal PV system (due to being integrated in a construction material and adding extra layers or changing the color) [34], it can increase the energy efficiency of the building [35]. BIPV

systems can generate electricity while also providing insulation and protection to the building, which can reduce the overall energy consumption of the building. Aesthetics is one of the key factors of BIPV systems against BAPV, which can be designed to match the appearance of the building and can be used as a design element. Durability is another advantage, BIPV systems are designed to last as long as the building itself, which can reduce the need for maintenance or replacement.

However, BIPV systems also have some disadvantages. For a construction or energy-related product, the cost is vital to decide. BIPV systems can be more expensive than traditional building materials and PV systems, which should be compensated with energy generation. The flexibility is limited in BIPV systems, which are integrated into the building structure, limiting the flexibility of the building design and the options for future expansion or renovation. Finally, BIPV systems can be more complex to install and maintain than traditional PV systems.

Overall, BIPV systems are becoming a more popular option for generating electricity in buildings, as they can help increase energy efficiency and reduce the environmental impact of buildings. Figures 2.2 and 2.3 can show the different BIPV options discussed above.



Figure 2.2: BIPV roof example [36].



Figure 2.3: Transparent BIPV construction example [37].

BIPV products are a type of building material that can be used to substitute several traditional building materials such as roofs, façades and glasses. Roofing and facade materials are essential components of any building, providing protection from the elements and giving the building its characteristic appearance. Here are the most commonly used materials for roofing and facade construction [38]:

- Tiles: Tiles are a popular roofing material that can be made from clay or concrete. They are durable, long-lasting, and offer excellent insulation against heat and cold. They come in a variety of colors and shapes, which can add an attractive look to any building. However, they are heavy and require a strong support structure.
- Concrete: Concrete is a versatile and durable material that is commonly used for both roofing and facades. It can be poured into any shape or size, and is relatively inexpensive. It is also fire-resistant and can withstand harsh weather conditions. However, it can be heavy and require additional support, and may crack over time due to expansion and contraction.
- Brick: Brick is a traditional material that is commonly used for facade construction. It is durable, fire-resistant, and requires minimal maintenance. It also has a unique aesthetic appeal that can add value to any building. However, it is heavy and may require additional support, and can be expensive compared to other materials.

- **Stone:** Stone is a natural material that can be used for both roofing and facade construction. It is durable, long-lasting, and requires little maintenance. It also has a unique and attractive appearance that can add value to any building. However, it is heavy and may require additional support, and can be expensive compared to other materials.
- **Metal:** Metal roofing and facade materials are becoming increasingly popular due to their durability, low maintenance, and modern aesthetic appeal. They can be made of various metals, such as steel, aluminum, copper, or zinc. They are also lightweight and easy to install, which can reduce construction time and cost. However, they can be noisy during rain or hail, and may dent or scratch over time.
- **Shingles:** Shingles are a popular roofing material that can be made of various materials, such as asphalt, wood, or metal. They are easy to install, relatively inexpensive, and come in a variety of colors and shapes. However, they may not be as durable as other roofing materials, and may require more maintenance over time.

In summary, each roofing and facade material has its own advantages and disadvantages [39]. The choice of material depends on several factors, such as budget, climate, building type, and aesthetic preferences. In Denmark, concrete tiles, concrete, and metal are commonly used for roofing and facade construction, while brick and stone are more commonly used for traditional and historic buildings [40].

2.5.1 Color difference

Color difference is a measure of the perceptual difference between two colors. It is an important factor in assessing the difference between BIPV materials and construction materials because the visual appearance of a building is an important consideration in architectural design. If the color difference between the BIPV and construction materials is too great, it can affect the overall aesthetic of the building. It is important to assess the color difference in a quantitative way so that architects and designers can make informed decisions about the color of building materials. This can help to ensure that the building has a harmonious visual appearance.

In Denmark, as in other regions, color difference is an important consideration in architectural design. In architectural practice, ensuring a uniform color for building materials is often a requirement in compliance with regulatory standards and industry best practices. BIPV materials are becoming increasingly popular in Denmark and other regions, and it is important to consider the color difference between these materials and traditional construction materials to ensure that the building has a harmonious visual appearance.

As color difference is a crucial aspect in color science, several numerical methods have been developed to calculate it. Some of the most widely used methods are CIEDE2000 and one based on the CIELAB color space. These methods consider the variation in lightness, chroma, and hue between two colors. The CIELAB color space is the fundamental one used for computing the color difference. It involves calculating the Euclidean distance between two points in the space using the formula:

$$\Delta E_{ab} = \sqrt{\Delta L^2 + \Delta a^2 + \Delta b^2} \quad (2.18)$$

However, this approach doesn't account for the human perception of color, which can vary significantly [41]. To overcome this limitation, the CIE developed another formula, CIEDE2000, which yields results that are more closely related to the human perception of color. This function provides a more accurate differentiation in the Lightness (L^*) and blue region of the space.

Thus, the CIEDE2000 formula is often preferred for color difference calculations, especially in industries where color accuracy is essential, such as textiles and graphic design [42].

$$\Delta E_{00} = \sqrt{\left(\frac{\Delta L}{k_L * S_L}\right)^2 + \left(\frac{\Delta C}{k_C * S_C}\right)^2 + \left(\frac{\Delta H}{k_H * S_H}\right)^2 + R_T * \frac{\Delta C}{k_C * S_C} * \frac{\Delta H}{k_H * S_H}} \quad (2.19)$$

$$\Delta L = L_2^* - L_1^* \quad (2.20)$$

$$\bar{L} = \frac{L_2^* + L_1^*}{2} \quad (2.21)$$

$$\bar{C} = \frac{C_2^* + C_1^*}{2} \quad (2.22)$$

$$a'_1 = a_1^* + \frac{a_1^*}{2} \left(1 - \sqrt{\frac{\bar{C}^7}{\bar{C}^7 + 25^7}}\right) \quad (2.23)$$

$$a'_2 = a_2^* + \frac{a_2^*}{2} \left(1 - \sqrt{\frac{\bar{C}^7}{\bar{C}^7 + 25^7}}\right) \quad (2.24)$$

$$C' = \frac{C'_1 + C'_2}{2} \quad (2.25)$$

$$\Delta C' = C'_2 - C'_1 \quad (2.26)$$

$$C'_1 = \sqrt{a_1'^2 + b_1^{*2}} \quad (2.27)$$

$$C'_2 = \sqrt{a_2'^2 + b_2^{*2}} \quad (2.28)$$

$$h'_1 = \text{atan}_2(b_1^*, a_1') \quad \text{mod} \quad 360^\circ \quad (2.29)$$

$$h'_2 = \text{atan}_2(b_2^*, a_2') \quad \text{mod} \quad 360^\circ \quad (2.30)$$

$$\Delta h' = \begin{cases} h'_2 - h'_1 & \text{for } |h'_1 - h'_2| \leq 180 \\ h'_2 - h'_1 + 360 & \text{for } |h'_1 - h'_2| > 180, h'_2 \leq h'_1 \\ h'_2 - h'_1 - 360 & \text{for } |h'_1 - h'_2| > 180, h'_2 > h'_1 \end{cases} \quad (2.31)$$

$$\Delta H' = 2\sqrt{C'_1 C'_2} \sin(\Delta h'/2) \quad (2.32)$$

$$H' = \begin{cases} (h'_2 + h'_1)/2 & \text{for } |h'_1 - h'_2| \leq 180 \\ (h'_2 + h'_1 + 360)/2 & \text{for } |h'_1 - h'_2| > 180, h'_2 + h'_1 < 360 \\ (h'_2 + h'_1 - 360)/2 & \text{for } |h'_1 - h'_2| > 180, h'_2 + h'_1 \geq 360 \end{cases} \quad (2.33)$$

$$T = 1 - 0.17 \cos(\bar{H}' - 30) + 0.24 \cos(2\bar{H}') + 0.32 \cos(3\bar{H}' + 6) - 0.2 \cos(4\bar{H}' - 63) \quad (2.34)$$

$$S_L = 1 + \frac{0.015(\bar{L} - 50)^2}{\sqrt{20 + (\bar{L} - 50)^2}} \quad (2.35)$$

$$S_C = 1 + 0.045\bar{C}' \quad (2.36)$$

$$S_H = 1 + 0.015\bar{C}'T \quad (2.37)$$

$$R_T = -2\sqrt{\frac{\bar{C}'^7}{\bar{C}'^7 + 25^7}} \sin\left[60 \cdot \exp\left(-\left[\frac{\bar{H}' - 275}{25}\right]^2\right)\right] \quad (2.38)$$

In conclusion, the CIEDE2000 function is a complex color difference formula that takes into account the non-linear relationship between color differences and color perception. It provides a better differentiation of color differences in the lightness and chromaticity regions of the color

space. The formula includes various corrections, such as the hue rotation function, which helps to solve the known hue distortion problem. The resulting value of the CIEDE2000 function represents the closest numerical approximation to the perceptual color difference between two colors. Its implementation requires a precise knowledge of the initial and target colors, and it is widely used in many applications, such as color quality control in the textile and printing industries, colorimetric analyses in digital imaging, and color matching in graphic design and interior decoration.

3 BRDF methodology

The appearance of BIPV materials is critical in determining their acceptance in construction. One way to assess their appearance is through the measurement of their BRDF. The BRDF measurement provides a quantitative description of the way in which light is reflected from a surface in different directions and is influenced by surface properties such as roughness, gloss, and color. In this section, we present the methodology used to measure the BRDF of the BIPV samples and compare it with that of the construction materials.

Part 3.1 describes the setup used for the BRDF measurements, including the instrumentation and the measurement geometry. Part 3.2 details the BRDF calculations and analysis, including the evaluation of the shape and symmetry of the reflectance profile. Part 3.3 explains the white reference correction to remove any systematic errors in the BRDF measurements. Furthermore, in Part 3.4, the transformations from BRDF measurements to colorimetry results are elucidated.

3.1 Setup description

This section presents a comprehensive overview of the experimental setup utilized in this master thesis. The setup construction and configuration have been extensively documented in Markus Babin’s thesis, which serves as the primary reference for replication [6]. Only few modifications have been applied for the present project.

3.1.1 Equipment description

The primary purpose of this section is to present a comprehensive overview of the equipment and its specifications, enabling readers to understand the essential elements involved in the measurement process. Table 3.1 presents the key characteristics of the instruments utilized in the research, offering a concise summary of their main features [6].

Table 3.1: Laboratory equipment

Equipment	Manufacturer	Model	Properties
LDLS	Energetiq	EQ-99X	-
Secondary light source	Ocean Optics	DH-2000 Ultra-Violet (UV)-NIR	tungsten halogen and deuterium channels
OAP mirror	Newport	50329AL	RFL = 2 in
OAP mirror	Newport	50338AL	RFL = 4 in
Reflective collimator	Thorlabs	RC04SMA-F01	Table 3.4
Spectrometer	Ocean Optics	QE65000	operating at room temperature

Table 3.2: Parameters of the reflective collimator used as sensor

Sensor aperture diameter	Numerical Aperture	Reflected focal length
d_s	NA	RFL
11 mm	0.36	15 mm

3.1.2 Setup

The initial setup was prepared to measure Bidirectional Scattering Distribution Function (BSDF), so it was not enough to meet the required specifications [43]. The limitations and reasons behind the inadequacy of the initial setup are thoroughly explained. Consequently, significant modifications were implemented to enhance the setup, particularly in achieving well-collimated light [6].

The resulting distribution of the setup is depicted in Figure 3.1, providing a visual representation of the arrangement. Furthermore, Figure 3.2 showcases the assembled setup, offering a three-dimensional perspective of its configuration.

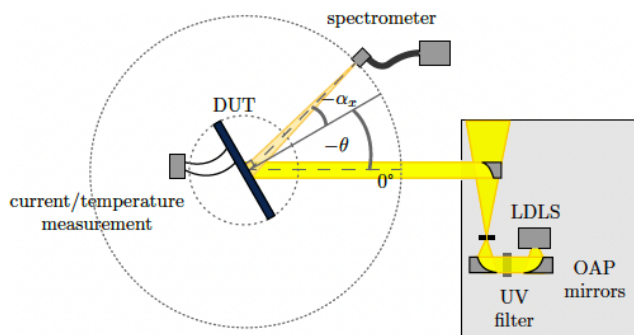


Figure 3.1: 2D representation of the setup [6]

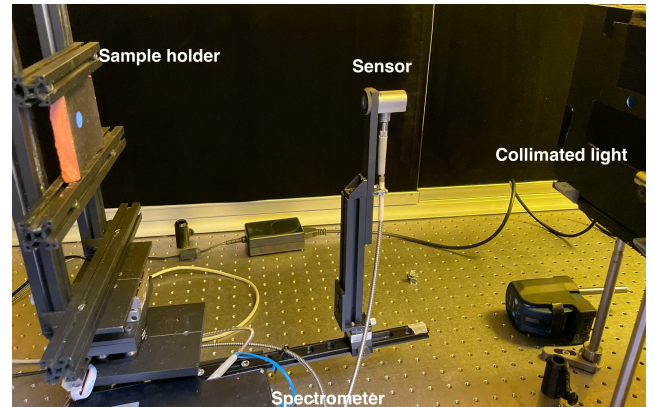


Figure 3.2: Real representation of the setup

The setup description can be divided into three main sections: the sample holder, the spectrometer, and the light source. The sample holder serves the purpose of securely positioning and maintaining the desired orientation of the studied sample. It offers a 360° rotational capability along its axis to accommodate different measurement angles.

The spectrometer, along with the sensor, plays the role of an observer in capturing the reflected or emitted light from the sample. Afterwards the initial data will be converted using a code into BRDF results and ultimately providing numerical color information for the material. Similar to the sample holder, the spectrometer can rotate 360° along the rotational axis of the sample holder, ensuring comprehensive data collection.

The light source is a broadband light source which illuminates the sample, in order to take measurements. It consists of an arranged setup comprising three OAP mirrors and a Laser-Driven Light Source (LDLS). The entire light source system is encased in a black-painted housing to prevent the interference of stray light that could distort the results [6].

Two identical OAP mirrors are employed to generate collimated light, which is then directed through a pinhole to eliminate most of the divergent components. The third OAP mirror is responsible for collimating the light that illuminates the sample. This system provides a consistent and adjustable light source.

To ensure the safety of human observers, an UV filter is incorporated, reducing harmful radiation. However, this filter results in an approximate 18% reduction in light intensity.

3.1.3 Measurement configuration

The focus is on the measurement configurations and considerations for this study. The measurement range for the sensor angle α_x is from -90° to 90°, with data above |75°| being unreliable. The sample angles θ are measured from 0° to 75° in 15° increments to examine reflectance variations across different viewing angles. It should be noted that only positive angles are considered, as explained in Section 2.4.

Various measurement configurations are important to address in this research. The integration time, typically ranging from 0.1 to 10 s, will be set to 0.2 s unless the signal saturates. To reduce signal noise, the data will be averaged over 5 measurements. The spectrometer will be maintained at room temperature throughout the experiment. Background noise measurements are also crucial for each configuration. This involves blocking the LDLS and capturing measurements for all sensor angles to detect any ambient reflections. The obtained background noise will be subtracted from the measurements to ensure accurate results.

In BRDF measurements, the alignment of the measurement plane is a critical aspect to consider. Specifically, it determines the level at which the spectrometer is positioned to receive the reflected light from the sample. In this study, the sensor is placed at the same level as the light source to maximize the capture of reflected light. Although this arrangement effectively blocks the light source at an absolute 0 angle, the emphasis is placed on capturing the overall trend of the results rather than the precise value at that specific angle. The position of the sensor relative to the measurement plane is illustrated in Figure 3.3.

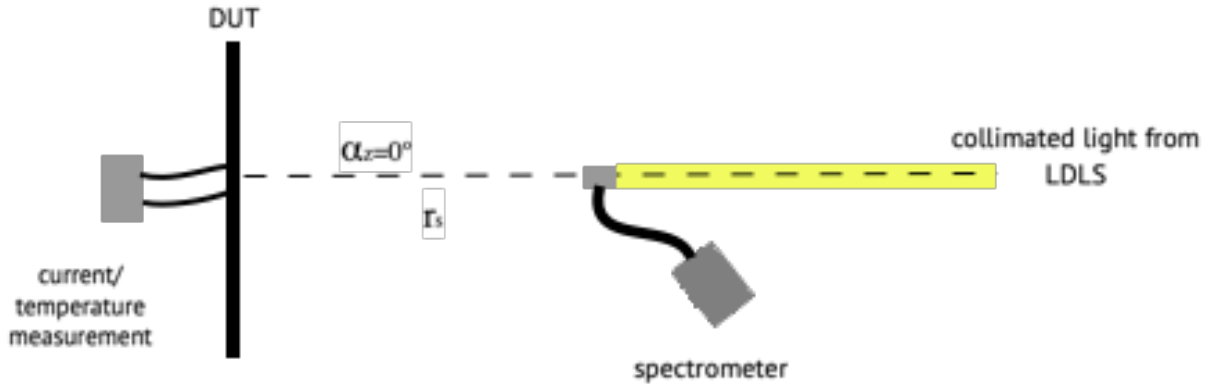


Figure 3.3: Sensor position at the plane of illumination

3.2 Calculations

This section encompasses the complete process related to the analysis of BRDF measurements, beginning from the acquisition of the raw data in the form of counts, and culminating in the calculation of the final BRDF values. The following subsections provide a detailed account of each step involved in this process, including the procedures utilized to transform the raw data into usable form, as well as the algorithms employed for the BRDF calculations.

3.2.1 Raw data conversion

In order to begin the analysis of BRDF measurements, the first step is to convert the raw data N_λ into a radiometric quantity. This raw data, which is acquired in the form of counts, represents the number of photons detected by the instrument within a given time frame. To convert these counts into a radiometric quantity, it is necessary to apply a calibration factor that relates the counts to the incident radiant flux:

Spectrometer calibration

In order to ensure accurate measurements, the spectrometer utilized in this study is calibrated using an external setup, which yields a calibration factor denoted as C_λ , and expressed in units of $\frac{\mu W_s}{cm^2 \cdot nm} / \frac{counts}{s}$. This calibration factor enables the calculation of the spectral flux by applying equation 3.1 to the raw data obtained from the measurements. However, in addition to the calibration factor, several other parameters must be considered when using this formula, including the integration time of the measurement t_{int} , the integration time of the external calibration measurement $t_{int,c}$, and the aperture area of the sensor A_s :

$$\Phi_{\lambda,s}(\alpha) = N_{\lambda,s}(\alpha) \cdot C_\lambda \cdot \frac{1}{t_{int,c}} \cdot \frac{1}{t_{int}} \cdot A_s \quad (3.1)$$

When measuring the spectral flux emitted by the sample, it is important to note that the sensor receives light not only from the α direction, but from all directions within the field of view between the sample and the sensor. To account for this, it is necessary to consider the distance between the sample and the sensor (r_s) and the solid angle of the sensor's field of view (Ω_s) [10]. These factors play a crucial role in accurately interpreting the measured data.

The reflective collimator, serving as the sensor, effectively captures incident light within angles below its divergence half angle ϕ_s . Consequently, when calculating the solid angle Ω_n , the entire sensor aperture area A_s becomes irrelevant. Furthermore, under the assumption that the sensor is situated in the far field, the solid angle Ω_n formed by the active area of the sensor as perceived by the sample is equivalent to the solid angle Ω_s formed by the apparent sample area A'_n as perceived from the sensor's vantage point. This relationship is illustrated in Figure 3.4, highlighting the shared divergence half angle for both solid angles [6].

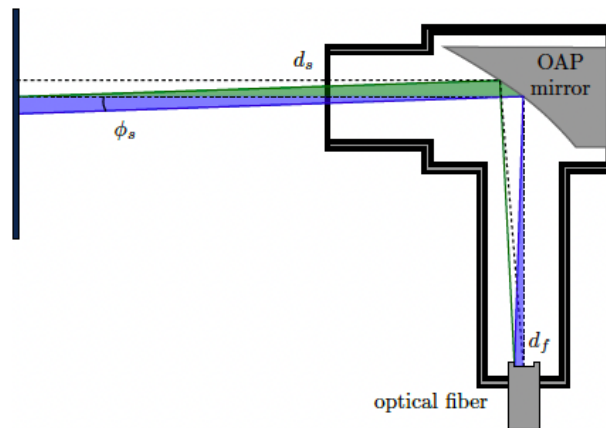


Figure 3.4: Reflective collimator internal composition [6]

Sensor divergence

Theoretical calculations based on the sensor specifications indicate that the maximum divergence half-angle is 1.15° . Consequently, the area of the sample observed by the spectrometer exceeds its clear aperture area and is influenced by the distance between the sample and the sensor. For practical purposes, assuming a spot diameter of 18 mm and a distance of 28 cm, the resulting divergence half-angle is 0.72° . This value, derived from these parameters, will be consistently applied throughout the obtained results [6].

Apparent sample area and correction factor

The calculation of the apparent sample area, as perceived by the sensor, is determined using Equation 3.2. Since the sensor is positioned in the plane of irradiance, the relevant angle to consider is the sensor angle α .

$$A'_n(\alpha) = \left(\frac{d_s}{2} + r_s \cdot \tan\phi_s\right)^2 \frac{\pi}{\cos\alpha} \quad (3.2)$$

In some cases, the sensor may not directly measure the entire illuminated area. Therefore, to prevent an underestimation of the irradiance E , which involves dividing the flux by the apparent area, a correction factor k_A is calculated. This correction factor takes into account the portion of the apparent area that is effectively illuminated. By applying this correction factor, the measured irradiance can be adjusted accurately.

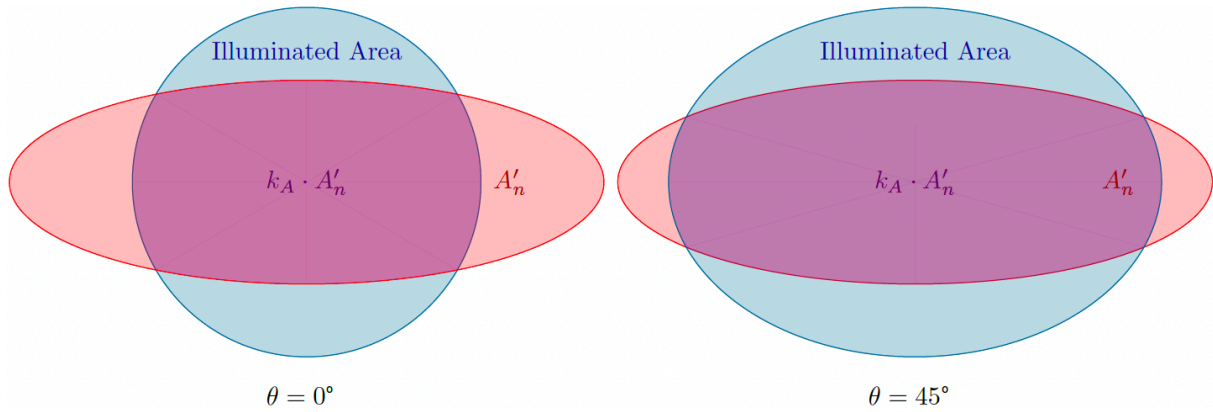


Figure 3.5: Area correction factor at $\alpha_z = 70$ [6]

The correction factor accounts for the intensity distribution considering both the sample angle and the sensor angle. It is obtained by taking images with a luminance camera and determining the relative intensity overlap between the illuminated area and the area "seen" by the sensor. The resulting correction factor is depicted in Figure 3.6.

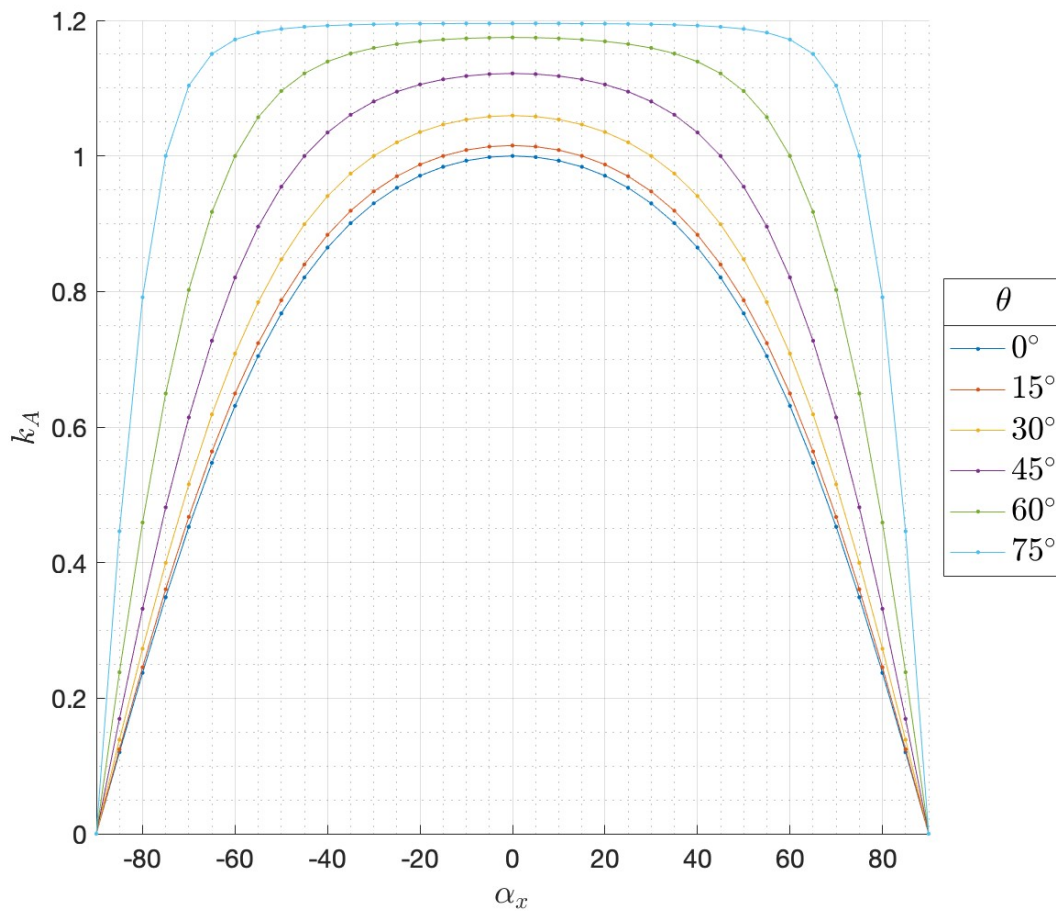


Figure 3.6: k_A correction factor

Solid angle and reflected spectral intensity

The reflected spectral intensity can be calculated using equation 3.3, which uses the spectral flux and the solid angle calculated below.

$$I_{\lambda,\Omega} = \frac{\Phi_{\lambda,s}(\alpha)}{\Omega_n} \quad (3.3)$$

By utilizing the previously determined sensor divergence, it becomes possible to model the reflective collimator by extending the sensor's viewing lines until they intersect, thus forming a cone, as depicted in Figure 3.7 [6]. Since the sensor captures light from its entire field of view, it is more appropriate to consider a constant solid angle rather than a constant area, denoted as A_n . The solid angle of the sample corresponds to that of the spectrometer, which can be computed using Equation 3.4.

$$\Omega_n = \Omega_s = \frac{A'_n(0)}{(r_s + \Delta r_s)^2} = \frac{((r_s + \Delta r_s)\tan\phi_s)^2 * \pi}{(r_s + \Delta r_s)^2} = \tan^2\phi_s * \pi \quad (3.4)$$

Equation 3.4 shows that the solid angle only depends on the sensor divergence half-angle.

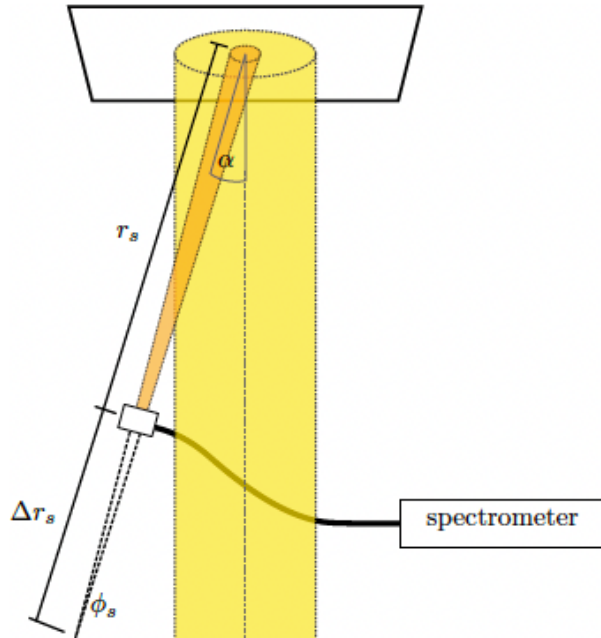


Figure 3.7: Sensor geometry [6]

3.2.2 Spectral irradiance

To establish a correlation between the reflectance obtained from the BRDF setup and the incident light, a white reference sample made of Spectralon[®] will be employed. Spectralon[®] simulates a Lambertian reflector at low incident angles [44]. Although the reference sample is not a perfect Lambertian reflector, it will be considered one, specially at low measured angles when subjected to the same spectral intensity $I_{\lambda,\Omega}$. Consequently, the spectral exitance $M_{\lambda,n}$ of a sample can be calculated with a single measurement. To calculate the spectral exitance of the sample, the spectral data measured at the center position, which corresponds to an angle of $\alpha_x=0^\circ$, will be used.

Spectral irradiance E_λ is calculated using the formula 3.5. The reflectance R_λ is obtained from

the data sheet of the reference sample, Spectralon® [44]. Graph 3.8 shows the distribution of the spectral irradiance along the visible spectrum.

$$E_{\lambda} = \frac{M_{\lambda,n}}{R_{\lambda}} \quad (3.5)$$

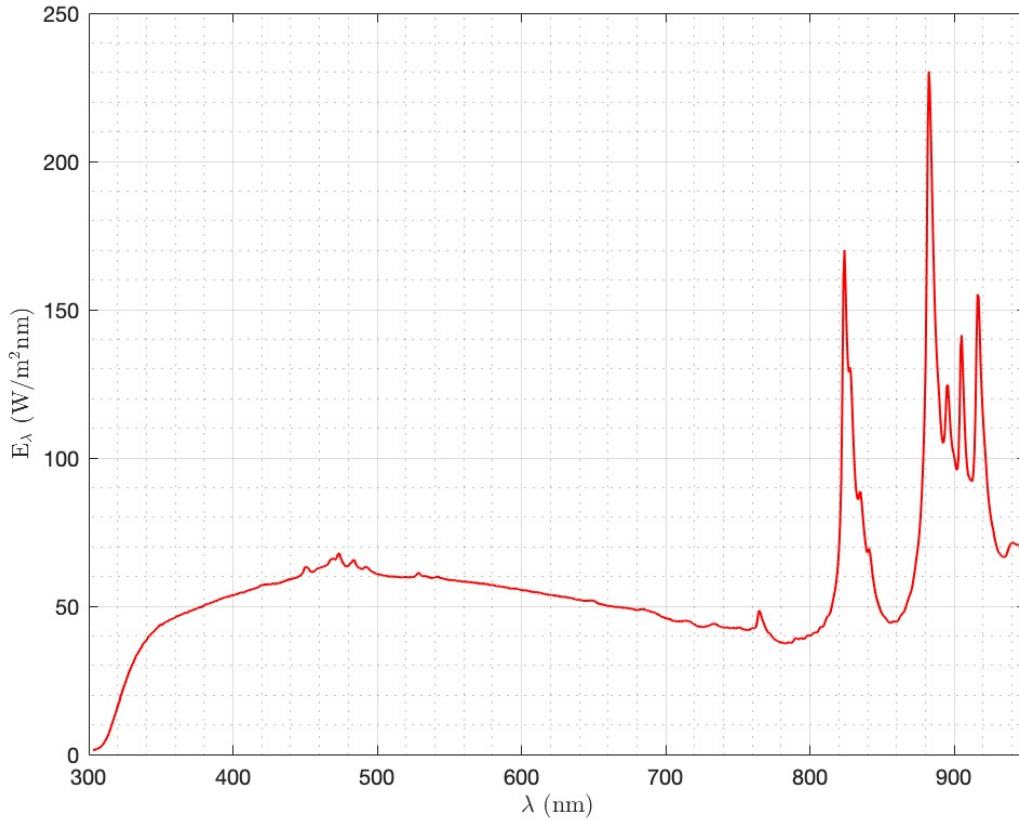


Figure 3.8: Sample spectral irradiance

3.2.3 Total reflectance

The relation between the spectral exitance $M_{\lambda,n}$ and the spectral irradiance E_{λ} of a sample can be used to calculate the total reflectance R_{λ} of the sample. This can be seen in Equation 3.6:

$$R_{\lambda} = \frac{M_{\lambda,n}}{E_{\lambda}} \quad (3.6)$$

In the previous section, the spectral radiance was calculated, but it is necessary to demonstrate how to compute the spectral exitance for the sample. The spectral radiance emitted from a sample in a certain direction (α) can be determined using Equation 3.7, which incorporates the correction factor k_A to account for the illuminated area:

$$L_{\Omega,\lambda,n}(\alpha) = \frac{I_{\lambda,\Omega}(\alpha)}{k_A \cdot A'_n(\alpha) \cdot \cos\alpha} \quad (3.7)$$

In order to obtain a manageable result for the calculation of the spectral exitance, it is necessary to simplify equation 3.8. This can be achieved by integrating over the whole hemisphere for

$\theta = 0$ and assuming isotropic materials [10]. By doing so, the calculation of the spectral exitance can be simplified and made more practical:

$$M_{\lambda,n} = \int_0^{2\pi} \int_0^{\pi/2} L_{\Omega,\lambda,n}(\alpha) \cdot \cos\alpha \cdot \sin\alpha d\alpha d\phi = 2\pi \int_0^{\pi/2} L_{\Omega,\lambda,n}(\alpha) \cdot \frac{\sin(2\alpha)}{2} d\alpha \quad (3.8)$$

For all Angle of Incidence (AOI) calculations, the spectral exitance obtained previously will be utilized. Due to the presence of specular reflections that can distort the results, it is not feasible to integrate over different AOIs except for 0° with the current setup. Nonetheless, this issue is beyond the scope of this thesis.

3.3 White Reference

The BRDF calculation process will be applied to both the white reference and the samples, with the white reference used as a reference for the sample correction. The radiant flux is the first variable to consider in the calculation, and for a perfectly Lambertian surface, such as the white reference sample, the radiant flux Φ_s should remain constant across all sensor (α_x) and sample (θ) angles. However, as shown in Figure 3.9, the flux is not constant and drops sharply for $|\alpha_x| > 60$. This is possibly due to the sample area viewed by the sensor exceeding the illuminated area. To address this issue, a correction factor is necessary.

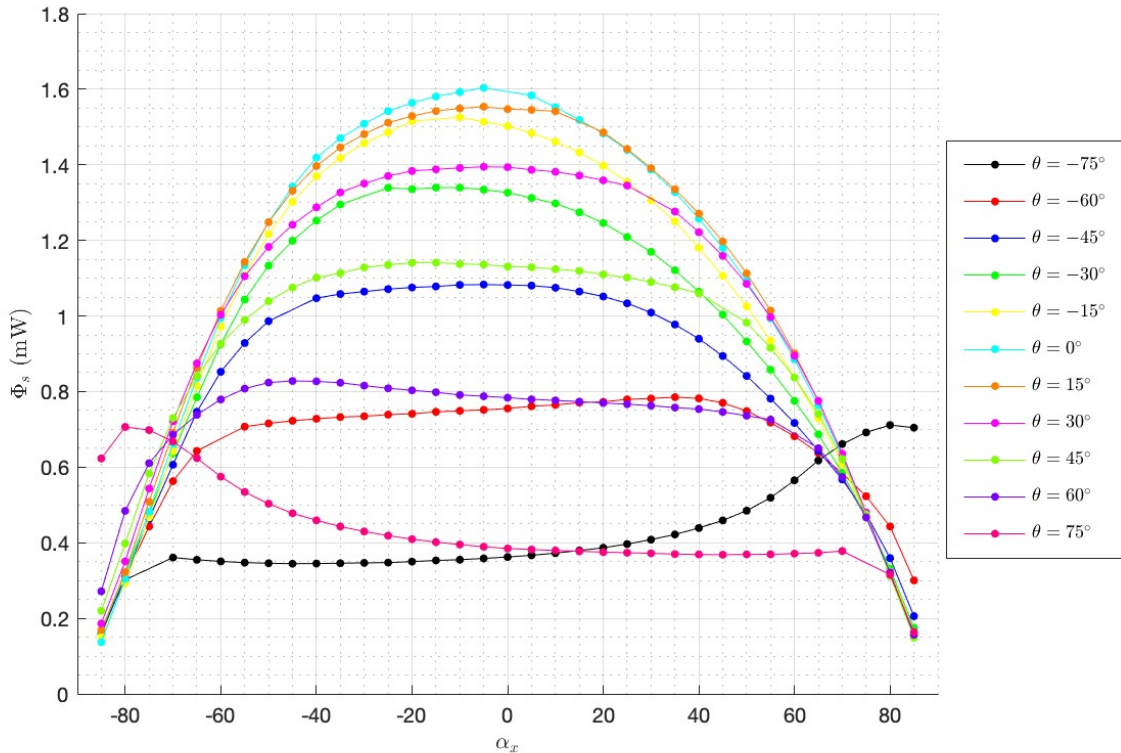


Figure 3.9: White reference sample Radiant flux

In order to validate the results and determine the necessary corrections, another variable of importance is the spectral radiance, denoted by $L_{\Omega,n}$. Figure 3.10 presents the spectral radiance as a function of the measured angles.

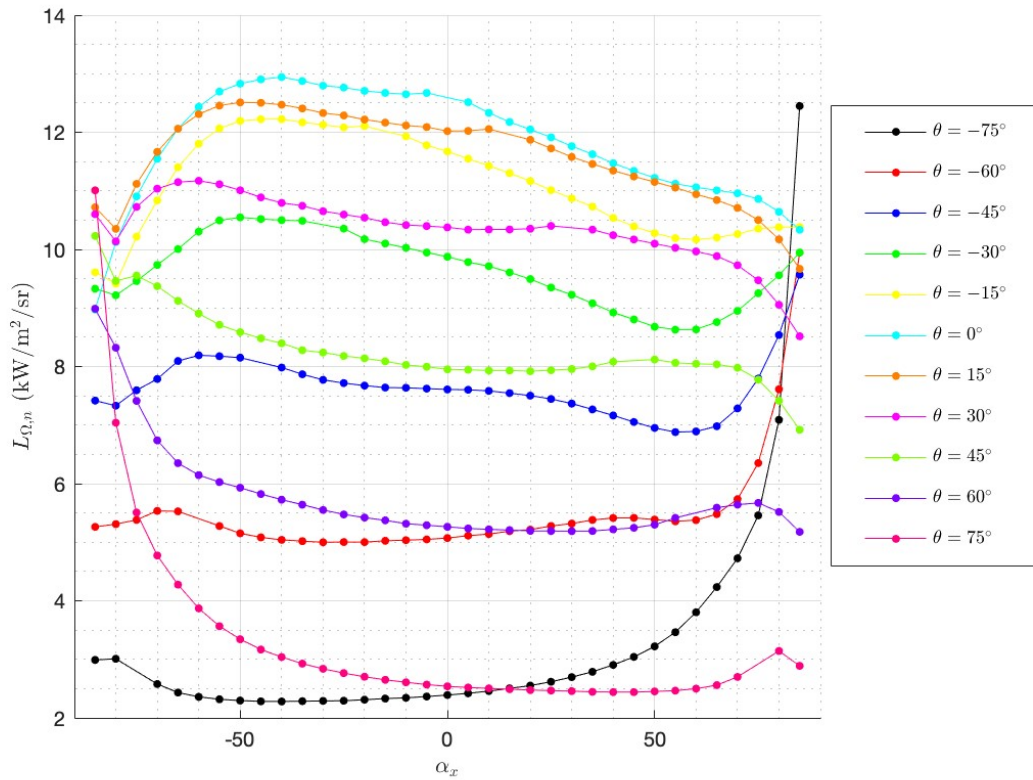


Figure 3.10: White reference sample Radiant flux

Upon thorough examination of the radiant flux for the white reference sample, it was observed that there are two correction factors that need to be taken into account. One of the factors is the difference in radiant flux between positive and negative sensor angles, which shows a higher variability at larger absolute angle values. This may indicate a slight misalignment between the rotational axis of the sensor and the sample holder. To calculate the directional correction factor k_{α} , measurement data at $\theta = 0$ can be utilized in equation 3.9.

$$k_{\alpha} = \frac{\Phi_s(\alpha_x)}{\frac{\Phi_s(\alpha_x) + \Phi_s(-\alpha_x)}{2}} \quad (3.9)$$

In addition, a second correction factor may be necessary to account for the slightly higher values observed in positive sample measurements compared to negative ones. This difference is likely due to an angular misalignment of the sample holder. To calculate the angular correction factor k_{θ} at $\alpha_x = 0$, Equation 3.10 can be used. The obtained results from the measurements support the need for this correction factor.

$$k_{\theta} = \frac{\Phi_s(\theta)}{\frac{\Phi_s(\theta) + \Phi_s(-\theta)}{2}} \quad (3.10)$$

In order to obtain the total BRDF for the white reference sample, as well as for the required sample, both the correction factors discussed earlier will be taken into account. Figure 3.11 and 3.12 display the angle distribution of the α and θ factors, respectively.

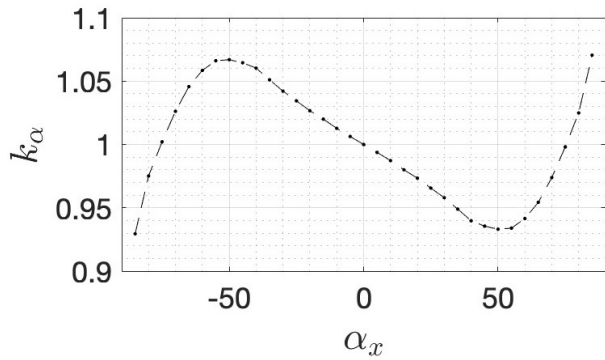


Figure 3.11: Correction factor k_α

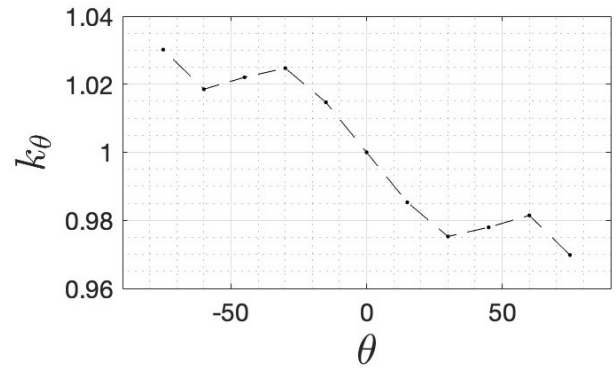


Figure 3.12: Correction factor k_θ

The total BRDF of the white reference sample will be calculated using Equation 3.11. This equation will also be utilized to determine the BRDF for the other samples. Additionally, a modified version of the same equation will be employed to compute the spectral BRDF. The results obtained from these calculations will be analyzed and compared to draw conclusions about the BRDF of the samples under study.

$$B_\lambda(\theta, \alpha_x) = \frac{L_{\Omega, \lambda, n}(\theta, \alpha_x)}{E_\lambda \cdot \cos\theta \cdot k_\alpha(\alpha_x) \cdot k_\theta(\theta)} \quad (3.11)$$

Upon comparing the obtained results of the total BRDF in Figure 3.13 with references [45] and [46], discernible disparities were observed. The technical guide [46] reported lower results compared to the actual measurements. In contrast, reference [45] showed results that aligned with the observable values within the range $[-75^\circ, 75^\circ]$. The dissimilarities observed are most likely attributed to the previously calculated correction factors.

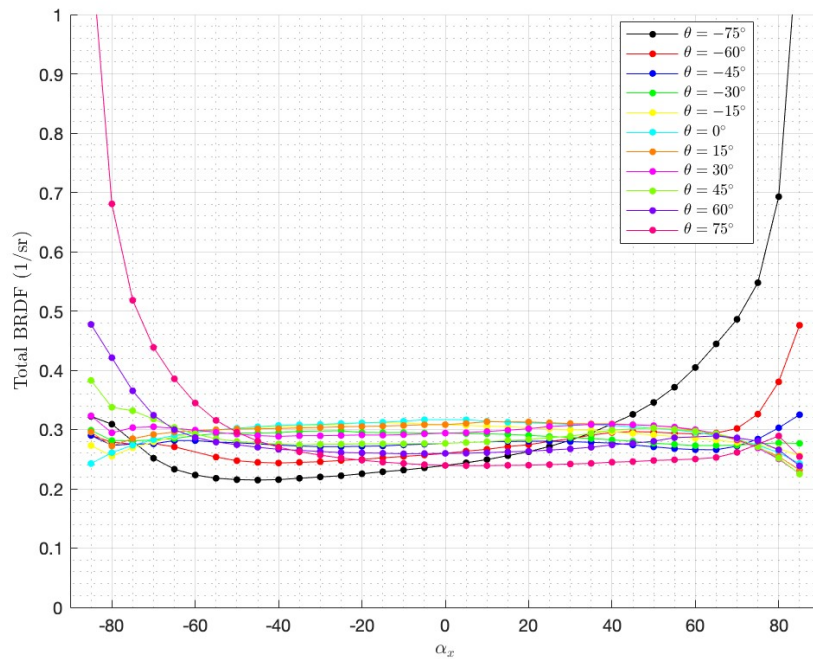


Figure 3.13: Total BRDF of white reference sample

3.3.1 Spectral BRDF

The spectral BRDF is an advanced form of the total BRDF that incorporates the spectral characteristics of light. It characterizes the reflectance of light at different wavelengths as a function of the incident and viewing angles. Applications of the spectral BRDF include spectroscopy and colorimetry, where the ability to quantify the color of materials is essential. Therefore, in the context of this thesis, it is crucial to calculate the spectral BRDF to draw meaningful conclusions about the properties of materials being studied. As the Spectralon data sheet shows, the reflectance is more or less constant between the studied spectrum (300 to 900 nm) [47]. The measured data shows a less constant spectral reflectance, mainly at high angles.

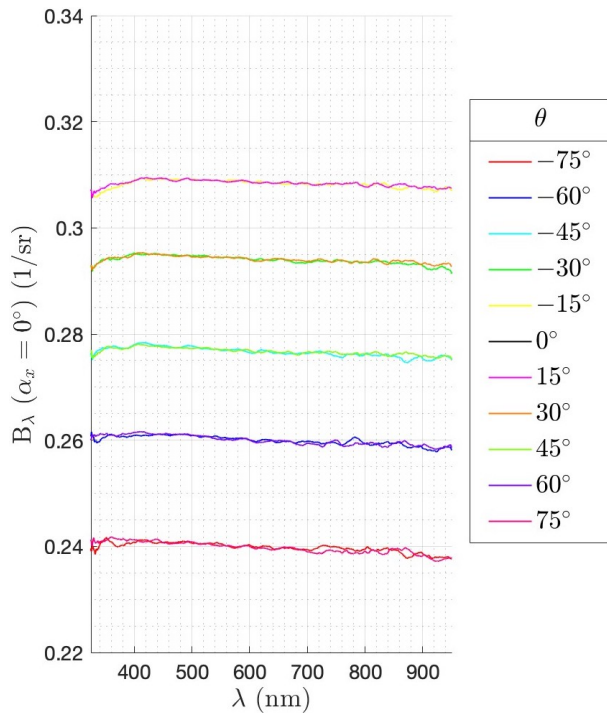


Figure 3.14: Spectral BRDF of white reference sample at $\alpha_x=0^\circ$

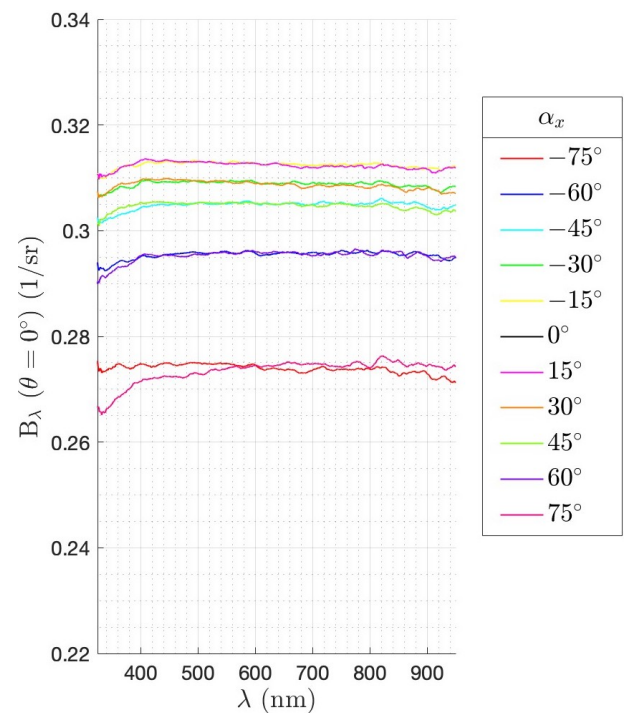


Figure 3.15: Spectral BRDF of white reference sample at $\theta=0^\circ$

Figures 3.14 and 3.15 demonstrate that the spectral BRDF remains nearly constant for each angle, which is consistent with expectations. It is noteworthy that the results for positive and negative angles are equivalent, indicating the sample's symmetry. Additionally, it is essential to note that a constant sample angle results in higher values than a constant sensor angle, emphasizing the sample's reflectivity's significance. Furthermore, it should be mentioned that measurements for 0° angles were not obtainable as the sensor was located in the middle of the light source, making it impossible to measure the sample. These findings have significant implications for understanding the sample's reflective properties.

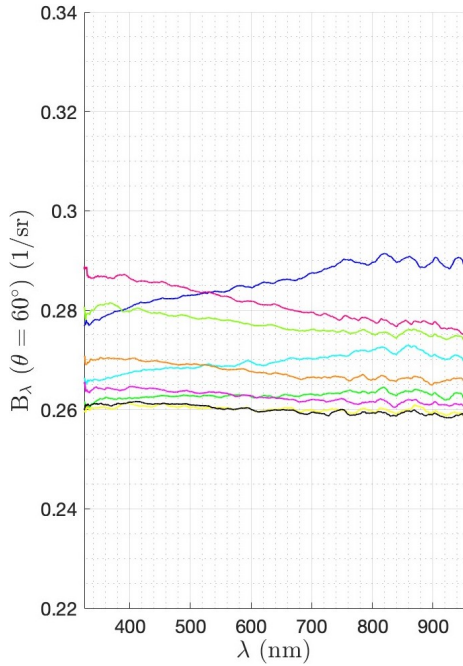


Figure 3.16: Spectral BRDF of white reference sample at $\theta=60^\circ$

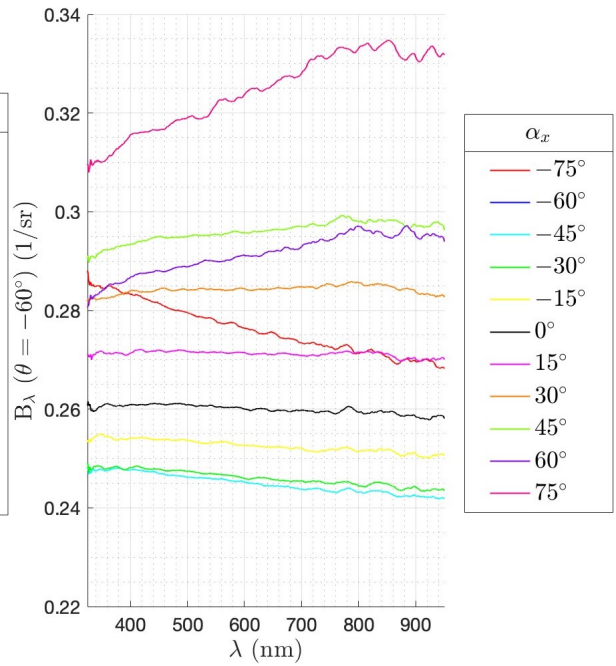


Figure 3.17: Spectral BRDF of white reference sample at $\theta=-60^\circ$

In examining Figures 3.16 and 3.17, it becomes evident that there exist significant disparities between the two directions under consideration. Specifically, the positive direction of the sample angles indicates more consistent and closely-related results than the negative direction. This observation leads to the inference that reflectance does not have a uniform effect in all directions, thereby introducing a loss of theoretical symmetry in the sample. The possible causes for this discrepancy may be attributed to misalignments in the experimental setup or random impurities in the sample. The former factor has been corrected for, leaving the latter as the most likely culprit.

3.4 Colorimetry transformations

In this section, the final step involves converting the BRDF variables into colorimetry results, which are essential for analyzing the samples. The conversion process, along with the relevant formulas, is extensively discussed in Chapter 2, specifically in sections 2.4 and 2.5. By applying these formulas a comprehensive analysis of the samples' color properties will be possible.

As outlined in Section 2.4, the initial stage involves computing the XYZ coordinates for the respective sample. These three coordinates will be determined for each orientation. An illustration depicting an example at a 0° sample angle can be observed in Figure 3.18. The figure demonstrates the progression across the entire sensor range, showcasing the variations in the XYZ coordinates.

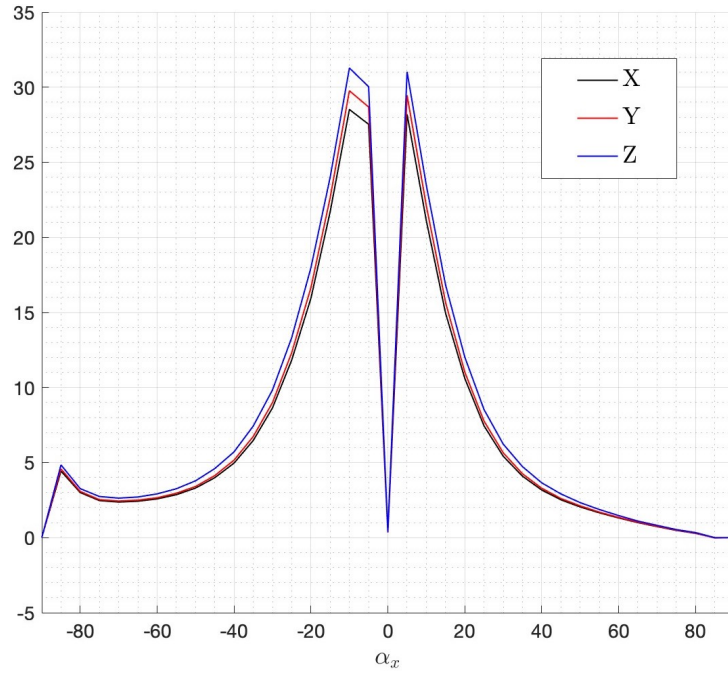


Figure 3.18: XYZ coordinates for a black sample

Subsequently, the converted color space of interest is the CIELAB space. This space allows for the utilization of the variables L^* , a^* , and b^* , which are crucial for conducting a qualitative comparison. The transformation process involves applying the relevant formulas outlined in Section 2.4.

Furthermore, the RGB coordinates are calculated based on the derived $L^*a^*b^*$ coordinates, as explained in Section 2.4. These calculations, along with the quantitative color difference results discussed in Section 2.5, serve as supporting elements to validate and verify the obtained outcomes.

4 Construction materials and BIPV samples

This section provides an overview of the construction and BIPV materials that will be utilized in the experimental investigation of appearance comparison between BIPV samples and construction materials. Part 4.1 will detail the selection of various construction materials that will serve as a basis of comparison for the BIPV samples. These construction materials will be chosen based on their specific properties, such as color and texture, which will be taken into consideration to ensure a fair and comprehensive comparison. The range of materials selected will be representative of those commonly used in building design, and will provide a benchmark for the visual appearance of conventional construction materials. Section 4.2 will describe the BIPV materials that will be used in the study. The selection of these materials has been carefully made to evaluate the visual appearance of BIPV materials in comparison to conventional construction materials. The aim of this investigation is to provide insights into the aesthetic considerations involved in integrating solar technology into building design and to evaluate the potential of BIPV materials to serve as a viable alternative to conventional construction materials.

4.1 Construction materials

As mentioned in the motivation of the project, the main focus is to assess the difference between BIPV samples and construction materials mainly for architectural designs/neighbourhoods that have strict visual characteristics. To be able to find where are the BIPV in respect to the construction materials, it is necessary first to provide which construction materials could be representative of the architectural trends. For that, samples from different providers have been selected, including Komproment, Randers Tegl, etc.

4.1.1 Randers Tegl

Randers Tegl is a Danish manufacturer and has offered five different roofing products to analyze. Some of them are representative of the Danish architectural design [48]. An image of the samples can be seen from Figure 4.1 to 4.5. All samples show a stable color at every point of the sample. However, the perceived appearance can change depending on the angle of the observer respect to the sample.

The RT 811 yellow roof tile (figure 4.1) is made of the same special clay blend as their problem-free red Højslev tiles, the yellow color is achieved by adding titanium dioxide to the unique red clay mixture. The Højslev tiles are classic roof tiles developed for Scandinavia's harsh climate [49].

The Black Noble Wing Engobed Interlocking Roof Tile, RT 845 Laumans IdealVariable (figure 4.2), is a high-quality roof tile produced by the German subsidiary of Randers Tegl Group. Its deep swung shape resembles a classic pantile [50].

The Black Engobed Højslev Pantile, RT 840 in Lille Dansk format (figure 4.3), is a roof tile suitable for Scandinavian weather conditions. Made from a special clay mixture, it is fired at a high temperature for durability. The tile's black engobe finish provides a smooth, matte, and non-reflective surface that is highly resistant to stains [51].

The red engobed wing interlocking roof tile, RT 841 Laumans IdealVariabel (figure 4.5), features a captivating silk matte surface that provides a watertight, strong surface without any reflections [52].

The RT 844 Laumans IdealVariabel (figure 4.4) is a natural red interlocking roof tile with a deep swung shape similar to a classic pantile [53].



Figure 4.1: RT 811 yellow roof tile [49]



Figure 4.2: RT 845 Laumans Glazed Black [50]



Figure 4.3: RT 840 Højslev Lille Black [51]



Figure 4.4: RT 844 Laumans Red [53]



Figure 4.5: RT 841 Laumans Dark Red [52]

4.1.2 Komproment

Komproment is a Danish company that specializes in sustainable building products. The company's construction materials include facade elements, roofing tiles, and shading products designed to minimize energy consumption [54]. Komproment has offered two facade products that represent the Nordic regions, and these products can be replaced without affecting the structural layout to incorporate BIPV samples.

There is a facade product known as the Faro model (figure 4.6) that is designed for lightweight brick exterior walls. It is specifically intended for use in both new construction and renovation projects. The Faro model offers a practical solution that can be easily incorporated into building designs without significant alterations to the structural layout. It is a low-maintenance option with a long lifespan, providing a reliable choice for facade applications [55].

Another material to consider is the Rustic Natural Slate (figure 4.7). This slate material is known for its durability and ability to withstand various environmental conditions. It is suitable for use in facades due to its resilience against water, snow, and frost. The Rustic Natural Slate requires minimal maintenance [56].



Figure 4.6: Faro Vidar Clay Shingles [55]



Figure 4.7: Natural Black Slate [56]

4.2 BIPV samples

Regarding the BIPV samples, eight of them have been carefully selected, from the DTU database, to facilitate a comprehensive comparison with conventional construction materials. The first four samples (Figures 4.8-4.14) are provided by the company Glaseksperten. Next to the image of the sample, there is a raw scheme of the sample's composition. They consist of a Monocrystalline Silicon (Mono-Si) PV cell with a Two Busbars (2BB) configuration. The samples incorporate an inkjet-printed layer and a polymer backsheet is employed to provide protection and insulation to the PV cell. Furthermore, a convenient peel strip is integrated, enhancing the sample's usability and convenience.

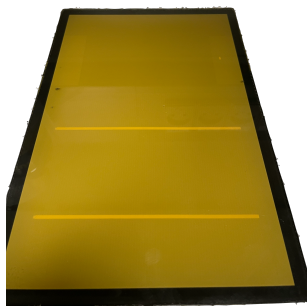


Figure 4.8: Yellow BIPV sample

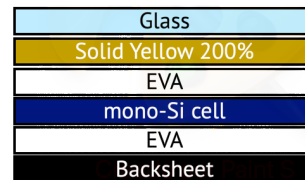


Figure 4.9: Yellow BIPV sample composition

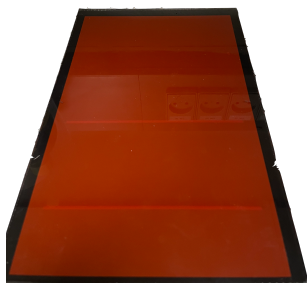


Figure 4.10: Dark Red BIPV sample

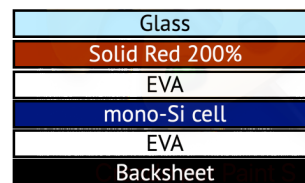


Figure 4.11: Dark Red BIPV sample composition

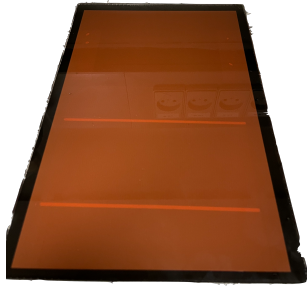


Figure 4.12: Clear Red BIPV sample

Glass
Solid Terracota 200%
EVA
mono-Si cell
EVA
Backsheet

Figure 4.13: Clear Red BIPV sample composition

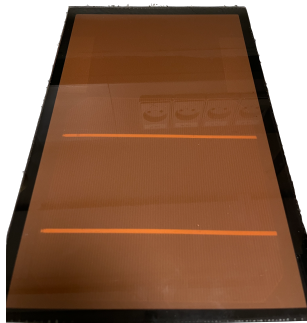


Figure 4.14: Red BIPV sample

Glass
Solid Terracota 100%
EVA
mono-Si cell
EVA
Backsheet

Figure 4.15: Red BIPV sample composition

The other samples have the same PV technology, a Mono-Si PV module with a 2BB configuration.

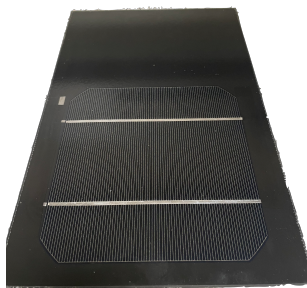


Figure 4.16: Black BIPV sample

Glass
EVA
mono-Si cell
EVA
Backsheet

Figure 4.17: Black BIPV sample composition

The fifth sample (Figure 4.16) features a smooth glass surface which ensures optimal light transmission and durability and protected by a Petraglass cover.

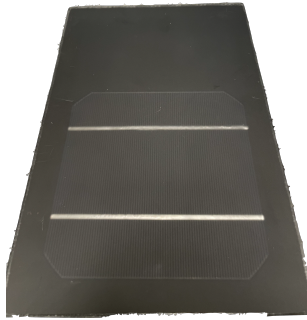


Figure 4.18: Normal Black BIPV sample

Glass
EVA
mono-Si cell
EVA
Backsheet

Figure 4.19: Normal Black BIPV sample composition

The sixth sample (Figure 4.18) has a satinated glass surface providing a unique texture and light diffusion.

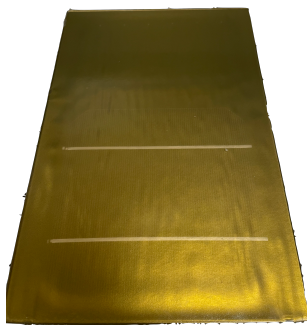


Figure 4.20: Gold BIPV sample

Glass
POE
Solaxess Gold
POE
mono-Si cell
POE
Backsheet

Figure 4.21: Gold BIPV sample composition

The seventh one (Figure 4.20) utilizes a high-transparency Polyolefin Elastomer (POE) encapsulant, known for its excellent light transmission properties. Furthermore, the sample is enhanced with a Solaxess Gold coating, which enhances light absorption and efficiency. The module is then protected by a Petraglass cover, ensuring durability and resistance to environmental factors.



Figure 4.22: Special Black BIPV sample

Sandlasted glass
EVA
mono-Si cell
EVA
Backsheet

Figure 4.23: Special Black BIPV sample composition

The last sample (Figure 4.22) is laminated with a sandblasted Costwold glass surface texture, which introduces diffuse reflections. The use of sandblasting enhances the scattering of light, resulting in a more uniform distribution of reflections. Additionally, the sample incorporates a black backsheet, further contributing to the absorption of incident light.

5 Results presentation

This section presents the results of the color comparison between BIPV materials and traditional construction materials, specifically focusing on their color representation in the CIELAB color space. The CIELAB color space provides a standardized and perceptually uniform system for quantifying and comparing color attributes, described by lightness (L^*), chroma (a^*), and hue (b^*). By mapping the color properties of both BIPV and construction materials onto the CIELAB space (described in section 2), a visual representation of their color differences and similarities is achieved.

The presentation of results in this master thesis will be organized into separate sections dedicated to each construction material, encompassing all the BIPV materials that can serve as substitutes for the respective construction material. In order to provide an effective representation based on the sample and sensor angle, not all the L^* , b^* , and a^* graphs will be included. Instead, two graphs will be selected to offer a comprehensive depiction. Specifically, the graphs included in the presentation of the results will be those taken at 0° and 45° angles, while the remaining graphs will be included in Appendix A. Graphs will show all the sensor angle results, with gaps at absolute 0° , due to the sensor blocking the source of light. Additionally, as lightness above 100 is misleading and under investigation, these values will be taken out too, resulting in a gap in the graph. All the samples taken into account have been explained in Chapter 4.

The purpose of this section in the master thesis is to present the results obtained and provide initial insights derived from them. However, for a more in-depth analysis of the results, Chapter 7 will be dedicated to thoroughly examining and interpreting the findings.

5.1 RT 811 Yellow Roof Tile

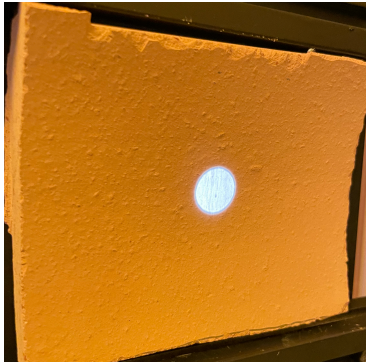


Figure 5.1: Yellow sample



Figure 5.2: Yellow sample rotated

For the purpose of analysis, the graphs in this section will feature four distinct samples. Among these, two samples will represent the construction material with different orientations, while the remaining two samples will represent the Yellow BIPV and Gold BIPV materials, respectively.

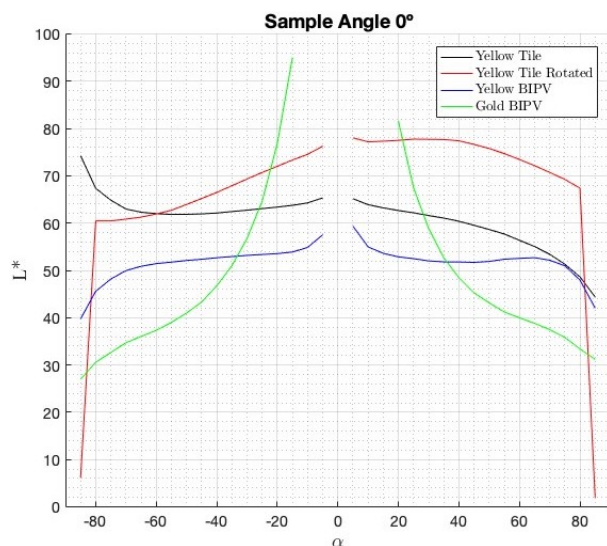


Figure 5.3: Yellow Tile L^* comparison at 0°

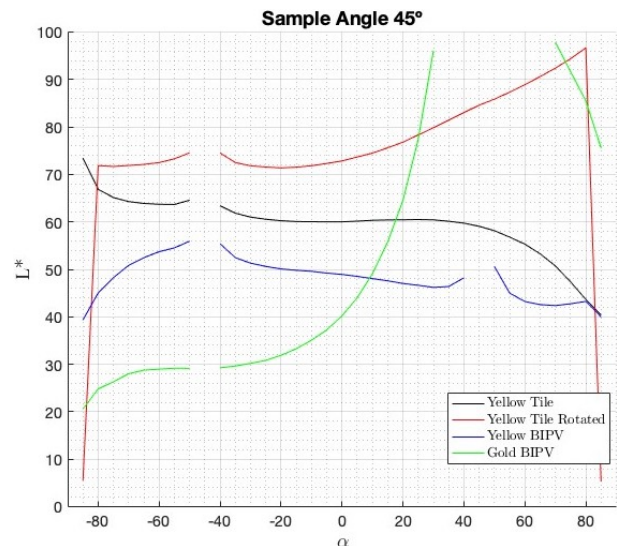


Figure 5.4: Yellow Tile L^* comparison at 45°

To begin with, it is evident that the average lightness of the yellow-colored samples is notably high, aligning with expectations. These samples exhibit a visually bright appearance, resulting in a considerable reflectance of projected light. Moreover, the tile material demonstrates a relatively isotropic behaviour, as indicated by results across all angles. Conversely, the Gold BIPV sample displays anticipated variability due to its inference base coloration technology. Another crucial observation is that the measured direction and point have a substantial impact on the final results. This significant disparity can be attributed to the curved nature of the tile material, which leads to the reflection of light in undesired directions, thereby affecting the measurements. In Figure 5.1 and 5.2 it is possible to see the curvature of the material, which can affect a lot to the measurement if it is not properly aligned. Even being properly aligned, some of the reflectance can be lost or directed in undesired directions.

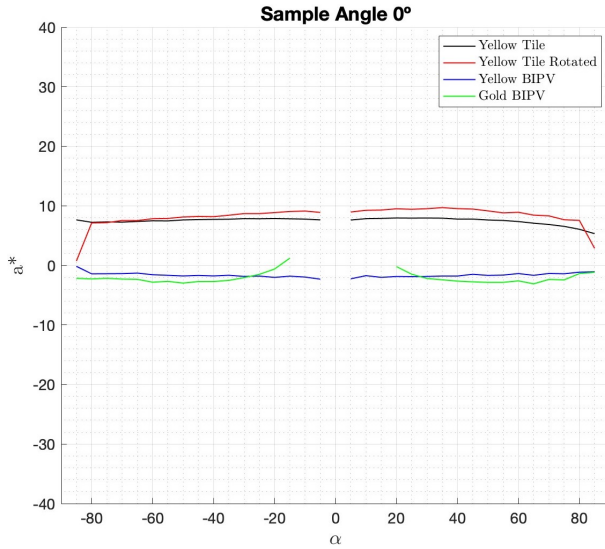


Figure 5.5: Yellow Tile a^* comparison at 0°

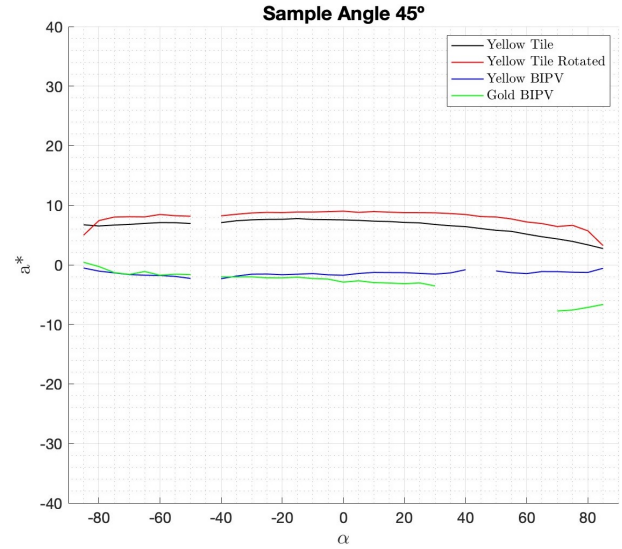


Figure 5.6: Yellow Tile a^* comparison at 45°

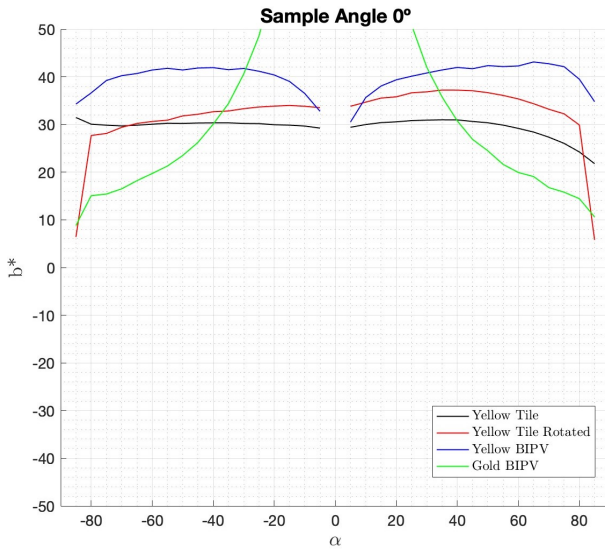


Figure 5.7: Yellow Tile b^* comparison at 0°

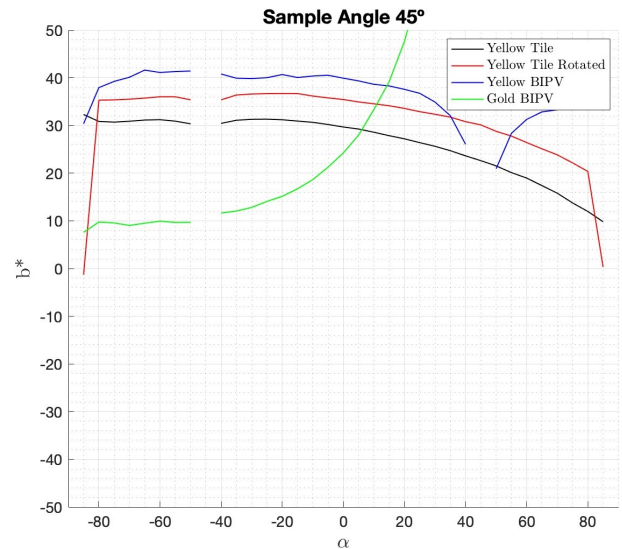


Figure 5.8: Yellow Tile b^* comparison at 45°

In relation to the a^* and b^* values, which provide coordinates for determining apparent color, the obtained results generally align with expectations for most of the samples. The a^* values tend to be low or close to zero. Furthermore, the tile material exhibits colors closer to the red spectrum, while the BIPV materials tend to lean towards blue. This distinction may be attributed to the presence of cells within the BIPV materials. On the other hand, the b^* values consistently indicate a direction towards yellow, which corresponds to the desired color representation. Both the tile samples and the Yellow BIPV samples consistently exhibit close and stable yellow values. However, the Gold BIPV samples are significantly impacted by their high reflectance, resulting in considerable variation among different angles. As a result, this variation shows an angular-dependent material.

5.2 RT 845 Laumans Glazed Black

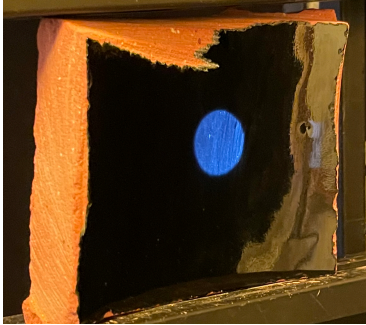


Figure 5.9: Black glazed sample



Figure 5.10: Black glazed sample rotated

Despite being considered a black sample, only two measurements for the glazed black tile, each taken in different directions, as well as individual measurements for the Black BIPV and Normal Black BIPV will be used. The Special Black BIPV will not be considered for comparison due its unique design.

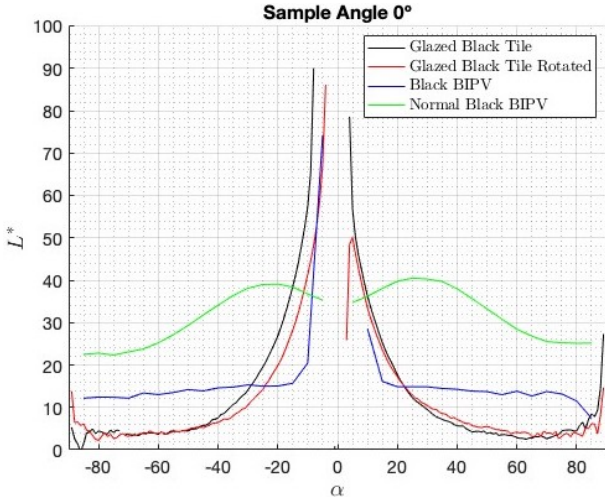


Figure 5.11: Glazed Black Tile L^* comparison at 0°

None of the BIPV materials analyzed in this study demonstrate characteristics that deem them suitable substitutes for the Glazed Black sample. Furthermore, it is important to acknowledge that the CIELAB comparison method may not be the most appropriate approach for assessing these materials. Therefore, to better understand and evaluate the results for these materials, the BRDF graphs will be utilized. The BRDF graphs offer a more comprehensive perspective on the reflective characteristics of the materials under investigation.

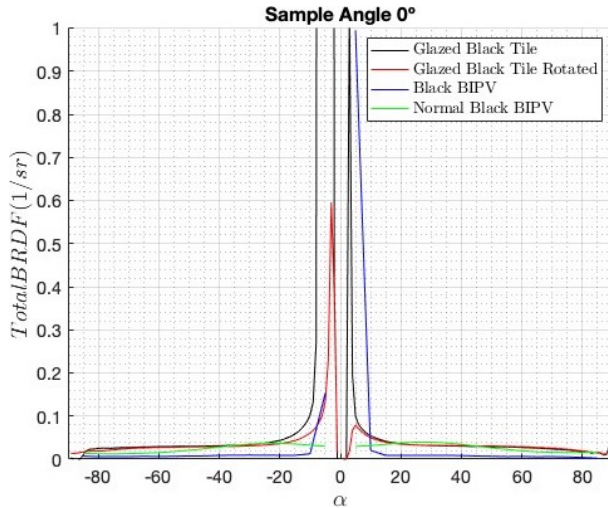


Figure 5.12: Total BRDF

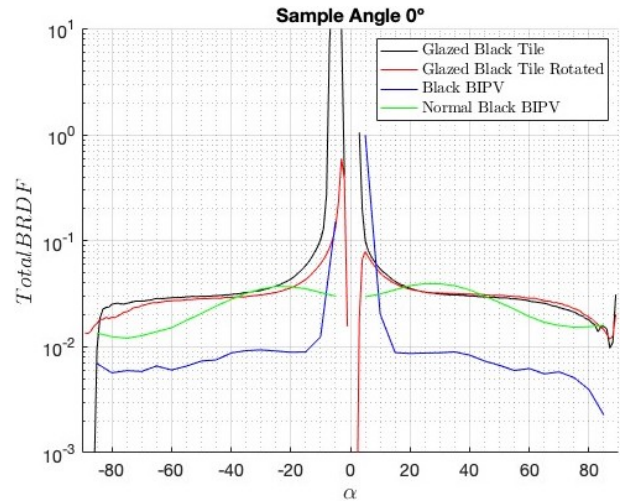


Figure 5.13: Total BRDF in logarithmic scale

Figures 5.12 and 5.13 present the BRDF values for the investigated samples, offering insights into their reflectance properties. By examining these graphs, it is possible to identify the peak values at a sample angle of 0° . The logarithmic scale allows for a clear observation of the trends exhibited by each sample in comparison to the others. Both the Glazed measurement and the Normal Black BIPV display similar trends, except in the central position where the results for the Glazed material significantly exceed 1, similar to the Black BIPV sample. Additionally, it is worth noting that the Black BIPV exhibits a lower baseline compared to the other measurements.

5.3 RT 840 Højslev Lille Black

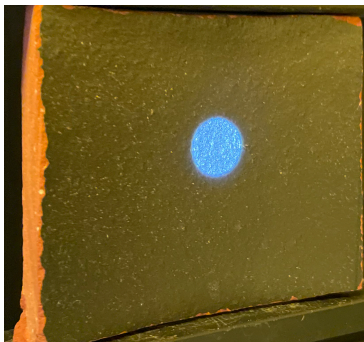


Figure 5.14: Black tile sample

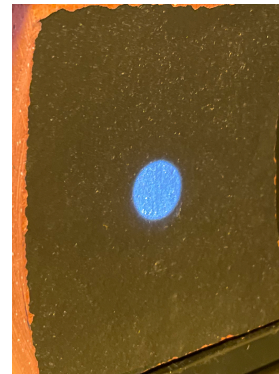


Figure 5.15: Black tile sample rotated

In this particular case, the comparison will involve six measurements. This includes two measurements for the black tile, each taken in different directions, as well as individual measurements for the Black BIPV, Normal Black BIPV, and two measurements in different directions for the Special Black BIPV.

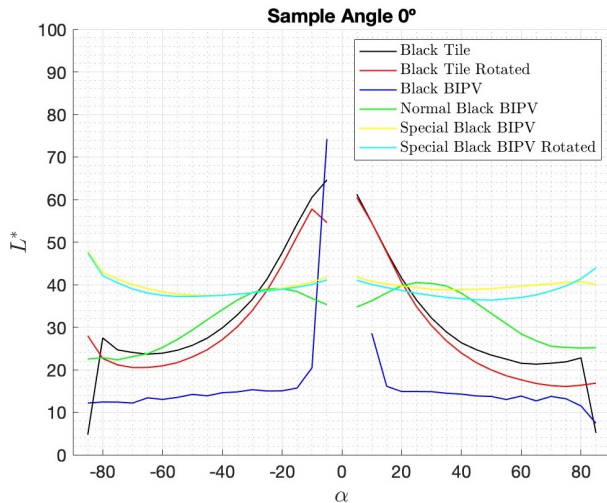


Figure 5.16: Black Tile L^* comparison at 0°

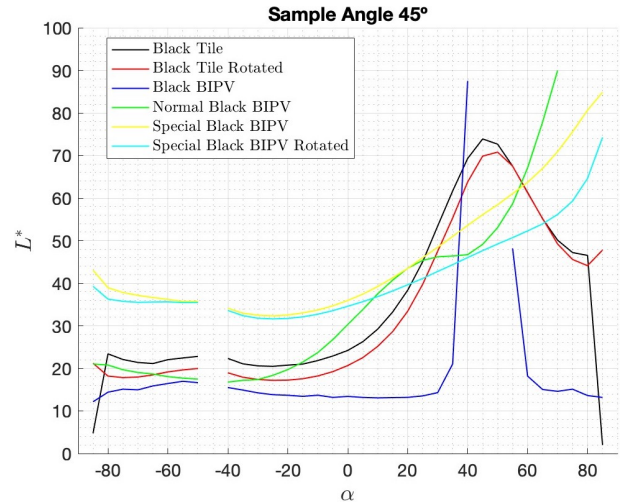


Figure 5.17: Black Tile L^* comparison at 45°

Initially, it is apparent that the measurement direction has a relatively lesser impact on black materials compared to colored materials. Both the black tile samples and the special BIPV samples exhibit similar levels of lightness and follow the same trend. Furthermore, it is noticeable that black materials display high reflectance when the sensor is positioned where specular reflection occurs. Another noteworthy finding is that the lightness remains consistent at low sensor angles, but is significantly affected by the material's reflectance at high sensor angles. Among the samples, the Normal Black BIPV demonstrates more variability in the results, making the comparison more challenging.

As expected for a black material, the a^* and b^* coordinates are either 0 or very close to 0. In this particular case, it is only necessary to verify that these values remain in proximity to 0 (check Appendix A for the graphs).

5.4 RT 844 Laumans Red

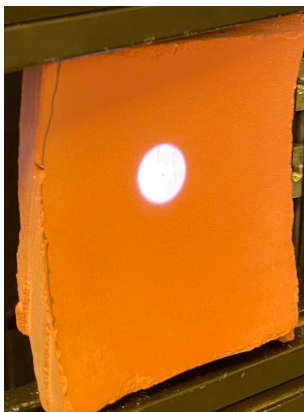


Figure 5.18: Clear red sample

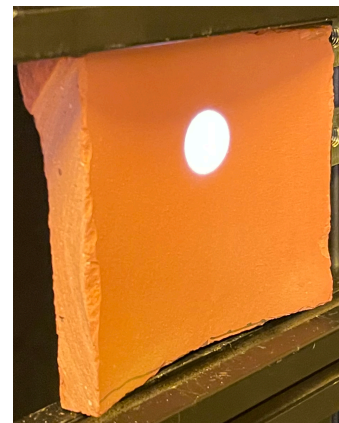


Figure 5.19: Clear red sample rotated

For the purpose of comparing the Clear Red materials, three distinct BIPV red samples will be examined alongside two tiles oriented in different directions.

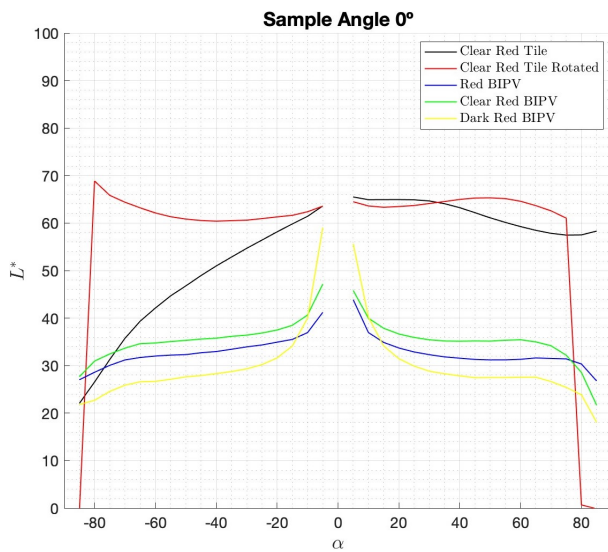


Figure 5.20: Clear Red Tile L^* comparison at 0°

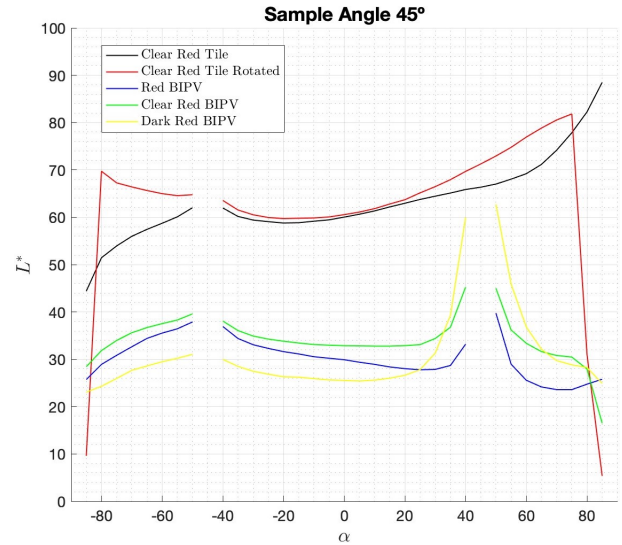


Figure 5.21: Clear Red Tile L^* comparison at 45°

The initial observation is that the BIPV materials exhibit similar lightness results with a consistent trend. Conversely, the tiles demonstrate higher lightness values. This difference in lightness can be attributed to the tiles' visually lighter appearance, similar to the Yellow tile when exposed to sunlight. Therefore, the higher reflectance of the tiles is expected. In this case, the curvature of the samples does have an impact, as the results vary depending on the measured direction. This variation could be attributed to the influence of the material's curves. Probably, if the curvature influence of the material is eliminated, it will show a fairly isotropic composition. However, a method to account for the curvature is necessary to develop.

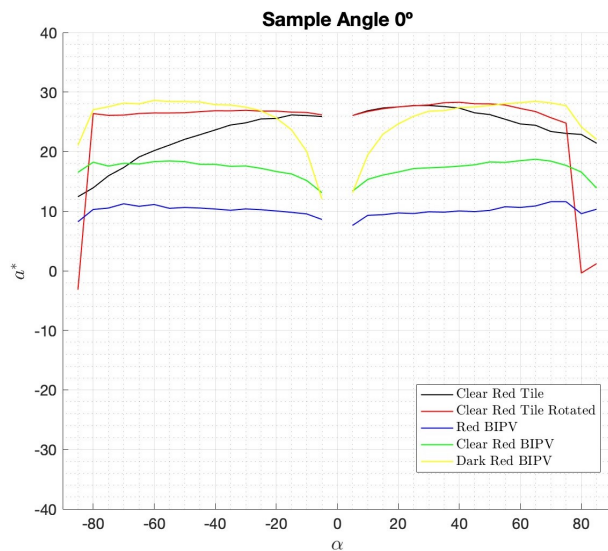


Figure 5.22: Clear Red Tile a^* comparison at 0°

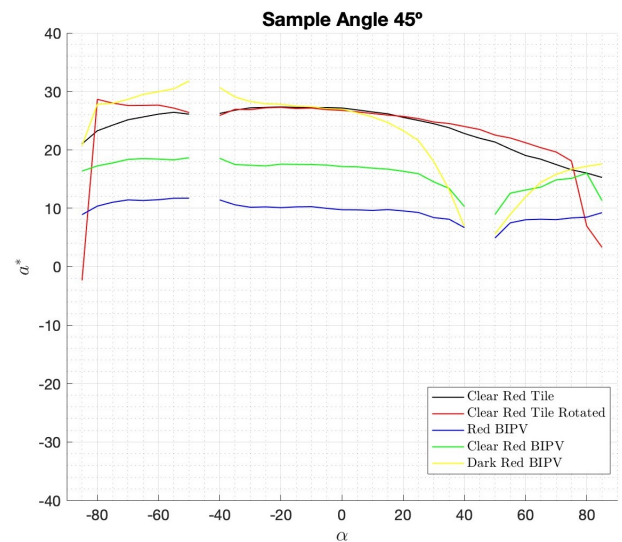


Figure 5.23: Clear Red Tile a^* comparison at 45°

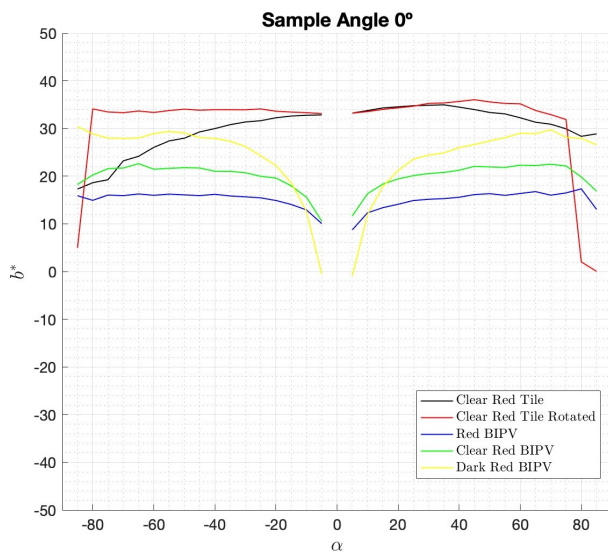


Figure 5.24: Clear Red Tile b^* comparison at 0°

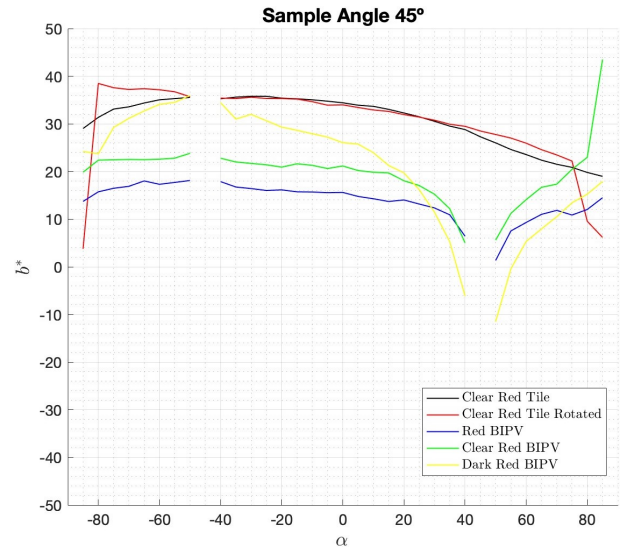


Figure 5.25: Clear Red Tile b^* comparison at 45°

Regarding the other coordinates, it is noticeable that the obtained values are closer to an orange color rather than a pure red. The results for both red and yellow are relatively similar across all angles. This consistency aligns with the anticipated values, as none of them exhibit a distinct red hue, but rather appear as mixed colors. However, it was initially expected to observe higher levels of red in the Dark Red BIPV samples.

5.5 RT 841 Laumans Dark Red

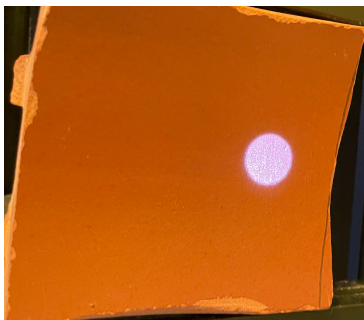


Figure 5.26: Dark red sample

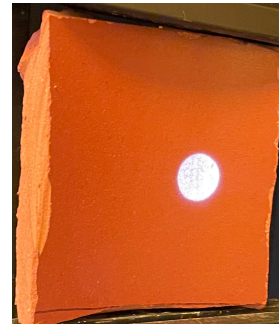


Figure 5.27: Dark red sample rotated

Similar to the previous scenario, the analysis will involve five samples. The BIPV materials will remain consistent, while the tile samples will be replaced with Dark Red Tiles for comparison.

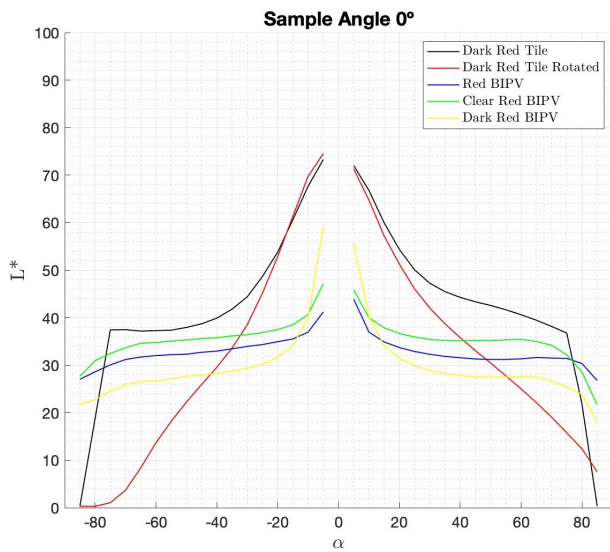


Figure 5.28: Dark Red Tile L^* comparison at 0°

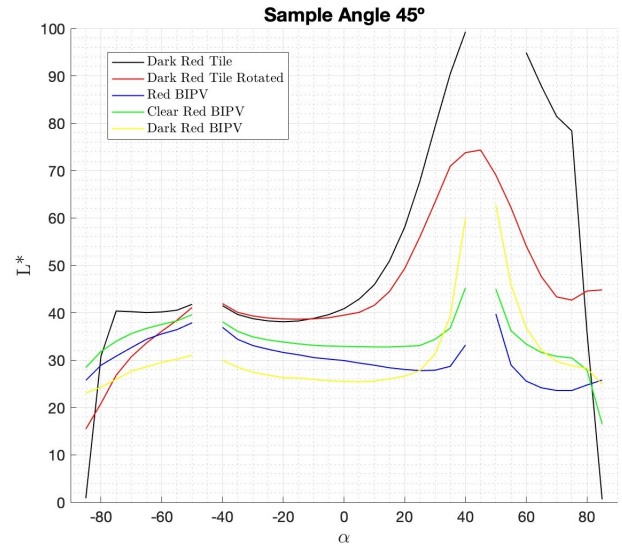


Figure 5.29: Dark Red Tile L^* comparison at 45°

The curvature of the samples significantly influences the results in this case, resulting in some losses in the measurements of the rotated tile sample. Nonetheless, all samples exhibit a similar trend with closely aligned lightness values. The Dark Red material appears darker compared to the previous red, yet it displays higher reflectance, as evidenced by the higher peaks and less consistent values observed in the measurements.

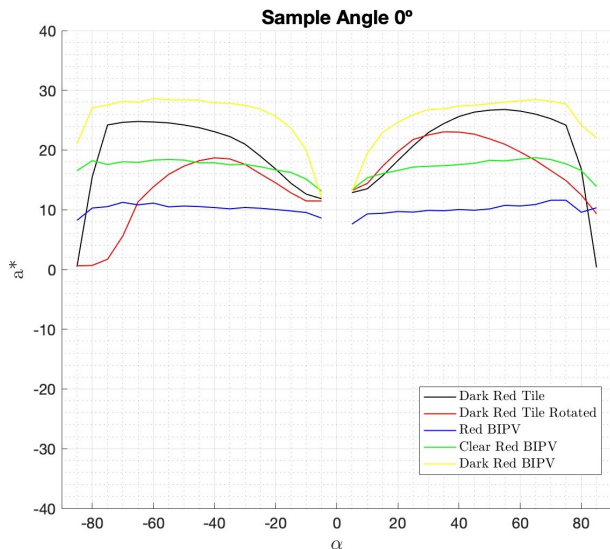


Figure 5.30: Dark Red Tile a^* comparison at 0°

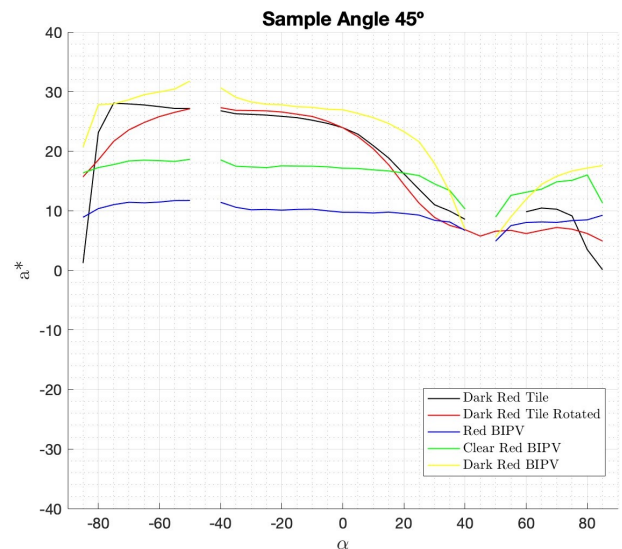


Figure 5.31: Dark Red Tile a^* comparison at 45°

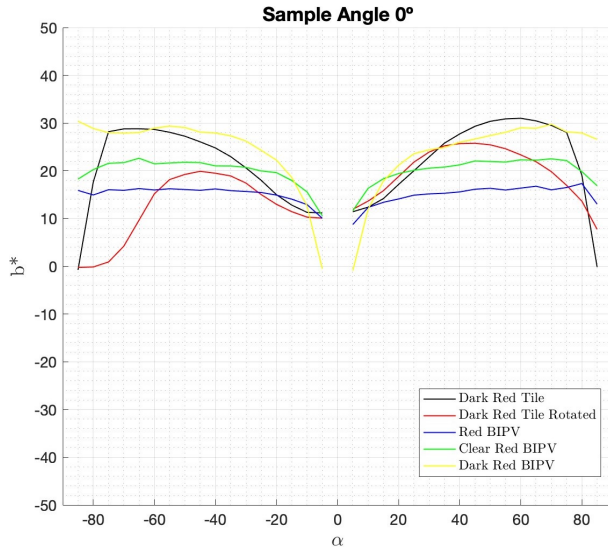


Figure 5.32: Dark Red Tile b^* comparison at 0°

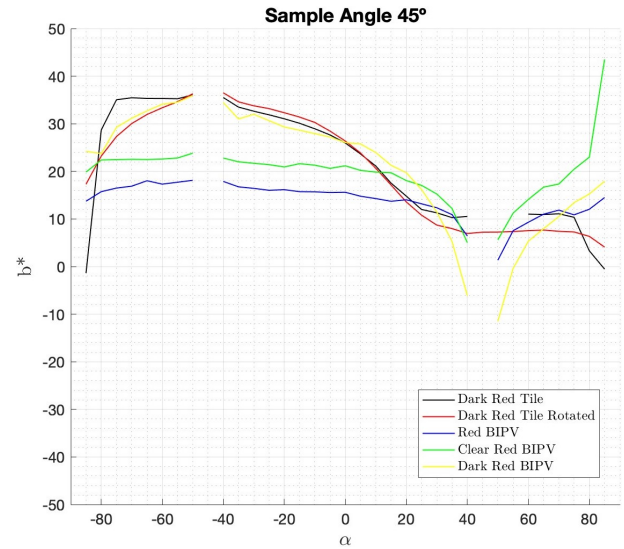


Figure 5.33: Dark Red Tile b^* comparison at 45°

When considering the observed color, it becomes apparent that, in this case, the average color appears to be more of an orange shade, similar to the previous red samples. However, it might have been expected to observe a more pronounced red color, given the material's appearance under sunlight.

5.6 Faro Vidar Clay Shingles

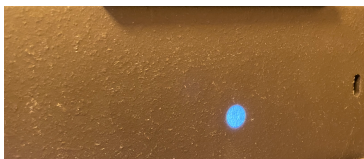


Figure 5.34: Black Komproment sample



Figure 5.35: Black Komproment sample rotated

For this comparison, the same BIPV samples used in the previous analysis of Black tiles will be considered. However, instead of using Black tiles, a Black Komproment sample will be utilized as a substitute.

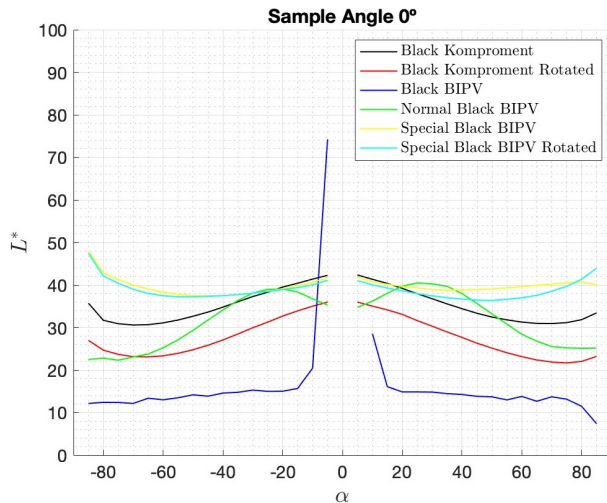


Figure 5.36: Black Komproment L^* comparison at 0°

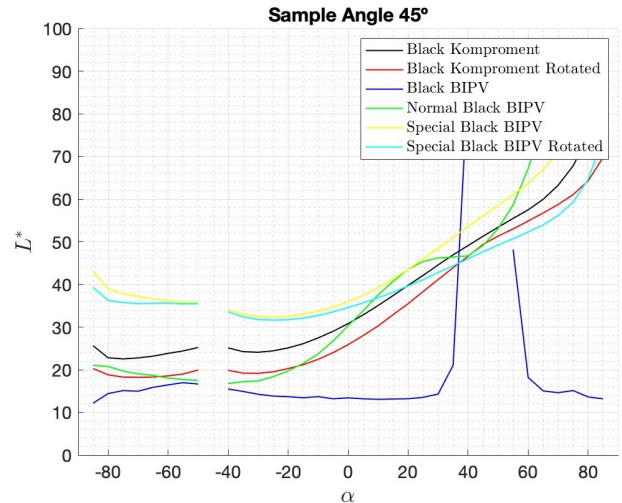


Figure 5.37: Black Komproment L^* comparison at 45°

All of the lightness values fall within a range of 10, with the exception of the Black BIPV sample. The observed trend is quite similar, suggesting that these materials could be closely related. It is noteworthy that the Komproment sample exhibits high reflectance at both high sample and sensor angles, resembling the behavior of the Normal Black BIPV sample. When disregarding the a^* and b^* values, it can be argued that the Normal Black BIPV sample could serve as a suitable substitute for the Komproment samples.

Similar to other black materials, the values of a^* and b^* for the samples under consideration are close to 0. These values are primarily included for the purpose of result verification.

5.7 Natural Black Slate



Figure 5.38: Black slate sample

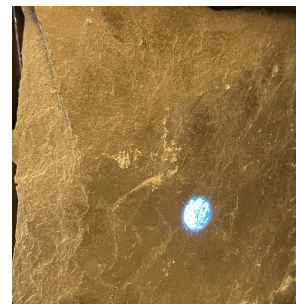


Figure 5.39: Black slate sample rotated

In the last comparison, the study utilizes the same BIPV samples as examined in the previous analysis of black materials. However, for this specific investigation, the black slate material is introduced as the black construction material, with measurements conducted in two distinct directions.

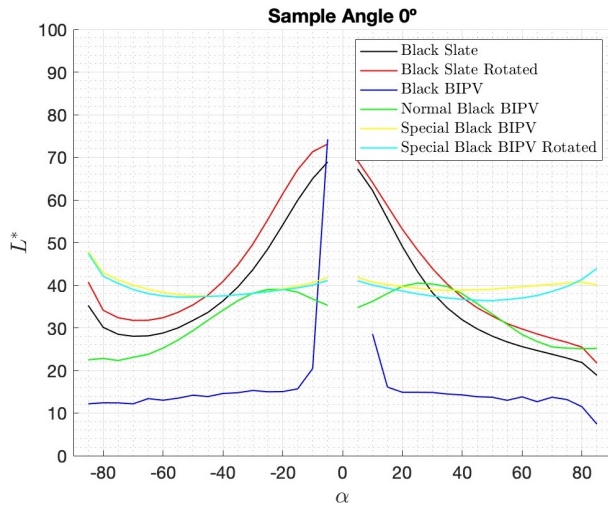


Figure 5.40: Black Slate L^* comparison at 0°

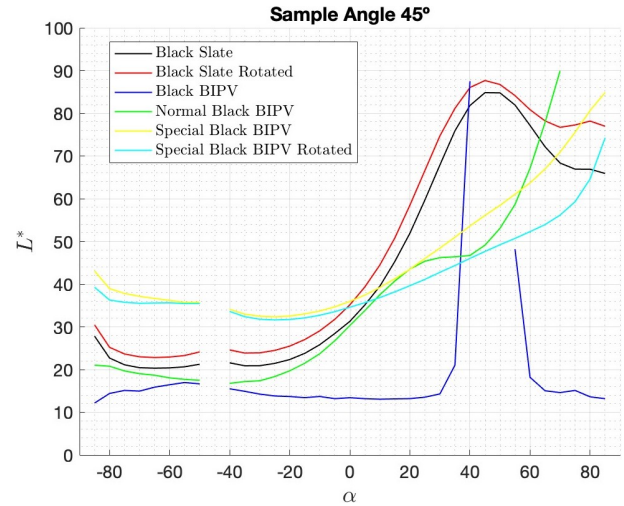


Figure 5.41: Black Slate L^* comparison at 45°

Similar to the previous analysis, the obtained results align with the expected outcomes, demonstrating low lightness values. However, they also reveal the high reflectance of the black slate material, reaching peak levels. This can be attributed to the morphology of the sample, which includes numerous imperfections that influence the reflected light. The black slate exhibits a similar trend to the Black BIPV samples but with a higher baseline lightness. In terms of the other coordinates, they are close to 0, indicating a black color.

6 Other results

Within the scope of color analysis, this section dives into several calculations aimed at providing a comprehensive evaluation of color characteristics. A closer examination of the RGB coordinates for both theoretical and observed colors is presented in Section 6.1. This comparison offers valuable insights into the accuracy and consistency of color reproduction. Moving forward, Section 6.2 explores quantitative color differences through the utilization of the CIELAB color space, a standardized and perceptually uniform measurement system. By analyzing color variations in this manner, a deeper understanding of perceptual distinctions between different color samples is achieved. Additionally, Section 6.3 addresses potential sources of uncertainty in the measurement process, taking into account factors such as lighting conditions and device calibration. The integration of these three sections provides a comprehensive framework for assessing and interpreting color data, ensuring the robustness and reliability of the color analysis within this study.






















6.1 Theoretical RGB vs Practical RGB

The theoretical color of the material will be compared with the color observed by the spectrometer, serving as a foundation for future improvements. To obtain the observed color, the Rapid Tables tool [57] will be utilized to generate an image. The reliability of the generated image will be confirmed by cross-referencing it with established color tables [58]. Subsequently, a comparison will be made between the measured color and the observed color to assess their similarity. This analysis will provide valuable insights into the consistency and accuracy of color representation for the material under investigation.

For the purpose of this master thesis, a results table will be employed to present the color coordinates. Specifically, the color coordinates will be extracted from the sample at $\theta = 0^\circ$ to minimize any potential distortions caused by reflectance effects. In order to assess the impact of reflectance, two sets of coordinates will be showcased: one corresponding to a sensor angle near 0° (Centered RGB) and the other at approximately 45° (Sided RGB). Regarding the Theoretical RGB, it is an approximate observed color putting into contrast the sample given by the manufacturer and using the tool [57]. This approach does not allow a completely accurate analysis, for further research, the Theoretical RGB must be assessed at the construction of the material by the manufacturer.

























Two distinct tables will be presented to showcase the color analysis results. The first table will focus on construction materials, providing a comprehensive overview of their color coordinates and related measurements. The second table, on the other hand, will be dedicated to BIPV materials, offering detailed insights into their color characteristics. By organizing the findings into separate tables, a clear distinction can be made between the color properties of construction materials and BIPV materials.

Table 6.1: Construction materials RGB coordinates

Material	Theoretical RGB	Theoretical Image	Centered RGB	Centered Image	Sided RGB	Sided Image
Yellow	[247,202,110]		[228,184,128]		[223,177,118]	
Glazed Black	[0,0,0]		[252,255,255]		[5,5,5]	
Lille Black	[64,64,64]		[150,147,144]		[64,62,63]	
Clear Red	[238,141,92]		[190,124,93]		[83,50,34]	
Dark Red	[219,99,29]		[209,170,159]		[149,85,61]	
Black Clay Shingles	[105,105,105]		[103,99,98]		[85,81,81]	
Natural Black Slate	[119,119,117]		[158,159,161]		[79,79,80]	

The analysis reveals that among the samples, only the Yellow Tile and Black Clay Shingles closely approximate the theoretical values at all measurement points. The red colors, however, appear more brownish rather than true red, primarily due to the limitations of the measurement setup. Conducting measurements in a dark environment with a single light source directed at a specific position can result in the loss of some information. The black samples highlight the substantial influence of reflectance, as evidenced by the significant variability between the measured and theoretical colors. The Black Clay Shingles exhibit lower variability across all points, which aligns with the sample's isotropic and smooth morphology. Similar behavior is observed for the Yellow Tile. In contrast, the Glazed Black Tile exhibits higher variability, which is expected considering its high reflectance characteristics. A comprehensive summary of these findings can be found in Table 6.1.

Table 6.2: Construction materials RGB coordinates

Material	Theoretical RGB	Theoretical Image	Centered RGB	Centered Image	Sided RGB	Sided Image
Black BIPV	[0,0,0]		[255,255,255]		[38,36,255]	
Clear Red BIPV	[195,88,17]		[255,102,93]		[119,73,255]	
Dark Red BIPV	[209,64,12]		[255,131,140]		[113,47,255]	
Red BIPV	[220,113,18]		[128,96,86]		[100,71,255]	
Gold BIPV	[205,199,16]		[255,255,255]		[132,118,255]	
Normal Black BIPV	[28,28,28]		[128,82,86]		[88,88,255]	
Special Black BIPV	[77,77,72]		[128,88,88]		[66,66,255]	
Yellow BIPV	[223,217,20]		[255,141,85]		[143,124,255]	

In the case of construction materials, the primary factors influencing the perceived color were the reflectance and morphology of the material, leading to variations in lighter or darker values. However, when considering BIPV materials, an additional factor comes into play: the cells incorporated within the BIPV material. These cells significantly impact the perceived color, resulting in violet or blue hues at certain viewing angles. In future research, it will be essential to consider and account for this factor in order to eliminate its influence on the results and normalize the color values effectively.

In conclusion, it is crucial to acknowledge that the materials studied in this research represent only a small subset of the entire spectrum of possibilities. Therefore, definitive conclusions cannot be drawn or confirmed based solely on these results. Rather, the findings presented here should be interpreted as indicative of trends and potential insights. It is important to view this section as a supplementary methodology, providing additional context and understanding, rather than a definitive determinant in the research outcomes.

6.2 Quantitative color difference

This section serves the purpose of creating a database for quantitative color differences, providing a foundation for future research in the field. The theoretical background, including formulas and threshold levels for detecting color differences, is discussed in Chapter 2. The primary objective is to identify and analyze the specific areas where color differences occur, such as variations in lightness, total color difference, and other color coordinates. To achieve this, a comparison matrix will be presented for each construction material, alongside its corresponding BIPV materials, following the methodology outlined in Chapter 5. The variables examined in the comparisons will include lightness, total color difference calculated using the CIEDE2000 formula, as well as chroma (C) and hue (H) coordinates.

In order to provide a comprehensive perspective, the focus of this analysis will be on presenting the average values at 0° sample angle. However, it is crucial to interpret these numbers within the context of further research. Understanding whether these differences are consistently present across the entire color spectrum or limited to specific points will be essential for identifying and eliminating potential sources of error.

Table 6.3: Yellow Tile comparison matrix

Material	ΔE	ΔL	ΔC	ΔH
Yellow BIPV	17.55	19.99	8.04	8.55
Gold BIPV	31.90	43.43	19.99	9.40

Table 6.4: Clear Red Tile comparison matrix

Material	ΔE	ΔL	ΔC	ΔH
Red BIPV	25.28	26.11	20.93	1.24
Dark Red BIPV	26.75	32.24	7.04	5.74
Clear Red BIPV	27.30	35.15	12.50	3.58

Table 6.5: Dark Red Tile comparison matrix

Material	ΔE	ΔL	ΔC	ΔH
Red BIPV	20.06	21.30	13.86	2.43
Dark Red BIPV	19.07	24.42	3.75	3.34
Clear Red BIPV	19.78	27.03	8.21	2.43

Table 6.6: Glazed Black Tile comparison matrix

Material	ΔE	ΔL	ΔC	ΔH
Black BIPV	11.98	16.68	1.56	1.76
Normal Black BIPV	14.91	18.71	1.55	2.48
Special Black BIPV	19.34	25.14	1.50	2.01

Table 6.7: Black Tile comparison matrix

Material	ΔE	ΔL	ΔC	ΔH
Black BIPV	12.98	18.04	0.71	1.35
Normal Black BIPV	9.77	10.31	0.83	1.58
Special Black BIPV	13.21	15.36	0.66	1.67

Table 6.8: Black Komproment comparison matrix

Material	ΔE	ΔL	ΔC	ΔH
Black BIPV	11.93	16.96	1.07	2.10
Normal Black BIPV	5.29	5.58	0.90	2.31
Special Black BIPV	6.56	7.22	1.49	2.24

Table 6.9: Black Slate comparison matrix

Material	ΔE	ΔL	ΔC	ΔH
Black BIPV	15.48	21.00	1.39	1.25
Normal Black BIPV	12.13	12.27	1.71	1.08
Special Black BIPV	13.54	14.94	0.89	0.57

After analyzing and comparing the obtained results, it is evident that further efforts are required to identify suitable substitutes for the construction materials that exhibit minimal perceptible differences. Among all the comparisons conducted, only one comparison matrix, as presented

in Table 6.8, approaches the acceptable threshold defined. It is important to highlight that for black materials, ΔC and ΔH have less importance, as they will be very close, but they are calculated in order to provide a stable structure and create an orientative database. The predominant factor influencing the comparisons is the lightness parameter, suggesting that the observed differences are likely influenced by the high reflectance of the materials rather than inherent color variations. To enhance the analysis, a potential direction for improvement would involve normalizing the values prior to comparison. Additionally, a thorough examination of the measurement thresholds is necessary to identify areas with substantial differences and ascertain their validity. It is plausible that at around the central point of measurement and at high sensor angles, the reflectance values are disproportionately high, thereby distorting the results.

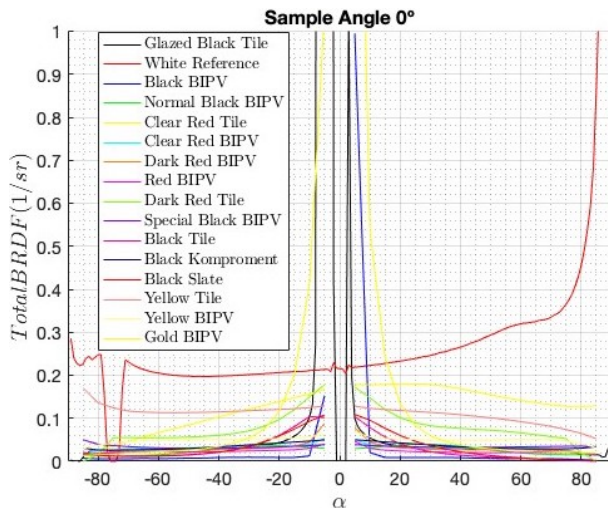


Figure 6.1: Total BRDF at 0° sample angle for all samples

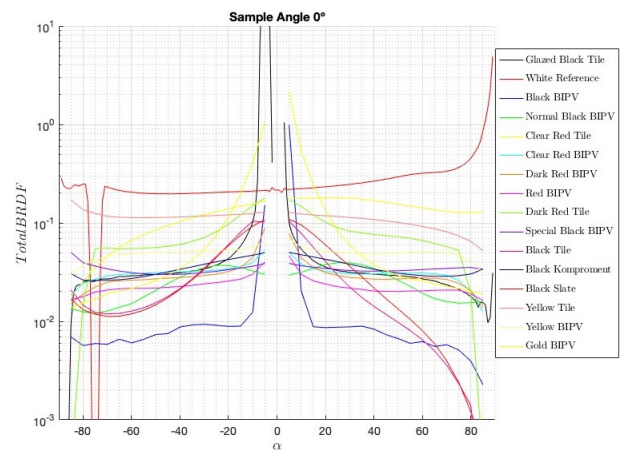


Figure 6.2: Total BRDF at 0° sample angle for all samples in logarithmic scale

To validate the aforementioned statement, the BRDF results for all the samples are depicted in Figures 6.1 and 6.2. It is evident that the baseline of the white reference is significantly higher compared to the other samples, which aligns with the expected behavior for white colors. However, closer examination of these graphs reveals certain issues. Firstly, there is a notable influence of high sensor angles, as observed in the white reference measurement, where values exceed 1. This distortion introduces a challenge in accurately quantifying the measurement differences. Secondly, for materials with high reflectance, results above 1 are observed around a sensor angle of 0°, further contributing to distorted outcomes.

Table 6.10: Yellow Tile comparison matrix modified

Material	ΔE	ΔL	ΔC	ΔH
Yellow BIPV	13.41	11.25	8.04	8.55
Gold BIPV	30.77	40.13	19.99	9.40

Table 6.11: Clear Red Tile comparison matrix modified

Material	ΔE	ΔL	ΔC	ΔH
Red BIPV	25.39	25.34	20.93	1.24
Dark Red BIPV	25.80	27.78	7.04	5.74
Clear Red BIPV	24.93	25.37	12.50	3.58

Table 6.12: Dark Red Tile comparison matrix modified

Material	ΔE	ΔL	ΔC	ΔH
Red BIPV	19.72	20.05	13.86	2.43
Dark Red BIPV	19.34	22.16	3.75	3.34
Clear Red BIPV	18.39	19.45	8.21	2.43

Table 6.13: Glazed Black Tile comparison matrix modified

Material	ΔE	ΔL	ΔC	ΔH
Black BIPV	10.75	13.70	1.56	1.76
Normal Black BIPV	13.15	16.44	1.55	2.48
Special Black BIPV	19.08	24.66	1.50	2.01

Table 6.14: Black Tile comparison matrix modified

Material	ΔE	ΔL	ΔC	ΔH
Black BIPV	11.62	14.43	0.71	1.35
Normal Black BIPV	8.29	8.52	0.83	1.58
Special Black BIPV	13.21	15.36	0.66	1.67

Table 6.15: Black Komproment comparison matrix modified

Material	ΔE	ΔL	ΔC	ΔH
Black BIPV	10.41	13.35	1.07	2.10
Normal Black BIPV	5.71	5.91	0.90	2.31
Special Black BIPV	6.53	7.22	1.49	2.24

Table 6.16: Black Slate comparison matrix modified

Material	ΔE	ΔL	ΔC	ΔH
Black BIPV	14.48	17.39	1.39	1.25
Normal Black BIPV	10.47	10.47	1.71	1.08
Special Black BIPV	13.54	14.94	0.89	0.57

By excluding the extreme values from the analysis, a smoother and more realistic set of values is obtained. These refined values, presented in Tables from 6.10 to 6.16, provide a clearer

representation of the data. Notably, the modifications primarily affect the lightness values, significantly impacting the overall color difference. However, it is important to acknowledge that the obtained results are still far from meeting the desired objectives.

In conclusion, this section serves as a crucial framework for establishing a quantitative methodology for material comparison rather than delving into the specific results. It is essential to acknowledge that the materials presented here may not represent the most optimized versions, as this is a limited sample within a broader spectrum of possibilities.

6.3 Measurement uncertainty

In color analysis experiments, it is crucial to address the potential sources of errors and uncertainties. The subjective nature of color perception by the human eye, as discussed in Chapter 2, poses a significant challenge. To mitigate this subjectivity, a standardized setup has been implemented in this project, aiming to establish consistent conditions for color evaluation and provide quantitative results. However, it is important to recognize that certain factors still warrant careful consideration and further investigation.

One significant consideration is the influence of reflectance on color analysis. Highly reflective materials, as depicted in Figure 4.2, exhibit a strong dependency on reflectance, resulting in observed colors that differ from their true appearances. Although this uncertainty cannot be entirely eliminated in the current project, it highlights the need for future research to address this issue and develop methodologies to obtain more reliable measurements.

Another aspect that can contribute to errors is misalignment, particularly when dealing with curved samples. The curvature of such samples can cause light to deviate from the measurement plane, leading to lower reflectance values than expected. Additionally, the curved surface may reflect light back onto the sample, resulting in higher reflectance and altered color perception, particularly in regions of higher lightness. While careful attention to vertical and horizontal alignment can partially mitigate this issue, it remains a non-trivial challenge. Therefore, it is imperative to explore standardized setups suitable for different sample morphologies, with the goal of minimizing the impact of misalignment on color analysis.

6.3.1 Repeatability

The reproducibility of measurements is a critical factor of uncertainty that warrants attention in this study. In the following section, a concise qualitative discussion will be presented, focusing on the feasibility of reproducing the measurements. While it is not within the scope of this thesis to provide a detailed description for all materials, all examined morphologies will be analyzed and supplemented with additional information in the Appendix for comprehensive understanding and reference.

Lightness values are chosen over BRDF values for comparing reproducibility in color materials measurements due to their perceptual relevance, simplicity, and practicality. Lightness captures the overall brightness or darkness of materials, making it easier to interpret and compare across different samples. In contrast, BRDF values are complex and challenging to directly compare. By focusing on lightness, we can ensure a standardized and accessible approach to assessing reproducibility, enabling more meaningful comparisons in color measurements.

For each material, a graph displaying three different L^* values will be presented at a sample angle of 0° . Only lightness values will be included as it is easier to see the difference, a^* and b^* values are always closer and more constant. Additional graphs will be included in Appendix B for readers who wish to delve deeper into the analysis. However, it is worth noting that includ-

ing only the 0° graphs suffices, as the primary focus is on determining the reproducibility of the measurements.

The initial finding of this study indicates a high level of replicability and certainty in the measurements. Most of the measurements yield identical or nearly identical results. However, it is important to note the distinctions between BIPV materials and construction materials. The measurement setup is optimized for thin and flat samples like BIPV materials, making it easier to obtain consistent outcomes. On the other hand, construction materials, which are generally thicker and exhibit curvature, present challenges in replication. Despite these challenges, construction materials demonstrate similar trends, albeit with varying base levels.

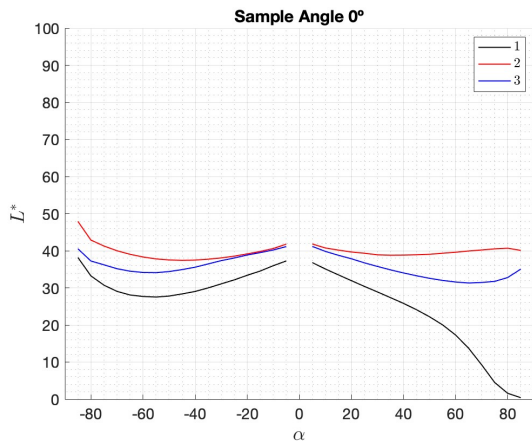


Figure 6.3: Reproducibility of Special Black BIPV at 0° sample angle

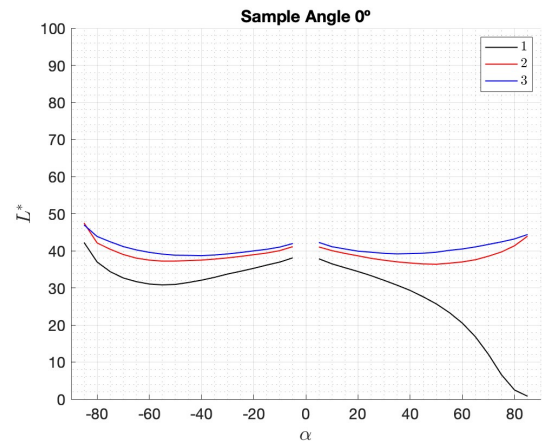


Figure 6.4: Reproducibility of Special Black BIPV Rotated at 0° sample angle

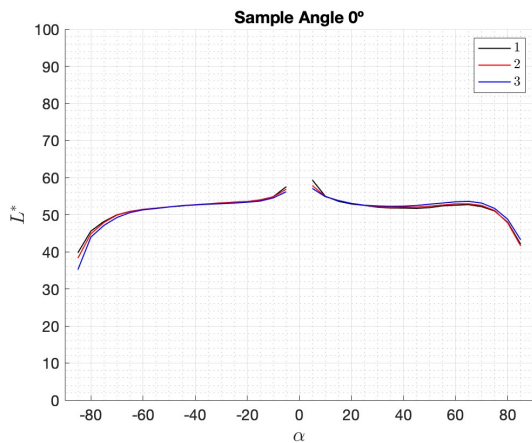


Figure 6.5: Reproducibility of Yellow BIPV at 0° sample angle

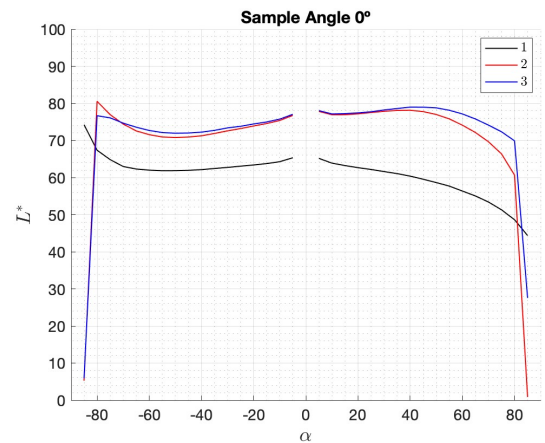


Figure 6.6: Reproducibility of Yellow Tile at 0° sample angle

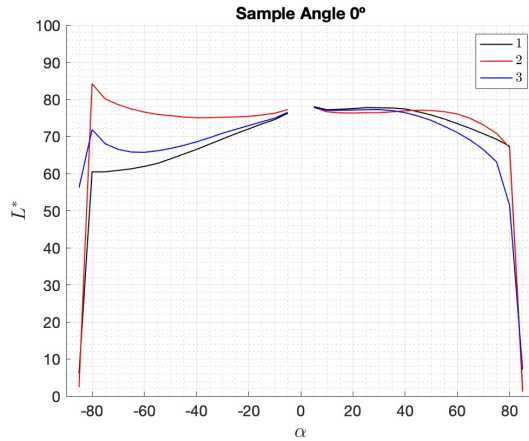


Figure 6.7: Reproducibility of Yellow Tile Rotated at 0° sample angle

For instance, in Figure 6.6, all measurements display the same trend but with slight variations in the baseline. This discrepancy may be attributed to misalignment during one of the measurements.

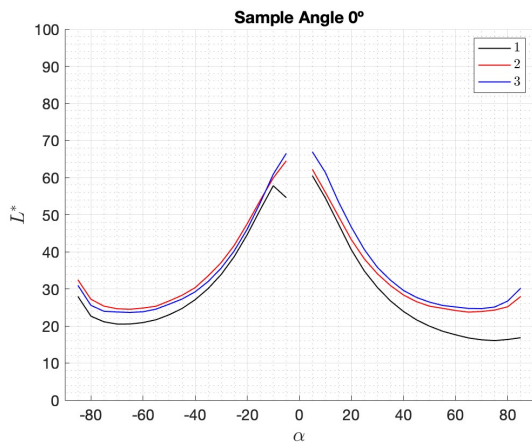


Figure 6.8: Reproducibility of Black Tile Rotated at 0° sample angle

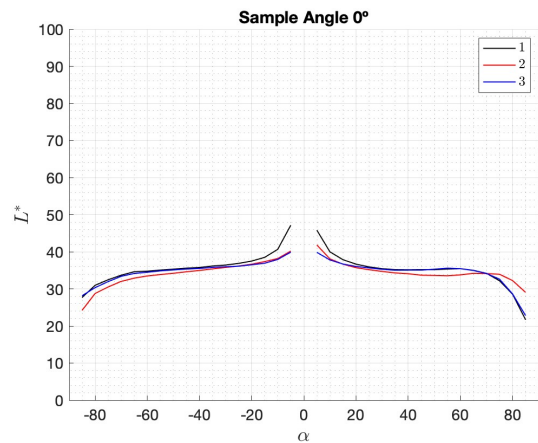


Figure 6.9: Reproducibility of Clear Red BIPV at 0° sample angle

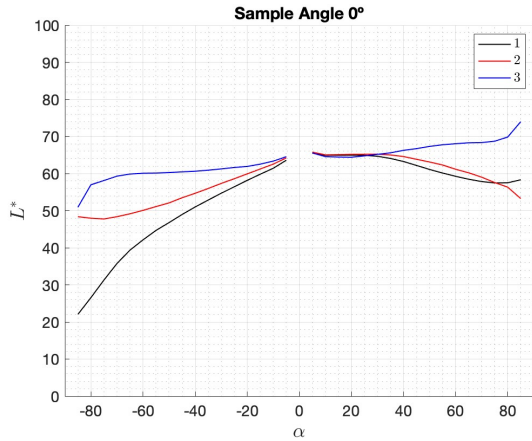


Figure 6.10: Reproducibility of Clear Red Tile at 0° sample angle

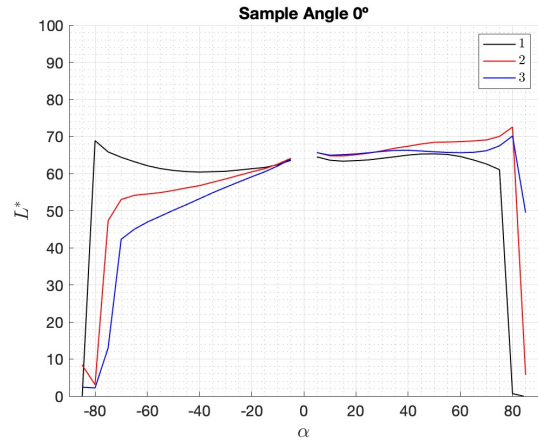


Figure 6.11: Reproducibility of Clear Red Tile Rotated at 0° sample angle

The morphology of the sample plays a crucial role, as observed in Figure 6.10, where the sample's curvature influences the results at high absolute sensor angles.

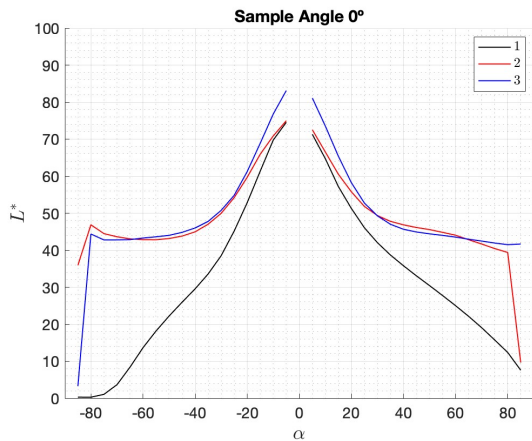


Figure 6.12: Reproducibility of Dark Red Tile Rotated at 0° sample angle

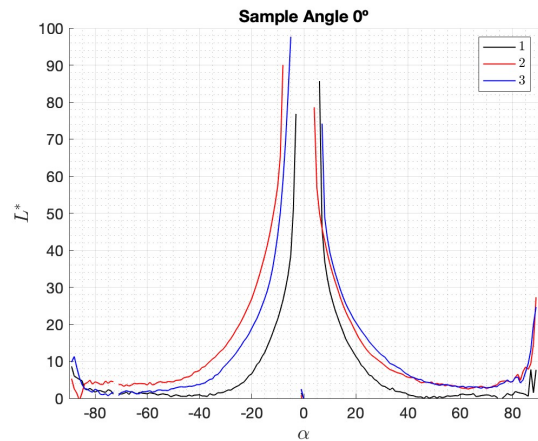


Figure 6.13: Reproducibility of Glazed Tile at 0° sample angle

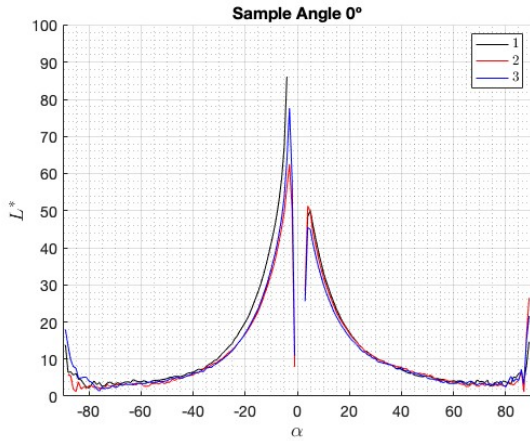


Figure 6.14: Reproducibility of Glazed Tile Rotated at 0° sample angle

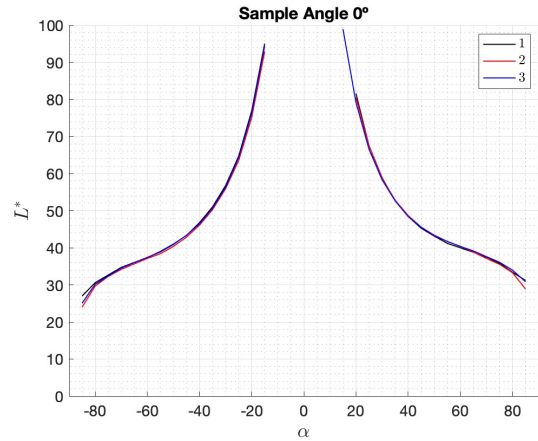


Figure 6.15: Reproducibility of Gold BIPV at 0° sample angle

In Figure 6.14 it is possible to see the influence of replicability even in highly reflecting materials.

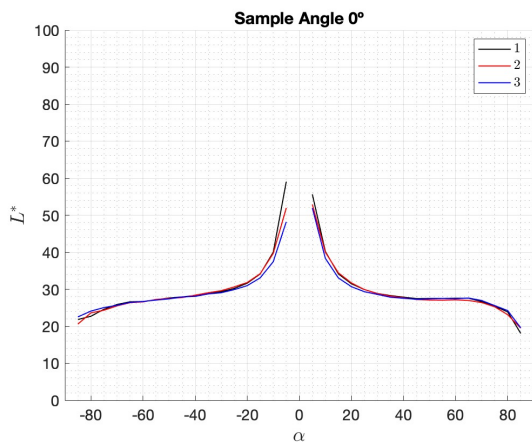


Figure 6.16: Reproducibility of Dark Red BIPV at 0° sample angle

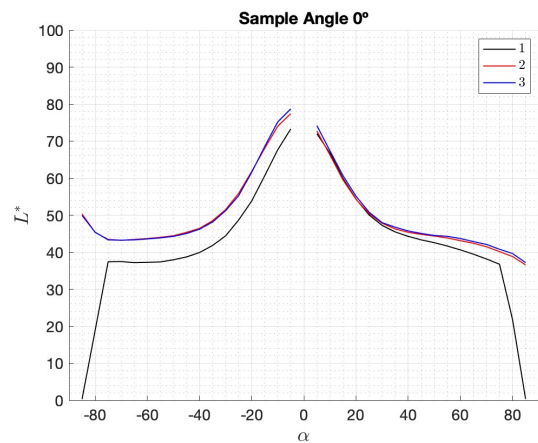


Figure 6.17: Reproducibility of Dark Red Tile at 0° sample angle

In Figure 6.17, an illustrative example demonstrates the potential impact of sample curvature on measurements. A misalignment can lead to variations in color coordinates that deviate from the expected values, resulting in the loss of valuable information across measured angles.

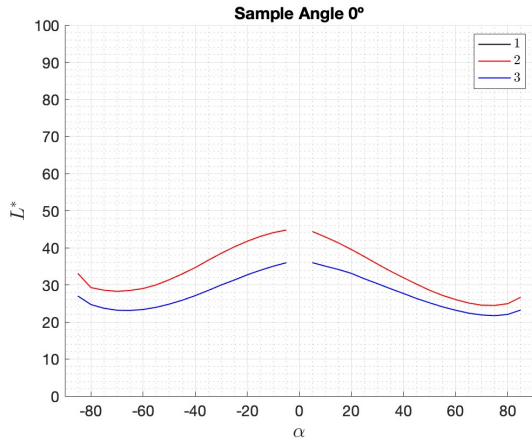


Figure 6.18: Reproducibility of Komproment Rotated at 0° sample angle

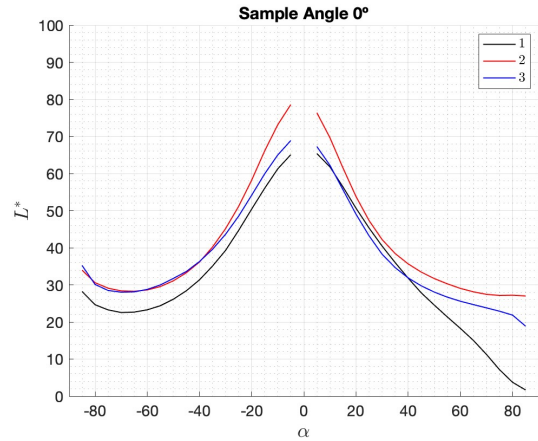


Figure 6.19: Reproducibility of Black Slate at 0° sample angle

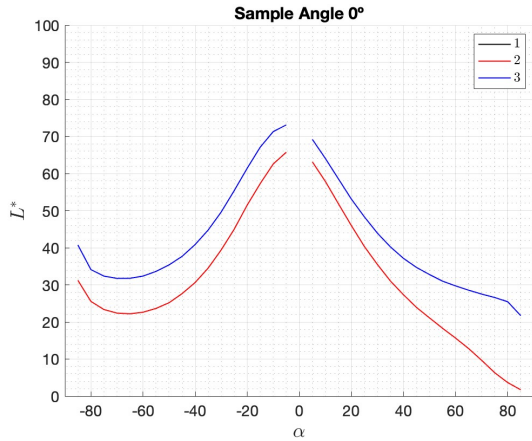


Figure 6.20: Reproducibility of Black Slate Rotated at 0° sample angle

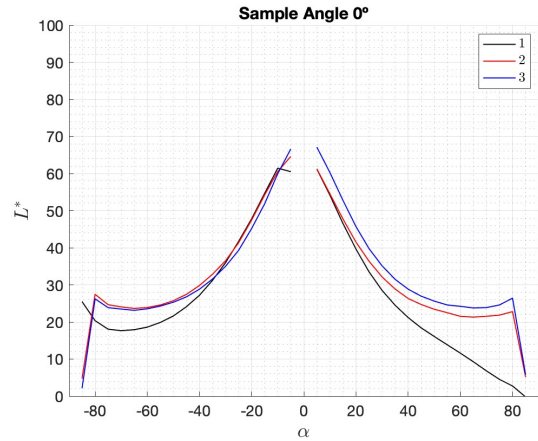


Figure 6.21: Reproducibility of Black Tile at 0° sample angle

Inconsistencies in alignment can also be observed in BIPV samples, as illustrated in Figures 6.19 and 6.20. These samples exhibit slight irregularities and disturbances that can potentially impact reflectance and affect the accuracy of measurements obtained by the sensor. Consequently, these factors may result in a partial loss of information during the measurement process.

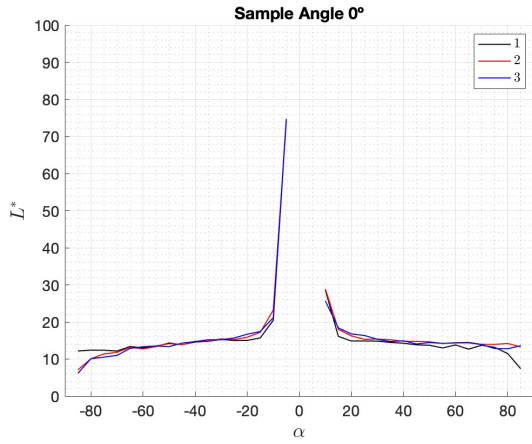


Figure 6.22: Reproducibility of Black BIPV at 0° sample angle

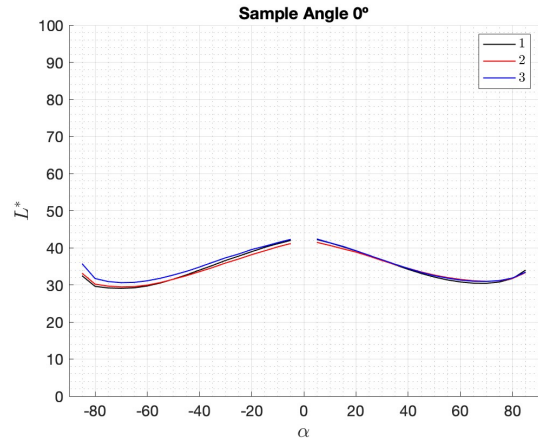


Figure 6.23: Reproducibility of Komproment at 0° sample angle

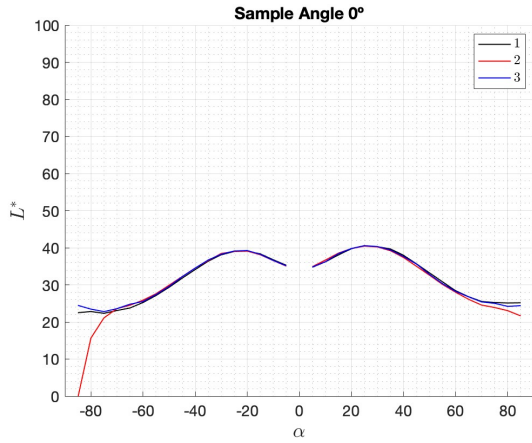


Figure 6.24: Reproducibility of Normal Black BIPV at 0° sample angle

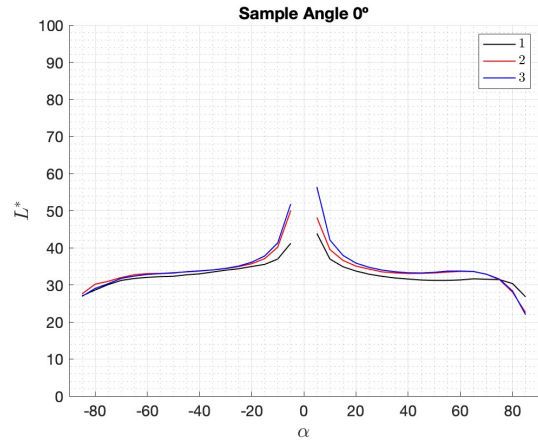


Figure 6.25: Reproducibility of Red BIPV at 0° sample angle

In conclusion, the measurements exhibit a reasonably high level of reproducibility, but it is essential to exercise caution and diligence in the measurement process.

7 Results analysis and further research

The following section focuses on the analysis of the color comparison results obtained from the various color measurement techniques employed. These results offer valuable insights into the similarities and differences between different color samples, shedding light on the effectiveness of the color reproduction processes. Through a comprehensive examination of the obtained data, including RGB coordinates, CIELAB color differences, and uncertainties, a deeper understanding of the color characteristics and their variations is attained. The analysis will provide meaningful interpretations of the color comparison results, highlighting any significant trends, patterns, or discrepancies. This thorough evaluation will contribute to the overall understanding of color performance and guide further investigations and improvements in color reproduction techniques. Furthermore, avenues for further research are identified to extend and enhance the understanding of color performance and its implications in the built environment. By addressing the limitations and gaps identified in this study, future research endeavors can contribute to advancing color reproduction techniques, exploring alternative color spaces, investigating color stability, and developing innovative approaches for color matching and reproduction.

7.1 Results analysis

Sections 5 and 6 of this thesis have been devoted to presenting the obtained results and conducting complementary calculations to facilitate their interpretation. The key emphasis lies in the combination of Section 5, which showcases the quantitative color comparison results, with the overall project development. It is important to acknowledge that the sample selection is limited in scope, thus the analysis and conclusions derived from it serve as guidance rather than definitive findings. The primary objective of this research is to establish a methodology and offer guidelines for future investigations in this field.

Currently, the technology for generating substitutes for construction materials does not seem to meet the stringent requirements of regulatory authorities. None of the BIPV samples closely resemble their corresponding construction materials, with noticeable differences, especially in colored samples. However, replicating black materials or differentiating between them proves to be relatively easier.

It is crucial to differentiate between satinated or smooth materials and highly reflective materials in terms of their characteristics. Satinated materials, such as the Yellow Tile or Clear Red Tile, exhibit relatively stable and angle-independent color coordinates and BRDF results. Although their baselines may be high, the overall trend remains consistent without significant fluctuations. However, it should be noted that the curvature or disposition of the sample can impact the results, potentially distorting them and deviating from expected values or comparisons with other measurements. On the other hand, highly reflective materials, like the Gold BIPV or the Glazed Black Tile, display significant variations in their values, indicating an angle-dependent behavior. This poses challenges in comparing such materials, particularly at specular plane positions where light is directly directed towards the sensor, resulting in high readings and saturation.

When comparing black construction materials to colored construction materials, it becomes evident that black materials exhibit greater variability, mainly in lightness. This can be attributed to the increased visibility of partially illuminated areas on black surfaces under dark measurement conditions compared to red or yellow materials.

One notable source of error or distortion in the results arises from measurements taken at high sensor and sample angles. In such cases, the obtained values exceed 100 in lightness with an upward trend, which in the case of specularly reflecting materials is a characteristic [59]. This issue is inherent to the experimental setup and should be addressed in future research to ensure accurate measurements and reliable comparisons.

By incorporating the quantitative results from Section 6.2 as a complementary analysis, the previous conclusions become evident. Eliminating extreme results, particularly those generated at specular planes and high sensor angles, brings the measurements closer to reality and facilitates meaningful comparisons. This can be observed by comparing tables used for quantitative color comparison. The modification primarily affects the lightness values, resulting in lower values compared to the original measurements.

It is important to note that this quantitative analysis represents an average at a 0° sample angle. For future research, it is recommended to consider all measurements, which would likely reveal greater differences since BIPV materials demonstrate a higher degree of angle dependency and reflectance compared to tile materials. Additionally, as it is an average, there is no comparison at each angle, which is essential. Merely appearing to be equal based on an average is insufficient. The color difference must fall within an acceptable range at every point. Failure to meet this criterion would render the material unsuitable for installation, potentially resulting in economic and reputational losses for the manufacturing company.

Moving on to the additional calculations presented in Section 6, several conclusions can be drawn. Firstly, the replicability of measurements is highly feasible, particularly for BIPV materials. This is primarily attributed to the setup being specifically designed flat and thin materials (such as BIPV), and not for the heavy and variable shape of the construction materials. However, even construction materials exhibit a reasonable level of replicability when careful alignment is ensured. It should be noted that due to the non-flat morphology of construction materials, characterized by curves and variations in composition, there may be certain points on the tile that cannot be measured accurately, especially when curvature interferes with proper light detection by the sensor. Conversely, BIPV materials are completely flat with consistent composition, except for the presence of solar cells.

The integration of solar cells into the analysis presented in Section 6.1 involves calculating RGB coordinates to assess the similarity between the measured and observed colors. Only two construction materials demonstrate close agreement between measured and observed colors. Notably, the Clear Red Tile appears darker to the sensor compared to the Dark Red Tile. This could be attributed to the higher reflectance exhibited by the Dark Red Tile, resulting in lighter measured results. The Glazed Black Tile is particularly noteworthy due to its significant variability across different measurement positions, a characteristic stemming from its mirror-like composition. Shifting focus to BIPV materials, achieving close proximity to the observed colors becomes even more challenging. The presence of a purple/blue appearance in the sidelight measurements is especially perplexing. This phenomenon arises from the influence of the solar cells embedded within the tile, which affects both the sidelight measurements and the centered measurement. This consideration should be taken into account in future research to normalize the values. Additionally, the presence of blue hues in the BIPV samples can be further understood by examining the a^* and b^* graphs, which reveal similar or nearly equal values for both coordinates, indicating a blue color tendency.

In conclusion, this thesis has shed light on the challenges of accurately replicating colors in construction materials and BIPV samples. While black materials show relatively higher replicability, colored materials pose greater difficulties. The distinction between satinated/smooth and highly reflective materials is crucial, as they exhibit different behaviors. The study highlights the

need to address measurement errors at high sensor and sample angles. Incorporating quantitative results improves comparability, and replicability is feasible with careful alignment. The integration of solar cells in BIPV materials adds complexity to color measurements. This research provides valuable insights and guidelines for future investigations, aiming to enhance color replication and regulatory compliance in the construction industry.

7.2 Further Research

Based on the comprehensive analysis conducted in this thesis, several research directions can be proposed to enhance the BIPV technology and address the existing challenges.

Firstly, future research should focus on expanding the database of construction and BIPV materials to minimize the color disparity between them. Standardizing the setup for measuring construction materials is crucial to reduce variability and ensure consistent measurements, similar to what is currently done for BIPV samples.

Secondly, considering the shape of the sample is essential to eliminate or minimize the influence of material curvature on measurements. Developing methods to obtain reliable data by accounting for sample shape will contribute to more accurate color replication.

Thirdly, solar cells affect to the appearance and perception of BIPV materials. This influence should be reduced in order to reduce the apparent difference between materials. An option could be to measure the cells separately and then subtract their influence from the overall measurements to normalize the values.

Fourthly, to mitigate the errors arising from measuring only a small portion of the sample, it is advantageous to extend the measured area or capture multiple points simultaneously and compute their average. It is important to consider that the area observed by an observer is influenced by the solid angle, which in turn depends on factors such as the distance to the object and the size of the object [60]. Notably, the area perceived by a person is typically greater than the area captured by the utilized sensor. Therefore, expanding both the illuminated area and the measured area by the sensor can contribute to obtaining more reliable and representative results.

Fifthly, further exploration and refinement of quantitative comparison results are necessary. Developing a system that enables comparison at every point and addressing extreme results will enhance the accuracy and reliability of color measurements.

Lastly, conducting measurements under real conditions, particularly sunlight, can provide insights into the behavior of these materials. However, it is important to consider potential challenges such as undesired reflections and higher illuminance, which may distort the results.

These research directions offer promising avenues to bridge the existing color disparity in the sector. While some challenges lie ahead, a meticulous and systematic approach will be invaluable for future advancements in the field.

8 Conclusions

This master thesis aimed to evaluate the visual disparities between BIPV products and construction materials, while also developing a methodology to facilitate this comparison and establish a foundation for future research. By utilizing a specialized setup for measuring BRDF, the objectives of the study have been successfully achieved, incorporating various techniques to ensure reliable and measurable comparisons.

The entire setup, calibrated with a white reference sample, enabled accurate reflectance measurements of samples at different viewing angles. These measurements were then transformed into BRDF data and further converted into color coordinates in the CIELAB color space.

Two sets of samples were evaluated, one comprising construction materials and the other containing BIPV samples. In addition to qualitative comparisons based on CIELAB coordinates, quantitative color difference metrics and RGB coordinates were calculated. The replicability of measurements was also assessed.

The analysis of color coordinate measurements revealed that further efforts are necessary to achieve visually indistinguishable samples. Highly reflective materials, such as Glazed Black Tile, exhibited angle-dependent results, particularly at the specular plane. Conversely, satin-finished materials like Clear Red Tile displayed relatively stable measurements across different viewing angles. The materials' shape influence was found to be important, as could result in the loss of some reflectance, thus leading to lower than expected results, mainly due to curvatures of the samples stepping in between the sensor and the source of light.

Regarding replicability, similar results were observed for all samples when measured multiple times, particularly for BIPV samples. However, it is important to note that the setup is optimized for flat and thin samples, whereas construction materials often deviate from this ideal and are typically heavier. Therefore, future research should focus on refining the setup to accommodate construction materials and minimize small differences, ultimately establishing a standardized measurement approach.

Furthermore, the influence of solar cells on the appearance of BIPV samples was found to be significant. This factor should be taken into account in future studies aimed at eliminating visual disparities in BIPV products.

Bibliography

- [1] United Nations Climate Change. *Las emisiones mundiales de CO2 repuntaron en 2021 hasta su nivel más alto de la historia*. 2022. URL: <https://unfccc.int/es/news/las-emisiones-mundiales-de-co2-repuntaron-en-2021-hasta-su-nivel-mas-alto-de-la-historia#:~:text=Las%20emisiones%20mundiales%20de%20di%20C3%B3xido,del%20carb%C3%B3n%20para%20impulsar%20ese>.
- [2] Global Alliance for Buildings and Construction. *2022 GLOBAL STATUS REPORT FOR BUILDINGS AND CONSTRUCTION*. 2022. URL: <https://globalabc.org/our-work/tracking-progress-global-status-report>.
- [3] Piotr Bojek. *Solar PV*. 2022. URL: <https://www.iea.org/reports/solar-pv>.
- [4] Photovoltaic Power Systems Programme. *Trends in Photovoltaic Applications*. Tech. rep. 2021. URL: <https://tecsol.blogs.com/files/iea-pvps-trends-report-2021-1.pdf>.
- [5] Michele Zinzi, Emiliano Carnielo, and Giuseppe Rossi. “Directional and angular response of construction materials solar properties: Characterisation and assessment”. In: *Solar Energy* 115 (2015), pp. 52–67. ISSN: 0038-092X. DOI: <https://doi.org/10.1016/j.solener.2015.02.015>. URL: <https://www.sciencedirect.com/science/article/pii/S0038092X15000857>.
- [6] Markus Babin. “Experimental characterization of angular dependent color perception of colored PV samples in combination with IAM measurements targeting building integrated photovoltaic products”. Master Thesis. 2020.
- [7] Sensient Industrial Colors. *How Do We Calculate a Perceptible Difference?* URL: <https://www.sensientindustrial.com/emea/color-college/how-to-choose-color/how-do-we-calculate-a-perceptible-difference>.
- [8] María M. Pérez et al. “CIEDE2000 lightness, chroma and hue human gingiva thresholds”. In: *Journal of Dentistry* 124 (2022), p. 104213. ISSN: 0300-5712. DOI: <https://doi.org/10.1016/j.jdent.2022.104213>. URL: <https://www.sciencedirect.com/science/article/pii/S030057122200269X>.
- [9] Nabil Alghazali et al. “Assessment of perceptibility and acceptability of color difference of denture teeth”. In: *Journal of Dentistry* 40 (2012). The Journal of Color and Appearance in Dentistry, e10–e17. ISSN: 0300-5712. DOI: <https://doi.org/10.1016/j.jdent.2012.04.023>. URL: <https://www.sciencedirect.com/science/article/pii/S0300571212001182>.
- [10] W. R. McCluney. *Introduction to Radiometry and Photometry, 2nd ed.* 2014. URL: https://www.academia.edu/17482167/Introduction_to_Radiometry_and_Photometry_Second_Edition_2014.
- [11] Asim Kumar Roy Choudhury. “2 - Object appearance and colour”. In: *Principles of Colour and Appearance Measurement*. Ed. by Asim Kumar Roy Choudhury. Woodhead Publishing, 2014, pp. 53–102. ISBN: 978-0-85709-229-8. DOI: <https://doi.org/10.1533/9780857099242.53>. URL: <https://www.sciencedirect.com/science/article/pii/B9780857092298500024>.
- [12] Matt Pharr, Wenzel Jakob, and Greg Humphreys. “08 - Reflection Models”. In: *Physically Based Rendering (Third Edition)*. Ed. by Matt Pharr, Wenzel Jakob, and Greg Humphreys. Third Edition. Boston: Morgan Kaufmann, 2017, pp. 507–568. ISBN: 978-0-12-800645-0. DOI: <https://doi.org/10.1016/B978-0-12-800645-0.50008-7>. URL: <https://www.sciencedirect.com/science/article/pii/B9780128006450500087>.
- [13] Ivan P. Kaminow, Tingye Li, and Alan E. Willner. *Optical Fiber Telecommunications*. sixth. Academic Press, 2013.
- [14] Robert D. Guenther. *Encyclopedia of Modern Optics*. Elsevier, 2005.
- [15] Fred E. Nicodemus. “Directional Reflectance and Emissivity of an Opaque Surface”. In: *Applied Optics* 4.7 (July 1965), pp. 767–775. DOI: 10.1364/AO.4.000767.

- [16] Hongsong Li et al. "Automated three-axis gonioreflectometer for computer graphics applications". In: *Cornell University* (2006).
- [17] W. Erb. "High-Accuracy Gonioreflectance Spectrometry at the Ptb". In: *Advances in Standards and Methodology in Spectrophotometry*. Ed. by C. Burgess and K.D. Mielenz. Vol. 2. Analytical Spectroscopy Library. Elsevier, 1987, pp. 87–98. DOI: <https://doi.org/10.1016/B978-0-444-42880-6.50009-X>. URL: <https://www.sciencedirect.com/science/article/pii/B978044442880650009X>.
- [18] Alison Gilchrist and Jim Nobbs. "Colorimetry, Theory". In: *Encyclopedia of Spectroscopy and Spectrometry (Third Edition)*. Ed. by John C. Lindon, George E. Tranter, and David W. Koppenaal. Third Edition. Oxford: Academic Press, 2017, pp. 328–333. ISBN: 978-0-12-803224-4. DOI: <https://doi.org/10.1016/B978-0-12-803224-4.00124-2>. URL: <https://www.sciencedirect.com/science/article/pii/B9780128032244001242>.
- [19] Jeff Johnson. "Chapter 5 - Our Color Vision is Limited". In: *Designing with the Mind in Mind*. Ed. by Jeff Johnson. Boston: Morgan Kaufmann, 2010, pp. 53–63. ISBN: 978-0-12-375030-3. DOI: <https://doi.org/10.1016/B978-0-12-375030-3.00005-3>. URL: <https://www.sciencedirect.com/science/article/pii/B9780123750303000053>.
- [20] *HUE, VALUE, SATURATION*. URL: <https://web.archive.org/web/20170630065346/http://learn.leighcotnoir.com/artspk/elements-color/hue-value-saturation/>.
- [21] Rolf G. Kuehni. "The early development of the Munsell system". In: *Color Research & Application* 27.1 (), pp. 20–27. DOI: <https://doi.org/10.1002/col.10002>. URL: <https://onlinelibrary.wiley.com/doi/abs/10.1002/col.10002>.
- [22] Redgeomática. *Capítulo V: el Color*. URL: http://redgeomatica.rediris.es/cart02/arbolB/cart0B/Bcap5/5_9_1.htm.
- [23] Dr. David Briggs. *The Difference Between Chroma and Saturation*. URL: <https://munsell.com/color-blog/difference-chroma-saturation/>.
- [24] Kristi Pelzel. *Color Theory: Lightness is the brightness of a color compared to its background*. 2022. URL: <https://medium.com/upskilling/color-theory-lightness-is-the-brightness-of-a-color-compared-to-its-background-51e2d389d264>.
- [25] Negar. *The Most Visible Colors For Human Eyes!* 2021. URL: <https://colors.dopely.top/inside-colors/the-most-visible-colors-for-human-eyes/>.
- [26] Robert T. Marcus. "chapter 2 - The Measurement of Color". In: *Color for Science, Art and Technology*. Ed. by Kurt Nassau. Vol. 1. AZimuth. North-Holland, 1998, pp. 31–96. DOI: [https://doi.org/10.1016/S1387-6783\(98\)80005-6](https://doi.org/10.1016/S1387-6783(98)80005-6). URL: <https://www.sciencedirect.com/science/article/pii/S1387678398800056>.
- [27] T. Huber T.P. Sakmar. *Rhodopsin*. 2009. URL: <https://www.sciencedirect.com/science/article/pii/B9780080450469009220>.
- [28] Christophe Yamahata. *CIE 1931 XYZ colour space*. URL: <https://observablehq.com/@christophe-yamahata/cie-1931-xy-chromaticity-diagram>.
- [29] T Smith and J Guild. "The C.I.E. colorimetric standards and their use". In: *Transactions of the Optical Society* 33.3 (Jan. 1931), p. 73. DOI: 10.1088/1475-4878/33/3/301. URL: <https://dx.doi.org/10.1088/1475-4878/33/3/301>.
- [30] R.W.G. Hunt. *Measuring Colour*. Measuring Colour. Fountain, 1998. ISBN: 9780863433870. URL: <https://books.google.dk/books?id=LodxQgAACAAJ>.
- [31] Wikipedia. *Espacio de color Lab*. 2023. URL: https://es.wikipedia.org/wiki/Espacio_de_color_Lab.
- [32] J. Schwiegerling. *Field Guide to Visual and Ophthalmic Optics*. SPIE Press, 2004.
- [33] Nuria Martín-Chivelet et al. "Building-Integrated Photovoltaic (BIPV) products and systems: A review of energy-related behavior". In: *Energy and Buildings* 262 (2022), p. 111998. ISSN: 0378-7788. DOI: <https://doi.org/10.1016/j.enbuild.2022.111998>. URL: <https://www.sciencedirect.com/science/article/pii/S0378778822001694>.

- [34] Nallapaneni Manoj Kumar, K. Sudhakar, and M. Samykano. "Performance comparison of BAPV and BIPV systems with c-Si, CIS and CdTe photovoltaic technologies under tropical weather conditions". In: *Case Studies in Thermal Engineering* (2019). DOI: <https://doi.org/10.1016/j.csite.2018.100374>. URL: <https://www.sciencedirect.com/science/article/pii/S2214157X18303940>.
- [35] Carlos Toledo et al. "BUILDING INTEGRATED PHOTOVOLTAICS (BIPV) VS. BUILDING ATTACHED PHOTOVOLTAICS (BAPV): BALANCE BETWEEN ENERGY PRODUCTION AND ARCHITECTURAL DESIGN". In: *Universidad Politécnica de Cartagena* (2016). URL: <https://www.aepro.com/files/congresos/2016cartagena/05023.4671.pdf>.
- [36] Tractile. *What is BIPV?* 2022. URL: <https://tractile.com.au/news/what-is-bipv/>.
- [37] Gramas. *Sistema fotovoltaico integrado en edificios (BIPV)*. 2021. URL: <https://gramaconsultores.wordpress.com/2013/10/21/sistema-fotovoltaico-integrado-en-edificios-bipv/>.
- [38] Ferrovia. *Materiales de Construcción*. URL: <https://www.ferrovial.com/es/recursos/materiales-construccion/>.
- [39] keobra. *Clasificación de los materiales de construcción*. 2020. URL: <https://keobra.com/clasificacion-de-los-materiales-de-construccion>.
- [40] Nationwide. *Different types of roofs*. 2022. URL: <https://www.nationwide.com/lc/resources/home/articles/types-of-roofing#:~:text=Asphalt%20shingles%20are%20the%20most,effective%20in%20all%20environmental%20conditions..>
- [41] Cristina Gómez-Polo et al. *Comparison of the CIE Lab and CIEDE2000 color difference formulas*. 2016. URL: <https://www.sciencedirect.com/science/article/pii/S0022391315003790>.
- [42] A.K. Roy Choudhury. *Colour-difference assessment*. 2015. URL: <https://www.sciencedirect.com/science/article/pii/B9781782423676500034>.
- [43] M.W. Andemeskel. "Broadband light source based angular resolved measurement of optical properties of materials and solar cells". PhD Thesis. Sep. 21, 2018.
- [44] Labsphere, "Optical-grade Spectralon® reflectance material," *Datasheet*. URL: <https://www.labsphere.com/product/spectralon-diffuse-reflectance-standards/>.
- [45] James J. Butler Georgi T Georgiev. *BRDF study of gray-scale Spectralon*. 2008. URL: https://www.researchgate.net/publication/252227671_BRDF_study_of_gray-scale_Spectralon.
- [46] Labsphere. "Reflectance Materials and coatings", *Technical Guide*. URL: https://www.systems-eng.co.jp/dcms_media/other/Guide_Reflectance_Materials_Coatings.pdf.
- [47] *Spectralon® Diffuse Reflectance Standards*. URL: <chrome-extension://efaidnbmninnibpcapjpcgiclfendmkaj/https://sphereoptics.de/en/wp-content/uploads/sites/3/2014/03/Labsphere-Diffuse-Reflectance-Standards-Spectralon.pdf>.
- [48] *Randers Tegl*. URL: <https://www.randerstegl.com/>.
- [49] *RT 811 Højslev Lille Dansk format*. URL: <https://www.randerstegl.com/en/roof-tiles/product/rt811-hoejslev-lille-dansk-format?PID=54527>.
- [50] *RT 845 Laumans IdealVariabel*. URL: <https://www.randerstegl.com/en/roof-tiles/product/rt845-laumans-idealvariabel?PID=54527>.
- [51] *RT 840 Højslev Lille Dansk format*. URL: <https://www.randerstegl.com/en/roof-tiles/product/rt840-hoejslev-lille-dansk-format?PID=54527>.
- [52] *RT 841 Laumans IdealVariabel*. URL: <https://www.randerstegl.com/en/roof-tiles/product/rt841-laumans-idealvariabel?PID=54527>.
- [53] *RT 844 Laumans IdealVariabel*. URL: <https://www.randerstegl.com/en/roof-tiles/product/rt844-laumans-idealvariabel?PID=54527>.
- [54] *Komproment*. URL: <https://komproment.com/>.
- [55] *FARO*. URL: <https://komproment.com/produkt/vidar-clay-shingles/faro/>.
- [56] *RUSTIC*. URL: <https://komproment.dk/produkt/naturskifer/rustik/>.
- [57] *RGB Color Codes Chart*. URL: https://www.rapidtables.com/web/color/RGB_Color.html.

- [58] *RGB*. URL: <https://es.wikipedia.org/wiki/RGB#>.
- [59] Markus Babin et al. "Glare Potential Evaluation of Structured PV Glass Based on Gonioreflectometry". In: *IEEE Journal of Photovoltaics* 12.6 (2022), pp. 1314–1318. DOI: 10.1109/JPHOTOV.2022.3189779.
- [60] Shwetank Mauria. *What is formula for solid angle labeled in the given figure as Ω ?* 2017. URL: <https://socratic.org/questions/what-is-formula-for-solid-angle-labeled-in-the-given-figure-as-omega>.

A Appendix A

In order to maintain the project's length within reasonable limits while ensuring the inclusion of all relevant information, a separate appendix will be dedicated exclusively to the excess comparison graphs pertaining to Chapter 5. This approach enables a thorough examination of all the influences without unnecessarily extending the main body of the thesis.

A.1 RT 811 Yellow Roof Tile

A.1.1 L^* values

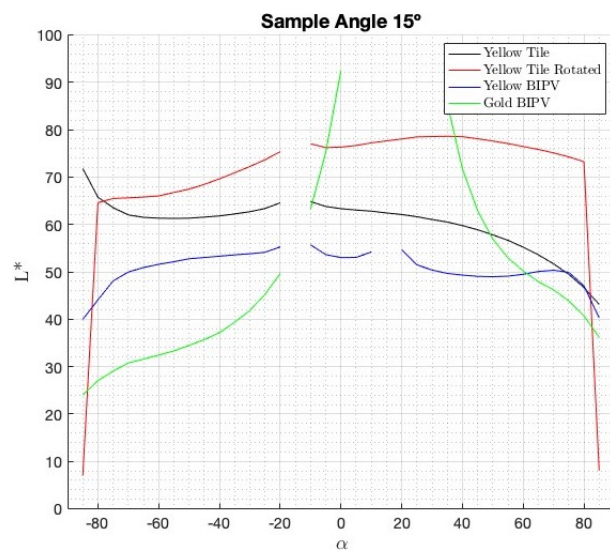


Figure A.1: Yellow Tile L^* comparison at 15°

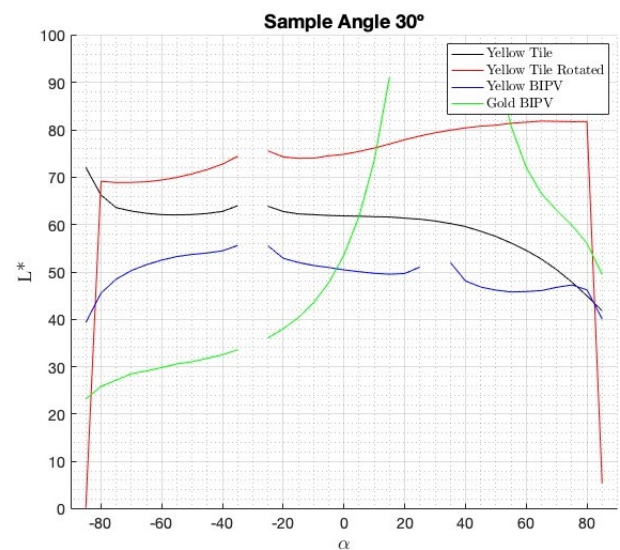


Figure A.2: Yellow Tile L^* comparison at 30°

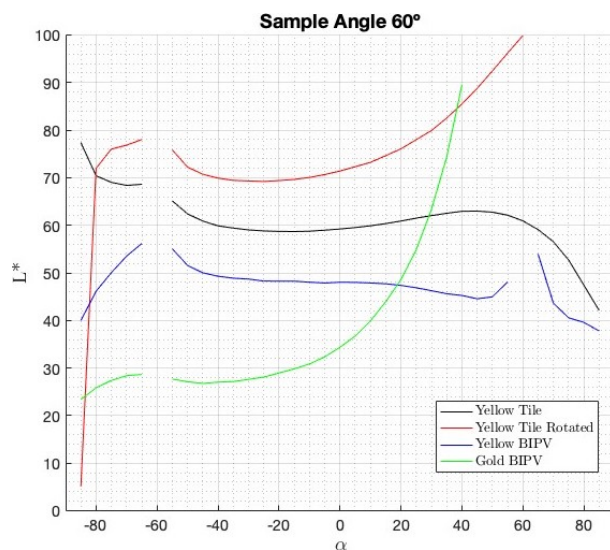


Figure A.3: Yellow Tile L^* comparison at 60°

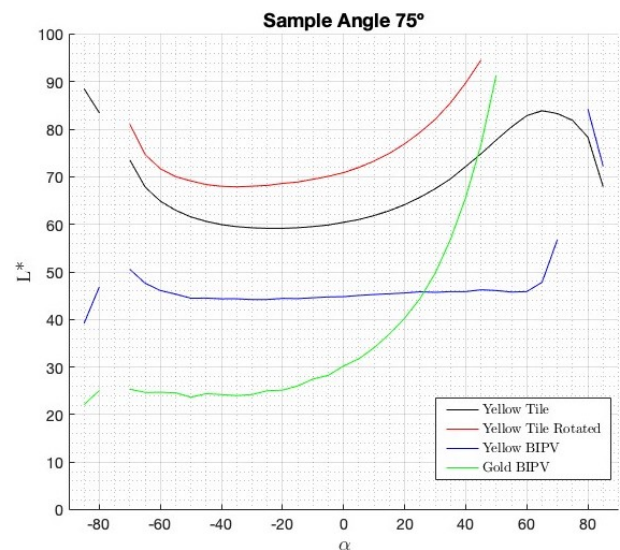


Figure A.4: Yellow Tile L^* comparison at 75°

A.1.2 a* values

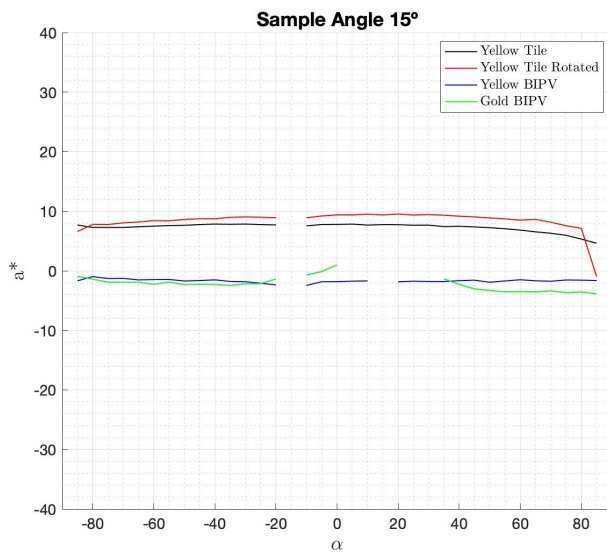


Figure A.5: Yellow Tile a^* comparison at 15°

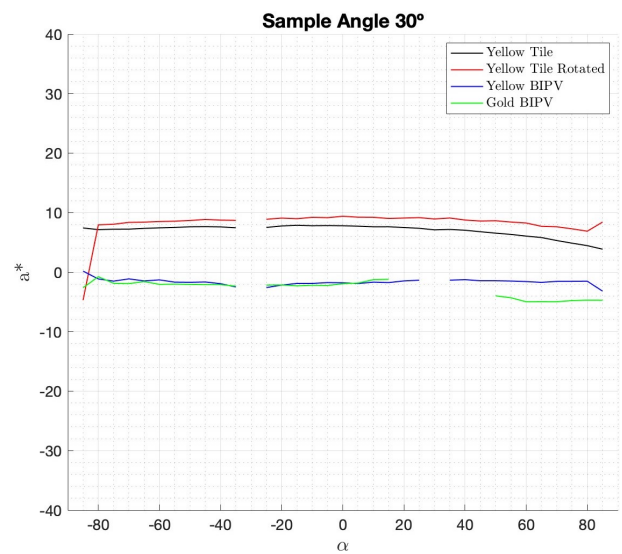


Figure A.6: Yellow Tile a^* comparison at 30°

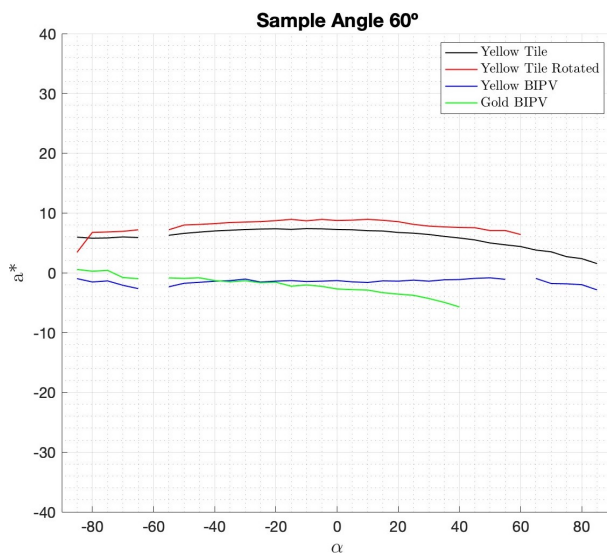


Figure A.7: Yellow Tile a^* comparison at 60°

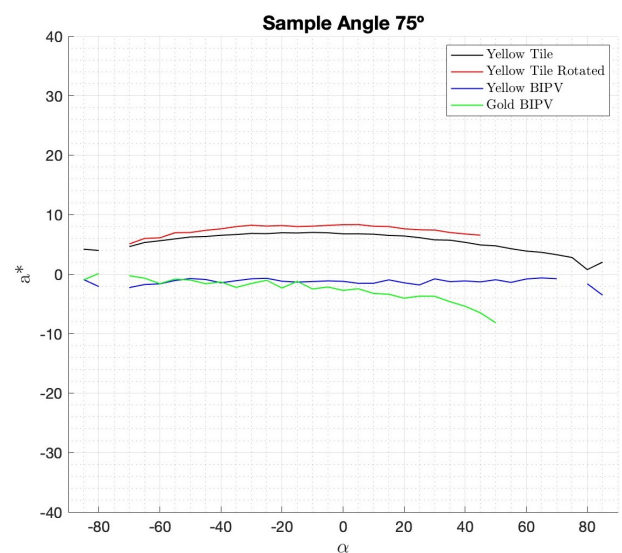


Figure A.8: Yellow Tile a^* comparison at 75°

A.1.3 b^* values

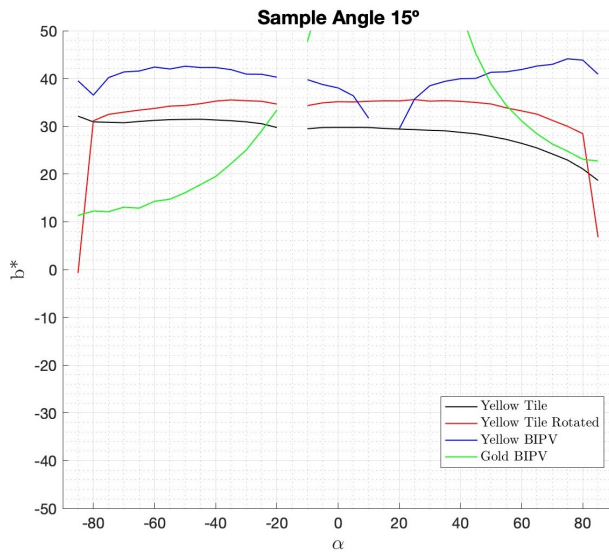


Figure A.9: Yellow Tile b^* comparison at 15°

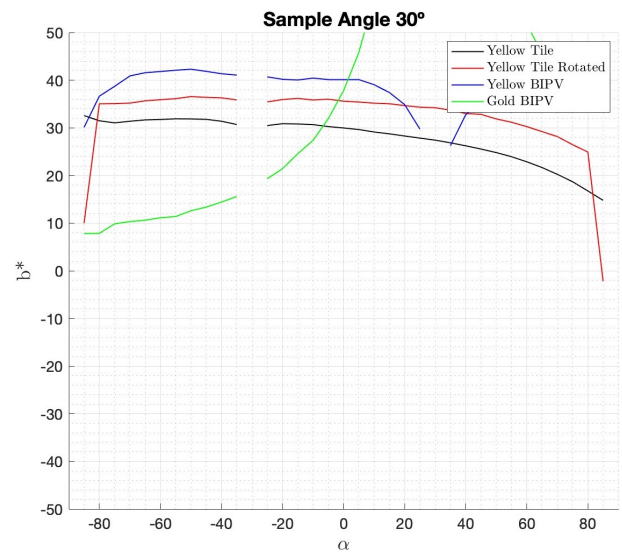


Figure A.10: Yellow Tile b^* comparison at 30°

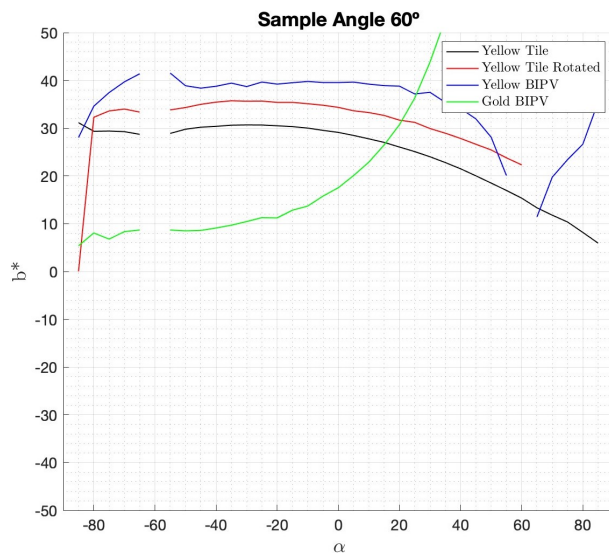


Figure A.11: Yellow Tile b^* comparison at 60°

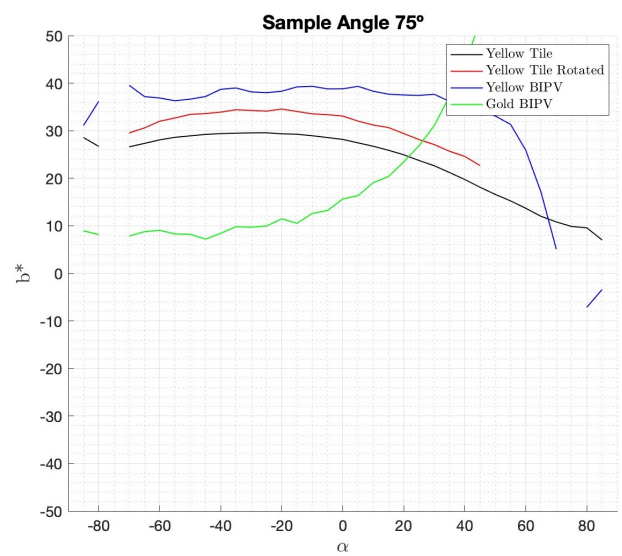


Figure A.12: Yellow Tile b^* comparison at 75°

A.2 RT 845 Laumans Glazed Black

A.2.1 L^* values

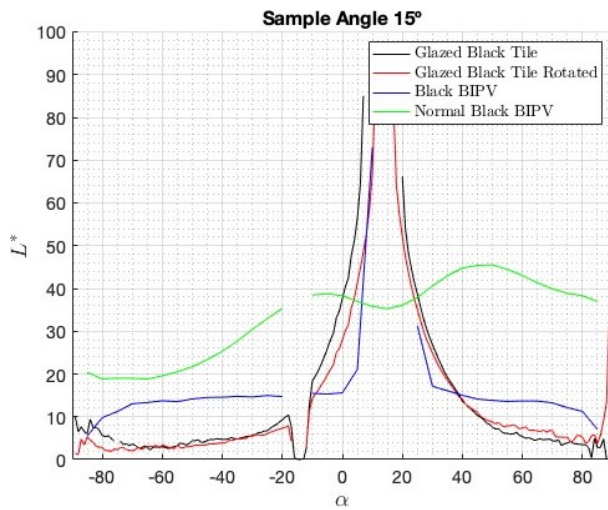


Figure A.13: Glazed Black Tile L^* comparison at 15°

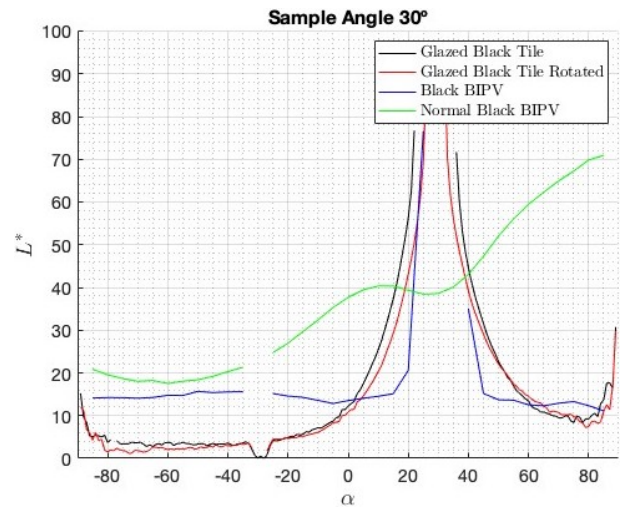


Figure A.14: Glazed Black Tile L^* comparison at 30°

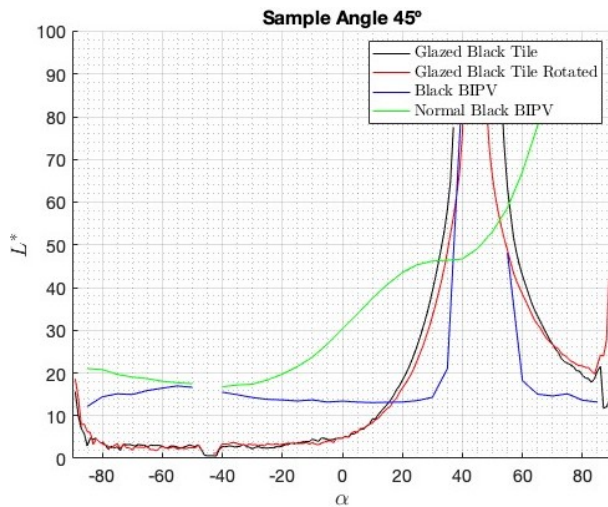


Figure A.15: Glazed Black Tile L^* comparison at 45°

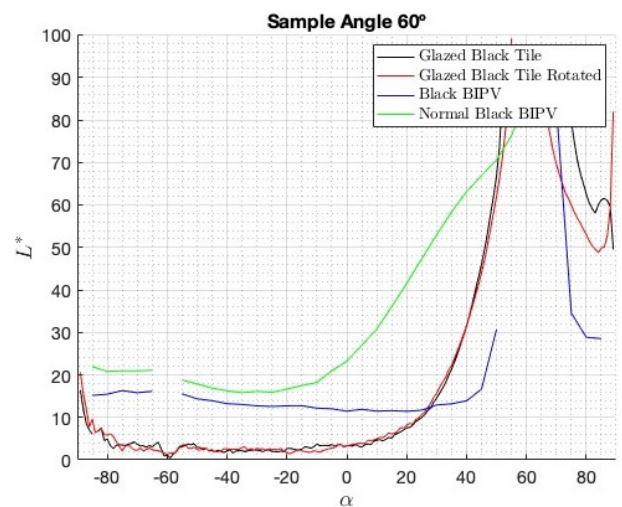


Figure A.16: Glazed Black Tile L^* comparison at 60°

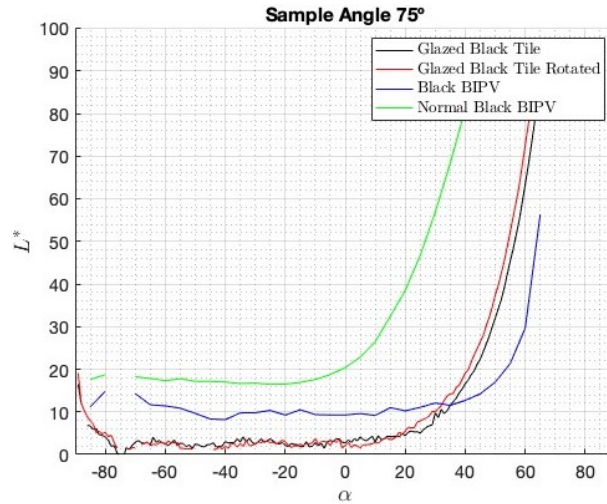


Figure A.17: Glazed Black Tile L^* comparison at 75°

A.2.2 a^* values

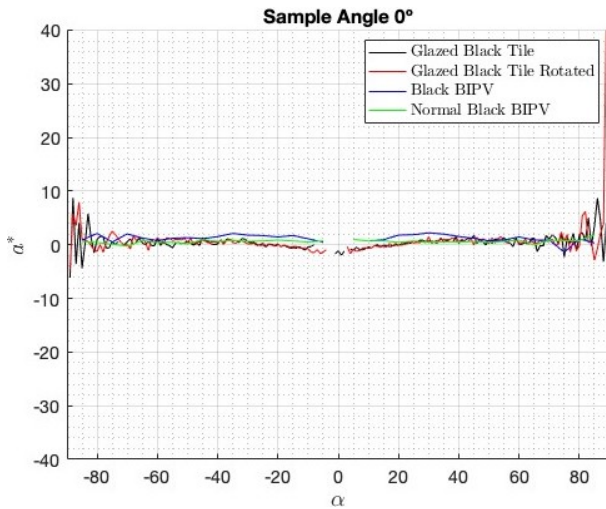


Figure A.18: Glazed Black Tile a^* comparison at 0°

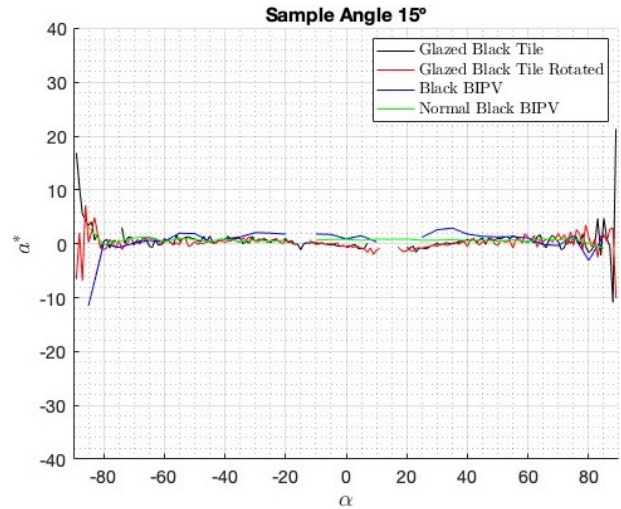


Figure A.19: Glazed Black Tile a^* comparison at 15°

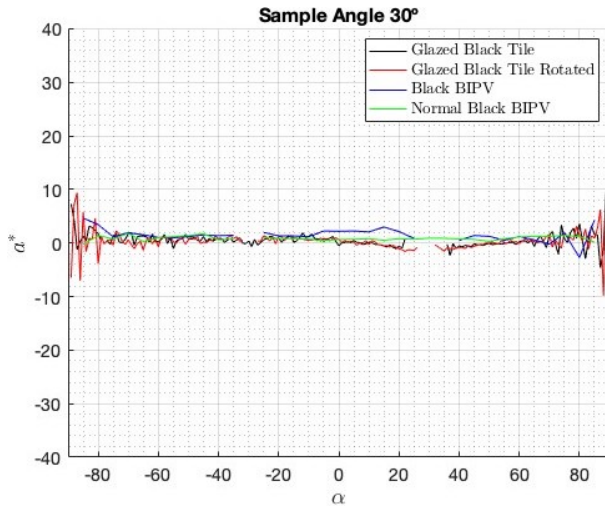


Figure A.20: Glazed Black Tile a^* comparison at 30°

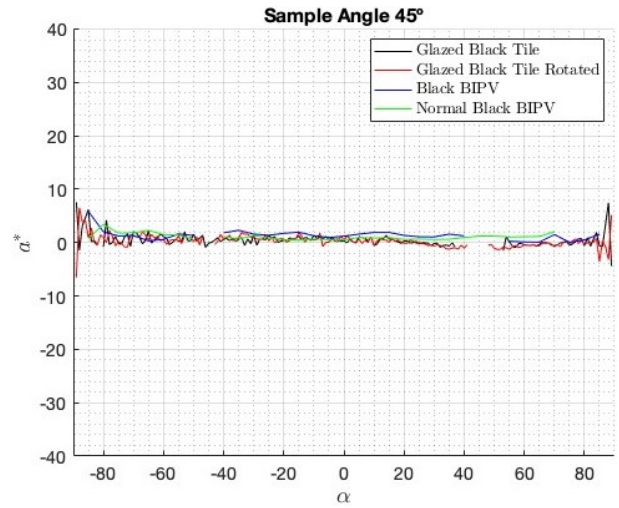


Figure A.21: Glazed Black Tile a^* comparison at 45°

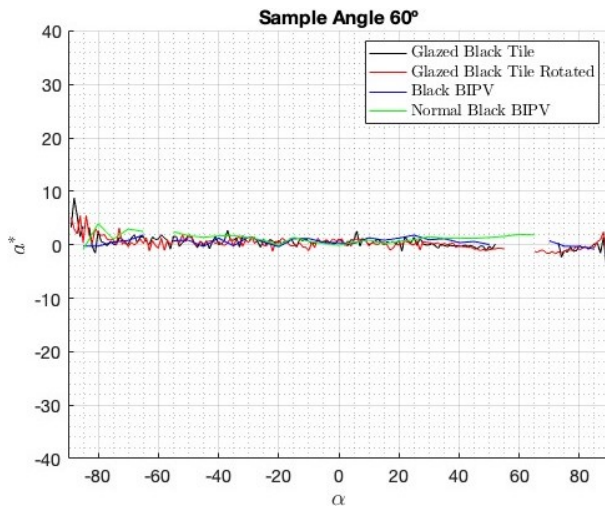


Figure A.22: Glazed Black Tile a^* comparison at 60°

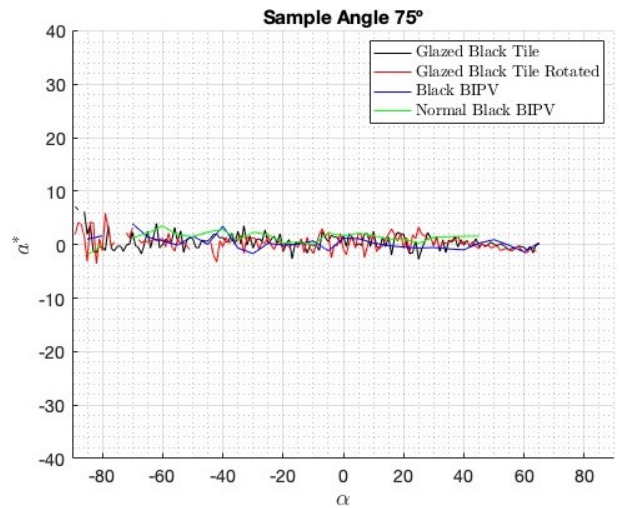


Figure A.23: Glazed Black Tile a^* comparison at 75°

A.2.3 b^* values

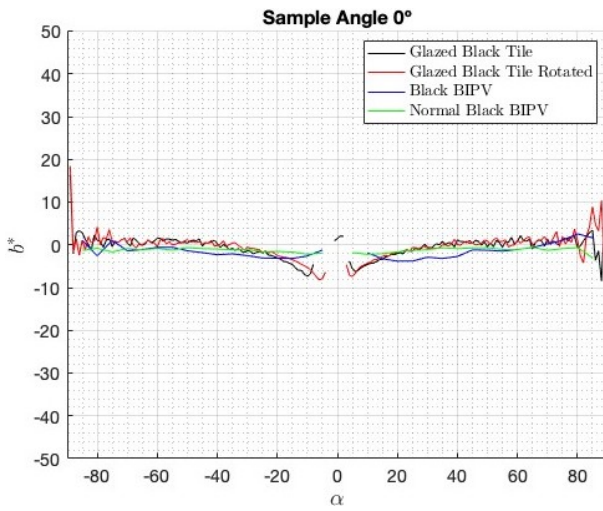


Figure A.24: Glazed Black Tile b^* comparison at 0°

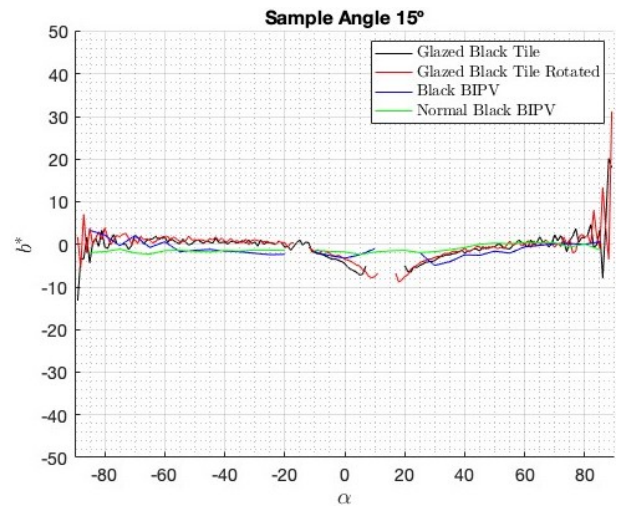


Figure A.25: Glazed Black Tile b^* comparison at 15°

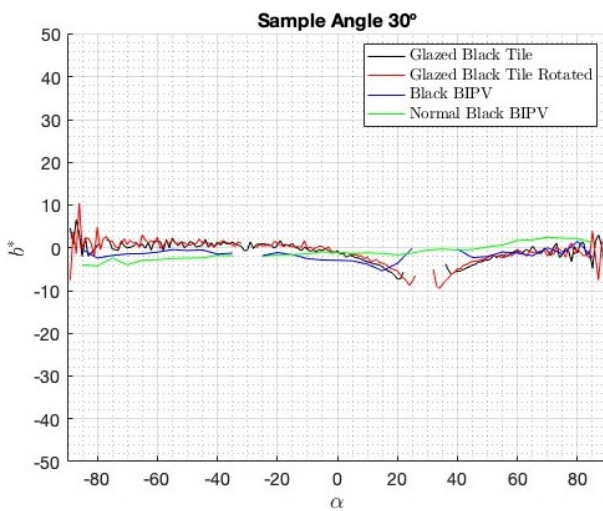


Figure A.26: Glazed Black Tile b^* comparison at 30°

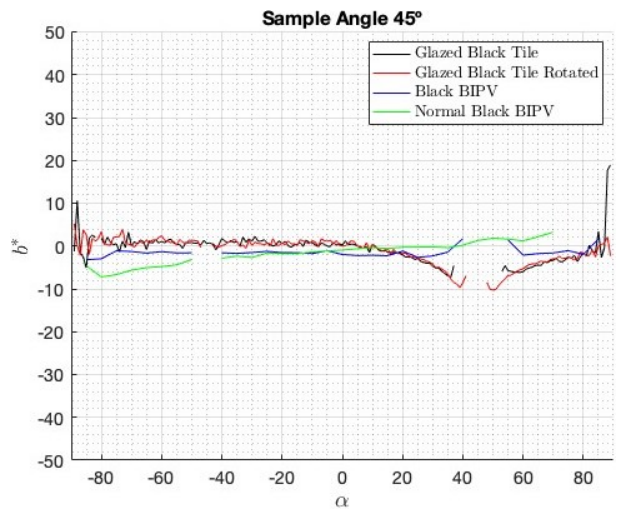


Figure A.27: Glazed Black Tile b^* comparison at 45°

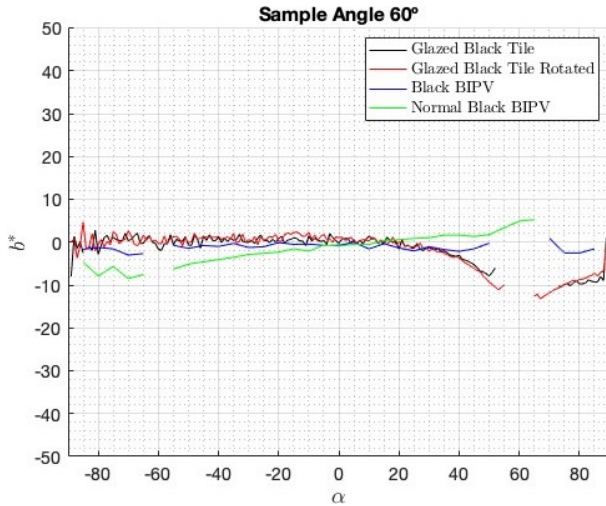


Figure A.28: Glazed Black Tile b^* comparison at 60°

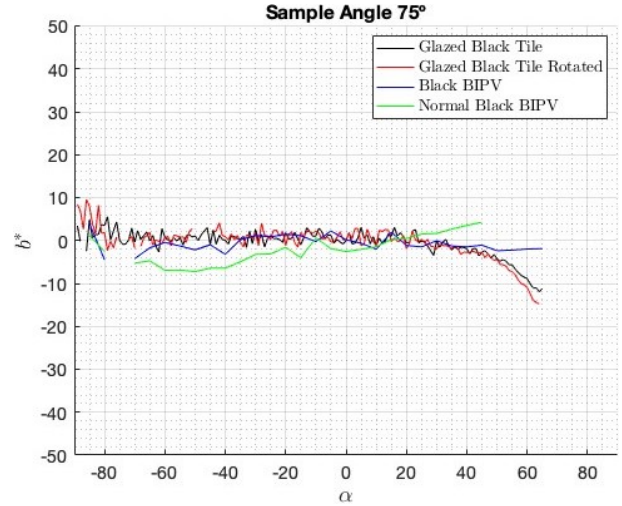


Figure A.29: Glazed Black Tile b^* comparison at 75°

A.2.4 BRDF values

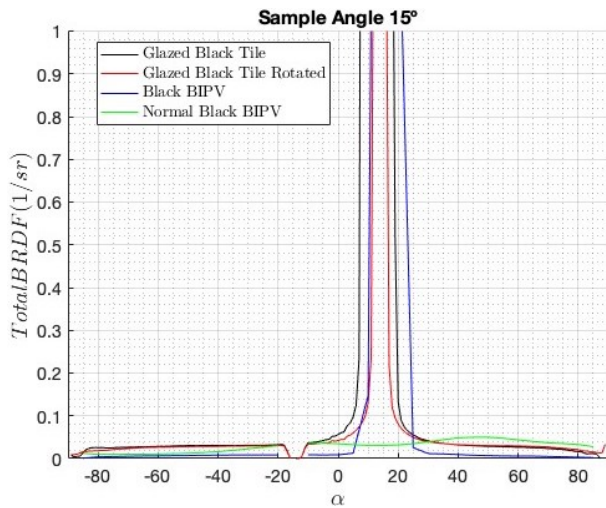


Figure A.30: Glazed Black Tile BRDF comparison at 15°

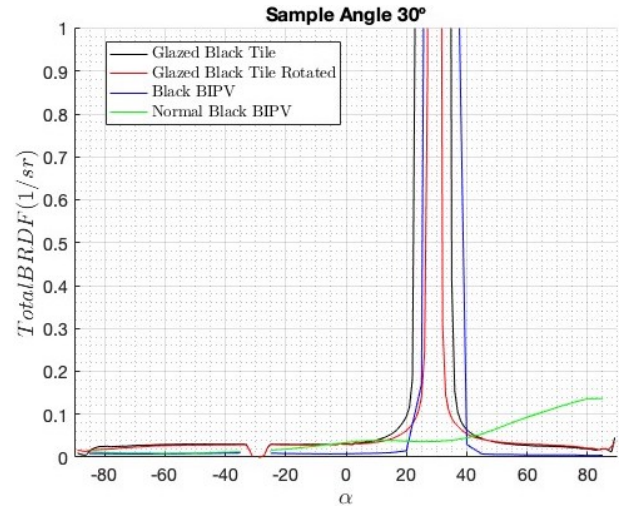


Figure A.31: Glazed Black Tile BRDF comparison at 30°

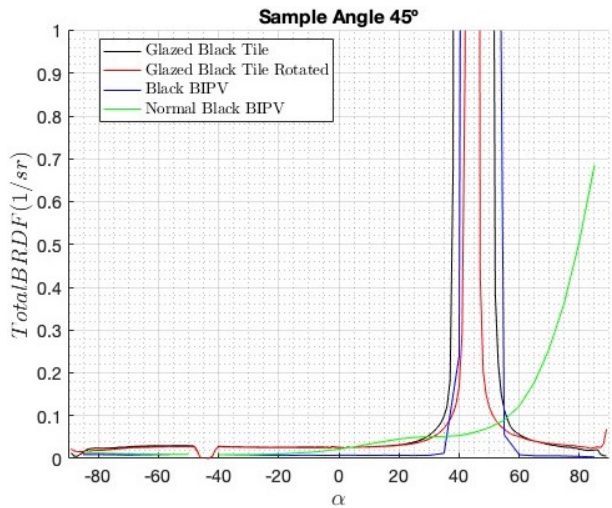


Figure A.32: Glazed Black Tile BRDF comparison at 45°

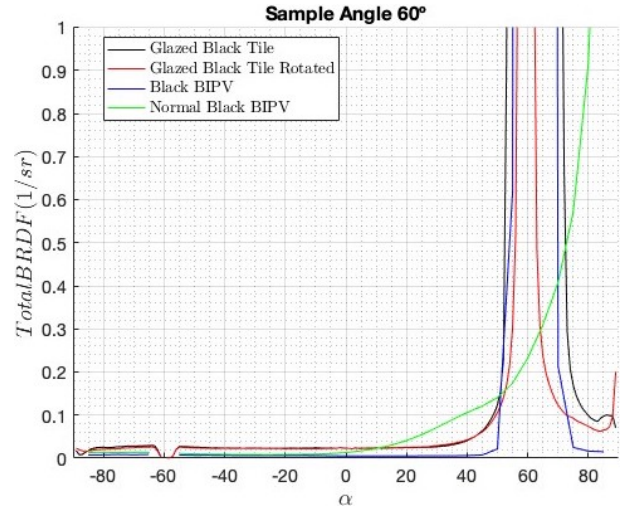


Figure A.33: Glazed Black Tile BRDF comparison at 60°

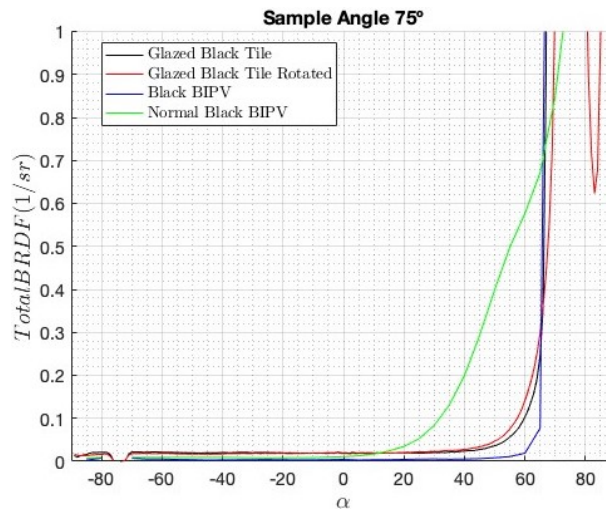


Figure A.34: Glazed Black Tile BRDF comparison at 75°

A.2.5 Logarithmic BRDF values

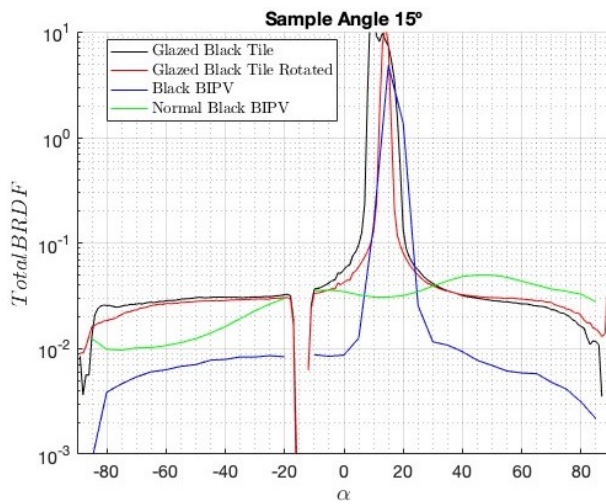


Figure A.35: Glazed Black Tile logarithmic BRDF comparison at 15°

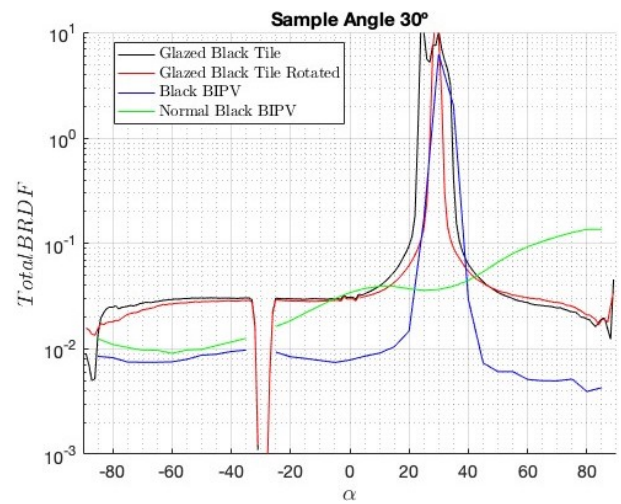


Figure A.36: Glazed Black Tile logarithmic BRDF comparison at 30°

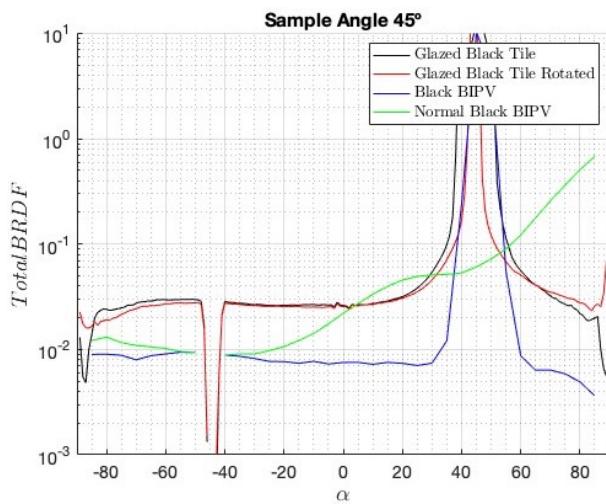


Figure A.37: Glazed Black Tile logarithmic BRDF comparison at 45°

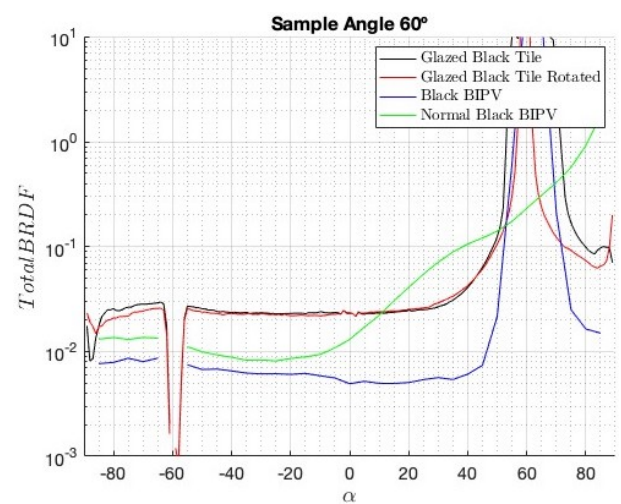


Figure A.38: Glazed Black Tile logarithmic BRDF comparison at 60°

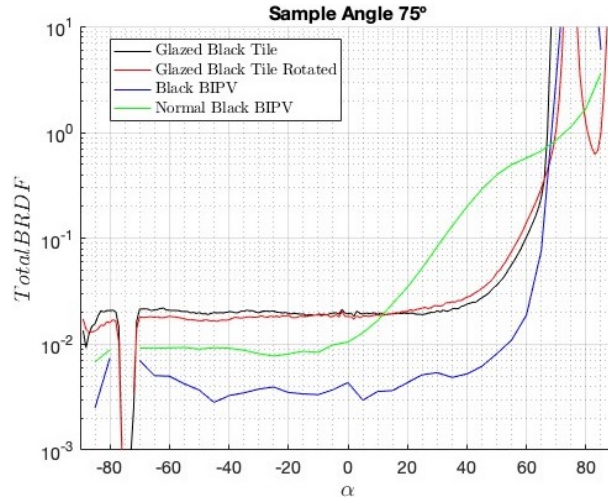


Figure A.39: Glazed Black Tile logarithmic BRDF comparison at 75°

A.3 RT 840 Højslev Lille Black

A.3.1 L* values

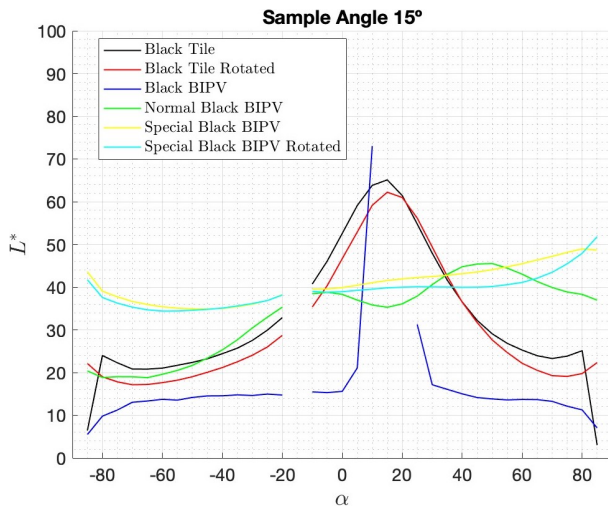


Figure A.40: Black Tile L^* comparison at 15°

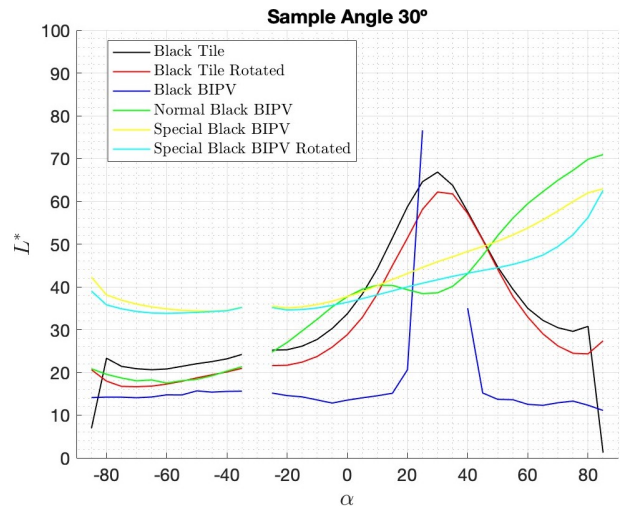


Figure A.41: Black Tile L^* comparison at 30°

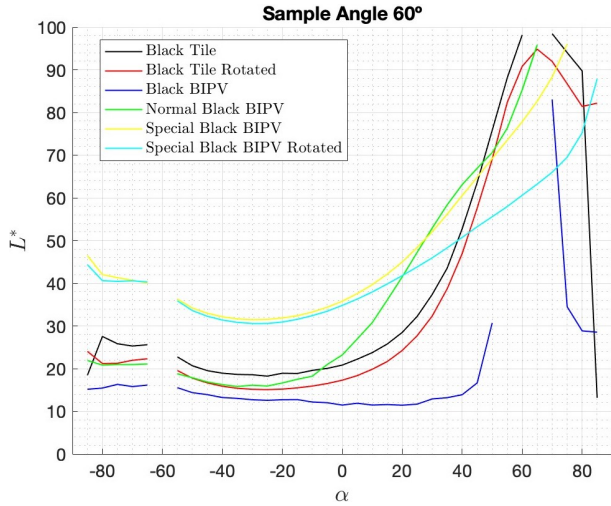


Figure A.42: Black Tile L^* comparison at 60°

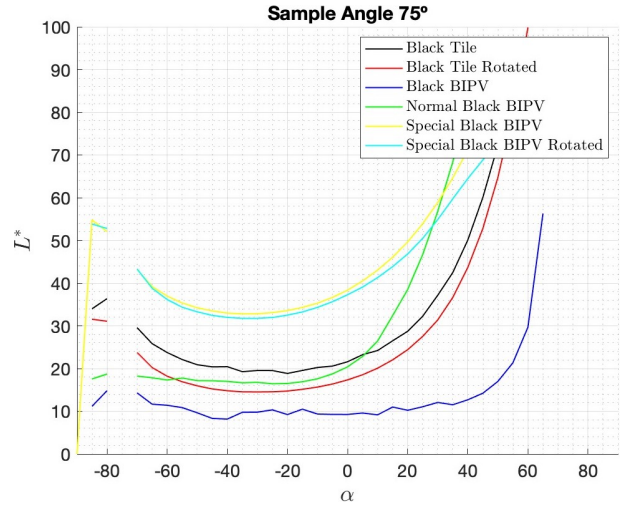


Figure A.43: Black Tile L^* comparison at 75°

A.3.2 a^* values

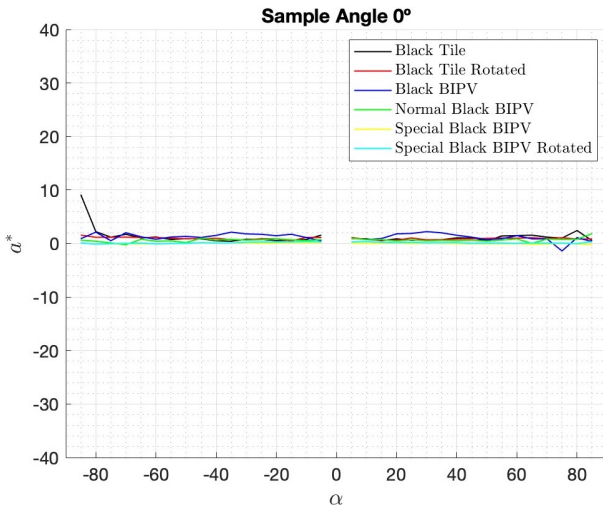


Figure A.44: Black Tile a^* comparison at 0°

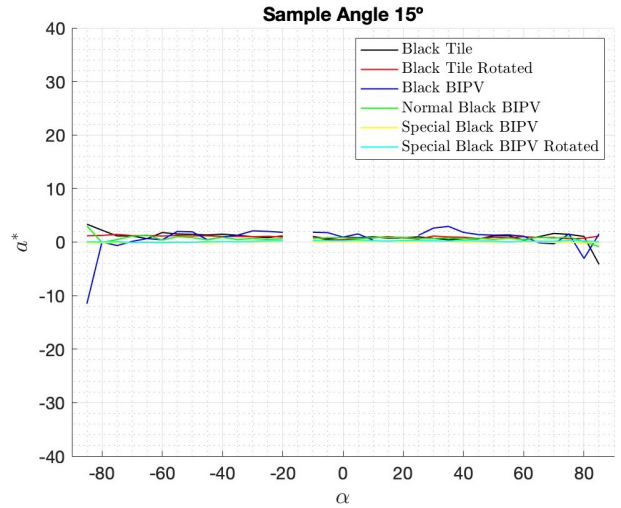


Figure A.45: Black Tile a^* comparison at 15°

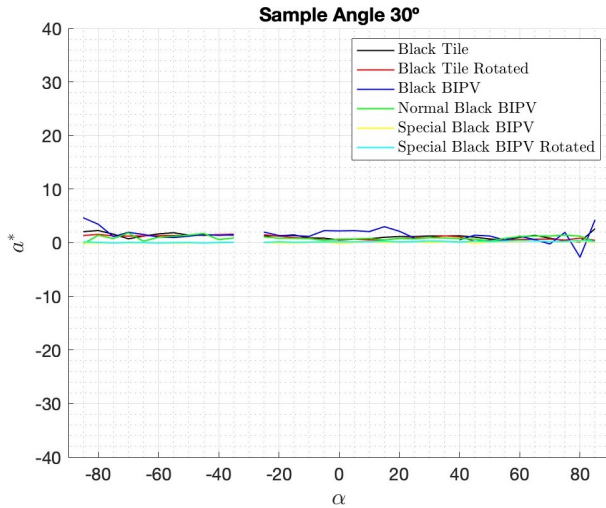


Figure A.46: Black Tile a^* comparison at 30°

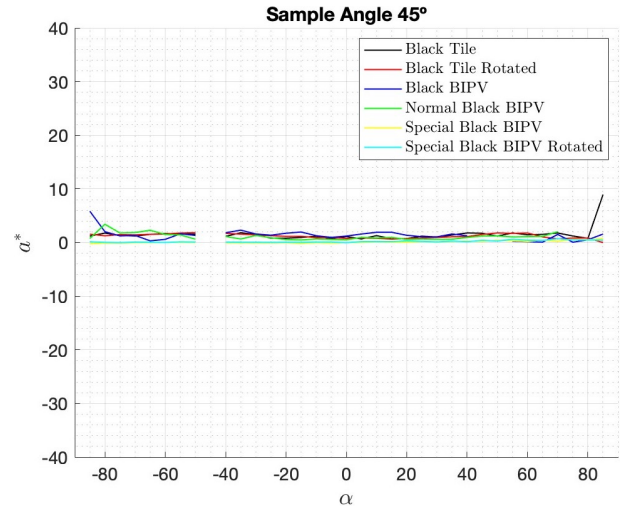


Figure A.47: Black Tile a^* comparison at 45°

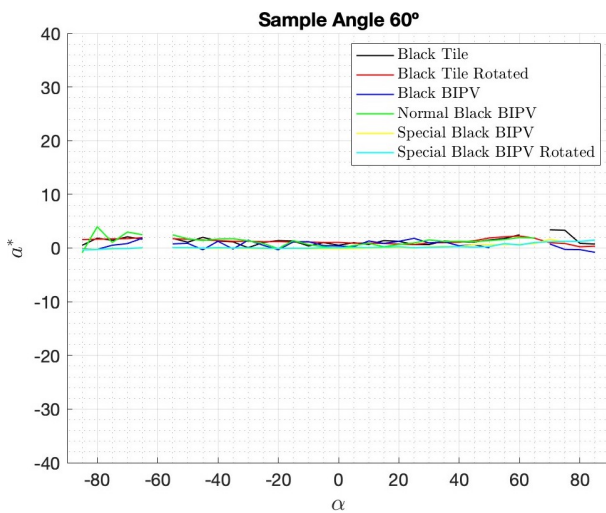


Figure A.48: Black Tile a^* comparison at 60°

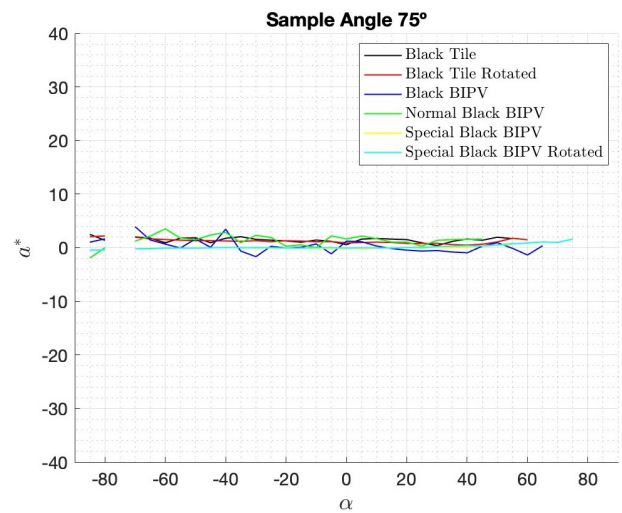


Figure A.49: Black Tile a^* comparison at 75°

A.3.3 b^* values

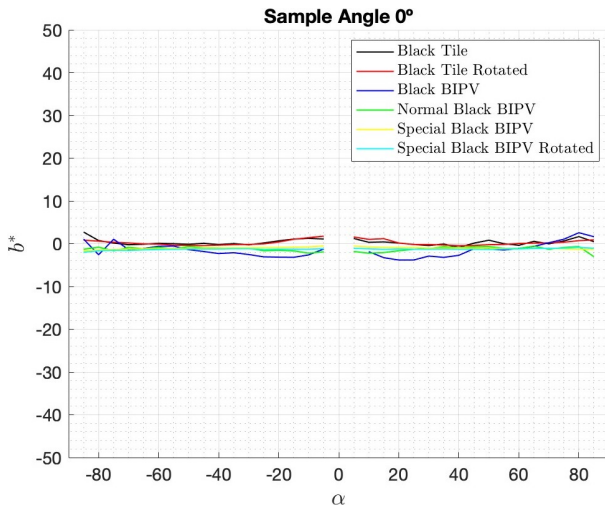


Figure A.50: Black Tile b^* comparison at 0°

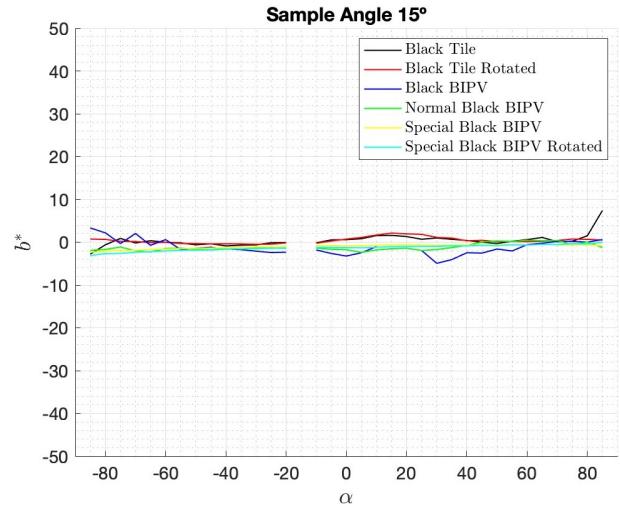


Figure A.51: Black Tile b^* comparison at 15°

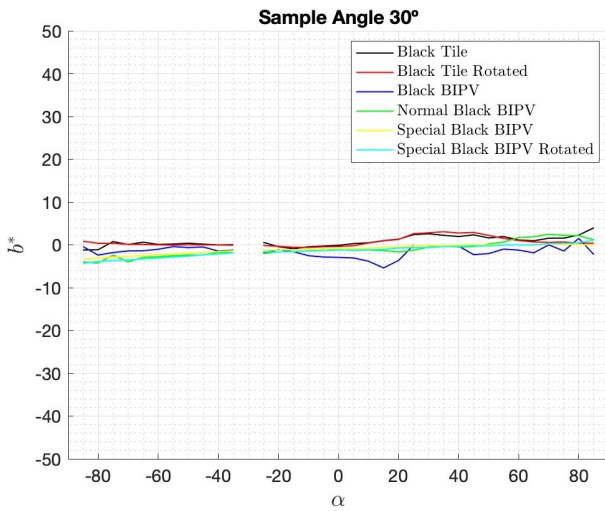


Figure A.52: Black Tile b^* comparison at 30°

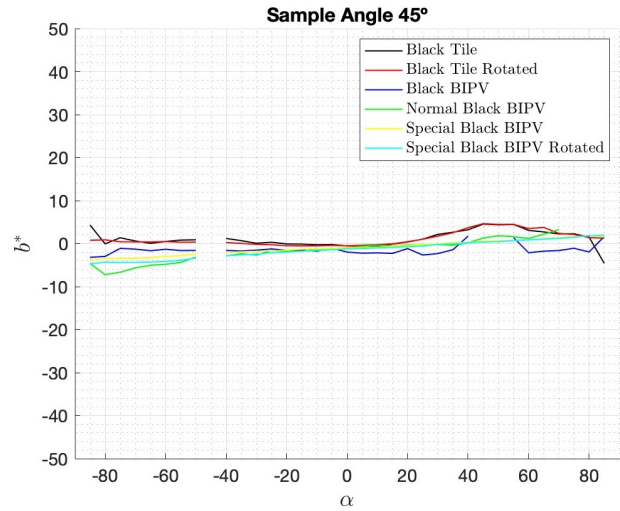


Figure A.53: Black Tile b^* comparison at 45°

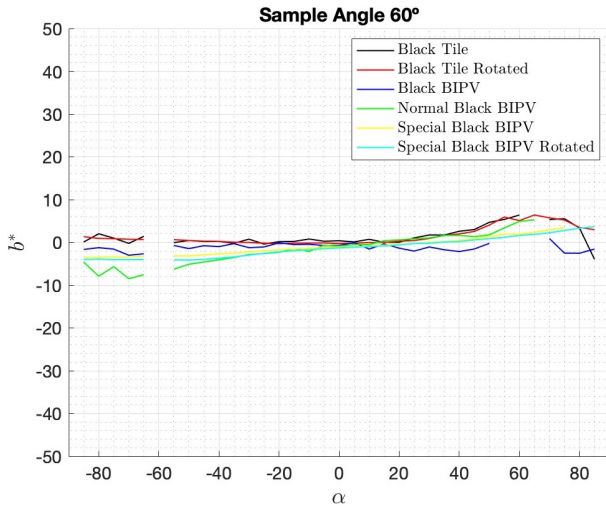


Figure A.54: Black Tile b^* comparison at 60°

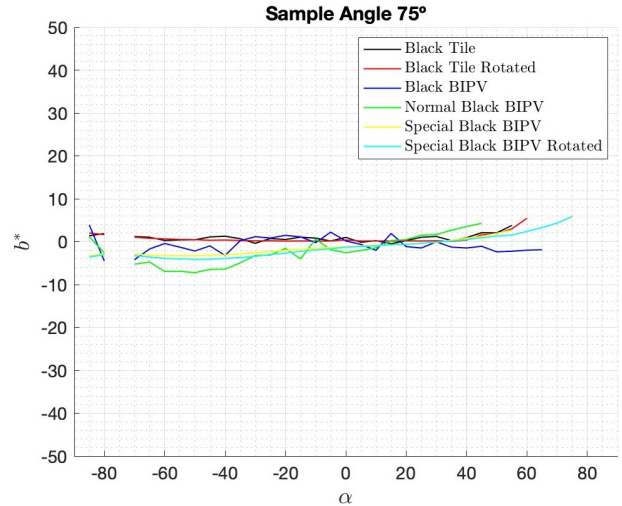


Figure A.55: Black Tile b^* comparison at 75°

A.4 RT 844 Laumans Red

A.4.1 L^* values

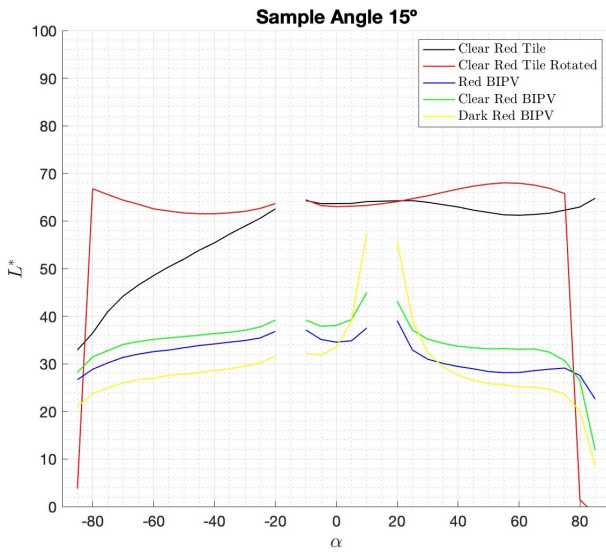


Figure A.56: Clear Red Tile L^* comparison at 15°

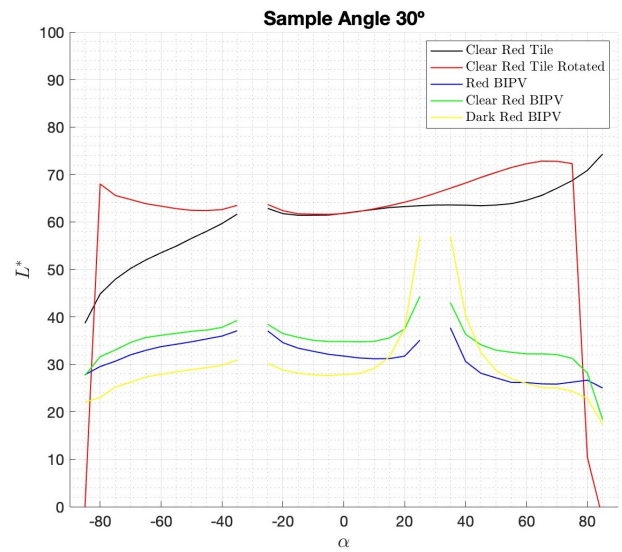


Figure A.57: Clear Red Tile L^* comparison at 30°

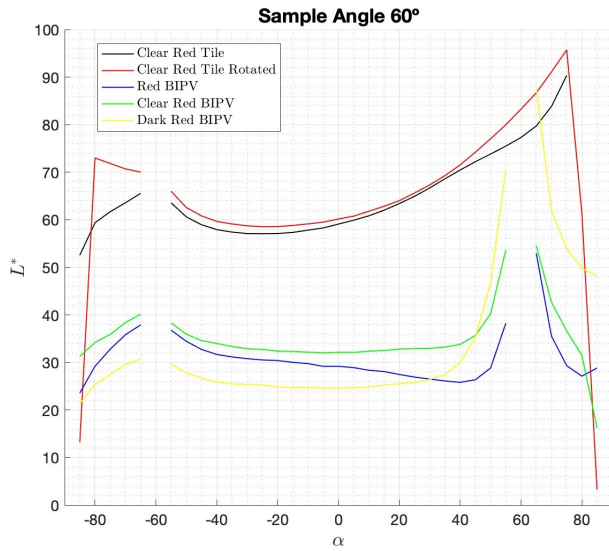


Figure A.58: Clear Red Tile L^* comparison at 60°

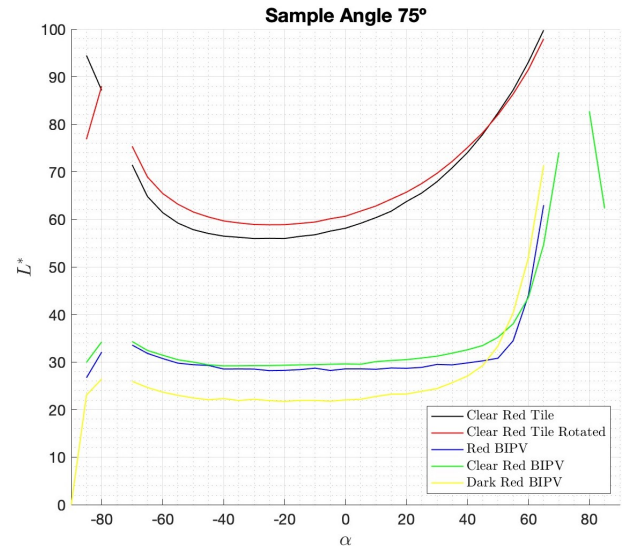


Figure A.59: Clear Red Tile L^* comparison at 75°

A.4.2 a^* values

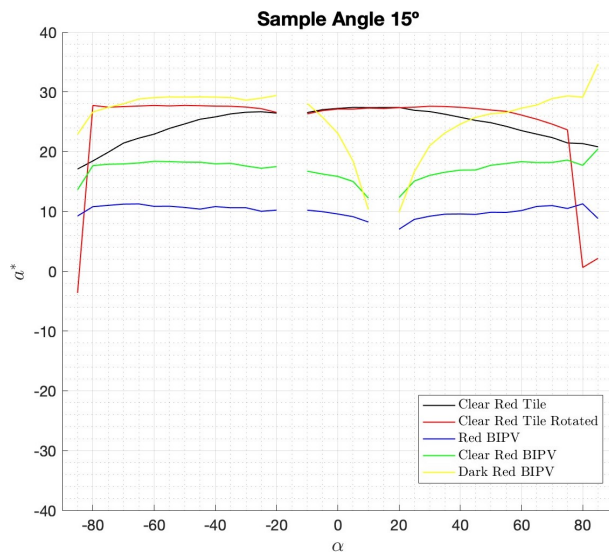


Figure A.60: Clear Red Tile a^* comparison at 15°

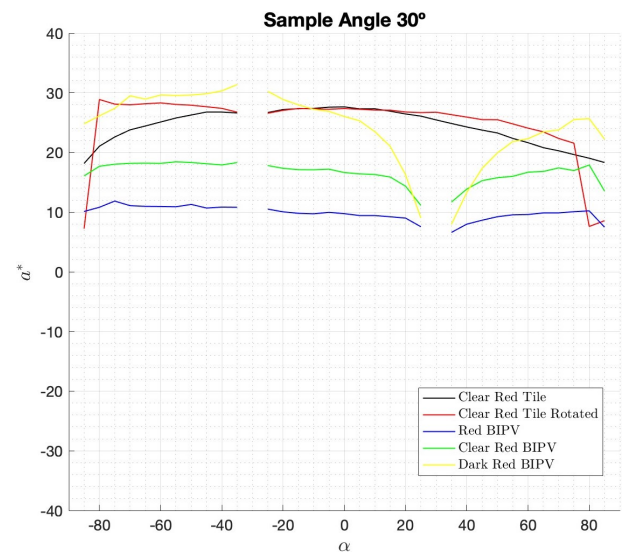


Figure A.61: Clear Red Tile a^* comparison at 30°

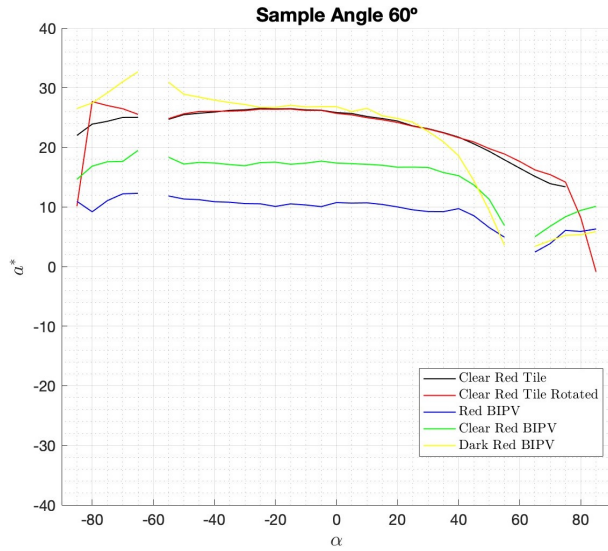


Figure A.62: Clear Red Tile a^* comparison at 60°

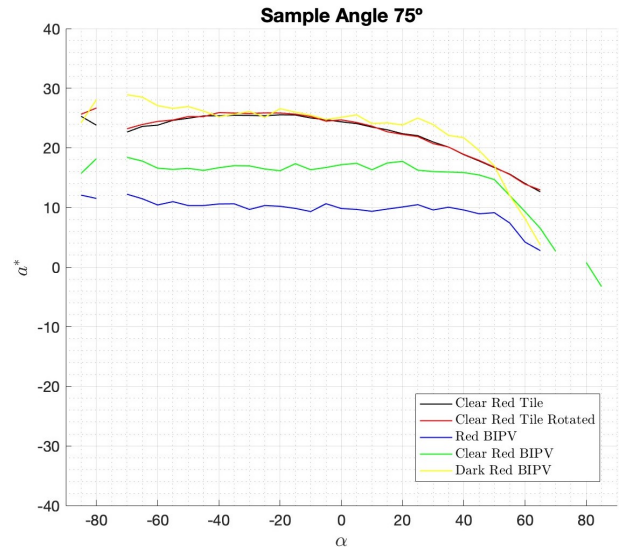


Figure A.63: Clear Red Tile a^* comparison at 75°

A.4.3 b^* values

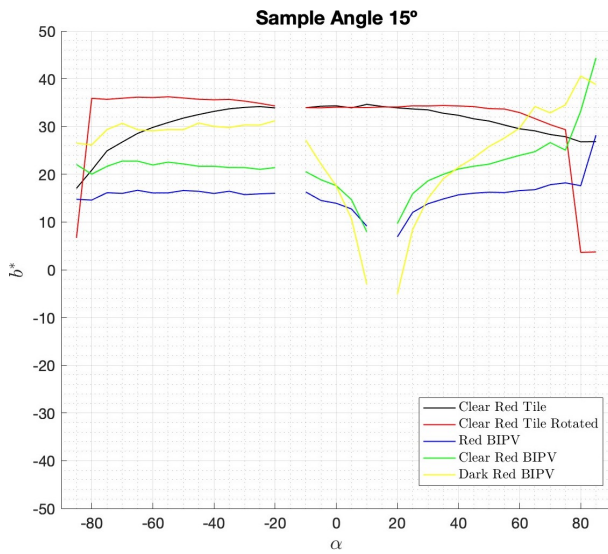


Figure A.64: Clear Red Tile b^* comparison at 15°

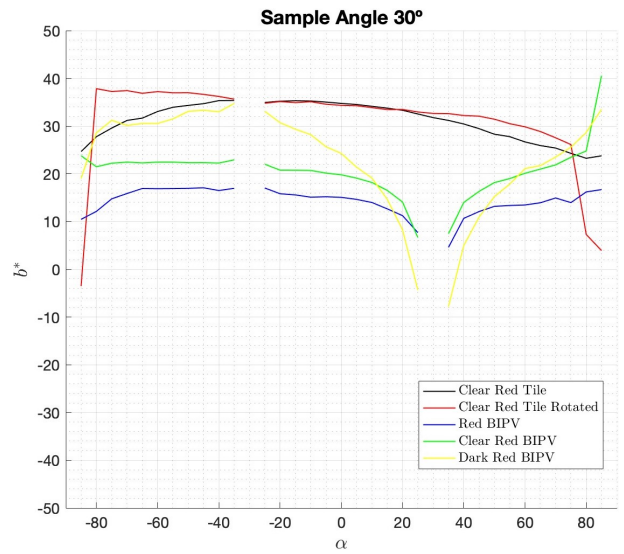


Figure A.65: Clear Red Tile b^* comparison at 30°

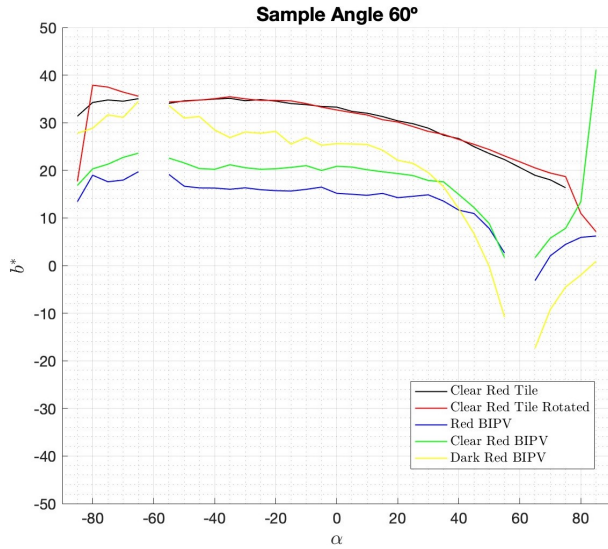


Figure A.66: Clear Red Tile b^* comparison at 60°

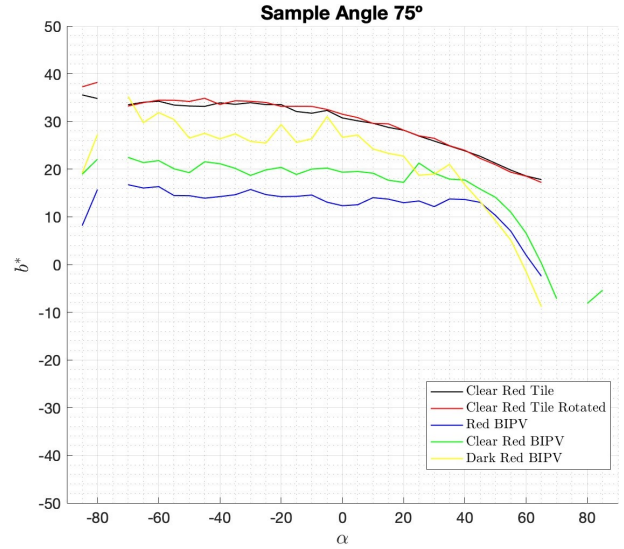


Figure A.67: Clear Red Tile b^* comparison at 75°

A.5 RT 841 Laumans Dark Red

A.5.1 L^* values

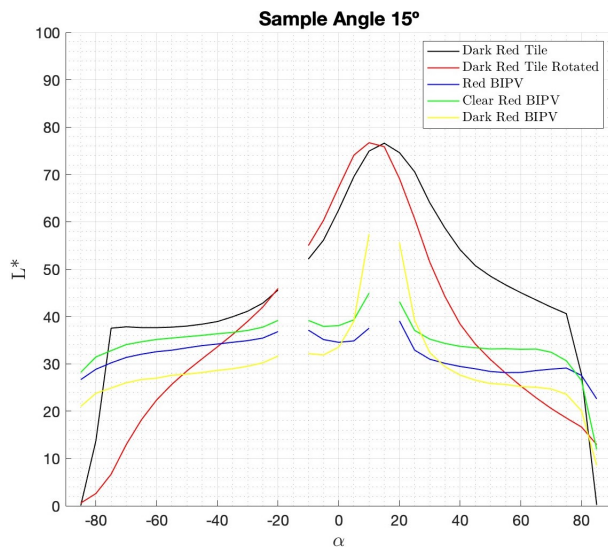


Figure A.68: Dark Red Tile L^* comparison at 15°

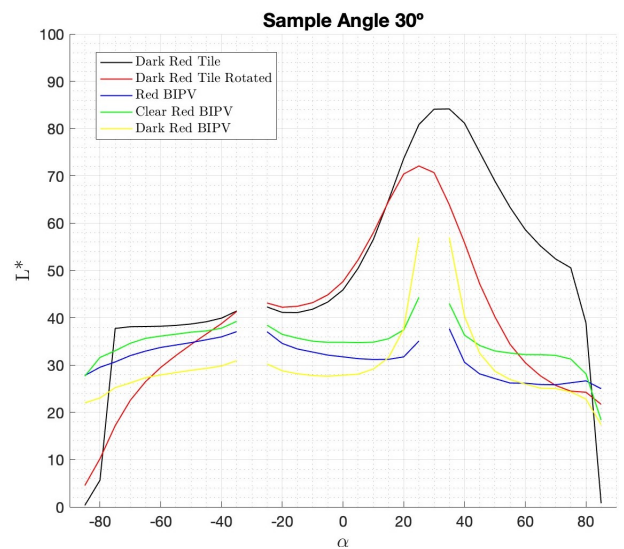


Figure A.69: Dark Red Tile L^* comparison at 30°

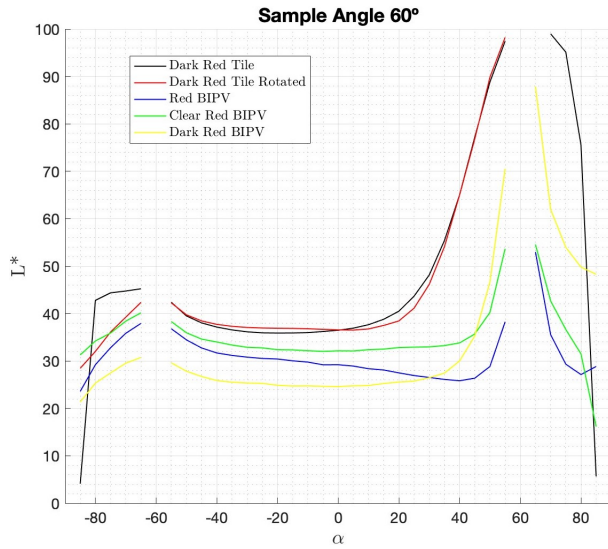


Figure A.70: Dark Red Tile L^* comparison at 60°

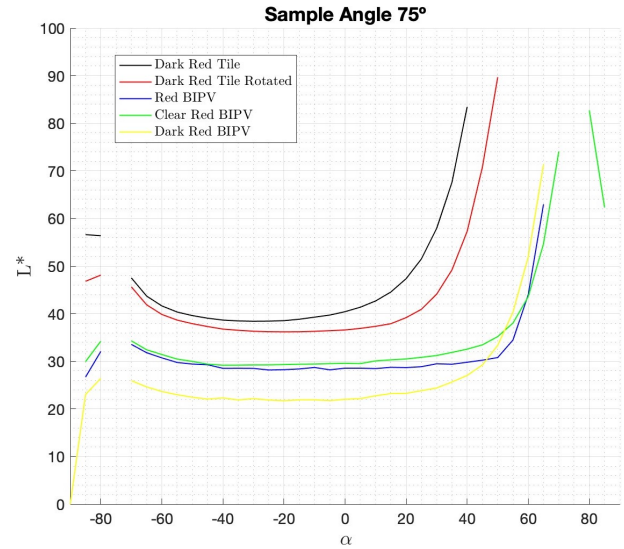


Figure A.71: Dark Red Tile L^* comparison at 75°

A.5.2 a^* values

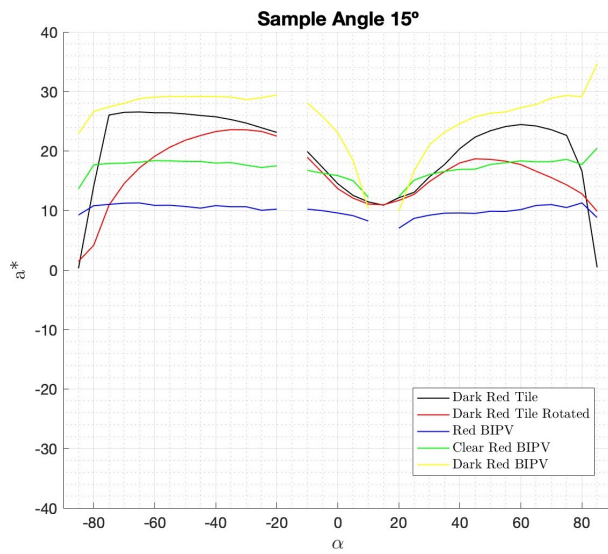


Figure A.72: Dark Red Tile a^* comparison at 15°

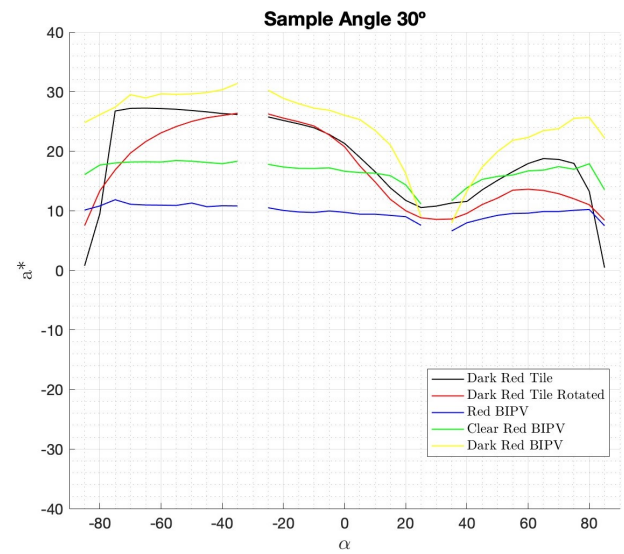


Figure A.73: Dark Red Tile a^* comparison at 30°

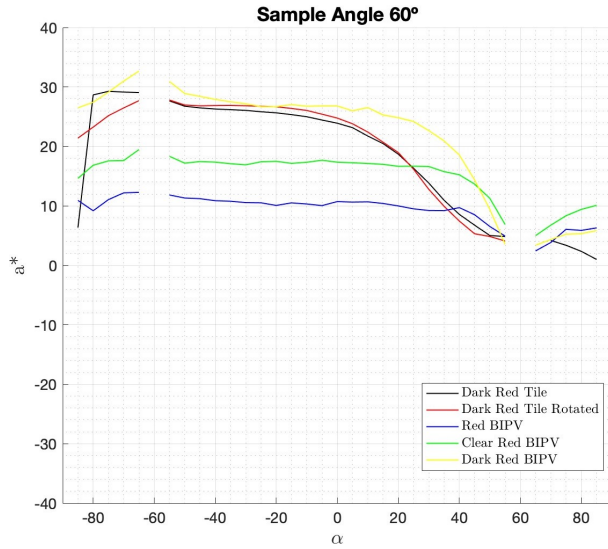


Figure A.74: Dark Red Tile a^* comparison at 60°

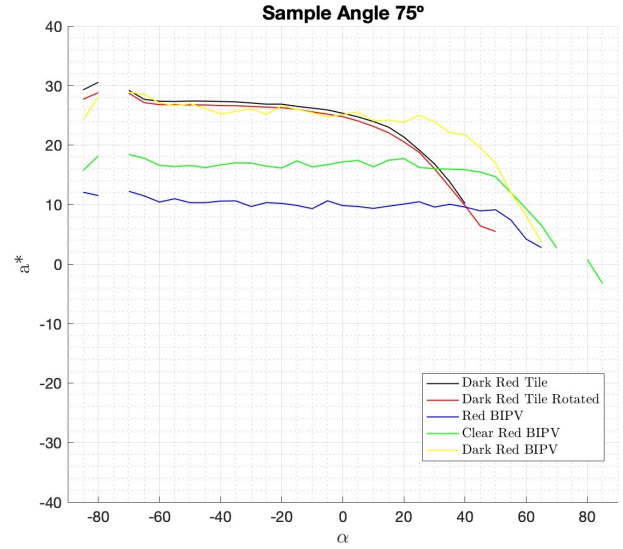


Figure A.75: Dark Red Tile a^* comparison at 75°

A.5.3 b^* values

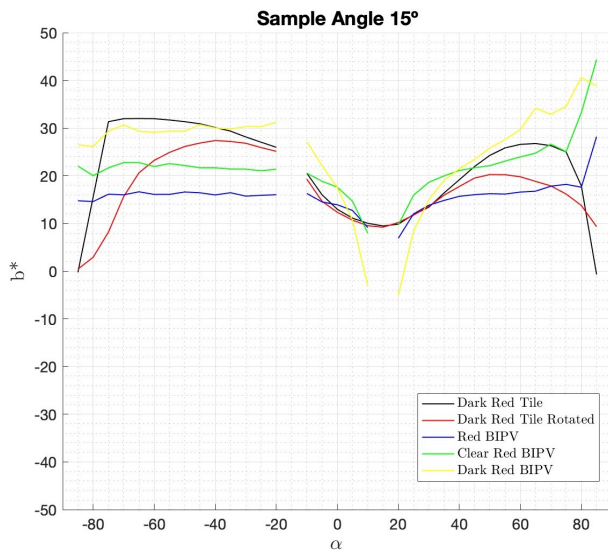


Figure A.76: Dark Red Tile b^* comparison at 15°

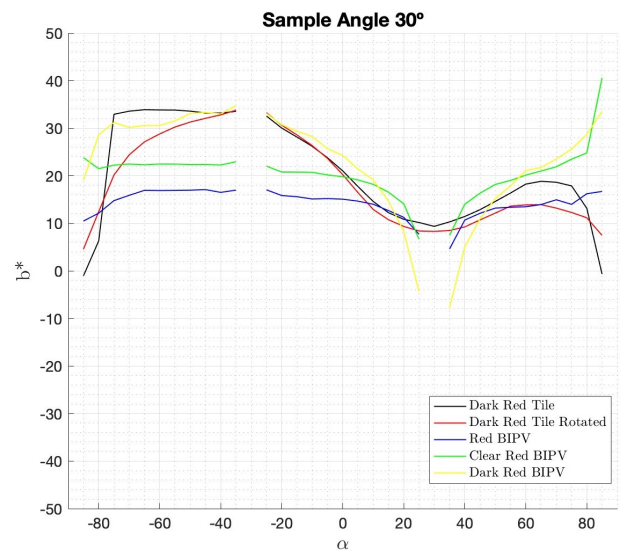


Figure A.77: Dark Red Tile b^* comparison at 30°

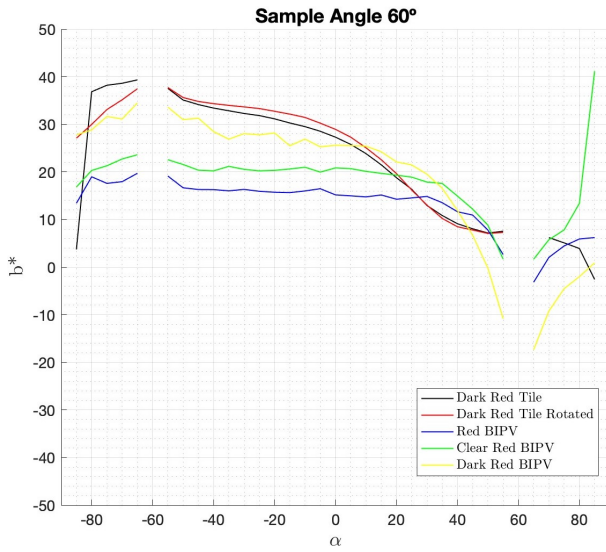


Figure A.78: Dark Red Tile b^* comparison at 60°

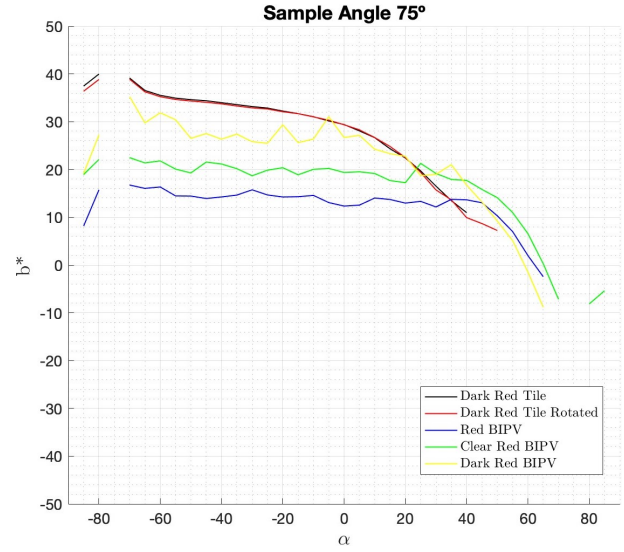


Figure A.79: Dark Red Tile b^* comparison at 75°

A.6 Faro Vidar Clay Shingles

A.6.1 L^* values

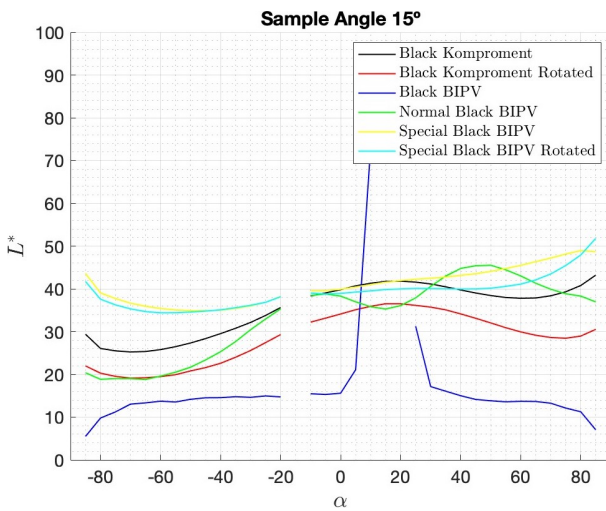


Figure A.80: Black Komproment L^* comparison at 15°

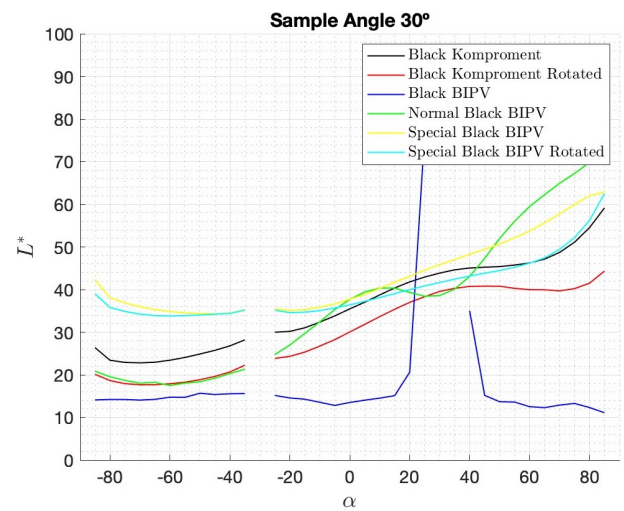


Figure A.81: Black Komproment L^* comparison at 30°

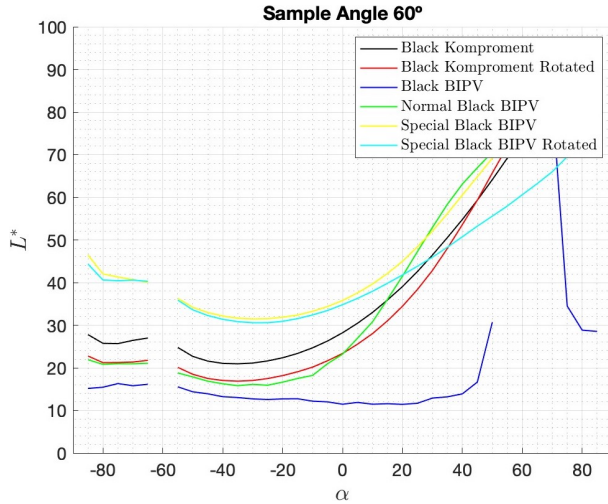


Figure A.82: Black Komproment L^* comparison at 60°

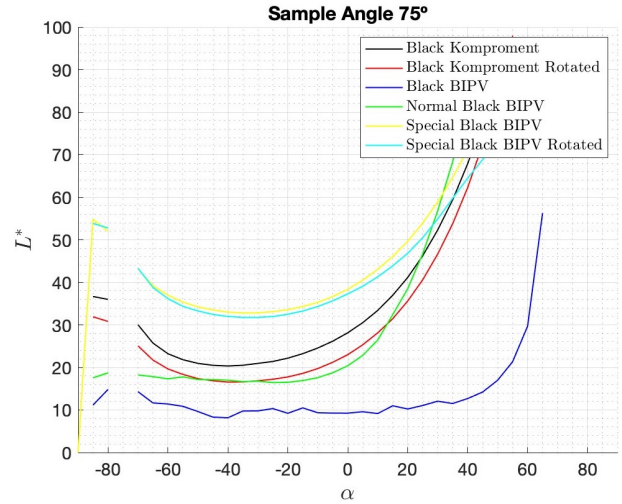


Figure A.83: Black Komproment L^* comparison at 75°

A.6.2 a^* values

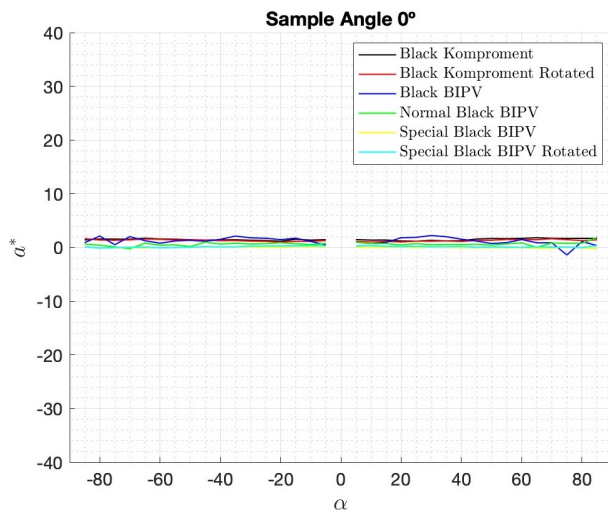


Figure A.84: Black Komproment a^* comparison at 0°

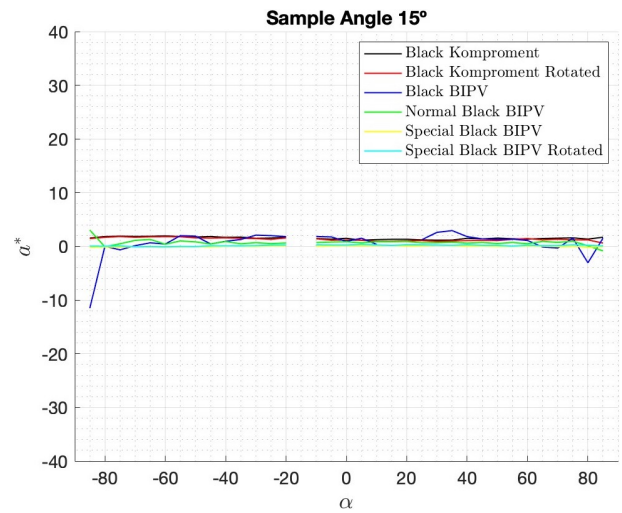


Figure A.85: Black Komproment a^* comparison at 15°

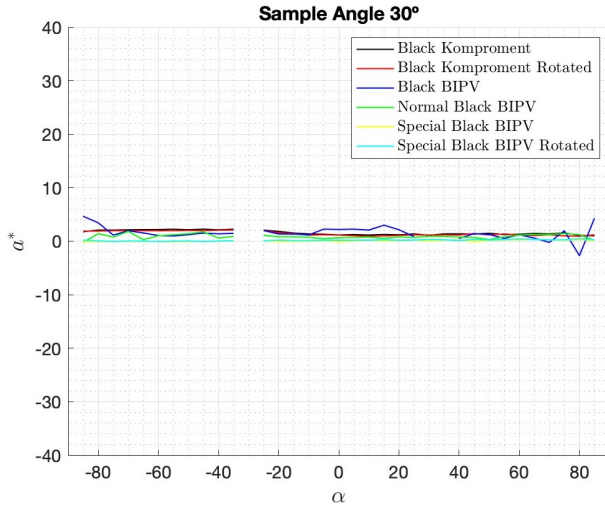


Figure A.86: Black Komproment a^* comparison at 30°

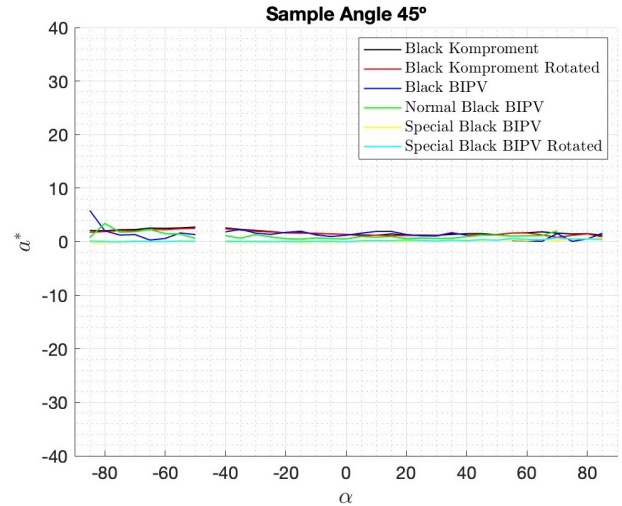


Figure A.87: Black Komproment a^* comparison at 45°

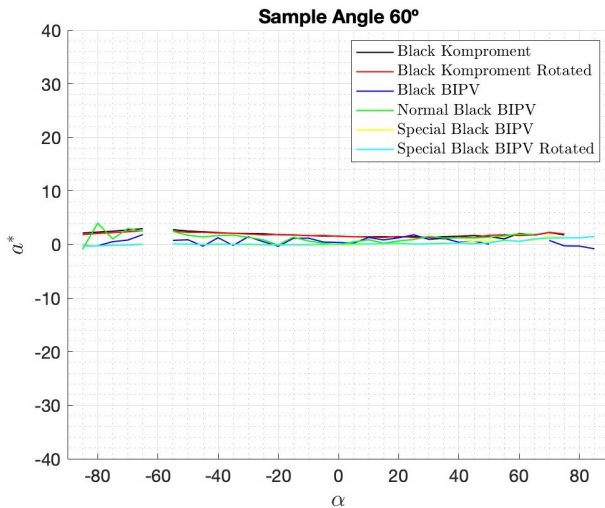


Figure A.88: Black Komproment a^* comparison at 60°

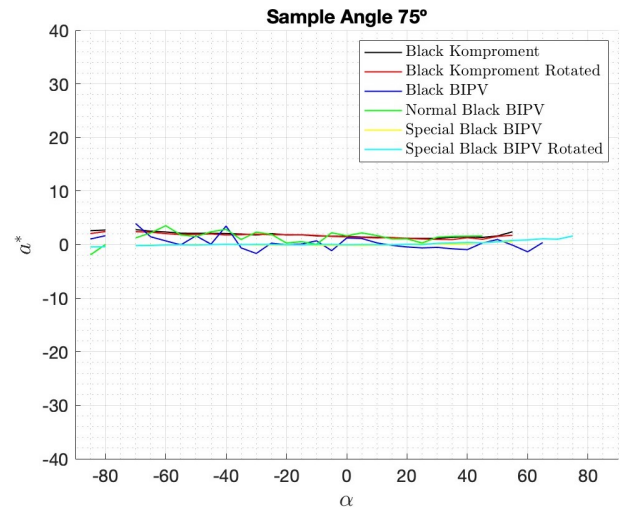


Figure A.89: Black Komproment a^* comparison at 75°

A.6.3 b^* values

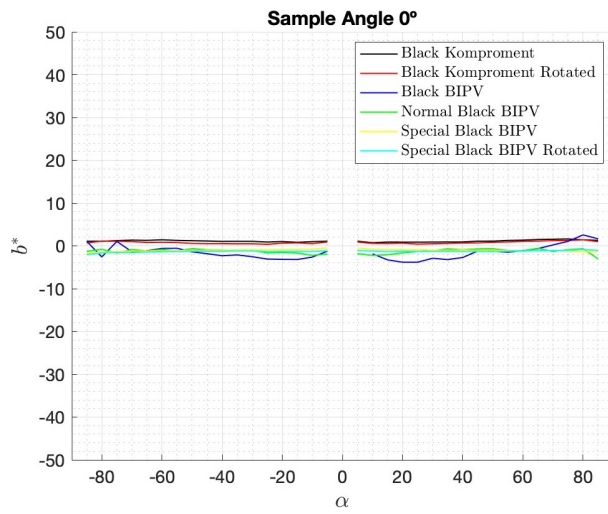


Figure A.90: Black Komproment b^* comparison at 0°

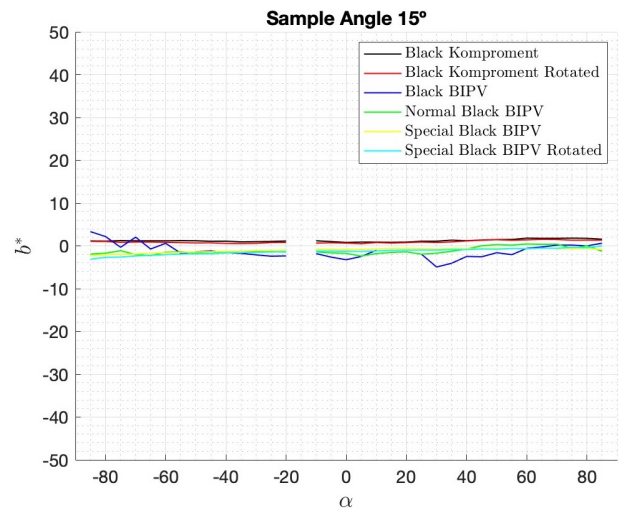


Figure A.91: Black Komproment b^* comparison at 15°

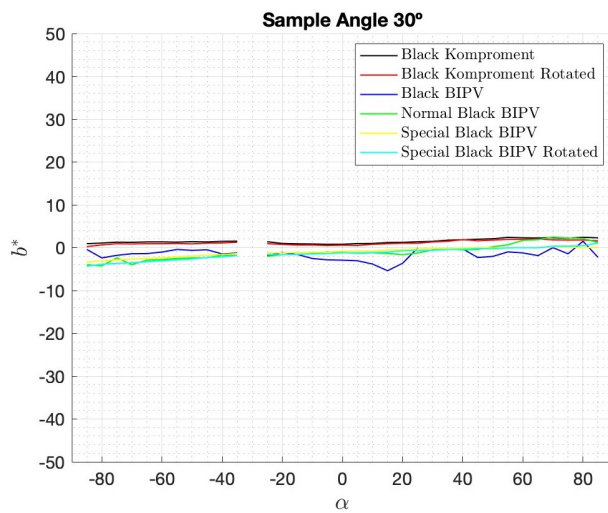


Figure A.92: Black Komproment b^* comparison at 30°

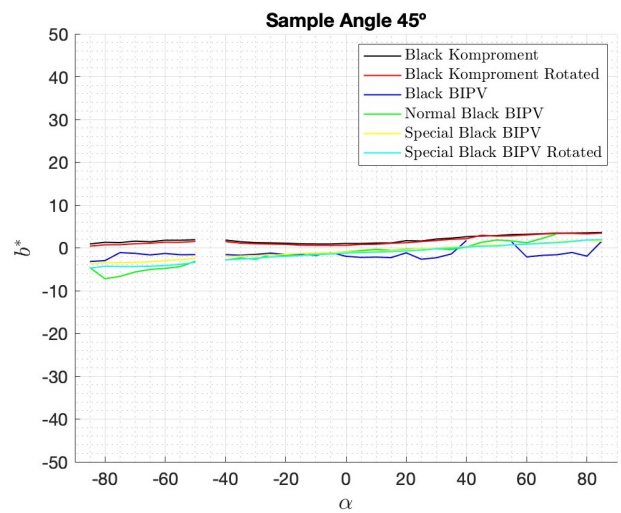


Figure A.93: Black Komproment b^* comparison at 45°

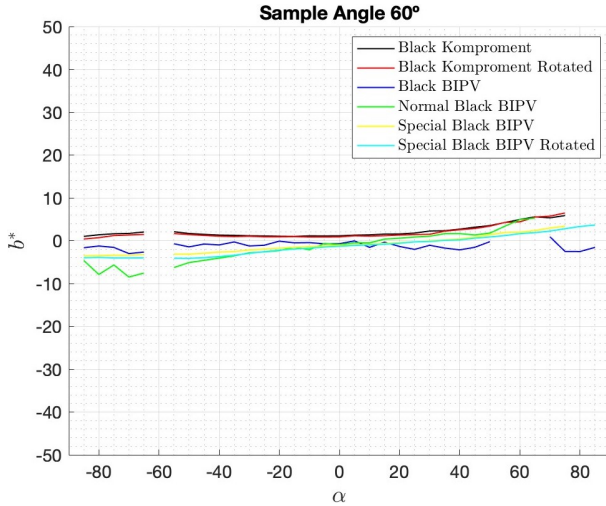


Figure A.94: Black Komproment b^* comparison at 60°

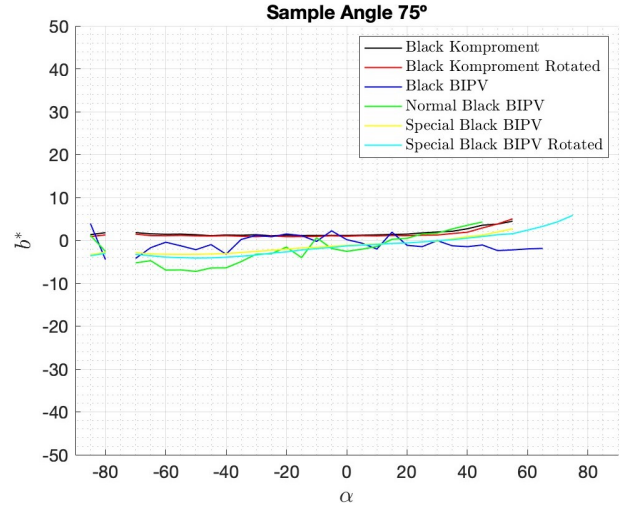


Figure A.95: Black Komproment b^* comparison at 75°

A.7 Natural Black Slate

A.7.1 L^* values

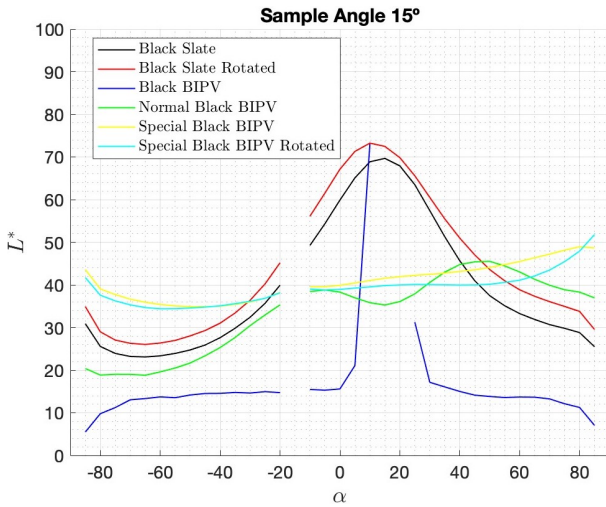


Figure A.96: Black Slate L^* comparison at 15°

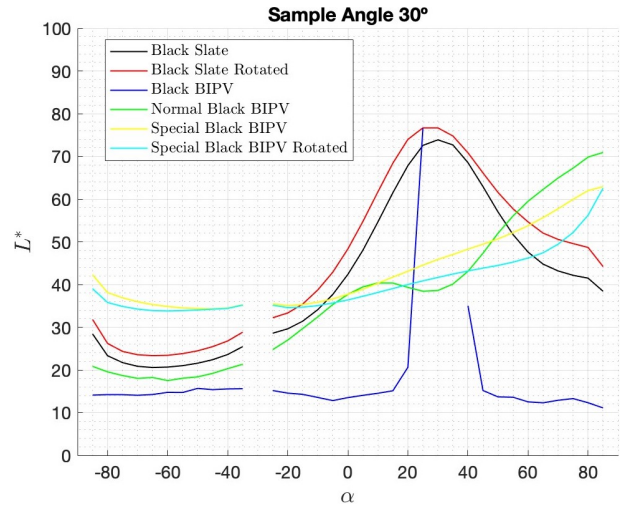


Figure A.97: Black Slate L^* comparison at 30°

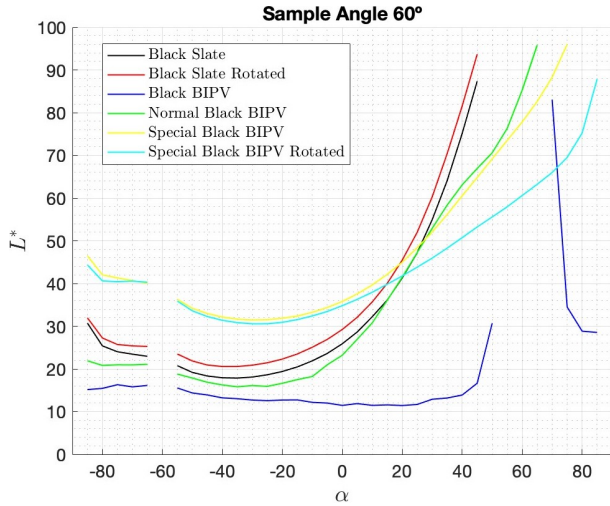


Figure A.98: Black Slate L^* comparison at 60°

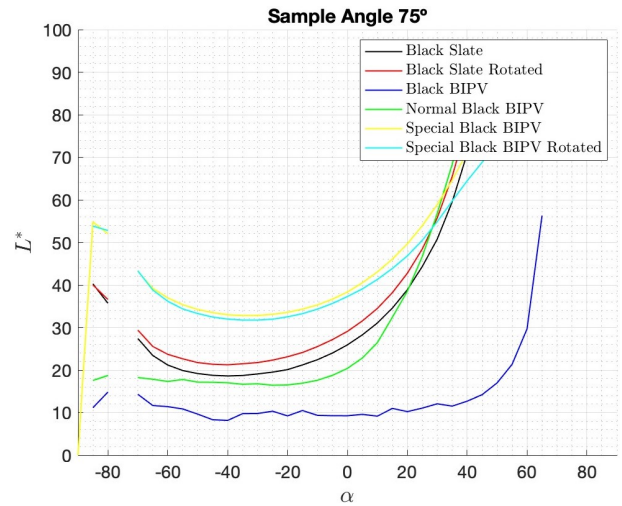


Figure A.99: Black Slate L^* comparison at 75°

A.7.2 a^* values

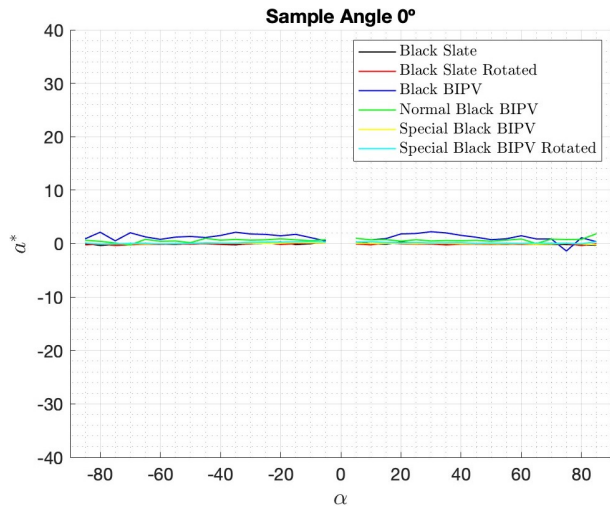


Figure A.100: Black Slate a^* comparison at 0°

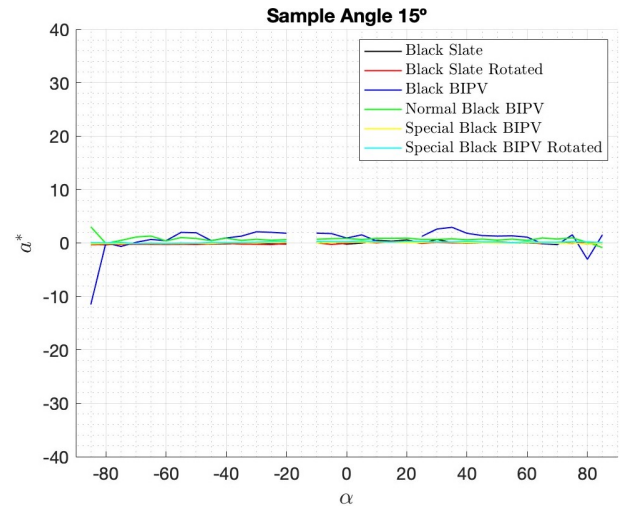


Figure A.101: Black Slate a^* comparison at 15°

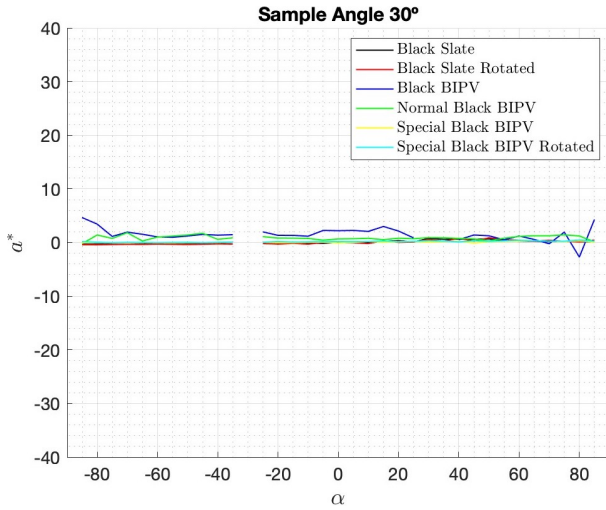


Figure A.102: Black Slate a^* comparison at 30°

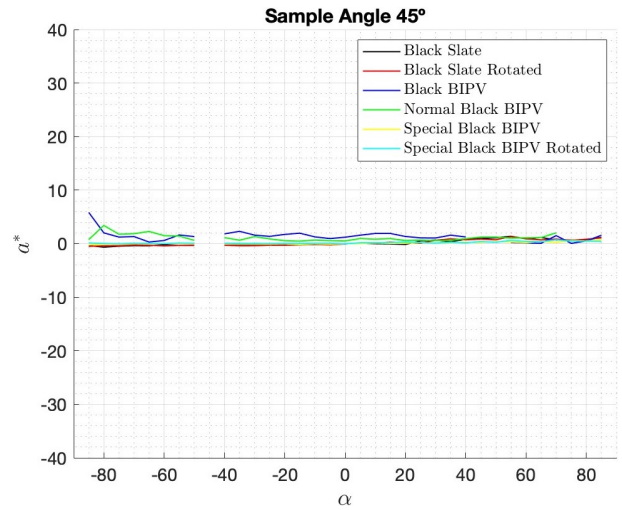


Figure A.103: Black Slate a^* comparison at 45°

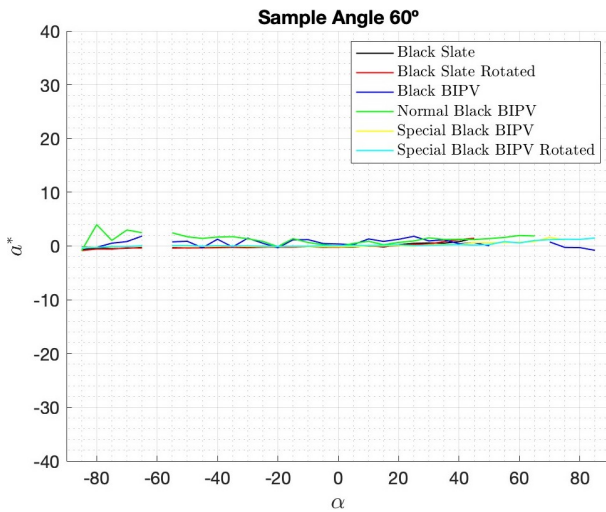


Figure A.104: Black Slate a^* comparison at 60°

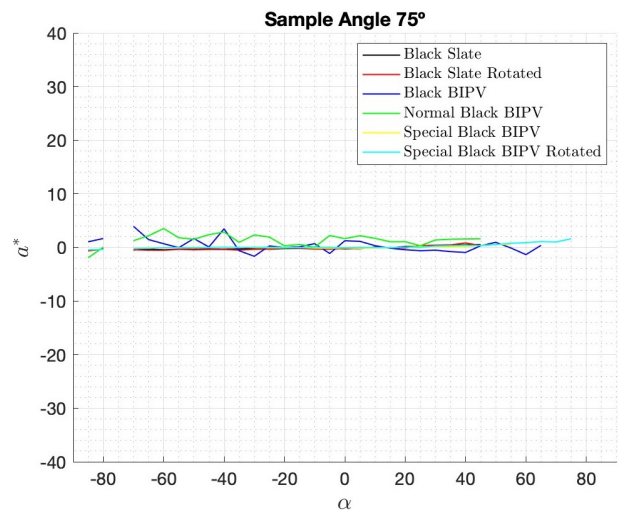


Figure A.105: Black Slate a^* comparison at 75°

A.7.3 b^* values

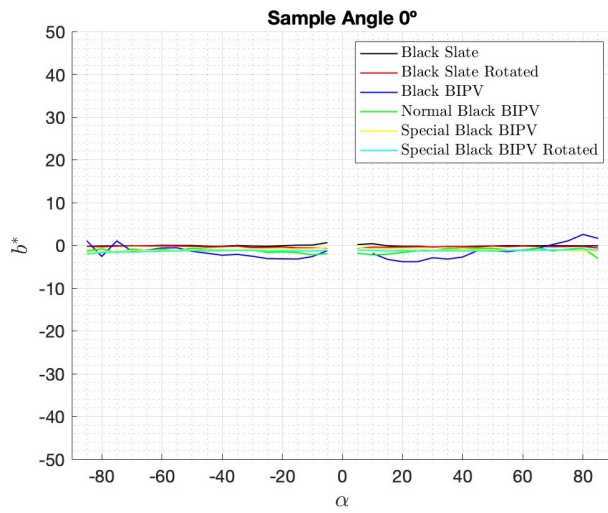


Figure A.106: Black Slate b^* comparison at 0°

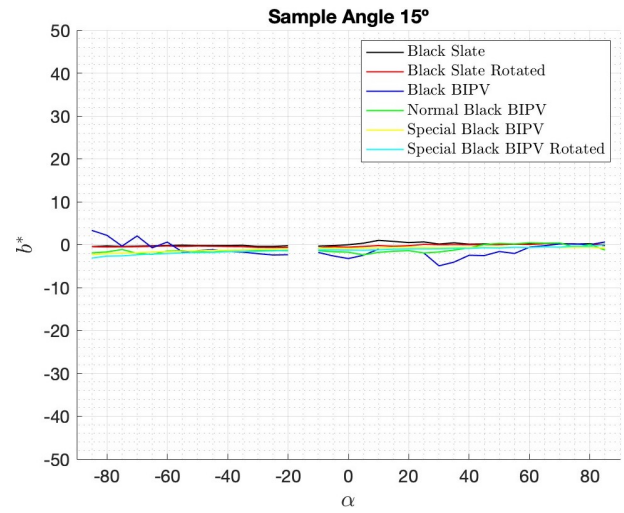


Figure A.107: Black Slate b^* comparison at 15°

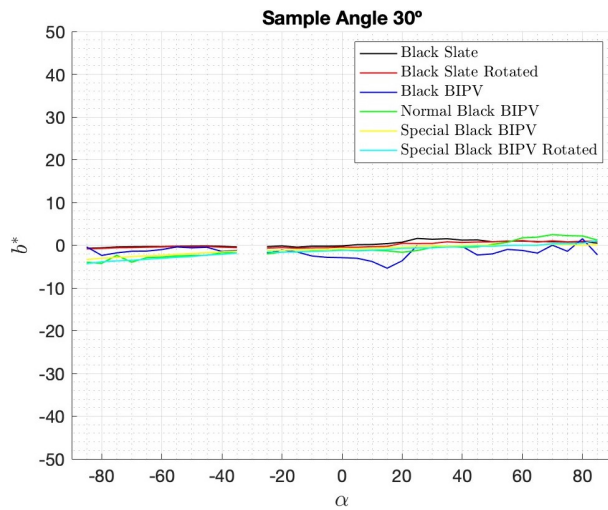


Figure A.108: Black Slate b^* comparison at 30°

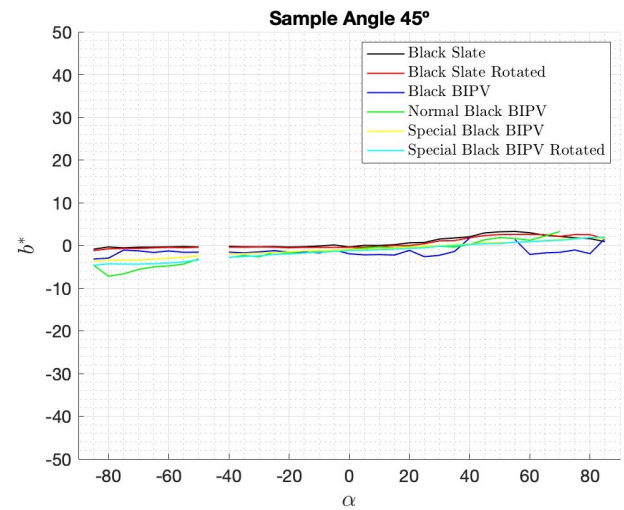


Figure A.109: Black Slate b^* comparison at 45°

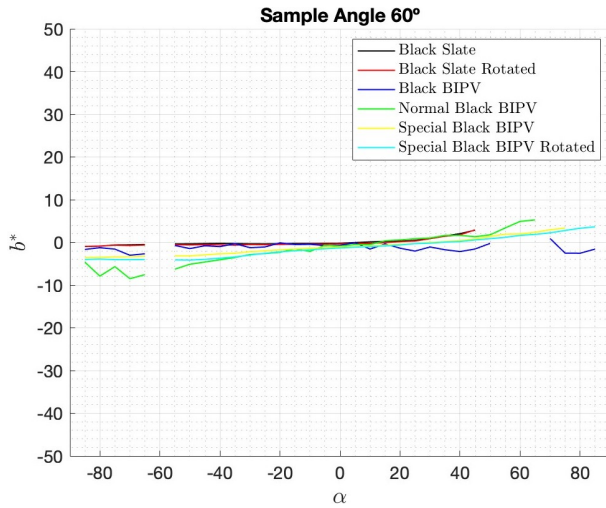


Figure A.110: Black Slate b^* comparison at 60°

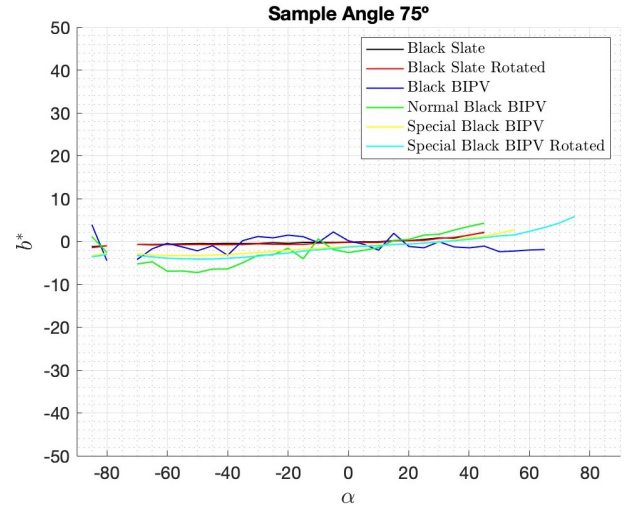


Figure A.111: Black Slate b^* comparison at 75°

B Appendix B

This section is only to complement the reproducibility Section 6.3.

B.1 Reproducibility of Black BIPV

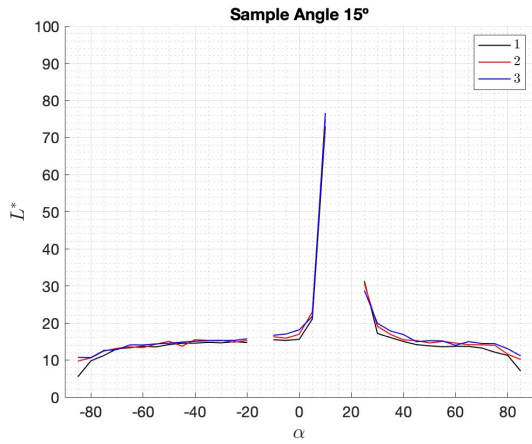


Figure B.1: Black BIPV L^* reproducibility at 15°

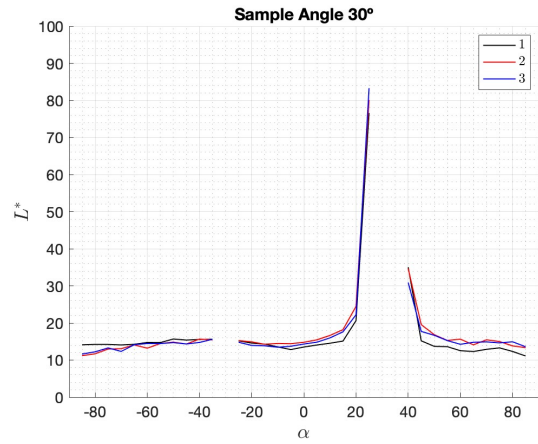


Figure B.2: Black BIPV L^* reproducibility at 30°

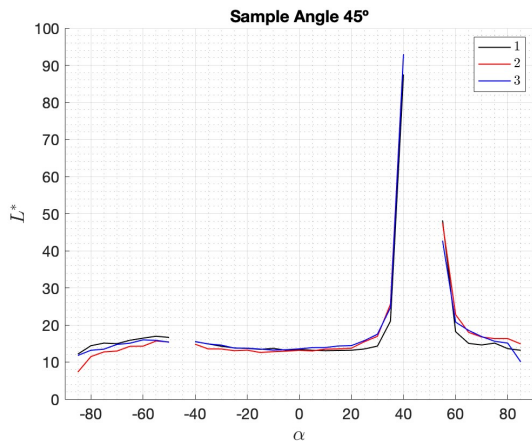


Figure B.3: Black BIPV L^* reproducibility at 45°

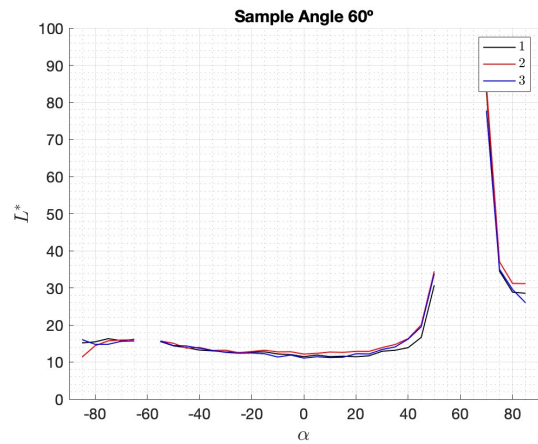


Figure B.4: Black BIPV L^* reproducibility at 60°

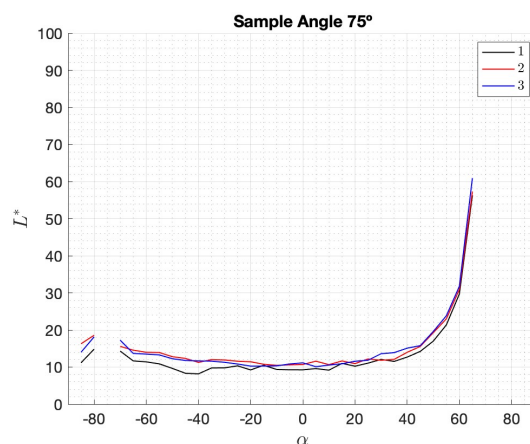


Figure B.5: Black BIPV L^* reproducibility at 75°

B.2 Reproducibility of Komproment

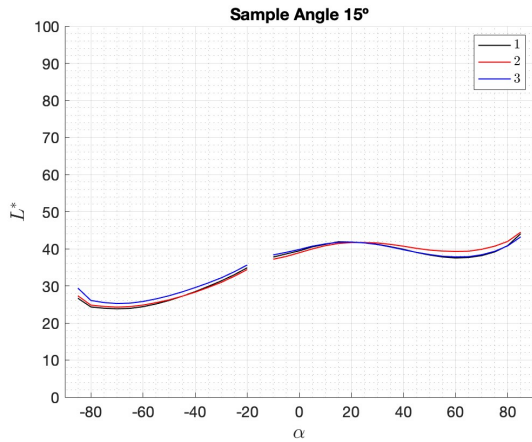


Figure B.6: Black Komproment L^* reproducibility at 15°

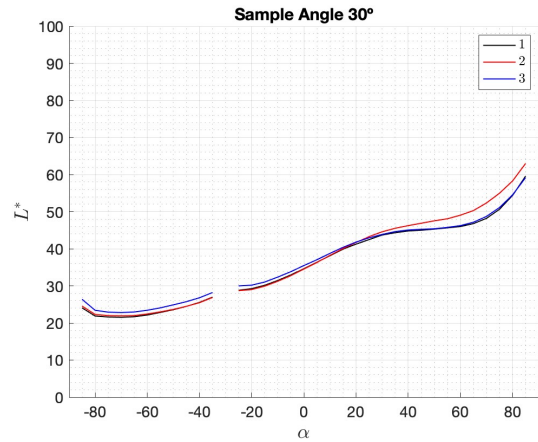


Figure B.7: Black Komproment L^* reproducibility at 30°

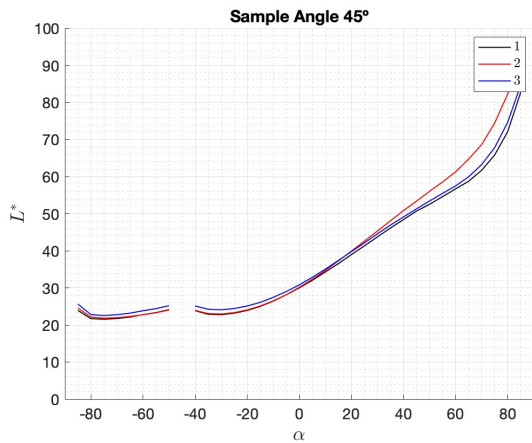


Figure B.8: Black Komproment L^* reproducibility at 45°

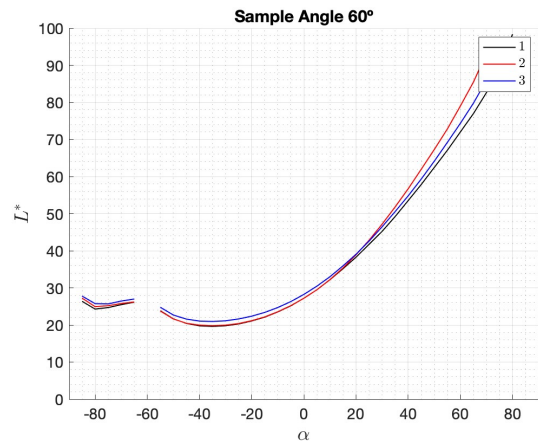


Figure B.9: Black Komproment L^* reproducibility at 60°

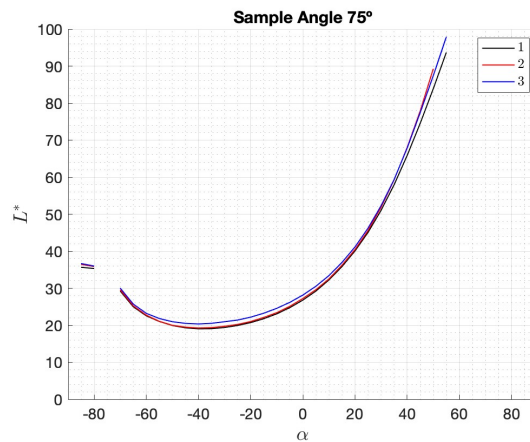


Figure B.10: Black Komproment L^* reproducibility at 75°

B.3 Reproducibility of Komproment Rotated

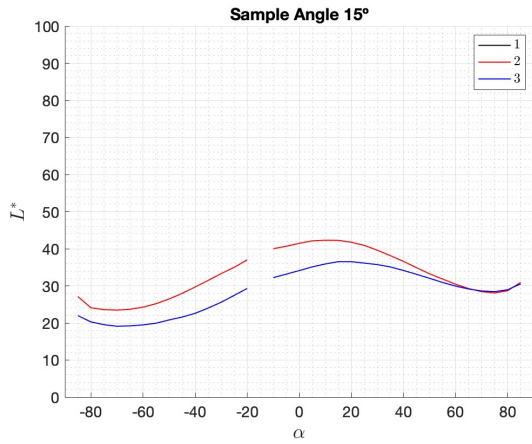


Figure B.11: Black Komproment Rotated L^* reproducibility at 15°

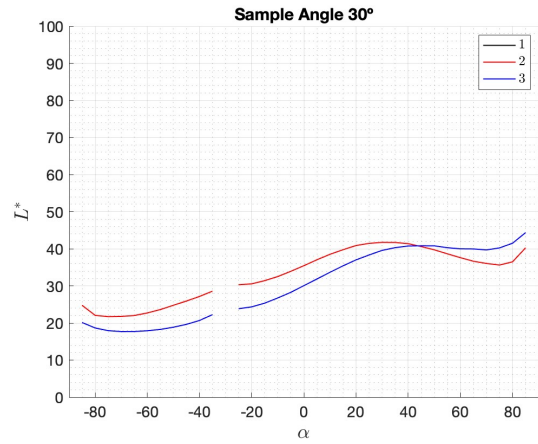


Figure B.12: Black Komproment Rotated L^* reproducibility at 30°

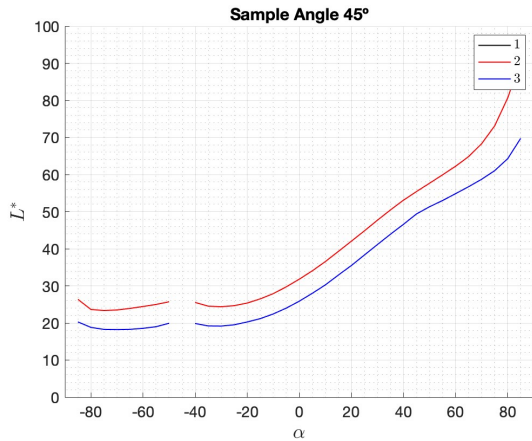


Figure B.13: Black Komproment Rotated L^* reproducibility at 45°

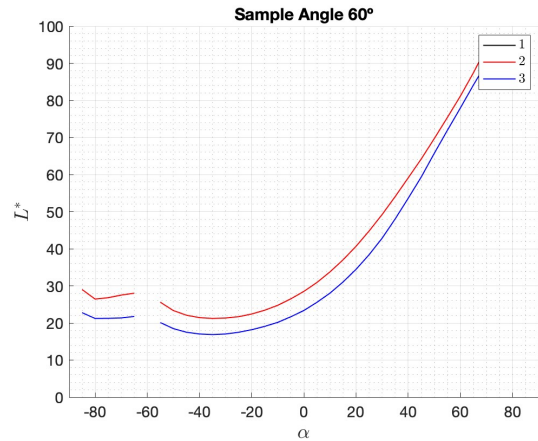


Figure B.14: Black Komproment Rotated L^* reproducibility at 60°

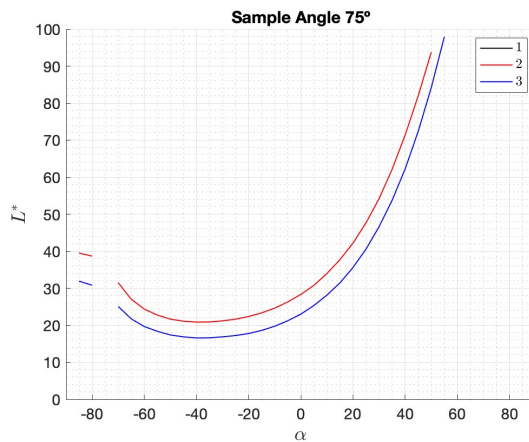


Figure B.15: Black Komproment Rotated L^* reproducibility at 75°

B.4 Reproducibility of Black Slate

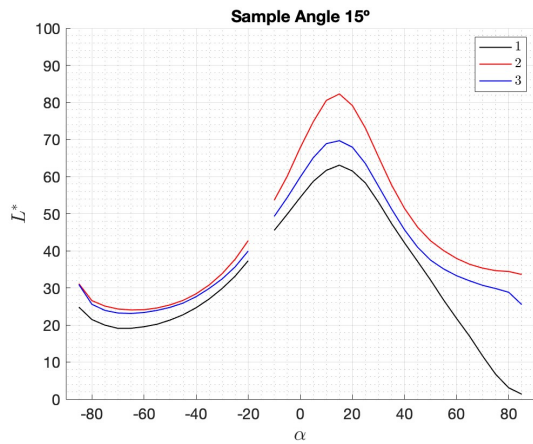


Figure B.16: Black Slate L^* reproducibility at 15°

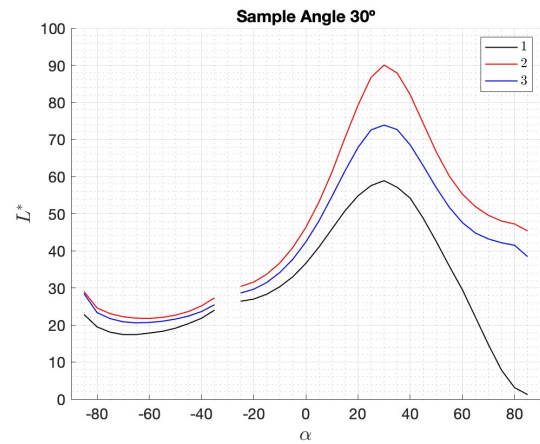


Figure B.17: Black Slate L^* reproducibility at 30°

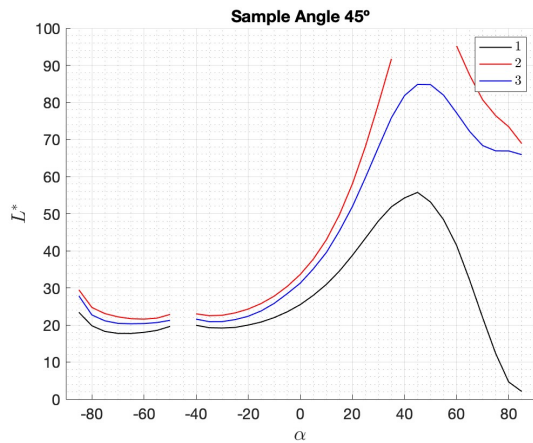


Figure B.18: Black Slate L^* reproducibility at 45°

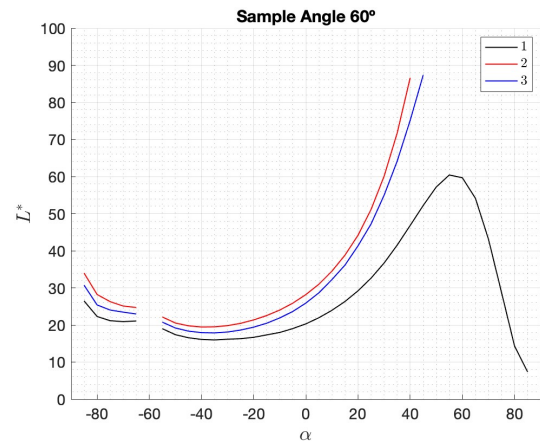


Figure B.19: Black Slate L^* reproducibility at 60°

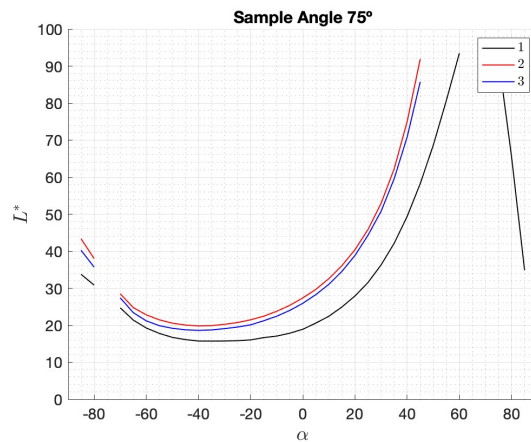


Figure B.20: Black Slate L^* reproducibility at 75°

B.5 Reproducibility of Black Slate Rotated

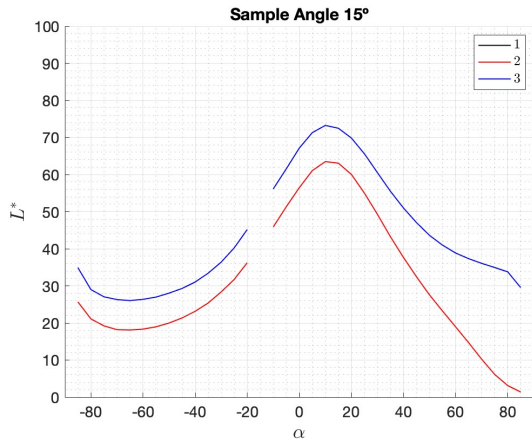


Figure B.21: Black Slate Rotated L^* reproducibility at 15°

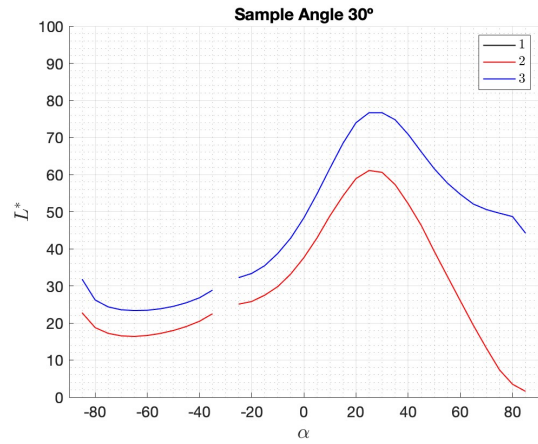


Figure B.22: Black Slate Rotated L^* reproducibility at 30°

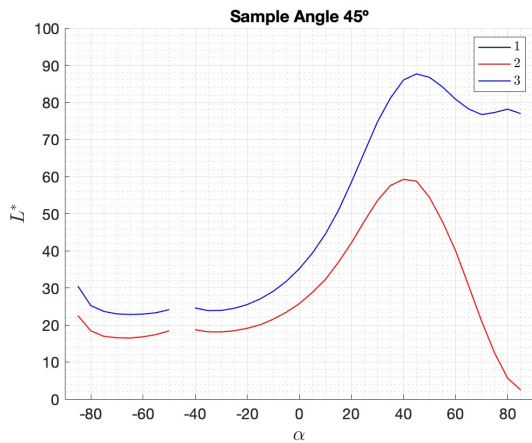


Figure B.23: Black Slate Rotated L^* reproducibility at 45°

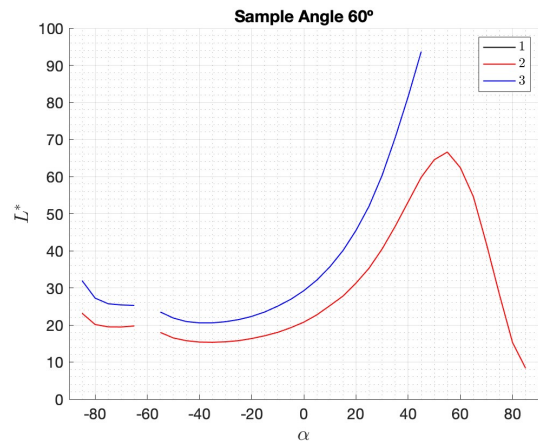


Figure B.24: Black Slate Rotated L^* reproducibility at 60°

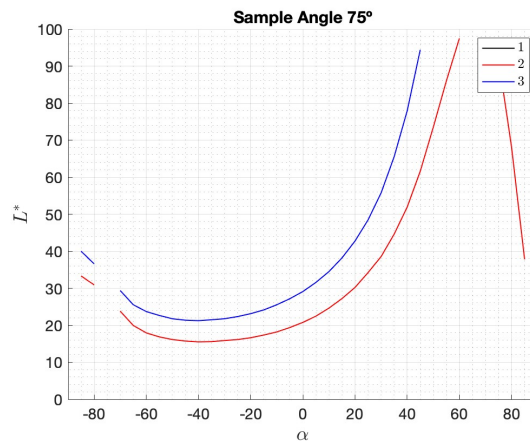


Figure B.25: Black Slate Rotated L^* reproducibility at 75°

B.6 Reproducibility of Black Tile

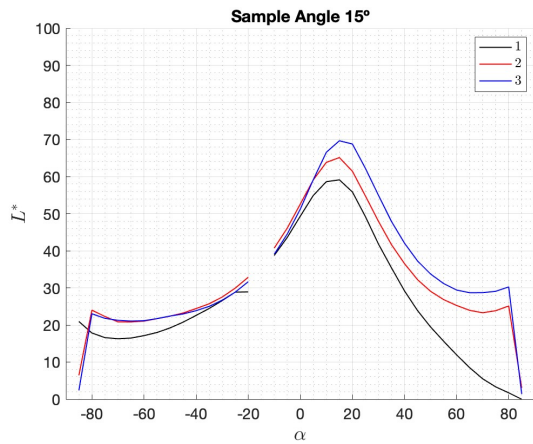


Figure B.26: Black Tile L^* reproducibility at 15°

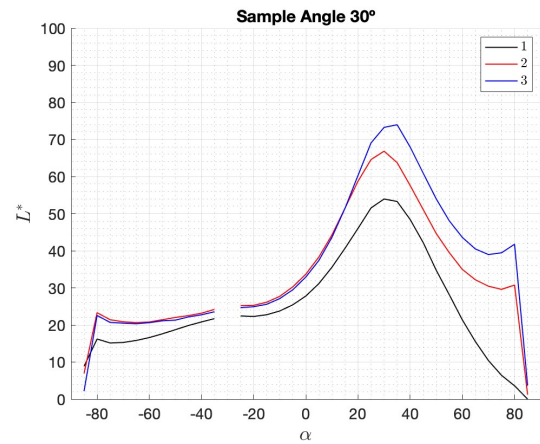


Figure B.27: Black Tile L^* reproducibility at 30°

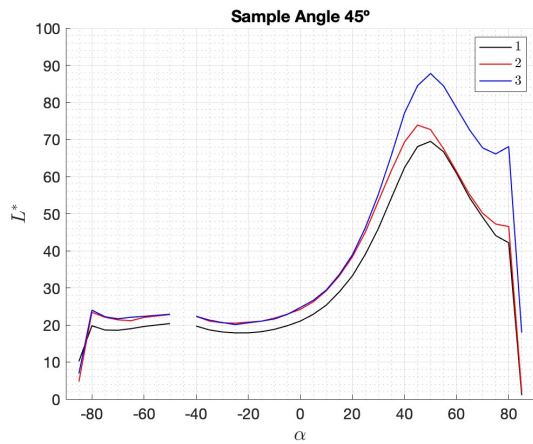


Figure B.28: Black Tile L^* reproducibility at 45°

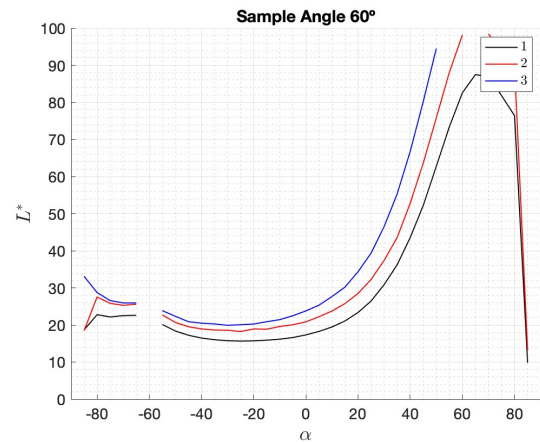


Figure B.29: Black Tile L^* reproducibility at 60°

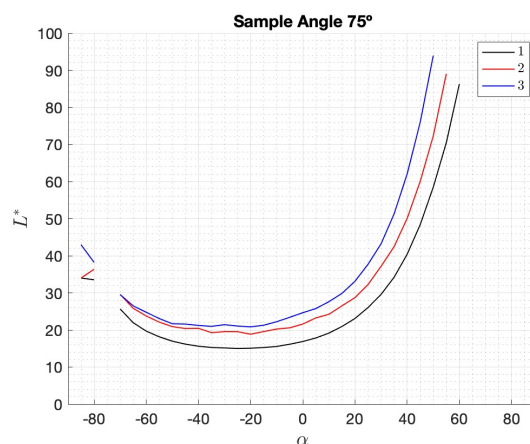


Figure B.30: Black Tile L^* reproducibility at 75°

B.7 Reproducibility of Black Tile Rotated

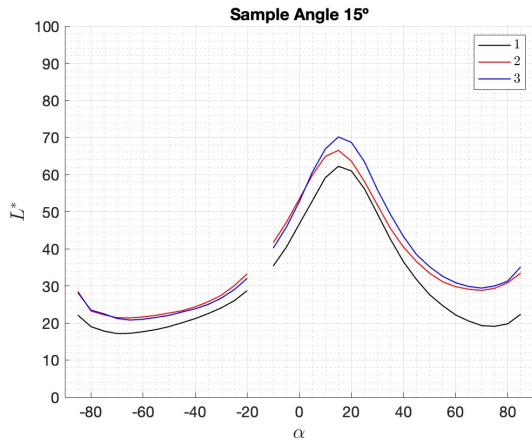


Figure B.31: Black Tile Rotated L^* reproducibility at 15°

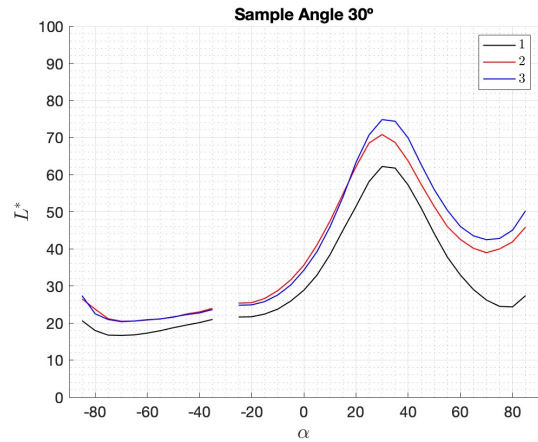


Figure B.32: Black Tile Rotated L^* reproducibility at 30°

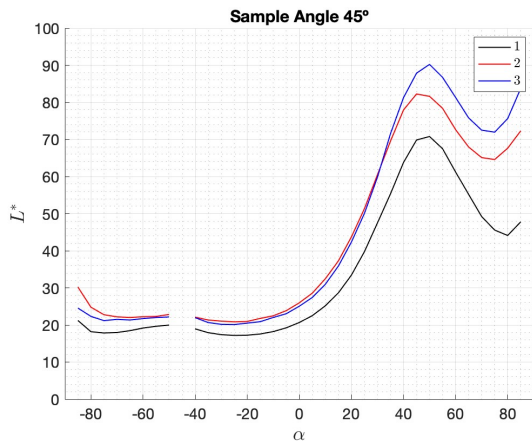


Figure B.33: Black Tile Rotated L^* reproducibility at 45°

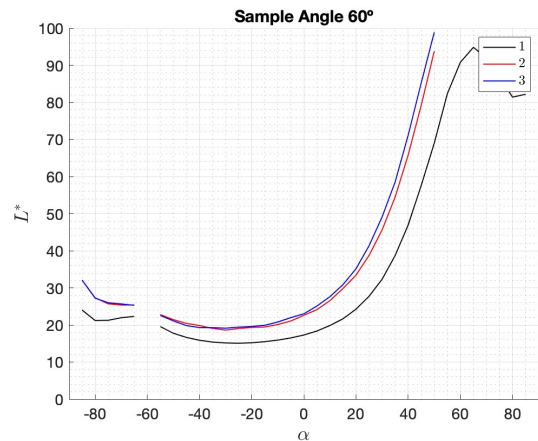


Figure B.34: Black Tile Rotated L^* reproducibility at 60°

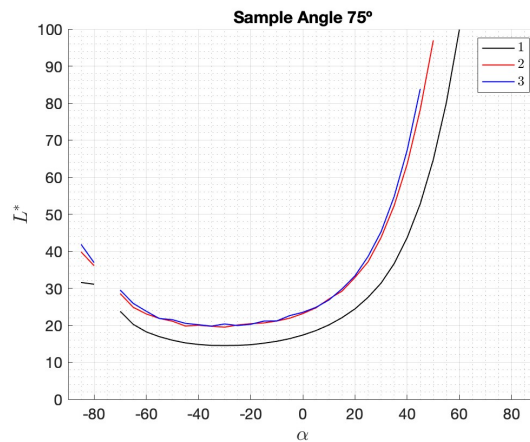


Figure B.35: Black Tile Rotated L^* reproducibility at 17°

B.8 Reproducibility of Clear Red BIPV

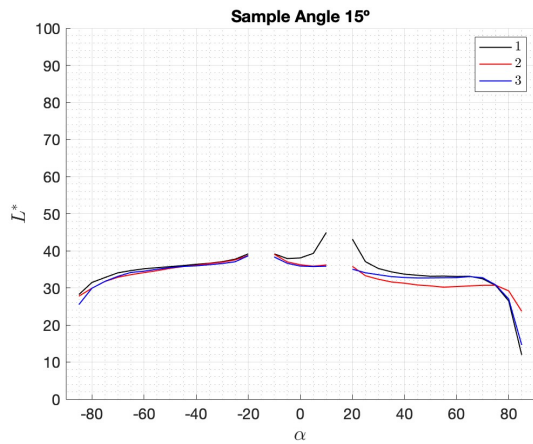


Figure B.36: Clear Red BIPV L^* reproducibility at 15°

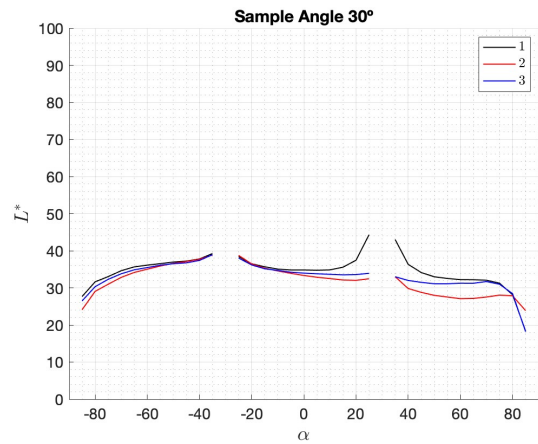


Figure B.37: Clear Red BIPV L^* reproducibility at 30°

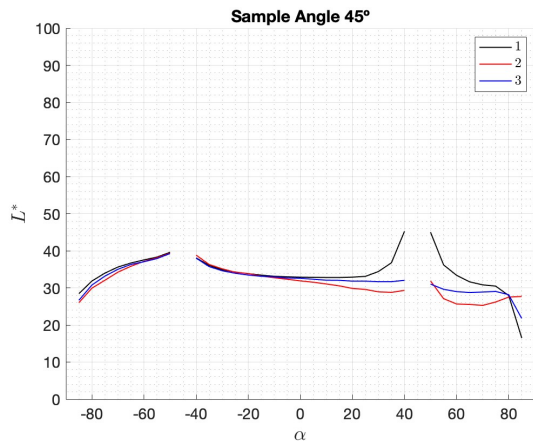


Figure B.38: Clear Red BIPV L^* reproducibility at 45°

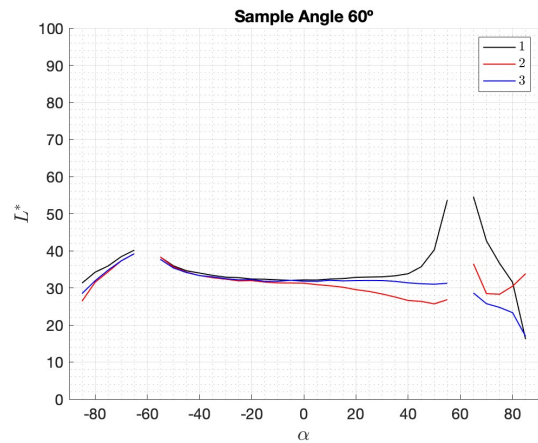


Figure B.39: Clear Red BIPV L^* reproducibility at 60°

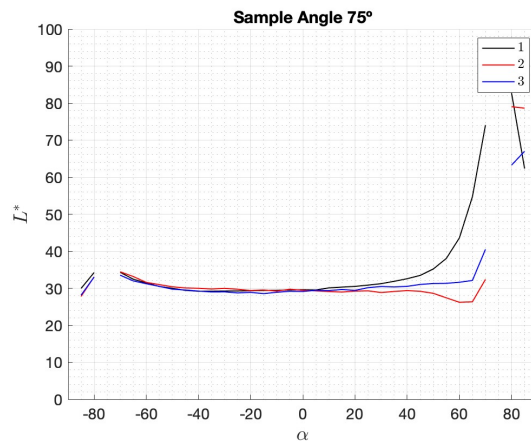


Figure B.40: Clear Red BIPV L^* reproducibility at 75°

B.9 Reproducibility of Clear Red Tile

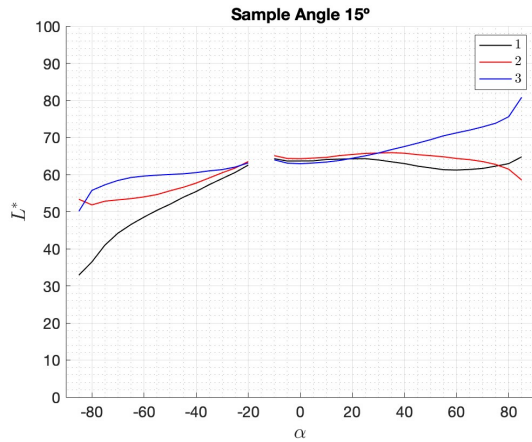


Figure B.41: Clear Red Tile L^* reproducibility at 15°

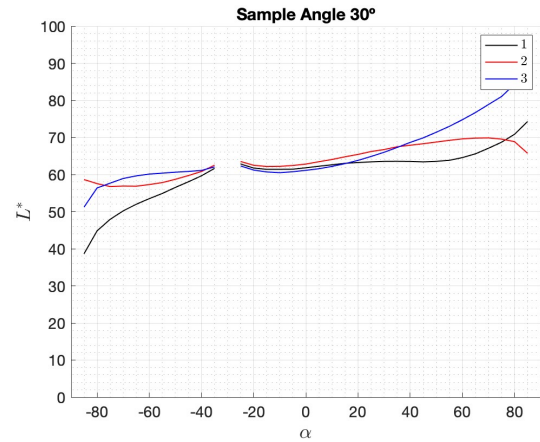


Figure B.42: Clear Red Tile L^* reproducibility at 30°

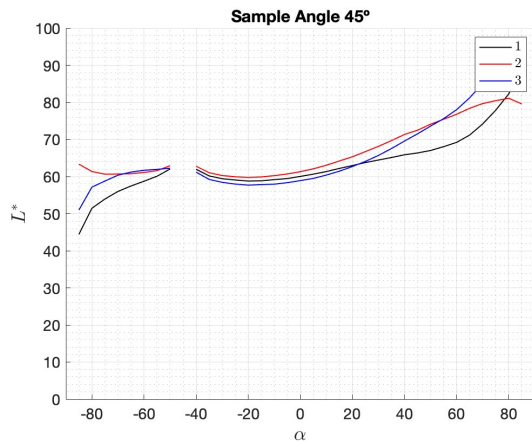


Figure B.43: Clear Red Tile L^* reproducibility at 45°

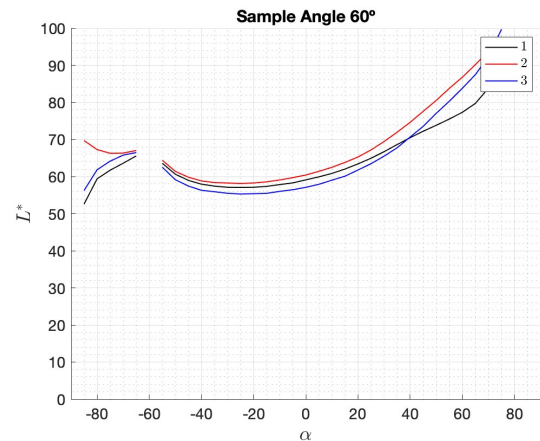


Figure B.44: Clear Red Tile L^* reproducibility at 60°

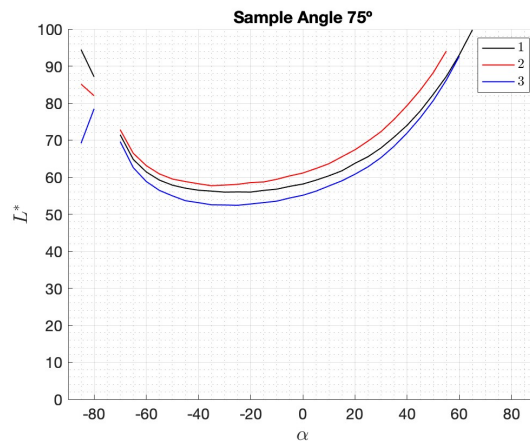


Figure B.45: Clear Red Tile L^* reproducibility at 75°

B.10 Reproducibility of Clear Red Tile Rotated

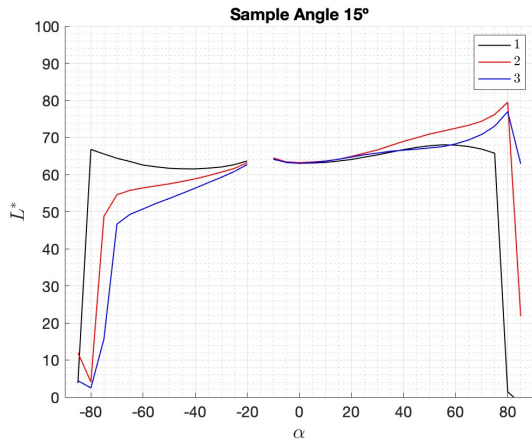


Figure B.46: Clear Red Tile Rotated L^* reproducibility at 15°

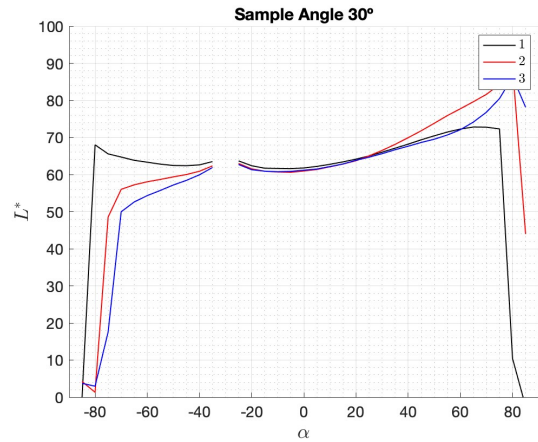


Figure B.47: Clear Red Tile Rotated L^* reproducibility at 30°

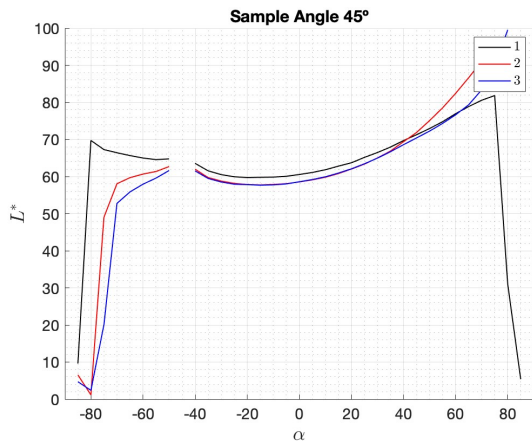


Figure B.48: Clear Red Tile Rotated L^* reproducibility at 45°

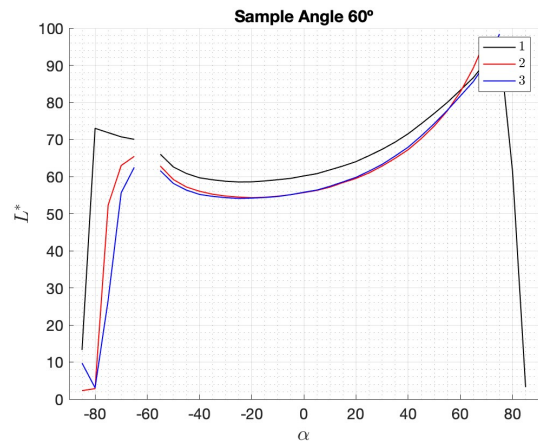


Figure B.49: Clear Red Tile Rotated L^* reproducibility at 60°

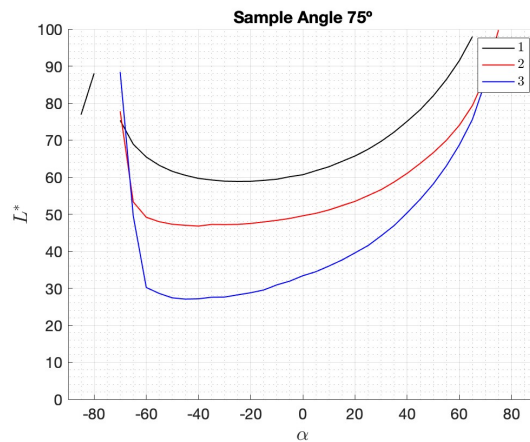


Figure B.50: Clear Red Tile Rotated L^* reproducibility at 75°

B.11 Reproducibility of Dark Red BIPV

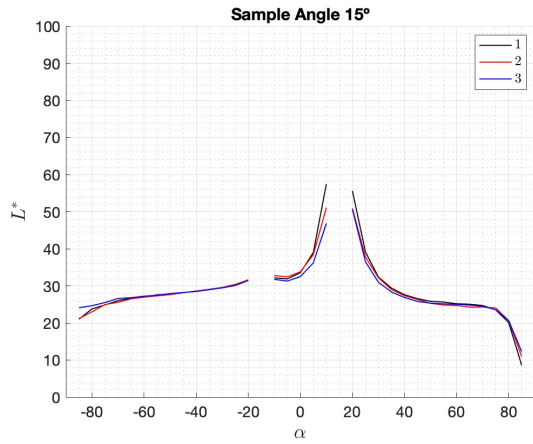


Figure B.51: Dark Red BIPV L^* reproducibility at 15°

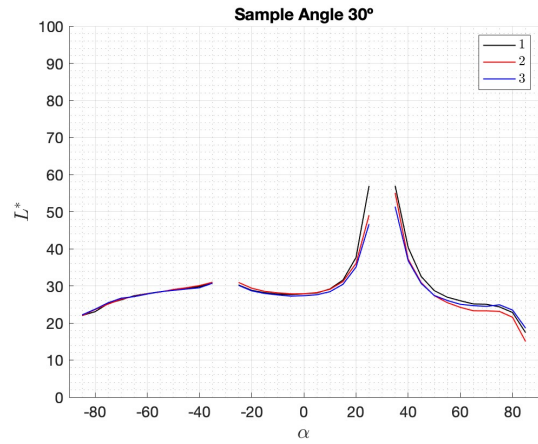


Figure B.52: Dark Red BIPV L^* reproducibility at 30°

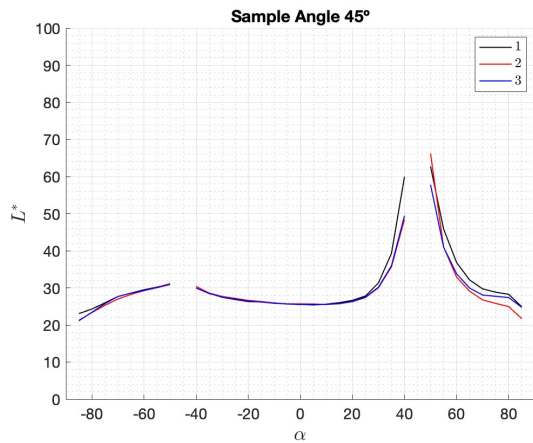


Figure B.53: Dark Red BIPV L^* reproducibility at 45°

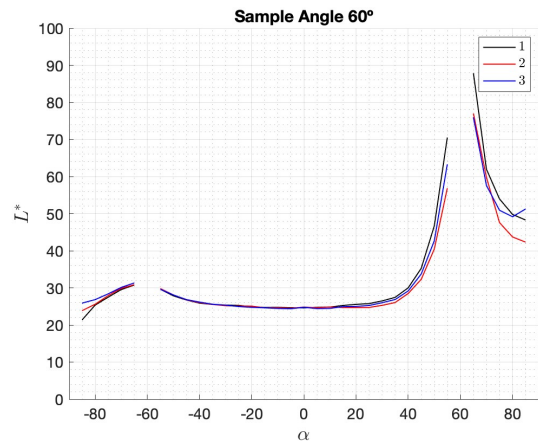


Figure B.54: Dark Red BIPV L^* reproducibility at 60°

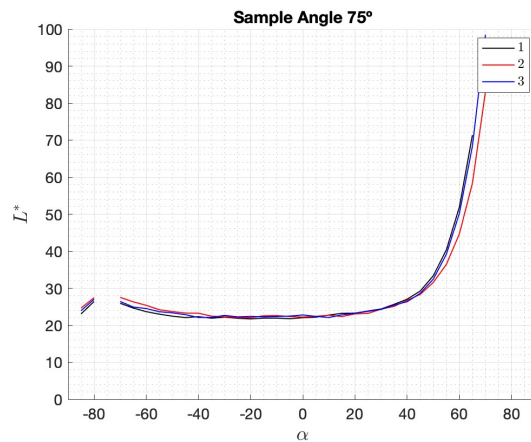


Figure B.55: Dark Red BIPV L^* reproducibility at 75°

B.12 Reproducibility of Dark Red Tile

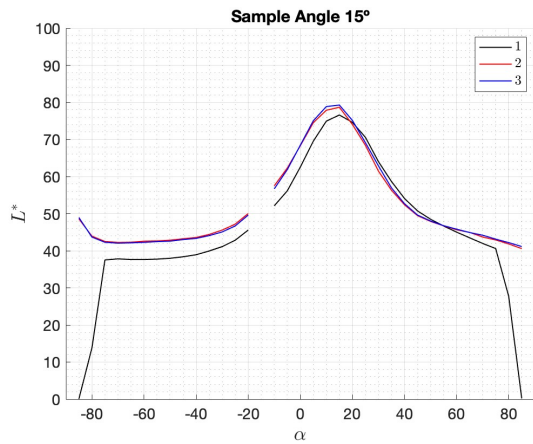


Figure B.56: Dark Red Tile L^* reproducibility at 15°

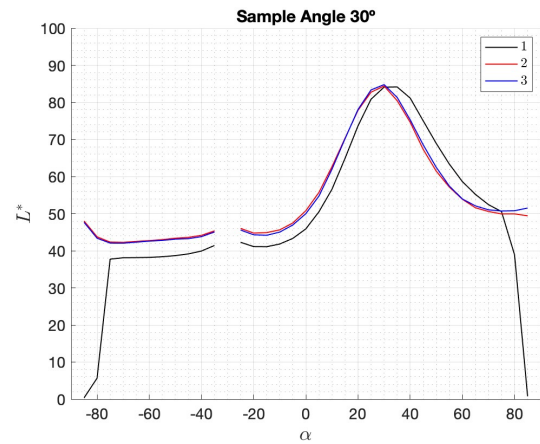


Figure B.57: Dark Red Tile L^* reproducibility at 30°

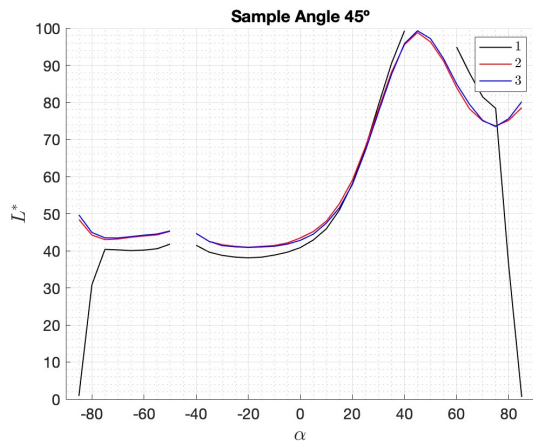


Figure B.58: Dark Red Tile L^* reproducibility at 45°

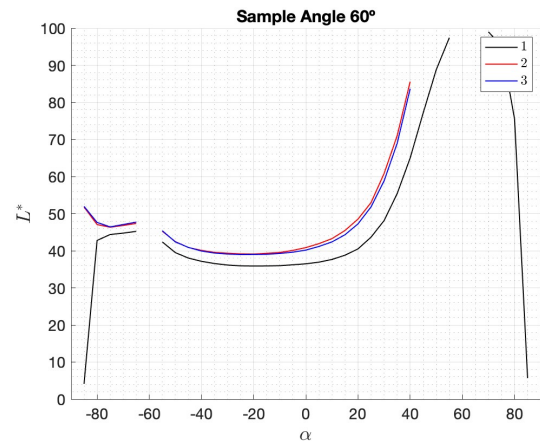


Figure B.59: Dark Red Tile L^* reproducibility at 60°

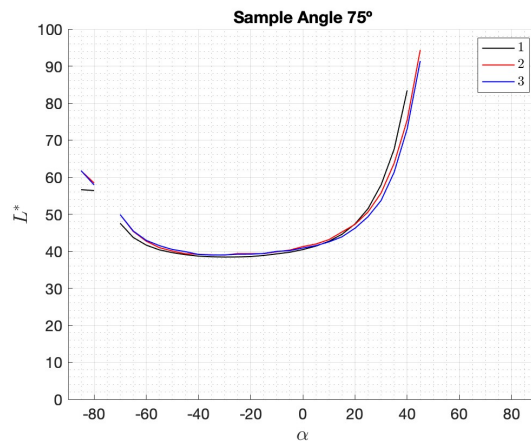


Figure B.60: Dark Red Tile L^* reproducibility at 75°

B.13 Reproducibility of Dark Red Tile Rotated

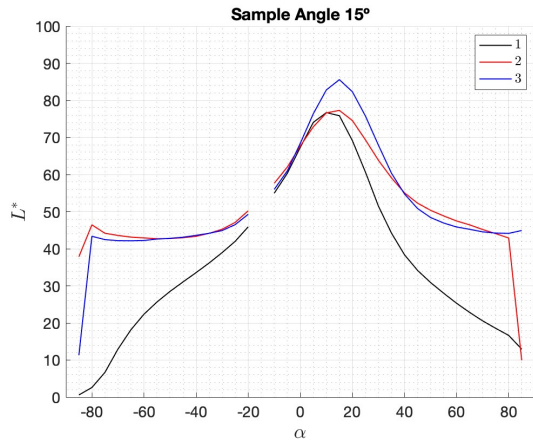


Figure B.61: Dark Red Tile Rotated L^* reproducibility at 15°

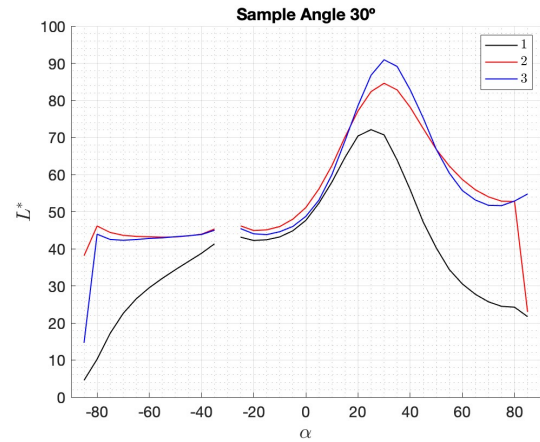


Figure B.62: Dark Red Tile Rotated L^* reproducibility at 30°

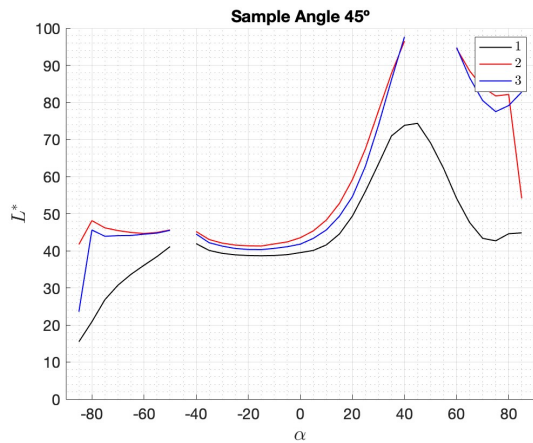


Figure B.63: Dark Red Tile Rotated L^* reproducibility at 45°

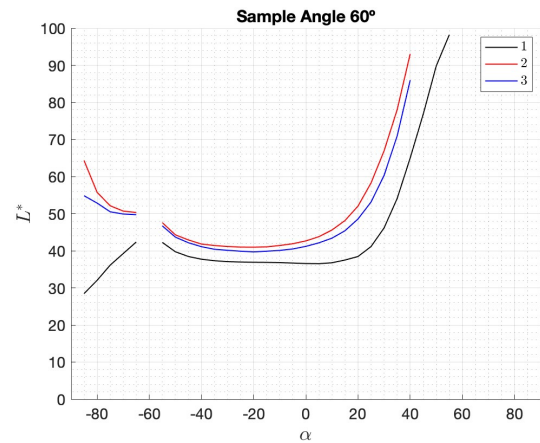


Figure B.64: Dark Red Tile Rotated L^* reproducibility at 60°

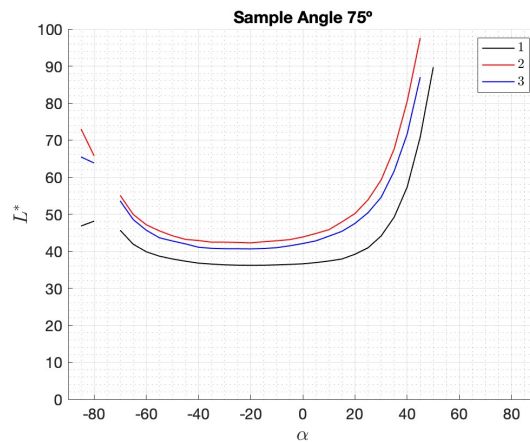


Figure B.65: Dark Red Tile Rotated L^* reproducibility at 75°

B.14 Reproducibility of Glazed Black Tile

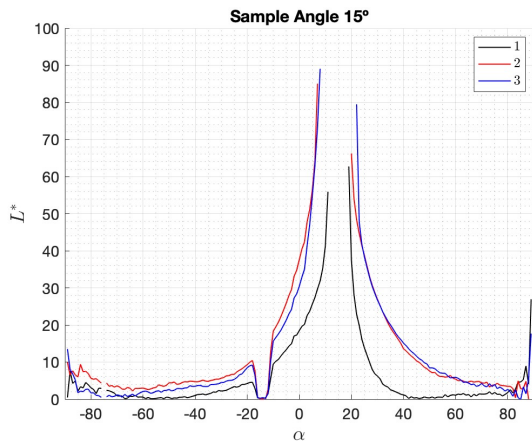


Figure B.66: Glazed Black Tile L^* reproducibility at 15°

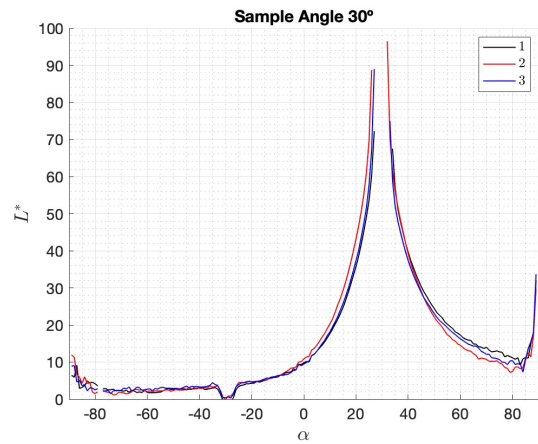


Figure B.67: Glazed Black Tile L^* reproducibility at 30°

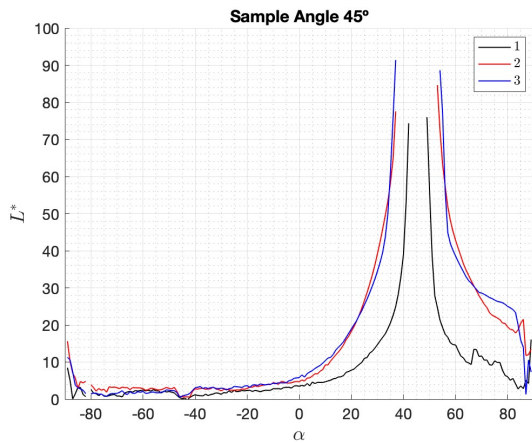


Figure B.68: Glazed Black Tile L^* reproducibility at 45°

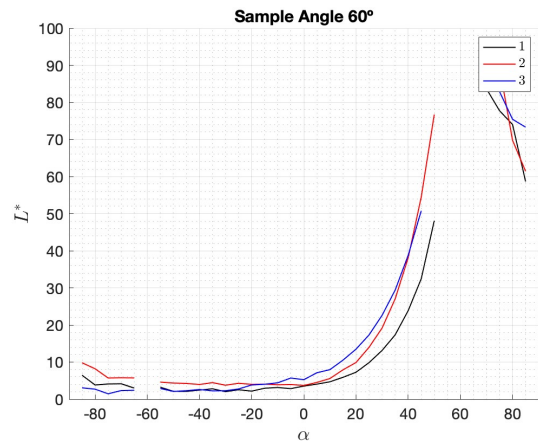


Figure B.69: Glazed Black Tile L^* reproducibility at 60°

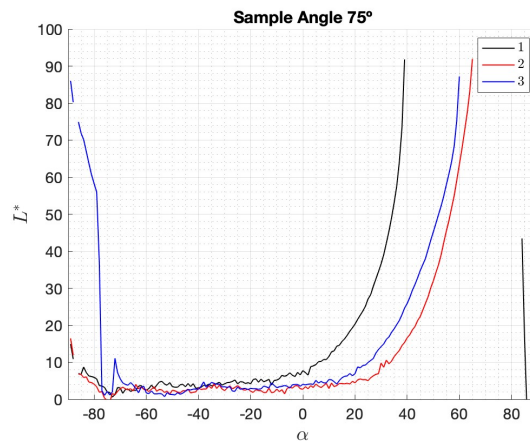


Figure B.70: Glazed Black Tile L^* reproducibility at 75°

B.15 Reproducibility of Glazed Black Tile Rotated

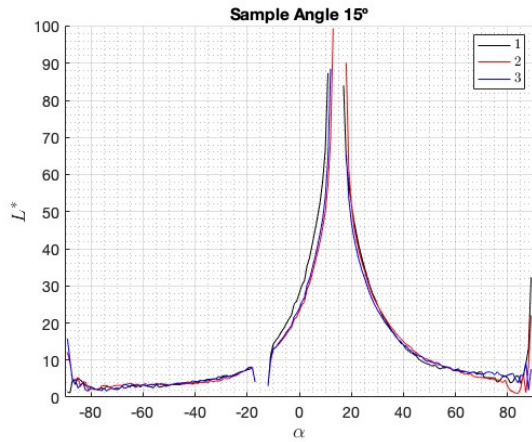


Figure B.71: Glazed Black Tile Rotated L^* reproducibility at 15°

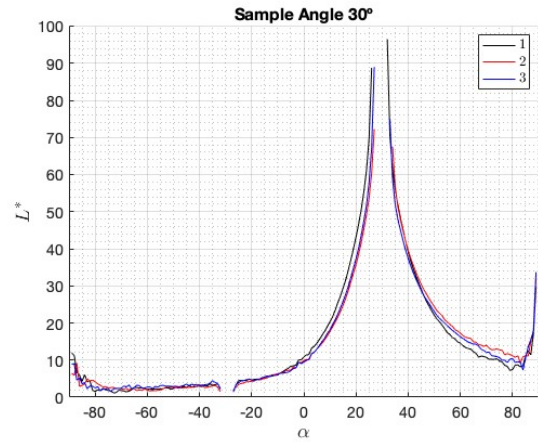


Figure B.72: Glazed Black Tile Rotated L^* reproducibility at 30°

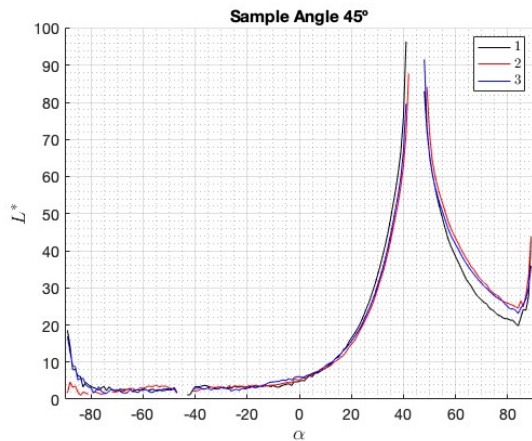


Figure B.73: Glazed Black Tile Rotated L^* reproducibility at 45°

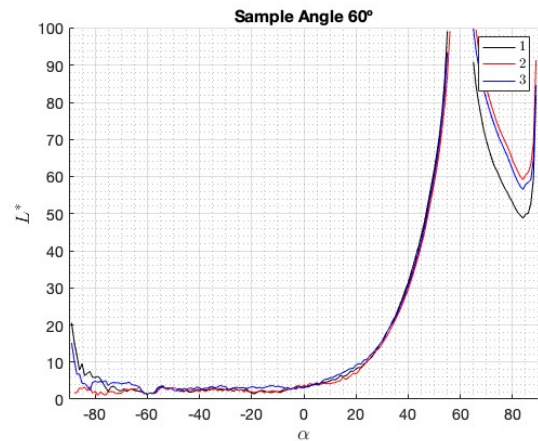


Figure B.74: Glazed Black Tile Rotated L^* reproducibility at 60°

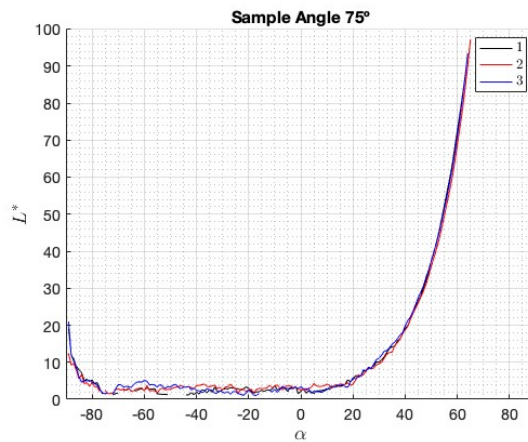


Figure B.75: Glazed Black Tile Rotated L^* reproducibility at 75°

B.16 Reproducibility of Gold BIPV

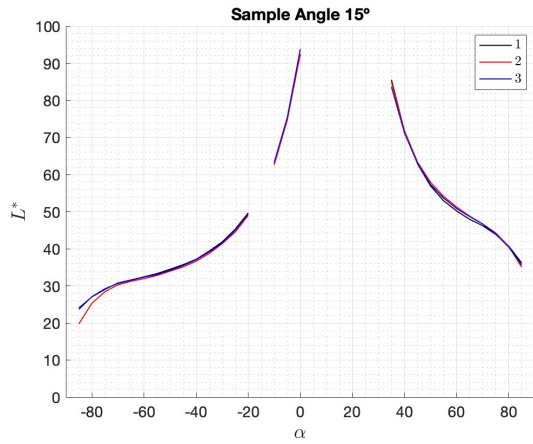


Figure B.76: Gold BIPV L^* reproducibility at 15°

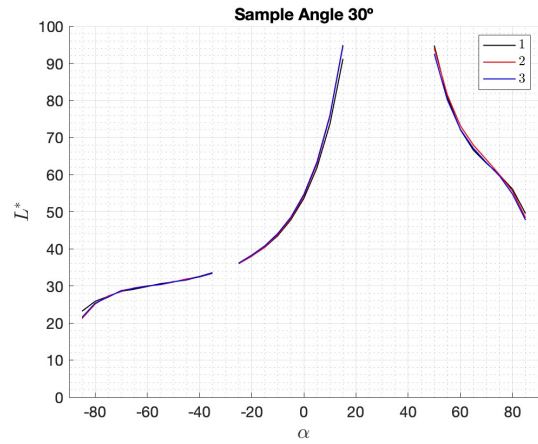


Figure B.77: Gold BIPV L^* reproducibility at 30°

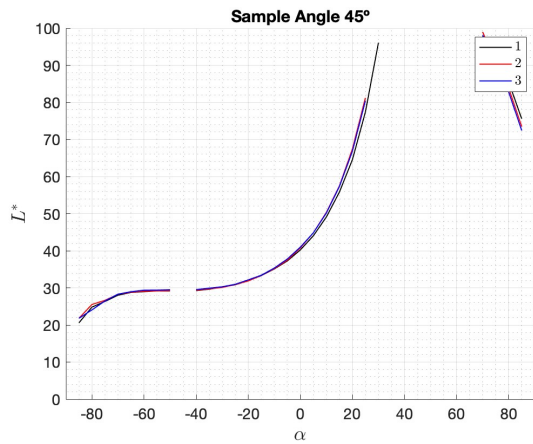


Figure B.78: Gold BIPV L^* reproducibility at 45°

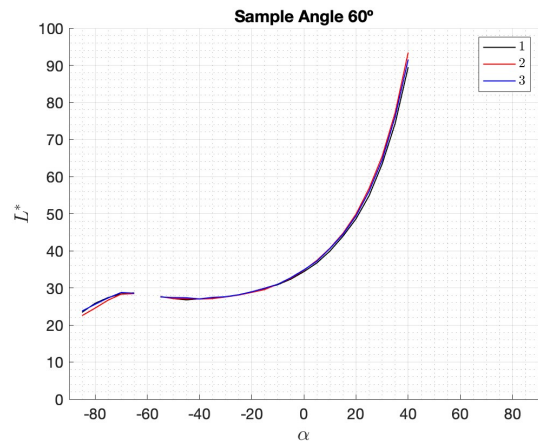


Figure B.79: Gold BIPV L^* reproducibility at 60°

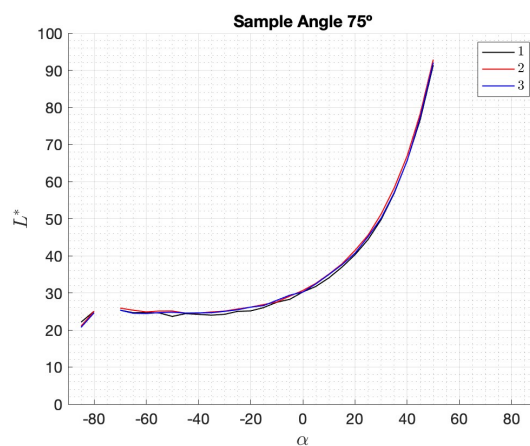


Figure B.80: Gold BIPV L^* reproducibility at 75°

B.17 Reproducibility of Normal Black BIPV

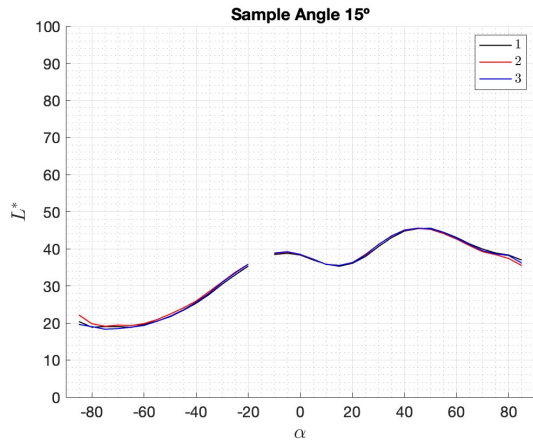


Figure B.81: Normal Black BIPV L^* reproducibility at 15°

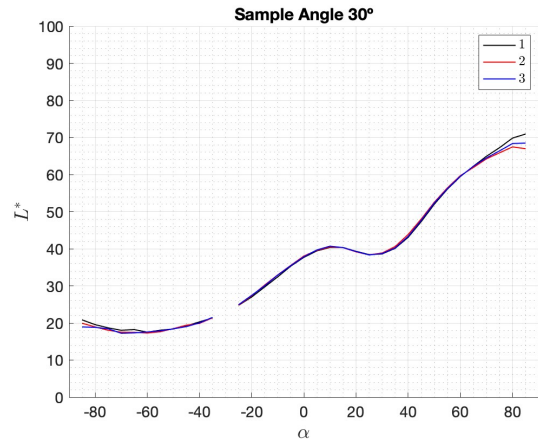


Figure B.82: Normal Black BIPV L^* reproducibility at 30°

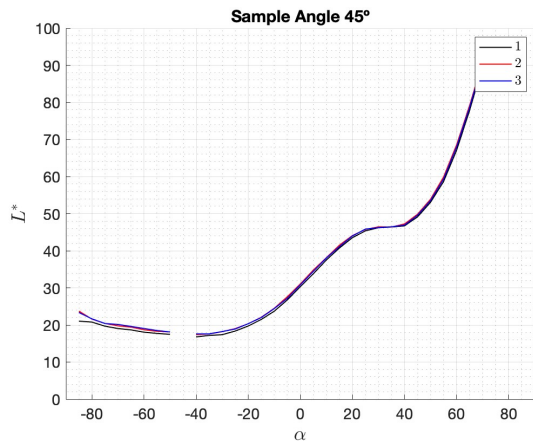


Figure B.83: Normal Black BIPV L^* reproducibility at 45°

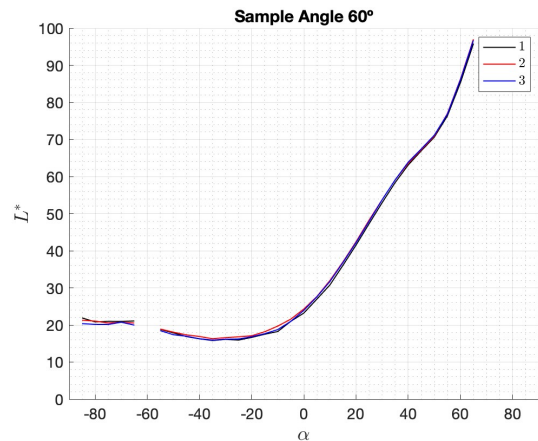


Figure B.84: Normal Black BIPV L^* reproducibility at 60°

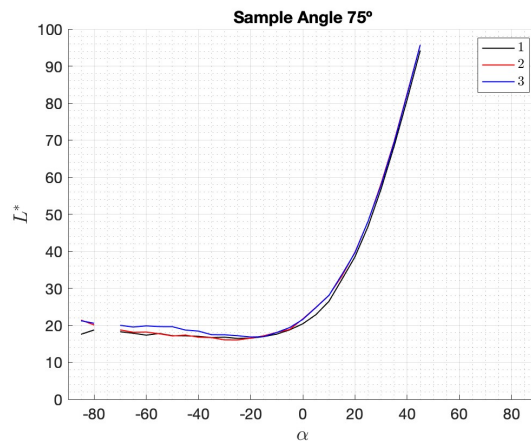


Figure B.85: Normal Black BIPV L^* reproducibility at 75°

B.18 Reproducibility of Red BIPV

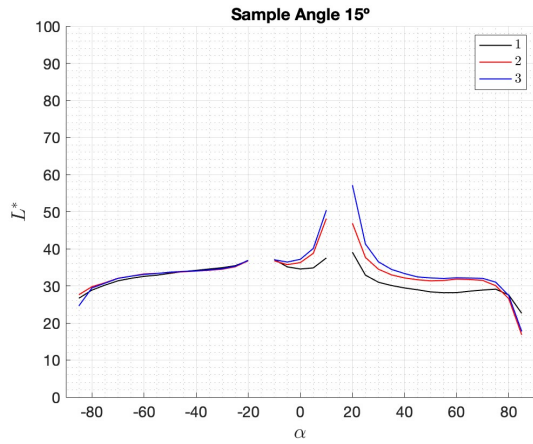


Figure B.86: Red BIPV L^* reproducibility at 15°

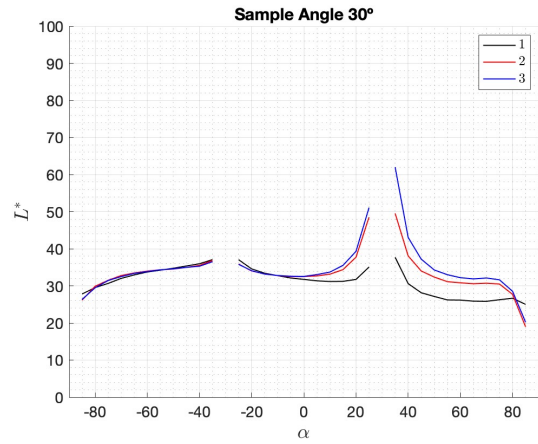


Figure B.87: Red BIPV L^* reproducibility at 30°

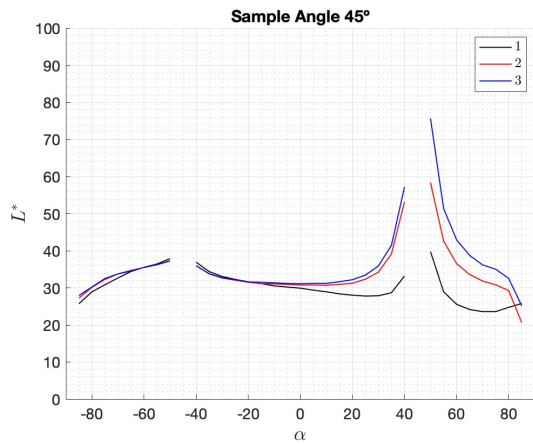


Figure B.88: Red BIPV L^* reproducibility at 45°

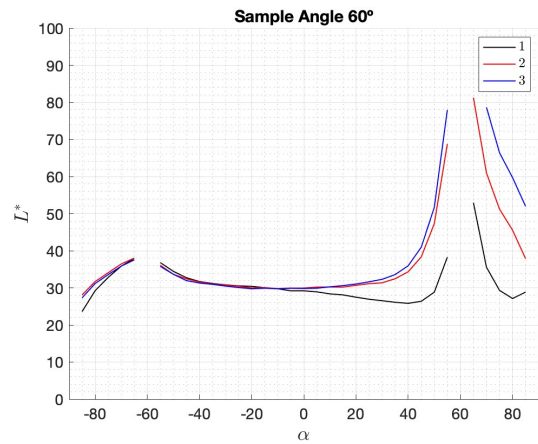


Figure B.89: Red BIPV L^* reproducibility at 60°

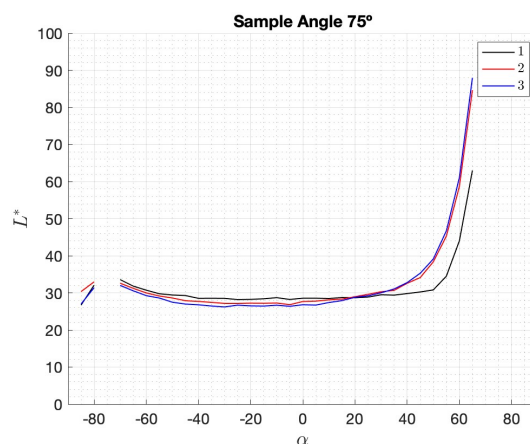


Figure B.90: Red BIPV L^* reproducibility at 75°

B.19 Reproducibility of Special Black BIPV

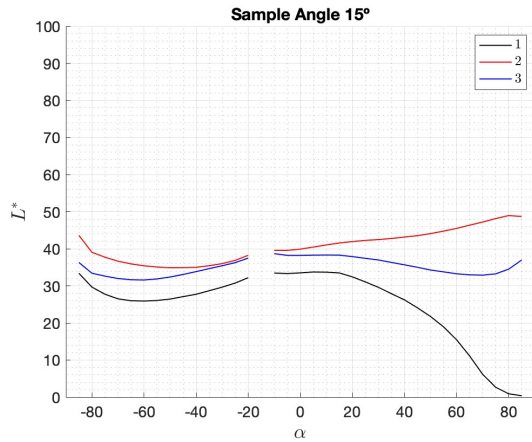


Figure B.91: Special Black BIPV L^* reproducibility at 15°

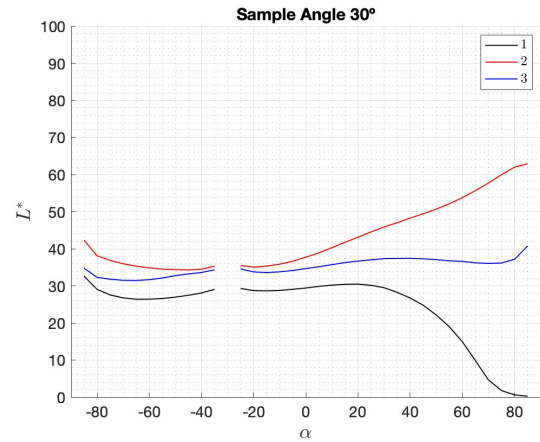


Figure B.92: Special Black BIPV L^* reproducibility at 30°

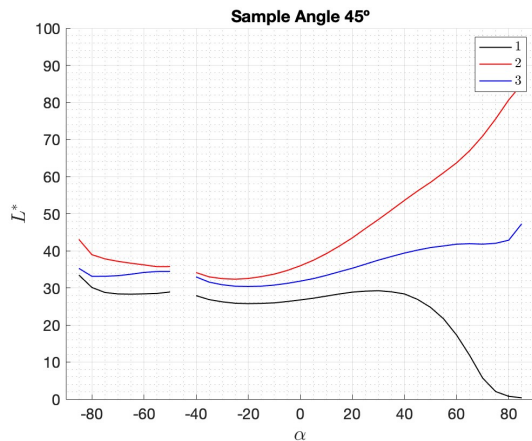


Figure B.93: Special Black BIPV L^* reproducibility at 45°

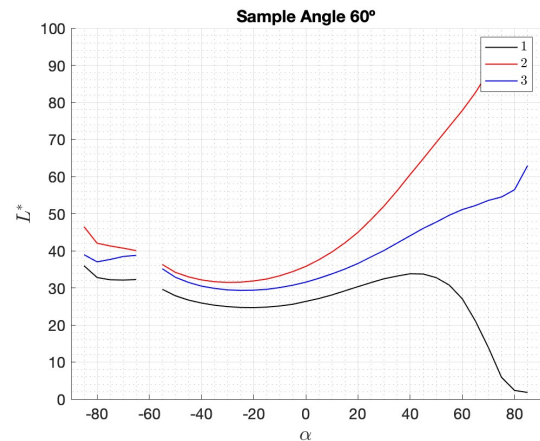


Figure B.94: Special Black BIPV L^* reproducibility at 60°

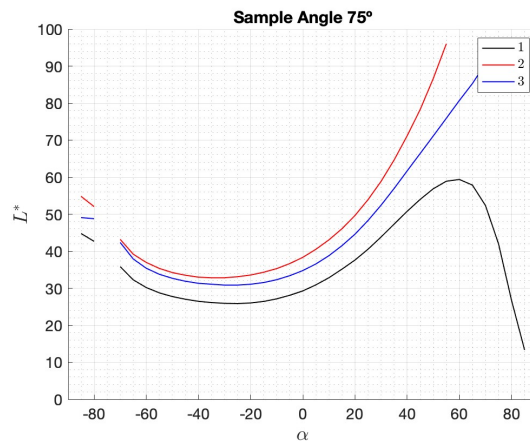


Figure B.95: Special Black BIPV L^* reproducibility at 75°

B.20 Reproducibility of Special Black BIPV Rotated

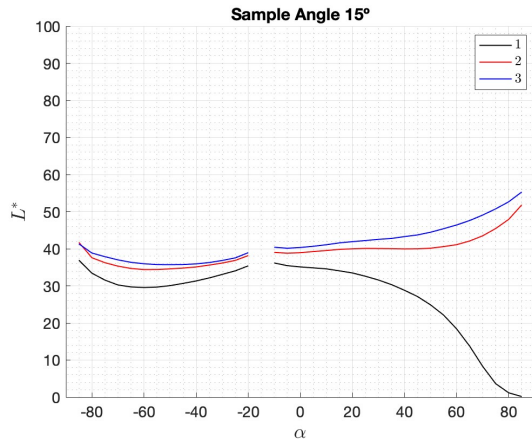


Figure B.96: Special Black BIPV Rotated L^* reproducibility at 15°

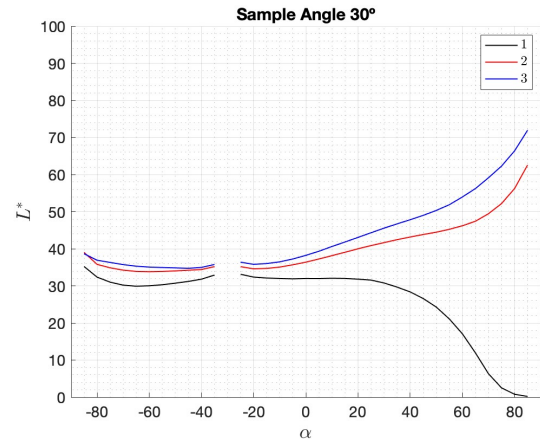


Figure B.97: Special Black BIPV Rotated L^* reproducibility at 30°

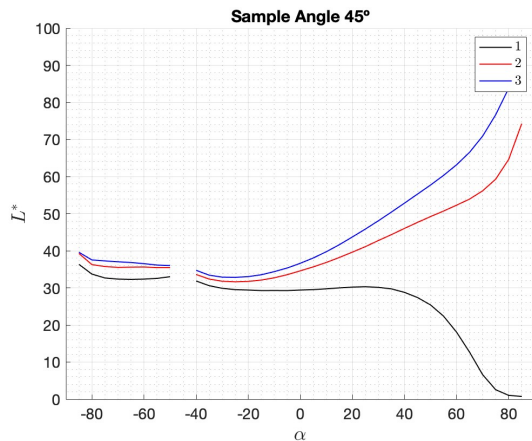


Figure B.98: Special Black BIPV Rotated L^* reproducibility at 45°

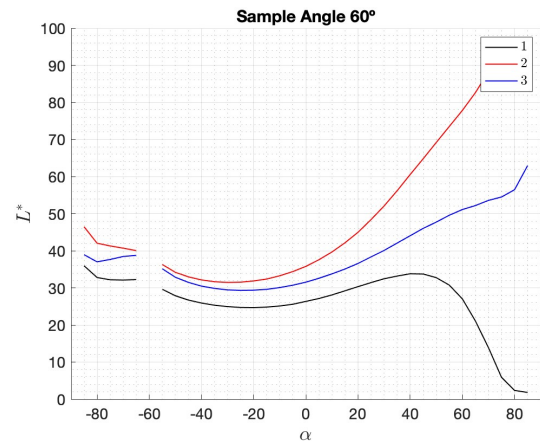


Figure B.99: Special Black BIPV Rotated L^* reproducibility at 60°

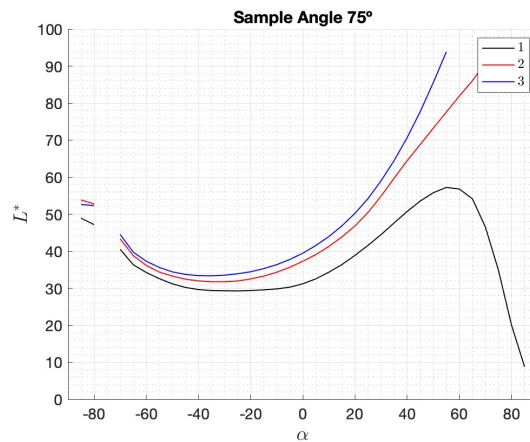


Figure B.100: Special Black BIPV Rotated L^* reproducibility at 75°

B.21 Reproducibility of Yellow BIPV

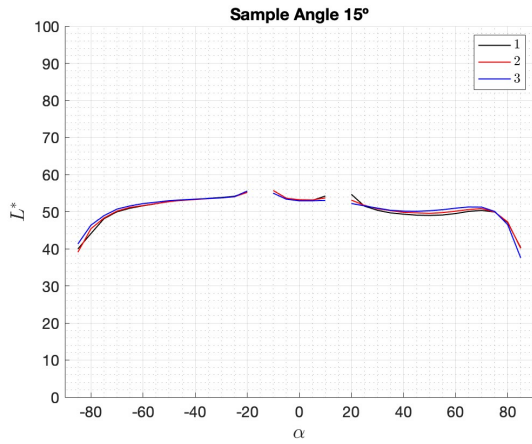


Figure B.101: Yellow BIPV L^* reproducibility at 15°

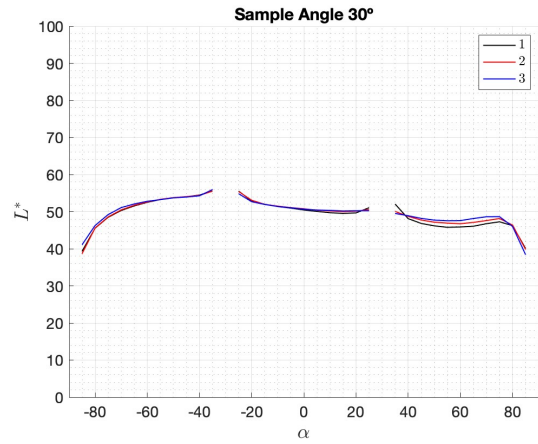


Figure B.102: Yellow BIPV L^* reproducibility at 30°

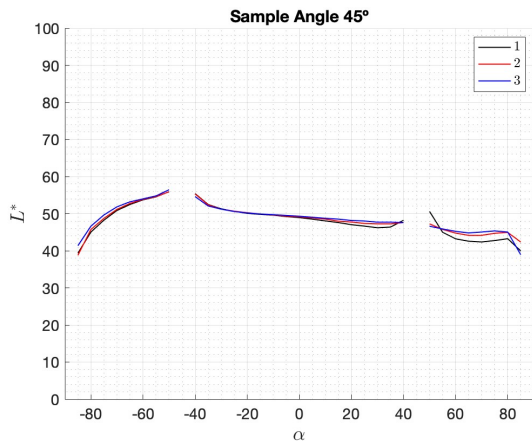


Figure B.103: Yellow BIPV L^* reproducibility at 45°

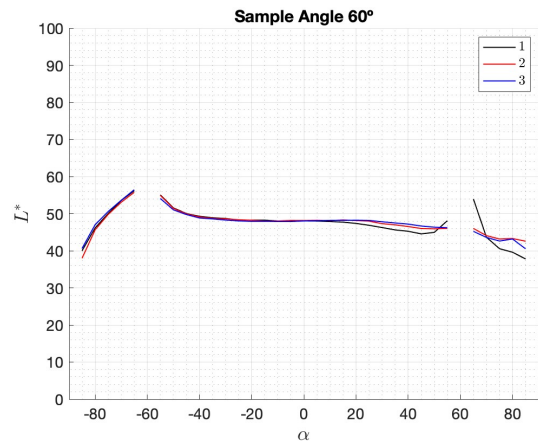


Figure B.104: Yellow BIPV L^* reproducibility at 60°

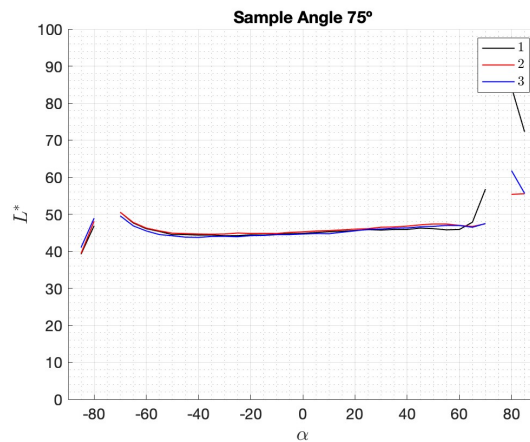


Figure B.105: Yellow BIPV L^* reproducibility at 75°

B.22 Reproducibility of Yellow Tile

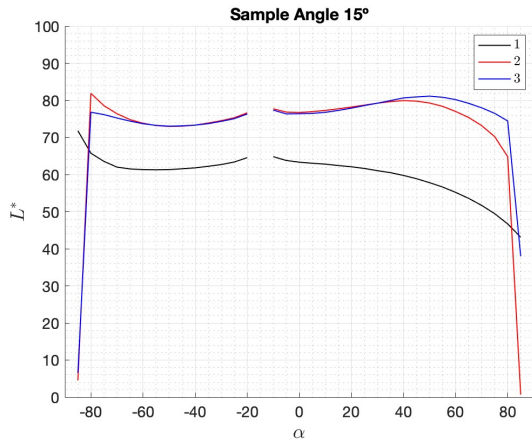


Figure B.106: Yellow Tile L^* reproducibility at 15°

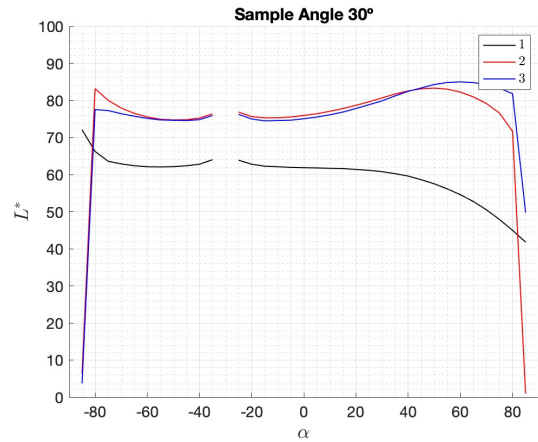


Figure B.107: Yellow Tile L^* reproducibility at 30°

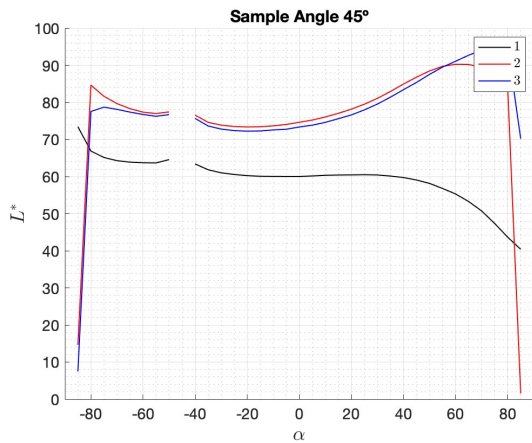


Figure B.108: Yellow Tile L^* reproducibility at 45°

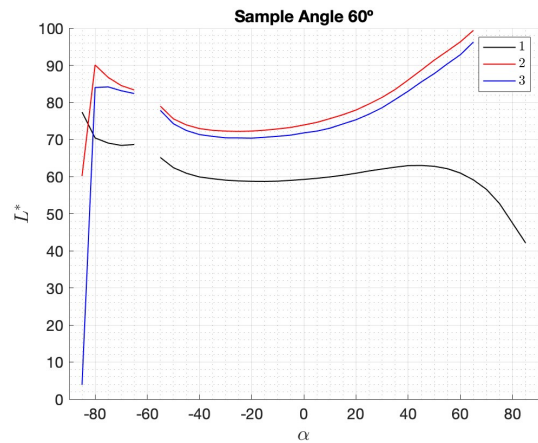


Figure B.109: Yellow Tile L^* reproducibility at 60°

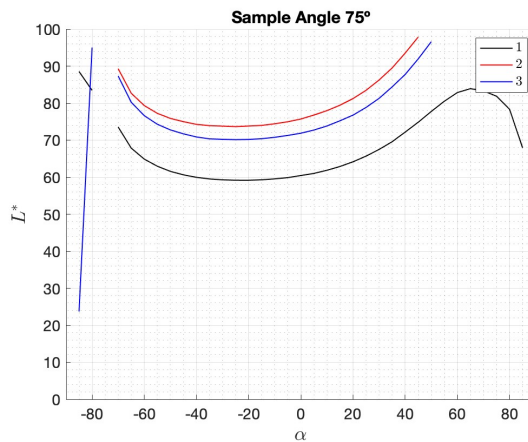


Figure B.110: Yellow Tile L^* reproducibility at 75°

B.23 Reproducibility of Yellow Tile Rotated

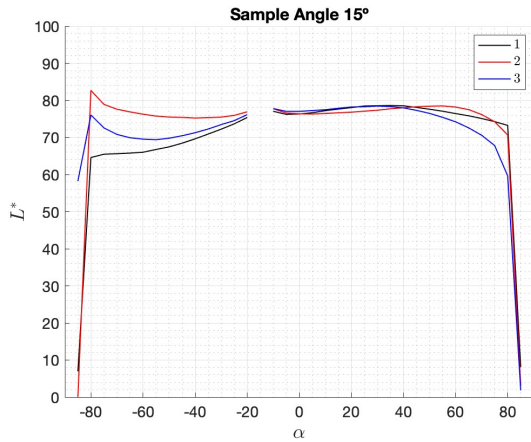


Figure B.111: Yellow Tile Rotated L^* reproducibility at 15°

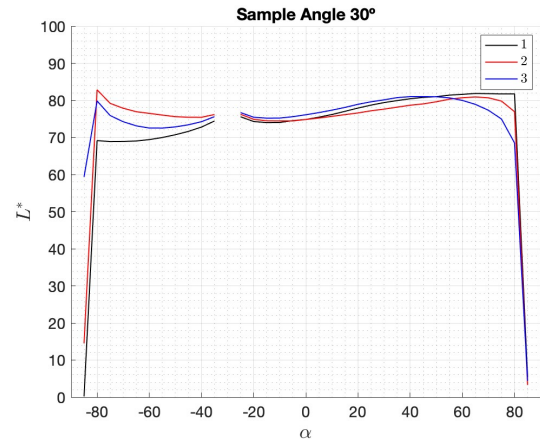


Figure B.112: Yellow Tile Rotated L^* reproducibility at 30°

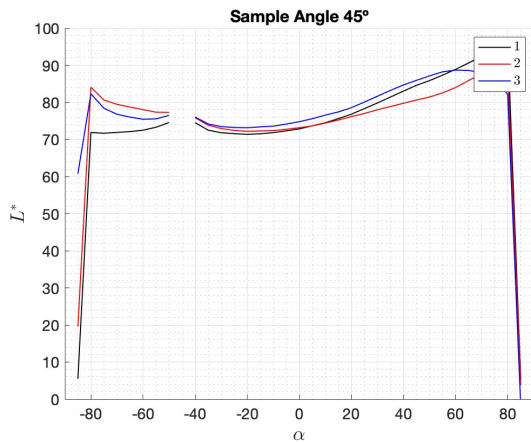


Figure B.113: Yellow Tile Rotated L^* reproducibility at 45°

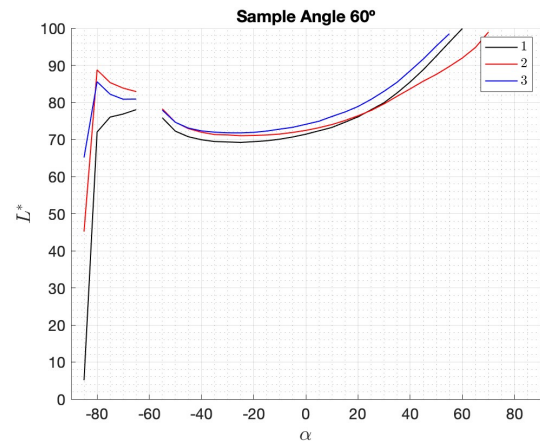


Figure B.114: Yellow Tile Rotated L^* reproducibility at 60°

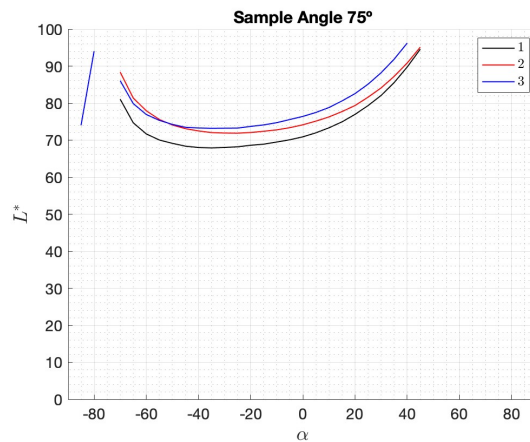


Figure B.115: Yellow Tile Rotated L^* reproducibility at 75°

Technical
University of
Denmark

Ørsteds Plads, Bygning 343
2800 Kgs. Lyngby
Tlf. +45 4525 6352

<https://electro.dtu.dk/>